Newcastle University
Faculty of Science, Agriculture and Engineering
School of Civil Engineering and Geosciences

Observability and estimation of geocentre motion using multi-satellite laser ranging

Ciprian Bogdan Spatar

Thesis submitted for the degree of
Doctor of Philosophy

June 2016

Abstract

Artificial satellites orbit about the Earth's system centre of mass, a point known as the geocentre that conventionally defines the long-term origin of the terrestrial reference frame (TRF). In a frame attached to the Earth's crust, the geocentre exhibits motions on sub-daily to secular time scales due to various geophysical processes. Annual variations induced by the redistribution of fluid mass in the Earth's surface layer are most prominent and can bias ice mass balance and sea level change estimates if neglected. Theoretically, these annual variations are directly observable by any satellite geodetic technique, but orbit modelling complications affect the retrieval of geocentre motion from Global Navigation Satellite Systems (GNSS) and Doppler Orbitography and Radiopositioning Integrated by Satellite (DORIS) data. This study focuses on Satellite Laser Ranging (SLR), the only technique proven to yield reliable geocentre motion estimates via translational approaches.

By means of collinearity diagnosis applied to the determination of geocentre motion using the network shift approach, it is shown that, subject to certain parameterisation constraints, the low Earth orbiters (LEOs) Starlette, Ajisai and the Laser Relativity Satellite (LARES) can beneficially supplement the traditionally employed pair Laser Geodynamics Satellite (LAGEOS) 1 and 2. In particular, the combination of LAGEOS-1 and 2 with LARES data can improve the observability of the geocentre coordinates by 25–30% on average compared to LAGEOS–only solutions due to both the larger number of observations and the proven higher sensitivity of LARES to geocentre motion. Tests involving different satellite combinations show that the contribution of Stella is minor owing to its quasi-polar orbit, whereas observations to the medium Earth orbiters (MEOs) Etalon-1 and 2 are too infrequently acquired to benefit the retrieval of geocentre motion and possibly other parameters of geophysical interest. An analysis of SLR data spanning two decades partitioned in weekly batches reveals that geocentre motion estimates derived from LAGEOS–Starlette–Stella–Ajisai combinations are contaminated by modelling errors to a larger extent than in LAGEOS–only solutions and, without considerable advances in orbit modelling, the exploitation of the high sensitivity of Starlette and Ajisai to geocentre motion appears remote. Compounded by the short tracking history of LARES, a conclusive assessment of the long-term quality of LAGEOS–LARES solutions is infeasible at present.

Similar to other geodetic parameters, the geocentre coordinates exhibit temporal correlations that have been typically neglected in previous studies. The power spectral densities (PSDs) of weekly derived geocentre coordinates display a power-law behaviour at long periods and white noise flattening for frequencies above 4 cycles per year (cpy). When temporal dependencies are appropriately modelled using one of the readily available maximum likelihood estimation (MLE) software implementations, the uncertainties of the annual amplitude and phase estimates inflate by an average factor of 1.6 for weekly time series over 12 years in length. The formal errors of the linear and quadratic trend estimates amplify by a larger factor of 2.2–2.3. First-order autoregressive noise plus white noise and power-law noise are the preferred stochastic models in most cases based on model-selection criteria. As demonstrated through the analysis of independent time series, for sampling periods longer than one week the first-order autoregressive model becomes more competitive on its own due to the suppression of white noise at high frequencies, but the power-law noise model is also occasionally preferred.

Kinematic estimates of geocentre coordinates are highly coherent with network shift results across the entire frequency range only when station positions are simultaneously solved for. Additionally, network shift estimates are more coherent with kinematic results when the scale parameter is omitted from the functional model of the similarity transformation linking the quasi-instantaneous frames and the secular frame. In addition to draconitic errors related to solar radiation pressure modelling, long-period tidal aliases due to mismodelled tidal constituents also contaminate geocentre motion estimates. Independent geodetic estimates and geophysical model predictions validating the results from this study agree that the annual geocentre motion signals have amplitudes of 2–3 mm in the equatorial components and 4–6 mm in the Z component. The maximum geocentre vector magnitude of about 7 mm is attained in July.

Acknowledgements

Many individuals and institutions acknowledged here have contributed either directly or indirectly to the successful completion of this thesis. First, I would like to express my gratitude to my supervisors, Professor Philip Moore and Professor Peter Clarke, for their patience, invaluable advice and constructive comments that highly improved the quality of this manuscript. Special thanks go to Professor Matt King, currently based at the University of Tasmania, for offering me the opportunity to study at Newcastle University and for his supervision during the early stages of my studies.

I am indebted to Dr Nigel Penna for the offer to work on a collateral project that enhanced my research skills and provided much needed funding to conduct the work underlying this thesis. Thanks are also due to other academic and support staff from the School of Civil Engineering and Geosciences for their help at different stages of the project. My peers from the Geodesy group are also acknowledged for occasional support in debugging software and understanding theoretical concepts, as well as for the enjoyable social activities we were engaged in together.

I am also grateful to all friends and acquaintances for keeping me entertained outside the long office hours. Last but not least, my deepest gratitude goes to my family for their uninterrupted moral support, their financial support at times of need and warm welcomes each time I visited them. Without their substantial contribution this work would have been incomplete.

This research was partly funded by Newcastle University, the Dinu Patriciu Foundation and the Romanian–American Foundation. The International Laser Ranging Service (ILRS; *Pearlman et al.*, 2002) provided SLR data through its two data centres. This thesis was prepared using the LaTeX typesetting system and most figures were generated using the Python plotting library `matplotlib` (*Hunter*, 2007), the Generic Mapping Tools (GMT; *Wessel et al.*, 2013) and CorelDRAW.

Contents

List of Figures **xi**

List of Tables **xv**

Abbreviations **xvii**

1 Introduction **1**

1.1 The geocentre and associated terminology 1

1.2 Causes of geocentre motion 4

1.3 Geodetic implications of geocentre motion 5

1.4 Research motivation and objectives 6

1.5 Thesis outline 8

2 Fundamentals of reference systems and satellite geodesy **9**

2.1 Terrestrial reference systems and frames 9

2.1.1 International Terrestrial Reference System and Frame 9

2.1.2 Earth orientation parameters 11

2.2 Satellite orbits 12

2.2.1 Keplerian motion 12

2.2.2 Perturbed motion 14

2.3 Satellite laser ranging 16

2.3.1 Data acquisition and processing 16

2.3.2 Spherical geodetic satellites 18

2.3.3 Tracking stations 22

2.4 Faust updates 23

3 Geocentre motion modelling approaches **25**

3.1 Introduction 25

3.2 Translational approaches 25

3.2.1 The dynamic approach 26

3.2.2 The network shift approach 30

3.2.3 The kinematic approach 32

3.3 Deformation approaches . . . 33
3.3.1 Geopotential and surface mass . . . 34
3.3.2 The degree-1 deformation approach . . . 37
3.3.3 The CM method . . . 41
3.3.4 Rigorous parameter combination . . . 42
3.4 Forward modelling . . . 44
3.5 Inverse modelling . . . 49
3.6 Secular geocentre motion . . . 51
3.7 Summary . . . 54

4 Collinearity assessment of geocentre coordinates 57
4.1 Introduction . . . 57
4.2 Collinearity diagnosis in geodetic data analysis . . . 58
4.3 Satellite data and processing strategy . . . 61
4.3.1 Data, network and conventions . . . 61
4.3.2 Standard parameterisation . . . 66
4.3.3 Drag coefficient modelling . . . 67
4.4 Results . . . 68
4.4.1 LAGEOS-1 and 2 solutions . . . 69
4.4.2 LAGEOS–Etalon combined solutions . . . 71
4.4.3 LAGEOS–Starlette–Stella–Ajisai combined solutions . . . 72
4.4.4 LAGEOS–LARES combined solutions . . . 76
4.4.5 Effects of solar radiation pressure modelling . . . 78
4.4.6 Comparison of solutions . . . 80
4.5 Summary . . . 83

5 Network shift estimates of geocentre coordinates 87
5.1 Introduction . . . 87
5.2 Model parameter estimation . . . 88
5.2.1 Functional model . . . 88
5.2.2 Stochastic model . . . 89
5.2.3 Maximum likelihood estimation . . . 90
5.3 Data statistics and processing strategy . . . 92
5.3.1 Network and satellite data . . . 92
5.3.2 Analysis strategy . . . 94
5.4 Geocentre motion time series . . . 96
5.4.1 LAGEOS-1 and 2 solution . . . 96
5.4.2 LAGEOS–Etalon combined solution . . . 106
5.4.3 LAGEOS–Starlette–Stella–Ajisai combined solution . . . 109

5.4.4 LAGEOS–LARES combined solution . . . 113
5.5 Effects of network geometry changes . . . 115
5.6 Comparisons . . . 118
5.6.1 Annual signals . . . 118
5.6.2 Velocities and accelerations . . . 120
5.7 Summary . . . 121

6 Kinematic estimates of geocentre coordinates 125
6.1 Introduction . . . 125
6.2 Validation of the processing strategy . . . 126
6.3 Geocentre motion time series . . . 130
6.3.1 Kinematic estimates with fixed datum . . . 130
6.3.2 Seasonally adjusted series . . . 132
6.3.3 Systematic and network geometry effects . . . 134
6.3.4 CSR monthly LAGEOS-1 and 2 solution . . . 136
6.4 Comparisons with independent results . . . 138
6.4.1 Annual signals . . . 139
6.4.2 Velocities and accelerations . . . 141
6.5 Summary . . . 143

7 Conclusions and outlook 145
7.1 Summary of findings . . . 145
7.2 Perspectives and directions for future work . . . 148

References 151

List of Figures

1.1 Schematic representation of the reference frames used in geodesy 2

2.1 Keplerian orbit 13
2.2 Timeline of geodetic satellite launches since 1975 18
2.3 The LAGEOS-1 and Etalon-1 satellites 19
2.4 The Starlette, Ajisai and LARES satellites 20
2.5 The ILRS tracking network in mid-2016 22

3.1 Cartesian and spherical coordinates of a satellite and CM in the CF frame 26
3.2 Observation geometry of the geocentre vector in the kinematic approach . 32
3.3 Average atmospheric surface pressure in July 2015 from NCEP/NCAR . . 45

4.1 The SLR network during 30 December 2012 – 28 December 2013 61
4.2 Station distribution 62
4.3 Number of stations with more than 20 NPs and number of NPs 63
4.4 Ground tracks of LAGEOS-1/2 and LARES, 28 July – 3 August, 2013 . . 63
4.5 Drag coefficients as piecewise constant and piecewise linear functions . . . 68
4.6 Median formal errors of the geocentre coordinates as a function of drag coefficient spacing 72
4.7 Differences in the RMS of observation residuals between the solution with weekly drag coefficients and the solution with daily drag coefficients 73
4.8 Signature and proper signature of a 1 cm geocentre offset along each axis on ranges to LAGEOS-1/2, Starlette, Stella and Ajisai 75
4.9 Median formal errors of the geocentre coordinates in different solutions . . 76
4.10 Differences in the RMS of LARES observation residuals 78
4.11 Median formal errors of the geocentre coordinates when the SRP coefficients of all satellites are estimated 79
4.12 Median formal errors of the geocentre coordinates in eight solutions 80
4.13 Formal error box plots for the Z geocentre coordinate in eight solutions . . 81
4.14 Geocentre coordinates obtained via the network shift approach 82

5.1 The SLR network during 1995.0–2015.0 92

5.2 Station distribution in LAGEOS-1/2 solutions 93
5.3 Number of stations and number of NPs in LAGEOS-1/2, LAGEOS–Starlette–Stella–Ajisai and LAGEOS–LARES solutions 94
5.4 Weekly RMS of observation residuals for LAGEOS-1/2 97
5.5 Geocentre coordinates from LAGEOS data via the network shift approach 98
5.6 Amplitude spectra of the geocentre coordinates from the LAGEOS-1/2 solution 99
5.7 Histograms of the geocentre coordinate residuals from LAGEOS-1/2 100
5.8 Correlograms of the geocentre coordinate residuals from LAGEOS-1/2 . . . 101
5.9 Quadratic, annual and semi-annual fits to LAGEOS-1/2 series 103
5.10 Power spectra of the geocentre coordinate residuals from LAGEOS-1/2 and power spectra of three best-fit noise models 104
5.11 Differences between the geocentre coordinates estimated without and alongside a scale parameter from the LAGEOS-1/2 solution 105
5.12 Correlograms of the geocentre coordinate residuals from the LAGEOS–Etalon solution 107
5.13 Quadratic, annual and semi-annual fits to LAGEOS–Etalon series 108
5.14 Correlogram of the Z geocentre coordinate whitened residuals from the LAGEOS–Etalon solution 109
5.15 Smoothed LAGEOS–only and LAGEOS–Starlette–Stella–Ajisai geocentre motion time series 109
5.16 Amplitude spectra of the geocentre coordinates from the LAGEOS–Starlette–Stella–Ajisai solution and the LAGEOS-1/2 solution 110
5.17 Quadratic, annual and semi-annual fits to LAGEOS–Starlette–Stella–Ajisai series 111
5.18 Power spectra of the geocentre coordinate residuals from the LAGEOS–Starlette–Stella–Ajisai solution 112
5.19 Unfiltered geocentre coordinates from the LAGEOS–only and LAGEOS–LARES solutions over 2012.1–2015.0 113
5.20 Amplitude spectra of the geocentre coordinates from the LAGEOS–LARES solution and the LAGEOS-1/2 solution 115
5.21 Correlograms of the geocentre coordinate residuals from the LAGEOS–LARES solution 116
5.22 The SLR sub-network used for the estimation of geocentre motion from LAGEOS-1/2 data 117
5.23 Geocentre coordinates from LAGEOS-1/2 data using the sub-network depicted in Figure 5.22 118
5.24 Scale factors for the uncertainties of the geocentre motion annual amplitudes obtained under assumption of WN only 119

5.25 Scale factors for the uncertainties of the geocentre velocities obtained under assumption of WN only 121

6.1 LAGEOS–only geocentre motion time series obtained using the kinematic approach by estimating (KA_est) and fixing (KA_fix) station positions . . 127
6.2 One-sided coherence spectra and phase spectra between network shift and kinematic (KA_est and KA_fix) geocentre motion estimates 129
6.3 Amplitude spectra of the geocentre coordinates from the KA_fix and KA_est solutions 131
6.4 Power spectra of the geocentre coordinate residuals from KA_est 133
6.5 Smoothed KA_est, KA_allrb and KA_subnet time series 135
6.6 Ground track and magnitude of the geocentre vector 136
6.7 Decimated KA_subnet time series and CSR monthly series 137
6.8 Power spectra of the geocentre coordinate residuals from the CSR series . . 138
6.9 Phasor diagrams of the annual geocentre motion estimates 141

List of Tables

2.1 Selected orbital parameters of spherical geodetic satellites 21
2.2 Faust updates performed during this project 23

3.1 Degree-1 load Love numbers for different reference frames 38
3.2 Geophysical fluid models and model parameters 48

4.1 Selected physical parameters of spherical geodetic satellites 64
4.2 Data processing standards, models and conventions 65
4.3 Estimated orbital and global parameters in standard solutions 66
4.4 Median formal errors of the geocentre coordinates 70

5.1 A priori and estimated SRP coefficients for spherical geodetic satellites . . 95
5.2 Estimated global parameters and their a priori standard deviations 96
5.3 Percent reductions in AIC and BIC values for each functional-stochastic model with respect to a linear and WN functional-stochastic model 102
5.4 Summary statistics of the geocentre coordinates from the LAGEOS–only and LAGEOS–LARES solutions over 2012.1–2015.0 114
5.5 Amplitude and phase of annual geocentre motion from different solutions . 119
5.6 Geocentre velocities and accelerations obtained from different solutions . . 120

6.1 Summary statistics of the network shift and kinematic geocentre motion estimates from LAGEOS-1/2 data over 1995.0–2015.0 130
6.2 Aliased periods for the diurnal and semi-diurnal tidal constituents 133
6.3 Summary statistics of the kinematic geocentre motion estimates from different LAGEOS-1/2 solutions over 1995.0–2015.0 135
6.4 Selected estimates of annual geocentre motion 140
6.5 Selected estimates of GIA and PDMT-induced geocentre velocities 142
6.6 Selected estimates of geocentre accelerations 142

Abbreviations

AC	Analysis Centre
ACF	Autocorrelation Function
AIC	Akaike Information Criterion
AR	Autoregressive
ASI	Agenzia Spaziale Italiana
AWG	Analysis Working Group
BIC	Bayesian Information Criterion
BIH	Bureau International de l'Heure
BLITS	Ball Lens In The Space
CATS	Create and Analyse Time Series
CCR	Corner Cube Reflector
CDDIS	Crustal Dynamics Data Information System
CE	Centre of mass of the solid Earth
CF	Centre of surface Figure
CH	Centre of surface Height figure
CIP	Celestial Intermediate Pole
CL	Centre of surface Lateral figure
CM	Centre of Mass of the Earth system
CN	Centre of Network
CNES	Centre National d'Études Spatiales
CSR	Center of Space Research
DORIS	Doppler Orbitography and Radiopositioning Integrated by Satellite
ECCO	Estimating the Circulation and Climate of the Ocean
ECMWF	European Centre for Medium-Range Weather Forecasts
EDC	EUROLAS Data Center
EDoF	Equivalent Degrees of Freedom
EGS	Experimental Geodetic Satellite
EOP	Earth Orientation Parameter
ERA	Earth Rotation Angle
ERP	Earth Rotation Parameter
ESA	European Space Agency
EWH	Equivalent Water Height

FE	Fluid Envelope
FES	Finite Element Solution
FESOM	Finite Element Sea Ice–Ocean Model
GCRS	Geocentric Celestial Reference System
GFS	Global Forecast System
GFZ	GeoForschungsZentrum
GGM	Generalised Gauss–Markov
GGOS	Global Geodetic Observing System
GIA	Glacial Isostatic Adjustment
GLDAS	Global Land Data Assimilation System
GLIMS	Global Land Ice Measurements from Space
GLONASS	Global'naya Navigatsionnaya Sputnikovaya Sistema
GMSL	Global Mean Sea Level
GNSS	Global Navigation Satellite Systems
GOT	Goddard Ocean Tide
GPS	Global Positioning System
GRACE	Gravity Recovery and Climate Experiment
GRS	Geocentric Reference System
IAG	International Association of Geodesy
IAU	International Astronomical Union
IB	Inverted Barometer
ICRF	International Celestial Reference Frame
ICRS	International Celestial Reference System
IDS	International DORIS service
IERS	International Earth Rotation and Reference Systems Service
IGS	International GNSS Service
ILRS	International Laser Ranging Service
ITRF	International Terrestrial Reference Frame
ITRS	International Terrestrial Reference System
IUGG	International Union of Geodesy and Geophysics
IVS	International VLBI Service
JAXA	Japan Aerospace Exploration Agency
JPL	Jet Propulsion Laboratory
LaD	Land Dynamics
LAGEOS	Laser Geodynamics Satellite
LARES	Laser Relativity Satellite
Laser	Light amplification by stimulated emission of radiation
LEO	Low Earth Orbiter
LOD	Length Of Day
LSDM	Land Surface Discharge Model

LSM	Land Surface Model
Mac-PDM	Macro-scale–Probability-Distributed Moisture model
MCP	Micro-Channel Plate
MEO	Medium Earth Orbiter
MLE	Maximum Likelihood Estimation
NASA	National Aeronautics and Space Administration
NASDA	National Space Development Agency
NCAR	National Center for Atmospheric Research
NCEP	National Centers for Environmental Prediction
Nd:YAG	Neodymium-doped Yttrium Aluminium Garnet
NERC	Natural Environment Research Council
NIB	Non-Inverted Barometer
NNR	No-Net-Rotation
NNT	No-Net-Translation
NORAD	North American Aerospace Defense Command
OBP	Ocean Bottom Pressure
OGCM	Oceanic General Circulation Model
OMCT	Ocean Model for Circulation and Tides
OPR	Once Per Revolution
PDMT	Present-Day Mass Trend
PL	Power-Law
POD	Precise Orbit Determination
PREM	Preliminary Reference Earth Model
PSD	Power Spectral Density
RMS	Root Mean Square
SD	Standard Deviation
SI	Système International d'unités
SINEX	Solution Independent Exchange
SLE	Sea Level Equation
SLR	Satellite Laser Ranging
SLRF	Satellite Laser Ranging Frame
SOFA	Standards of Fundamental Astronomy
SPAD	Single-Photon Avalanche Diode
SPOT	Satellite Pour l'Observation de la Terre
SRP	Solar Radiation Pressure
TCG	Geocentric Coordinate Time
TRF	Terrestrial Reference Frame
TRS	Terrestrial Reference System
TT	Terrestrial Time
TWS	Terrestrial Water Storage

UT	Universal Time
UTC	Coordinated Universal Time
VIF	Variance Inflation Factor
VLBI	Very Long Baseline Interferometry
WASMOD-M	Water And Snow balance Modeling system–Macro-scale
WBM	Water Balance Model
WESTPAC	Western Pacific Laser Tracking Network Satellite
WGHM	WaterGAP Global Hydrology Model
WGI	World Glacier Inventory
WN	White Noise
WRMS	Weighted Root Mean Square

Chapter 1

Introduction

The Earth system composed of the solid Earth and its fluid envelope (FE) formed by the hydrosphere and the atmosphere undergoes changes on broad spatio-temporal scales. Physical processes acting within the dynamic Earth system and interactions with the Moon and the Sun alter the Earth's geometric shape, orientation in space and gravity field, the three pillars underpinning the science of geodesy. The representation and monitoring of such changes using geodetic observations require the adoption of reference systems and their realisation as reference frames. Challenging scientific applications such as the study of sea level change, the determination of surface deformations and the precise orbit determination (POD) of artificial satellites place high demands on the accuracy and stability of reference frames.

Long known to the geophysical community, the degree-1 mode of Earth deformation due to surface loading (*Farrell*, 1972) has come under increased scrutiny of late due to its implications for various geodetic products (e.g. *Wu et al.*, 2012). The theory of degree-1 deformation (*Blewitt*, 2003) relates to the geocentre motion phenomenon describing the translational offset between two reference frames, as defined in this introductory chapter. Geocentre motion has been studied via different estimation approaches using Satellite Laser Ranging (SLR), Global Navigation Satellite Systems (GNSS), Doppler Orbitography and Radiopositioning Integrated by Satellite (DORIS), models of geophysical fluids and integrations of data and model outputs (see references in Chapter 3). Among the satellite geodetic techniques, SLR is generally held to provide the most reliable geocentre motion estimates. The determination of geocentre motion from laser ranging observations of spherical satellites constitutes the broad topic of this thesis.

1.1 The geocentre and associated terminology

According to the International Earth Rotation and Reference Systems Service (IERS) Conventions (2010) (*Petit and Luzum*, 2010), the geocentre represents the centre of mass of the Earth system (CM), a static point in inertial space with respect to satellite orbits.

As fluid mass redistributes within the Earth system and loads the crust, the geocentre moves with respect to the centre of mass of the solid Earth (CE). An observer external to the Earth would, however, perceive the reverse motion (i.e. the motion of CE relative to CM). CM and CE are the origins of two reference systems or frames used in geodesy and geophysics (Figure 1.1). A *reference frame* constitutes a realisation of a reference system through discrete physical points with locations determined by observation. A *reference system* is an abstract coordinate system in three-dimensional space with conventionally chosen origin, scale and orientation. Reference systems and frames have terrestrial and celestial variants used for positioning and tracking objects on the Earth's surface and distant celestial bodies, respectively. Any reference system whose origin lies at CM is known as a geocentric reference system.

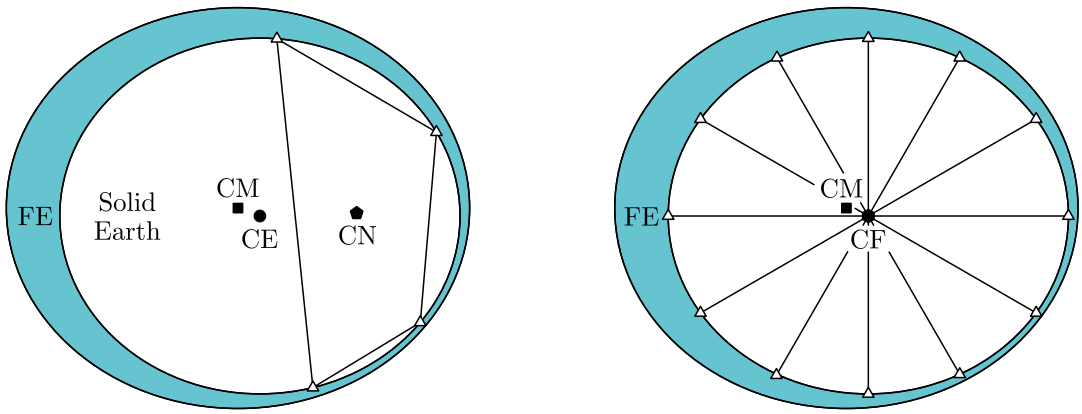

Figure 1.1 Schematic representation of the reference frames used in geodesy and geophysics (adapted from *Tregoning and van Dam*, 2005)

The CM frame is the natural choice for modelling orbital dynamics and is practically realised via quasi-instantaneous tracking networks that deform under surface loading. Solid Earth deformation is naturally modelled using load Love numbers in the CE frame (*Farrell*, 1972), which is, however, inaccessible to direct observation (*Blewitt*, 2003). A close approximation of the CE frame is the centre of surface figure (CF) frame (*Trupin et al.*, 1992; *Dong et al.*, 1997), theoretically materialised through an infinitely dense network of uniformly distributed stations anchored to the lithosphere. Only long-term station motions due to internal Earth processes such as tectonic plate motions and glacial isostatic adjustment (GIA) are considered in the CF frame (e.g. *Dong et al.*, 2003).

With over 70% of the Earth's surface covered by oceans, there are obvious limitations for the practical realisation of the CF frame. Recognising these limitations, *Wu et al.* (2002, 2003) introduced the concept of centre of network (CN), which defines the centroid of the polyhedron formed by operating ground stations at a particular epoch. Two other frames discussed by *Blewitt* (2003) are the centre of surface lateral figure (CL) frame and the centre of surface height figure (CH) frame. These frames allow no-net horizontal displacement and no-net vertical displacement, respectively.

In this study, the *geocentre vector* is defined with the direction from CF towards CM and a time-varying magnitude describing the *geocentre motion* or the *geocentre variations*. The components of the geocentre vector in a three-dimensional Cartesian coordinate system attached to a terrestrial reference frame (TRF) are known as the *geocentre coordinates*. This definition of geocentre motion is consistent with that provided in the IERS Conventions (2010) and several independent studies (*Vigue et al.*, 1992; *Malla et al.*, 1993; *Watkins and Eanes*, 1997; *Chen et al.*, 1999; *Bouillé et al.*, 2000; *Crétaux et al.*, 2002; *Wu et al.*, 2002, 2003, 2011, 2012, 2015; *Feissel-Vernier et al.*, 2006; *Swenson et al.*, 2008; *Collilieux et al.*, 2009; *Cheng et al.*, 2013a; *Meindl et al.*, 2013). Nevertheless, some authors (*Dong et al.*, 1997, 2003, 2014; *Kar*, 1997; *Blewitt and Clarke*, 2003; *Lavallée et al.*, 2006; *Métivier et al.*, 2010; *Klemann and Martinec*, 2011; *Rietbroek et al.*, 2012a) prefer to define geocentre motion as the variable offset of CF relative to CM, which implies a geocentre vector directed from CM towards CF and geocentre coordinates with opposite signs.

The TRF determined and maintained by the IERS is the International Terrestrial Reference Frame (ITRF). Each ITRF release constitutes a refined realisation of the International Terrestrial Reference System (ITRS). The latest two realisations, ITRF2008 (*Altamimi et al.*, 2011) and ITRF2014, are based on input time series of station positions and Earth orientation parameters (EOPs) from Very Long Baseline Interferometry (VLBI), SLR, GNSS and DORIS. The ITRF origin is currently constrained solely by the SLR input solution supplied by the International Laser Ranging Service (ILRS; *Pearlman et al.*, 2002), the International Association of Geodesy (IAG) service responsible for collecting and analysing SLR data.

Station positions have been traditionally modelled in the ITRF as piecewise linear functions containing one or more positions at a reference epoch (e.g. 2005.0 for ITRF2008) and an equivalent number of velocities for each Cartesian component. Discontinuities due to, for instance, equipment changes and earthquakes are implicitly accounted for by such a parameterisation, but their detection remains a challenging task best performed manually at present (*Gazeaux et al.*, 2013). Also implicitly considered by the current parameterisation of station positions are linear motions caused by geophysical phenomena acting on secular timescales (e.g. plate tectonics and GIA). As a consequence, the ITRF origin resembles CM on secular timescales, but short-term excursions from the long-term mean determined by SLR data are neglected. On seasonal and shorter timescales, the ITRF origin approaches CF but it is better described by CN given the sparseness and asymmetry of current tracking networks (*Dong et al.*, 2003). The IERS Conventions acknowledge this origin inconsistency and recommend the subtraction of non-linear geocentre motion from the regularised station positions supplied by the ITRF to compute quasi-instantaneous geocentric positions.

1.2 Causes of geocentre motion

Any geophysical process causing mass transport within the Earth or its surface layer contributes to geocentre motion. Starting on short timescales, semi-diurnal and diurnal ocean tides induce variations of less than 5 mm per constituent in the geocentre coordinates (*Watkins and Eanes*, 1997). The total ocean tidal contribution to the magnitude of the geocentre vector reaches 15–17 mm, as consistently predicted by modern ocean tide models (*Desai et al.*, 2014). Atmospheric pressure loading effects at diurnal S_1 and semi-diurnal S_2 periods have magnitudes of less than 1 mm (*de Viron et al.*, 2005). Tidal geocentre motion is considered well modelled and recommended as a correction to be applied to the a priori station coordinates by the IERS Conventions (2010) using the Finite Element Solution (FES) 2004 ocean tide model (*Lyard et al.*, 2006) and the S_1–S_2 pressure tide model of *Ray and Ponte* (2003). Geodetic estimates of geocentre motion should lack tidal contributions, but the presence of long-period aliases due to the mismodelling of tidal constituents is possible.

High-magnitude earthquakes have been recently shown to cause episodic geocentre variations of a few mm (*Sun and Dong*, 2014; *Zhou et al.*, 2015), which should not appear in geodetic estimates of geocentre motion if offsets are correctly identified in position time series and post-seismic deformations are appropriately modelled. However, the piecewise linear station motion model of ITRF2008 only coarsely approximates post-seismic deformations. To address this problem, the model is augmented with logarithmic and exponential functions (e.g. *Kreemer et al.*, 2006) in ITRF2014.[1]

The largest geocentre variations with amplitudes of several mm occur on seasonal timescales and are directly related to the terrestrial water cycle. Variable solar heating causes exchange of fluid mass between land, oceans and the atmosphere through processes such as surface and river run-off, groundwater flow, evaporation, evapotranspiration and precipitation. The geocentre motion induced by continental hydrology, oceans and the atmosphere has been evaluated by various authors using individual fluid models (*Dong et al.*, 1997; *Chen et al.*, 1999; *Bouillé et al.*, 2000; *Crétaux et al.*, 2002; *Moore and Wang*, 2003; *Feissel-Vernier et al.*, 2006; *Collilieux et al.*, 2009). Results tend to agree that continental hydrology is the primary contributor but also the least well constrained. The contributions of Antarctica, Greenland and alpine glaciers to seasonal geocentre motion are largely unknown.

On secular timescales, GIA and the present-day surface mass trend (PDMT) are the two primary contributors to geocentre motion. The signatures of GIA and PDMT can be decoupled using combinations of multiple data sets (*Wu et al.*, 2010; *Rietbroek et al.*, 2012b), whereas the effects of GIA alone may also be studied using models (*Greff-Lefftz*, 2000; *Klemann and Martinec*, 2011). Processes originating in the Earth's interior that

[1] http://itrf.ensg.ign.fr/ITRF_solutions/2014/doc/ITRF2014-PSD-model-eqs-IGN.pdf

span decadal to geological timescales are likely to induce negligible present-day geocentre motion (*Greff-Lefftz and Legros*, 2007; *Greff-Lefftz et al.*, 2010).

1.3 Geodetic implications of geocentre motion

As already mentioned, geocentre motion affects the nature of the ITRF origin, which follows CM only on secular timescales. The availability of a geocentric TRF on all timescales would benefit many scientific applications, including the monitoring of sea level change and surface mass variability using the Gravity Recovery and Climate Experiment (GRACE; *Tapley et al.*, 2004a) and satellite altimetry. One option to consistently reconcile the ITRF origin with CM is to expand the current piecewise linear parameterisation of station motion with annual and potentially semi-annual sinusoids accounting for the bulk of non-linear geocentre motion, as well as non-tidal loading effects at individual stations. A more radical alternative recently investigated by *Bloßfeld et al.* (2014) and *Wu et al.* (2015) is to derive coordinate time series valid over discrete (e.g. weekly) time intervals and thus embed non-linear motions of the geocentre and stations in quasi-instantaneous TRFs with CM as origin. With the current ITRF origin definition, the adoption of an annual geocentre motion model would support the geodetic and geophysical communities and ensure greater consistency among studies requiring such a model. Nevertheless, satellite geodetic techniques differ in their capability to retrieve geocentre motion (e.g. *Gobinddass et al.* 2009a; *Meindl et al.* 2013; *Rebischung et al.* 2014) and the use of an annual geocentre motion model from SLR, for example, in GNSS and DORIS applications may have detrimental effects.

As one of the most demanding scientific applications, the study of sea level change places stringent constraints on the ITRF origin accuracy and stability. Tide gauge records of relative sea level change require corrections for vertical land motion to derive absolute (geocentric) sea level change (e.g. *Church et al.*, 2004). The use of GNSS to infer these corrections has become standard practice in recent years (e.g. *Wöppelmann et al.*, 2009, 2014; *King et al.*, 2012; *Santamaría-Gómez et al.*, 2012), as it emerged that accounting only for the dominant effect of GIA using models is insufficient. Errors in the long-term realisation of the ITRF origin affect GNSS-derived vertical velocity estimates and propagate into the global mean sea level (GMSL) rate in a proportion that depends on the distribution of GNSS stations (*Collilieux and Wöppelmann*, 2011). Scale errors, however, map entirely into the GMSL trend derived from tide gauge data.

For altimetry-based determinations of GMSL, the largest detrimental effect originates from drift errors in the Z origin component (*Morel and Willis*, 2005; *Beckley et al.*, 2007). Recent assessments of the ITRF origin stability quote values of around 0.5 $\mathrm{mm\,yr^{-1}}$ for the equatorial components and 1 $\mathrm{mm\,yr^{-1}}$ for the Z component (*Wu et al.*, 2011; *Argus*, 2012). The latter figure may generate an error in the GMSL rate of about 0.2 $\mathrm{mm\,yr^{-1}}$ and even larger spurious effects on regional scales (e.g. *Blewitt et al.*, 2010). Sea level

studies require a TRF origin stable at the level of 0.1 mm yr^{-1}, as established through the Global Geodetic Observing System (GGOS) initiative (*Gross et al.*, 2009). Achieving this target will likely entail a reformulation of the station motion parameterisation within the ITRF, as well as substantial improvements in the realisation of the origin by SLR.

Neglecting seasonal geocentre motion during the orbit determination of altimetry satellites affects the consistency between Global Positioning System (GPS) and SLR/DORIS-derived orbits in the Z direction of the orbital frame (*Melachroinos et al.*, 2013; *Couhert et al.*, 2015). In particular, Jason-2 orbit differences display Z annual variations that can be reduced by a priori correcting ITRF station coordinates for geocentre motion (i.e. computing geocentric station positions). The SLR/DORIS-based orbits are more closely tied to the ITRF origin than GPS-based orbits for reasons attributed to GPS orbit modelling deficiencies (*Cerri et al.*, 2010). This inconsistency may affect inter-calibrations of satellite altimeters.

The geocentre coordinates are related to the degree-1 geopotential coefficients through a scale factor (see Chapter 3). Since the degree-1 geopotential coefficients equal zero in the CM frame, GRACE observations (i.e. inter-satellite ranges and their first and second time derivatives) inherently lack information on geocentre motion. Consequently, when quantifying mass variability in individual components of the Earth's fluid envelope, externally derived degree-1 geopotential coefficients need to be added to GRACE-inferred time-variable gravity fields. *Chambers et al.* (2004) showed that when including the SLR-derived annual geocentre motion model of *Chen et al.* (1999), GRACE estimates of seasonal oceanic mass variations are in better agreement with TOPEX/Poseidon and Jason-1 altimetry measurements corrected for steric effects. The incorporation of an annual geocentre motion model may also improve basin-scale terrestrial water storage (TWS) estimates derived from GRACE (*Chen et al.*, 2004). Although it is currently widely acknowledged that a geocentre motion model is required to complement GRACE observations, choosing from the multitude of available solutions is challenging and can even lead to the degradation of GRACE-derived products and potential biases in interpretation (*Chambers*, 2006; *Barletta et al.*, 2013). The regularly updated geocentre motion time series of *Swenson et al.* (2008) and *Cheng et al.* (2013a) are endorsed on the GRACE Tellus website.[2]

1.4 Research motivation and objectives

Geocentre motion has been known to the geodetic community since the 1970s (e.g *Stolz*, 1976a,b), but its determination from satellite tracking data only became feasible in the 1990s, as the satellite constellations matured and the tracking networks attained satisfactory global coverage. One of the first thorough investigations into the use of SLR data to derive geocentre motion was carried out by *Kar* (1997), whereas GPS results were

[2] http://grace.jpl.nasa.gov/data/get-data/geocenter/

reported earlier (e.g. *Vigue et al.*, 1992; *Malla et al.*, 1993). Recognising the importance of geocentre motion for scientific applications, the IERS initiated in 1997 a campaign aimed at improved understanding of the phenomenon using observational data and fluid models. The overall conclusion of the contributions collated in the IERS Technical Note No. 25 (*Ray*, 1999) was that seasonal variations, although small (less than ∼1 cm per component), are detectable by satellite geodetic techniques. While the tidal variations were already well determined, measurements and model predictions of the seasonal motion were only roughly consistent.

Tremendous progress has since been achieved with regard to the development of the ground infrastructures and space segments of satellite geodetic techniques, as well as the analysis of observations. Improvements in geocentre motion estimates naturally followed, but SLR solutions still typically feature only contributions from the two medium Earth orbiter (MEO) pairs Laser Geodynamics Satellite (LAGEOS) and Etalon, with few notable exceptions (e.g. *Cheng et al.*, 2013a; *Sośnica et al.*, 2014). A quantitative assessment of the potential benefits and pitfalls of augmenting LAGEOS and Etalon data with observations of the low Earth orbiters (LEOs) Starlette, Stella, Ajisai and Laser Relativity Satellite (LARES) is lacking. Furthermore, potential temporal dependencies between geocentre motion estimates are ordinarily neglected.

The aim of the current study is to appraise the observability of the geocentre coordinates in SLR solutions involving MEO–LEO data combinations and establish a framework for the rigorous analysis of geocentre motion time series. The objectives pursued to achieve this goal are the following:

- Undertake a survey of the existing geocentre motion modelling approaches.
- Establish the effects of supplementing LAGEOS observations with LEO data on the formal errors of the geocentre coordinates under different parameter setups.
- Verify the presence of temporal correlations in geocentre motion time series determined using the network shift approach.
- Assess the effects of modelling temporal correlations on the uncertainty estimates of seasonal and long-term signals.
- Validate the analysis strategy for the kinematic approach using the network shift results for benchmarking purposes.
- Examine the contamination level of geocentre motion time series by modelling errors.
- Compare the most robust geocentre motion model with published results.

By achieving these objectives, this study seeks to provide a platform for a better exploitation of the current constellation of spherical geodetic satellites to monitor geocentre motion. An improved tie of the ITRF origin to CM is the long-term endeavour. The findings of this study may benefit individuals and institutions that carry out research on the topics of reference frames, surface mass variability and sea level change.

1.5 Thesis outline

This thesis is divided into seven chapters, including the current one, which defined geocentre motion, discussed its geophysical causes and its effects on geodetic products and stated the aim and objectives of this study. The novel contributions of this study lie in Chapters 4, 5 and 6.

Chapter 2 expands on the topic of reference systems and frames by providing an overview of the ITRS and its latest realisations, ITRF2008 and ITRF2014. Fundamental concepts of satellite orbits and space geodetic techniques are also covered, with special focus on SLR and satellite missions tailored for geodetic applications.

Chapter 3 reviews existing approaches for the estimation of geocentre motion from satellite tracking data, global observations of load-induced deformations, geophysical fluid models and combinations of measurements and model outputs. The methods rely on the demonstrated proportionality between (1) the geocentre coordinates, (2) the degree-1 geopotential coefficients and (3) the degree-1 surface mass (or load) coefficients and supply estimates for one of these triplets. A discussion of secular geocentre motion induced by PDMT and GIA is also included in this chapter.

Chapter 4 introduces the concept of collinearity diagnosis in the context of geodetic data analysis, with particular emphasis on the determination of geocentre motion via the network shift approach. Following the description of the employed SLR data set spanning the year 2013 and of the analysis strategy, the observability of the geocentre coordinates is assessed for four different satellite combinations with variable parameter setups. This chapter has been published in a nearly identical form in the Journal of Geodesy (*Spatar et al.*, 2015).

Chapter 5 adopts the parameterisation constraints obtained in Chapter 4 for the derivation of geocentre motion time series with lengths of up to 20 years using the network shift approach. The series are analysed in the time and frequency domains to check for serial correlations, dominant periodic signals and modelling errors. The optimal functional-stochastic model is chosen for each series by means of maximum likelihood estimation (MLE) and model-selection criteria. A discussion of the implications of modelling temporal correlations for the estimated parameter uncertainties concludes the chapter.

Chapter 6 explores the level of agreement between kinematic estimates of geocentre motion obtained under different parameterisations and the network shift results from Chapter 5 to validate the analysis strategy for the kinematic approach. Time series with removed annual and semi-annual signals are analysed in the frequency domain to identify discrete spectral features that relate to aliasing errors. Comparisons between the most robust geocentre motion model from this study and published results are also performed.

Finally, Chapter 7 draws the conclusions of the study and suggests potential directions for future work in the area of geocentre motion estimation with SLR.

Chapter 2

Fundamentals of reference systems and satellite geodesy

Similar to other geodetic applications, the determination of geocentre motion is closely related to the concepts of reference systems, reference frames and satellite orbital motion. This chapter provides an overview of the ITRS and its realisation via the ITRF, briefly discusses the theory of orbit determination and introduces the principle of laser ranging to artificial satellites. The space and ground segments of SLR are also described.

2.1 Terrestrial reference systems and frames

A Terrestrial Reference System (TRS) is defined by the IERS Conventions as a spatial reference system co-rotating with the Earth in its diurnal motion in space (*Petit and Luzum*, 2010). The origin, orientation and scale completely define a TRS. Geocentric TRSs have the origin at CM, an equatorial orientation with the Z axis coinciding with the Earth's rotation axis at a conventional epoch and the scale close to the International System of Units (Système International d'unités, SI) metre. The transformation of Cartesian coordinates and their linear rates between two TRSs is performed via three-dimensional similarity transformations. A TRF is the realisation of TRS through discrete crust-fixed points with precisely determined coordinates from the analysis of geodetic observations.

2.1.1 International Terrestrial Reference System and Frame

The ITRS is the geocentric TRS defined and realised by IERS, formally adopted for scientific applications by the International Union of Geodesy and Geophysics (IUGG) in 2007. Its unit of length is the SI metre and its orientation coincides with that of the obsolete Bureau International de l'Heure (BIH) terrestrial system at epoch 1984.0. The time evolution of the ITRS orientation is aligned to the horizontal motion of tectonic plates through a no-net-rotation (NNR) constraint. Realisations of the ITRS are produced by IERS under the designation ITRF.

Thirteen ITRF solutions have been produced since 1988, the latest two being ITRF2008 (*Altamimi et al.*, 2011) and ITRF2014. Starting with ITRF94 (*Boucher et al.*, 1996), the sixth ITRS realisation, any station position $\mathbf{p} = \begin{bmatrix} X & Y & Z \end{bmatrix}^T$ at epoch t has been represented using the linear model

$$\mathbf{p}(t) = \mathbf{p}(t_0) + \dot{\mathbf{p}}(t - t_0), \tag{2.1}$$

where t_0 is the adopted reference epoch and $\dot{\mathbf{p}}$ represents the station velocity. The numerical values of $\mathbf{p}(t_0)$ and $\dot{\mathbf{p}}$ are the main ITRF products, but since ITRF2005 (*Altamimi et al.*, 2007) a subset of EOPs has also been disseminated (see Section 2.1.2). For ITRF2014, model (2.1) was extended with a post-seismic deformation correction.

All ITRS realisations from ITRF94 onwards include contributions from the space geodetic techniques VLBI, SLR, GNSS and DORIS. In the first stage of the ITRF development, individual analysis centres (ACs) reprocess geodetic observations in batches of varying length per technique to generate solutions for various parameters. Well modelled geophysical effects on the geopotential and station positions are reduced during data analysis using models recommended by the IERS. Currently, only short period crustal deformations caused by solid Earth tides, ocean tides, S_1–S_2 atmospheric tides, the pole tide and the ocean pole tide are conventionally accounted for by ACs.

Redundant parameters are eliminated from the normal equations by ACs and the single-technique solutions for station coordinates and EOPs are supplied in the Solution Independent Exchange (SINEX) format to the combination centres of the IAG technique services, namely the International VLBI Service (IVS; *Schuh and Behrend*, 2012), the ILRS (*Pearlman et al.*, 2002), the International GNSS Service (IGS; *Dow et al.*, 2009) and the International DORIS Service (IDS; *Willis et al.*, 2010). The combination centres perform the intra-technique combinations using the individual AC solutions and deliver their products to the IERS ITRS Centre either as unconstrained normal equations or as constrained solutions. Following the stacking of the combined solutions into technique-specific secular frames, the inter-technique combination is performed using local ties and imposing velocity equality constraints at co-located sites. Additional details about the ITRF computation are provided, for example, by *Rebischung* (2014).

Among the most crucial aspects of any ITRF release is the definition of the origin, the scale and the orientation (i.e. the *datum definition*). The orientation of any new ITRF release succeeding ITRF92 has been aligned by convention to the orientation of the previous version, whereas the orientation time evolution inherently follows the NNR–NUVEL–1A plate motion model (*DeMets et al.*, 1994). The scale and origin realisations are more critical for scientific applications, as outlined in Chapter 1. For ITRF2008 and ITRF2014, the scale and its rate were defined as the average of the SLR and VLBI scales and scale rates, whereas the origin information was extracted from the SLR input solutions

alone. The ITRF2008 and ITRF2014 origins coincide with CM and have zero drifts at epochs 2005.0 and 2010.0, respectively.

The linear station motion model of the ITRF accounts for secular station displacements due to plate tectonics and GIA, but disregards non-linear motions at individual stations and geocentre motion. Consequently, users requiring quasi-instantaneous geocentric positions need to include the neglected effects using the formula

$$\mathbf{p}(t) = \mathbf{p}(t_0) + \dot{\mathbf{p}}(t - t_0) + \sum_i \Delta\mathbf{p}_i(t) - \mathbf{r}_{\mathrm{CM-CF}}(t), \tag{2.2}$$

where the $\sum_i \Delta\mathbf{p}_i(t)$ comprises all displacements modelled in the CF frame at epoch t and $\mathbf{r}_{\mathrm{CM-CF}}(t)$ represents the quasi-instantaneous non-linear geocentre motion.

2.1.2 Earth orientation parameters

The celestial reference system defined by the IERS is the International Celestial Reference System (ICRS). It is realised via the International Celestial Reference Frame (ICRF) using VLBI observations of distant celestial objects (i.e. quasars), whose position in space can be assumed fixed. The ICRS origin is located at the barycentre of the solar system and its orientation is fixed with respect to the considered quasars. Satellite orbits are appropriately modelled in the Geocentric Celestial Reference System (GCRS), a translated ICRS with the origin at CM.

The connection between the ITRS and the GCRS is performed through the Celestial Intermediate Pole (CIP) defined by the International Astronomical Union (IAU) and a rotation about the CIP axis by the Earth Rotation Angle (ERA). The time derivative of ERA is the Earth's angular velocity. For an arbitrary position vector $\mathbf{p}$, the modern formulation of the ITRS-to-GCRS transformation at epoch t is given by

$$\mathbf{p}_{\mathrm{GCRS}} = \mathbf{R}_{\mathrm{BPN}}\,\mathbf{R}_{\mathrm{ER}}\,\mathbf{R}_{\mathrm{PM}}\,\mathbf{p}_{\mathrm{ITRS}}, \tag{2.3}$$

where

- $\mathbf{R}_{\mathrm{BPN}}$ rotation matrix for *frame bias* (i.e. small rotation between the GCRS and the J2000.0 dynamic system defined by the mean ecliptic and equator of the standard epoch 1.5 January 2000) and *precession-nutation* (i.e. the motion of the CIP in the GCRS),
- $\mathbf{R}_{\mathrm{ER}}$ rotation matrix accounting for the Earth's rotation around the CIP axis (i.e. ERA),
- $\mathbf{R}_{\mathrm{PM}}$ rotation matrix for *polar motion* (i.e. the motion of the CIP in the ITRS).

The CIP position in the GCRS is given by the *celestial pole coordinates* (X_p, Y_p) yielded by the IAU 2006/2000A precession-nutation model (e.g. *Wallace and Capitaine*, 2006) and corrections termed *celestial pole offsets* $(\Delta X_p, \Delta Y_p)$, determined from VLBI observations.

ERA is linearly related to ΔUT1, the difference between the Universal Time UT1 and the Coordinated Universal Time (UTC). The negative time derivative of ΔUT1, referred to as the *excess length of day* (ΔLOD), represents the residual Earth revolution period with respect to the nominal LOD of 86 400 s. The *pole coordinates* (x_p, y_p) express the CIP position in the ITRS and, together with ΔUT1, define the *Earth rotation parameters* (ERPs). Daily values of these parameters, the linear rates of the pole coordinates ($\dot{x}_p$, $\dot{y}_p$) and ΔLOD have been included in ITRS realisations since ITRF2005. In addition, IERS regularly publishes estimates of *Earth orientation parameters* (EOPs), a generic term that includes celestial pole offsets alongside the three ERPs. Celestial pole offsets and ΔUT1 can only be retrieved using VLBI due to the necessity to simultaneously estimate orbital parameters for satellite geodetic techniques.

2.2 Satellite orbits

2.2.1 Keplerian motion

According to the principles of Newtonian mechanics, the unperturbed orbital motion of an artificial satellite of negligible mass with respect to the Earth's mass is described by the second-order differential equation

$$\ddot{\mathbf{r}} = -\frac{GM}{r^3}\mathbf{r}, \tag{2.4}$$

where

$\mathbf{r}$	geocentric position vector of the satellite with $\|\mathbf{r}\| = r$,
$\ddot{\mathbf{r}} = \frac{d^2\mathbf{r}}{dt^2}$	geocentric acceleration vector of the satellite,
GM	geocentric gravitational constant.

The geocentric gravitational constant GM is the product of the universal gravitational constant G and the Earth's mass M, whereas t represents inertial (i.e. dynamic) time. According to the IERS Conventions (2010), the numerical value of GM is $(398\,600\,441.8 \pm 0.8) \cdot 10^6$ m^3 s^{-2}. This value is consistent with the time system of the Geocentric Reference System (GRS) defined by the IAU, known as Geocentric Coordinate Time (TCG). However, Terrestrial Time (TT), a quasi-inertial time system that differs from TCG by a constant factor, is used for the integration of the equation of satellite motion. The TT-compatible value of GM is (e.g *Ries et al.*, 1992; *Chen et al.*, 2015)

$$GM = (398\,600\,441.5 \pm 0.8) \cdot 10^6 \text{ m}^3\,\text{s}^{-2}. \tag{2.5}$$

The position vector $\mathbf{r}$ and the velocity vector $\dot{\mathbf{r}} = \frac{d\mathbf{r}}{dt}$ form the state vector of the satellite, which may be uniquely converted to the following six independent orbital elements (Figure 2.1):

a	semi-major axis of orbital ellipse,
e	numerical eccentricity of orbital ellipse,
i	inclination of orbital plane,
Ω	right ascension of ascending node,
ω	argument of perigee,
T_0	epoch of perigee passage.

Several celestial mechanics and orbit determination textbooks (e.g. *Montenbruck and Gill*, 2000; *Tapley et al.*, 2004b; *Beutler*, 2005) provide the explicit formulae for performing the conversion. The six orbital elements, also known as *Keplerian elements*, can be conveniently chosen as the integration constants of (2.4), so that

$$\begin{aligned} \mathbf{r}(t) &= \mathbf{r}(t; a, e, i, \Omega, \omega, T_0), \\ \dot{\mathbf{r}}(t) &= \dot{\mathbf{r}}(t; a, e, i, \Omega, \omega, T_0), \end{aligned} \tag{2.6}$$

represent a particular solution of the equation of motion.

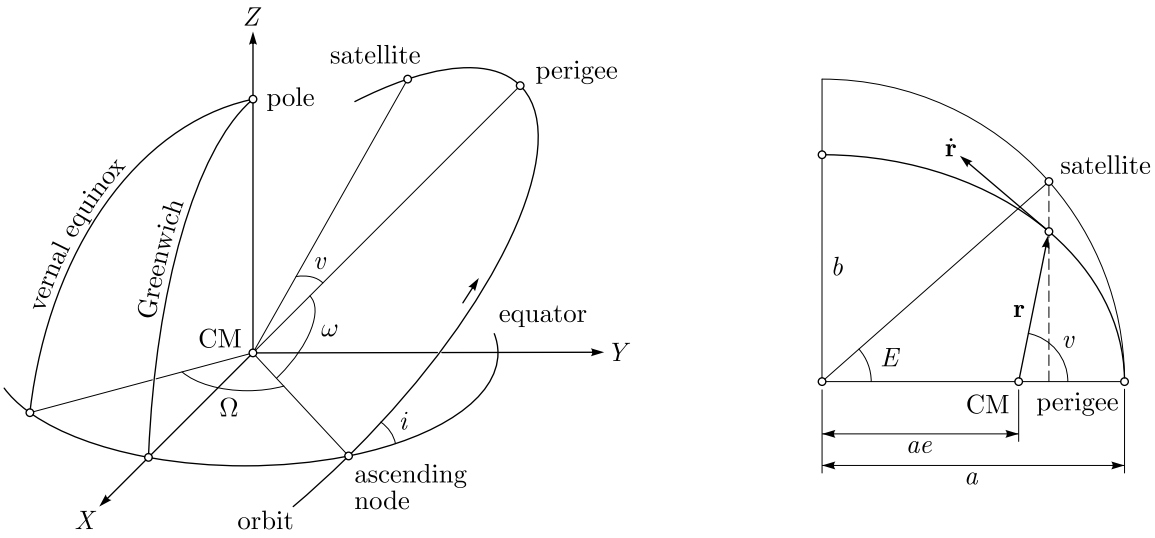

Figure 2.1 Graphical representation of the Keplerian orbit

From Kepler's third law, the mean angular velocity n of a satellite with revolution period P is given by

$$n = \frac{2\pi}{P} = \sqrt{\frac{GM}{a^3}}. \tag{2.7}$$

Three angular quantities known as *anomalies* describe the instantaneous position of a satellite within its orbit. The *eccentric anomaly* $E(t)$ and the *true anomaly* $v(t)$ are geometric quantities, whereas the *mean anomaly* $M(t)$ is an abstract quantity related to the mean angular velocity by

$$M(t) = n\,(t - T_0)\,. \tag{2.8}$$

The mean anomaly can thus replace T_0 in the set of six defining orbital elements.

2.2.2 Perturbed motion

One of the underlying assumptions of the equation of motion (2.4) is that of a spherically symmetric mass distribution within the Earth system. The Newtonian (or monopole) term $\frac{GM}{r^2}$ is the central force of orbital motion for artificial Earth satellites, but the actual inhomogeneous structure of the Earth and the interactions between artificial satellites and other celestial bodies give rise to additional gravitational forces. Moreover, the orbital motion is perturbed by forces of non-gravitational nature. The effects of perturbing forces can be accounted for by extending the equation of motion as follows:

$$\ddot{\mathbf{r}} = -\frac{GM}{r^3}\mathbf{r} + \ddot{\mathbf{r}}_p(t, \mathbf{r}, \dot{\mathbf{r}}, d_1, d_2, \ldots, d_u), \tag{2.9}$$

where $\ddot{\mathbf{r}}_p$ is the sum of all perturbing accelerations and d_1, d_2, …, d_u are u force model parameters. The following perturbing accelerations can be distinguished:

- $\ddot{\mathbf{r}}_e$ accelerations due to the non-spherical and inhomogeneous mass distribution within the Earth system,
- $\ddot{\mathbf{r}}_b$ accelerations due to the gravitational attraction of other celestial bodies, mainly the Sun and the Moon,
- $\ddot{\mathbf{r}}_t$ accelerations due to the solid Earth tides and ocean tides,
- $\ddot{\mathbf{r}}_{rel}$ accelerations due to general relativity,
- $\ddot{\mathbf{r}}_d$ accelerations due to atmospheric drag,
- $\ddot{\mathbf{r}}_{\mathrm{SRP}}$ accelerations due to direct and indirect solar radiation pressure (SRP),
- $\ddot{\mathbf{r}}_o$ other accelerations due to, for example, thrust forces, thermal forces and magnetically-induced forces.

The perturbing forces causing the accelerations $\ddot{\mathbf{r}}_e$, $\ddot{\mathbf{r}}_b$, $\ddot{\mathbf{r}}_t$ and $\ddot{\mathbf{r}}_{rel}$ are of gravitational origin, whereas all other forces are non-gravitational. The total acceleration given by

$$\ddot{\mathbf{r}}_p = \ddot{\mathbf{r}}_e + \ddot{\mathbf{r}}_b + \ddot{\mathbf{r}}_t + \ddot{\mathbf{r}}_{rel} + \ddot{\mathbf{r}}_d + \ddot{\mathbf{r}}_{\mathrm{SRP}} + \ddot{\mathbf{r}}_o \tag{2.10}$$

depends on the position $\mathbf{r}$ and velocity $\dot{\mathbf{r}}$ of the satellite at a given time t.

Mathematical models for the perturbing accelerations are provided, for example, by *Montenbruck and Gill* (2000) and *Seeber* (2003). They contain the dynamic parameters d_1, d_2, …, d_u, which may be either held fixed or determined from satellite tracking data during the orbit determination process. For demanding applications, empirical accelerations are introduced to accommodate force modelling imperfections and account for unmodelled accelerations. The empirical parameters typically solved for are piecewise constant or piecewise linear along-track parameters and one cycle per orbital revolution (OPR) parameters in the along-track (S_s, S_c) and cross-track (W_s, W_c) directions. A convenient model for the empirical along-track acceleration $\ddot{\mathbf{r}}_S$ in the local orbital frame is given by

$$\ddot{\mathbf{r}}_S = S_0 + S_s \sin v + S_c \cos v, \tag{2.11}$$

where S_0 is a constant parameter and v represents the true anomaly.

Precise orbit determination (POD) involves the integration of the extended equation of motion (2.9) using a numerical method, leading to the solution

$$\begin{aligned} \mathbf{r}(t) &= \mathbf{r}(t; a(t), e(t), i(t), \Omega(t), \omega(t), T_0(t)), \\ \dot{\mathbf{r}}(t) &= \dot{\mathbf{r}}(t; a(t), e(t), i(t), \Omega(t), \omega(t), T_0(t)), \end{aligned} \tag{2.12}$$

with time-variable orbital elements known as *osculating orbital elements*, characterising an *osculating orbit* at each epoch t. The actual orbit of a satellite is the envelope of all individual osculating orbits.

Numerical integration is preferred to analytical integration due to its high accuracy and universal applicability. A detailed review of numerical methods used for orbit computations in satellite geodesy is given by *Montenbruck and Gill* (2000). Predictor-corrector methods such as Cowell and Gauss-Jackson are most frequently employed. In numerical integration methods, the update rate of the osculating elements (or state vector) is controlled by the size of the integration time step. An appropriate step size represents a trade-off between orbit accuracy and truncation errors on one hand and computational load and accumulative round-off errors on the other hand. A small step size minimises the truncation errors due to the curtailed Taylor series expansions of the satellite state vector, but increases the round-off errors arising from the finite precision representation of real numbers in computers.

The gravitational acceleration due to the Earth's monopole typically exceeds the total perturbing acceleration $\ddot{\mathbf{r}}_p$ by at least three orders of magnitude. More than 95% of the acceleration $\ddot{\mathbf{r}}_e$ due to the Earth's non-sphericity is induced by the *oblateness coefficient* J_2 (also called the *dynamic form factor* of the Earth), which is directly related to the flattening of a best fitting reference ellipsoid (e.g. *Chao*, 2006). This term is responsible for the rotations of the nodal line (connecting the ascending node and the descending node) and of the apse line (connecting the perigee and the apogee), but also engenders secular perturbations of the orbital elements Ω, ω and M expressed as

$$\begin{aligned} \dot{\Omega} &= -\frac{3}{2}\, n\, a_e^2\, \frac{\cos i}{a^2\,(1-e^2)^2}\, J_2, \\ \dot{\omega} &= \frac{3}{4}\, n\, a_e^2\, \frac{5\cos^2 i - 1}{a^2\,(1-e^2)^2}\, J_2, \\ \dot{M} &= n + \frac{3}{4}\, n\, a_e^2\, \frac{3\cos^2 i - 1}{a^2\sqrt{(1-e^2)^3}}\, J_2, \end{aligned} \tag{2.13}$$

for non-circular and non-equatorial orbits, where a_e is the equatorial radius of the Earth. Given its uncertainty, the numerical value $a_e = 6\,378\,136.6 \pm 0.1$ m recommended by the IERS Conventions (2010) pertains in both the TCG system and the TT system. The J_2 value obtained by *Cheng et al.* (2013b) from the analysis of SLR observations spanning

35 years is

$$J_2 = (1\,082\,635.81 \pm 0.01) \cdot 10^{-9}. \tag{2.14}$$

This is a *zero tide* value that contains only the contribution of the permanent tidal deformation caused by the average gravitational pull of the Sun and the Moon on the Earth, among all tidal effects.

The Keplerian elements a, e and i lack secular perturbations. For analytical orbit computations, formulae analogous to (2.13) need to be derived for all perturbing forces to account for secular and periodic variations in the osculating orbital elements. The discontinuous nature of non-gravitational perturbations hinders the application of analytical methods to precise orbit computations.

The repeat period of the ascending node with respect to the Sun is frequently referred to as the *draconitic year* and may be obtained as

$$P_s = y_{tro}\,\dot{\Omega}\left(y_{tro} - \dot{\Omega}\right)^{-1} \tag{2.15}$$

or, following *Capderou* (2014), as function of the orbital elements a and i using

$$P_s = -y_{tro}\left[k\left(\frac{a_e}{a}\right)^{\frac{7}{2}}\cos i + 1\right]^{-1}, \tag{2.16}$$

where $y_{tro} = 365.242190402$ days represents the duration of a tropical year (i.e. the time interval between two consecutive vernal equinoxes) and $k = 10.10949$ is a dimensionless constant that depends on the Earth's motion around the Sun. For sun-synchronous orbits (i.e. $\dot{\Omega} = 0.9863°/\text{day}$), the draconitic year approaches infinity.

2.3 Satellite laser ranging

2.3.1 Data acquisition and processing

SLR is an optical geodetic technique whose observable is the return travel time Δt of an ultra-short laser pulse between a ground station and a satellite equipped with retroreflectors. The two-way travel time is derived at the ground station either by a time interval counter offering a direct measure of Δt or by an event timer. The latter determines Δt as the difference between the pulse transmission time and the reception time. In its simplest form, the observation equation is given by

$$\rho = \frac{1}{2}\,c\,\Delta t, \tag{2.17}$$

where ρ represents the station-satellite range and $c = 299\,792\,458\ \text{m}\,\text{s}^{-1}$ is the speed of light in a vacuum.

The attainable range accuracy strongly depends on the laser pulse width according to the rule of thumb 100 ps ≡ 15 mm (*Seeber*, 2003). Most current SLR systems operate with pulse widths of 50–200 ps (corresponding to 7.5–30 mm range accuracy) and high pulse repetition rates of up to a 2 kHz. The vast amount of highly correlated full-rate data acquired by these systems are screened for outliers and compressed into *normal point* (NP) data (also known as *quick-look* data) using a well established algorithm.[1] NPs are formed over fixed time intervals called *bins*, selected based on the altitude of each satellite. Modern SLR systems deliver a NP precision of 1–3 mm and an estimated accuracy of 1–2 cm (e.g. *Exertier et al.*, 2006).

Subsequent analysis of NP data imposes the inclusion of various corrections in (2.17) to suit the accuracy demands of SLR applications. The extended observation equation can be expressed as

$$\rho = \frac{1}{2} c\,\Delta t + \Delta\rho_g + \Delta\rho_s + \Delta\rho_{atm} + \Delta\rho_{rel} + \Delta\rho_{rb} + \varepsilon, \tag{2.18}$$

where

$\Delta\rho_g$	ground eccentricity correction,
$\Delta\rho_s$	satellite eccentricity correction,
$\Delta\rho_{atm}$	atmospheric refraction correction,
$\Delta\rho_{rel}$	relativistic propagation correction,
$\Delta\rho_{rb}$	station range bias,
ε	residual systematic and random errors.

The ground eccentricity correction $\Delta\rho_g$ represents the geometric distance between the optical reference point of the ranging system and the station marker. Likewise, the satellite eccentricity correction $\Delta\rho_s$, more commonly known as the centre of mass (CoM) correction, is the offset between the centre of mass of a particular satellite and the optical centre of one of its corner cube reflectors (CCRs). Constant CoM corrections determined during pre-launch calibrations have been traditionally used for spherical geodetic satellites. Nevertheless, analyses of the optical response functions of geodetic satellites revealed that CoM corrections also depend on the detector types and the ranging policies of SLR stations (*Otsubo and Appleby*, 2003; *Otsubo et al.*, 2015). As of 1 October 2013, time-variable system-dependent CoM corrections have been adopted by the ILRS for the LAGEOS, Etalon and Ajisai satellites.

Laser signals are negligibly affected by the ionosphere, but experience a delay in the stratosphere and the troposphere that typically ranges from about 2.3 to 2.5 m in the zenith direction at sea level (for the most common SLR wavelength of 532 nm), with a non-hydrostatic component of less than 1 cm. For more than three decades, the zenith atmospheric delay of laser signals had been modelled and mapped at different elevations

[1] http://ilrs.gsfc.nasa.gov/data_and_products/data/npt/npt_algorithm.html

using the model of *Marini and Murray* (1973). In October 2006, the ILRS adopted the more recent zenith delay model of *Mendes and Pavlis* (2004). When this model is used in conjunction with the FCULa mapping function developed by *Mendes et al.* (2002), the atmospheric refraction correction $\Delta\rho_{atm}$ can be derived with an accuracy of ∼7 mm. The relativistic propagation correction $\Delta\rho_{rel}$ is well modelled and documented in the IERS Conventions (2010). The range bias $\Delta\rho_{rb}$ absorbs remaining errors in the measured range if estimated, but it is correlated with station heights. Known range biases serving as mandatory corrections for selected stations are reported in the ILRS data handling file.[2]

2.3.2 Spherical geodetic satellites

Over 50 satellites fitted with retro-reflector arrays are currently tracked by ILRS stations. Geodetic satellites tailored for laser ranging have spherical shapes and low area-to-mass ratios that minimise non-gravitational orbital perturbations. They carry coated or uncoated CCRs and lack electronic components. Since 1975, twelve spherical geodetic satellites have been inserted in orbits at various altitudes by national space agencies or through international collaborations (Figure 2.2).

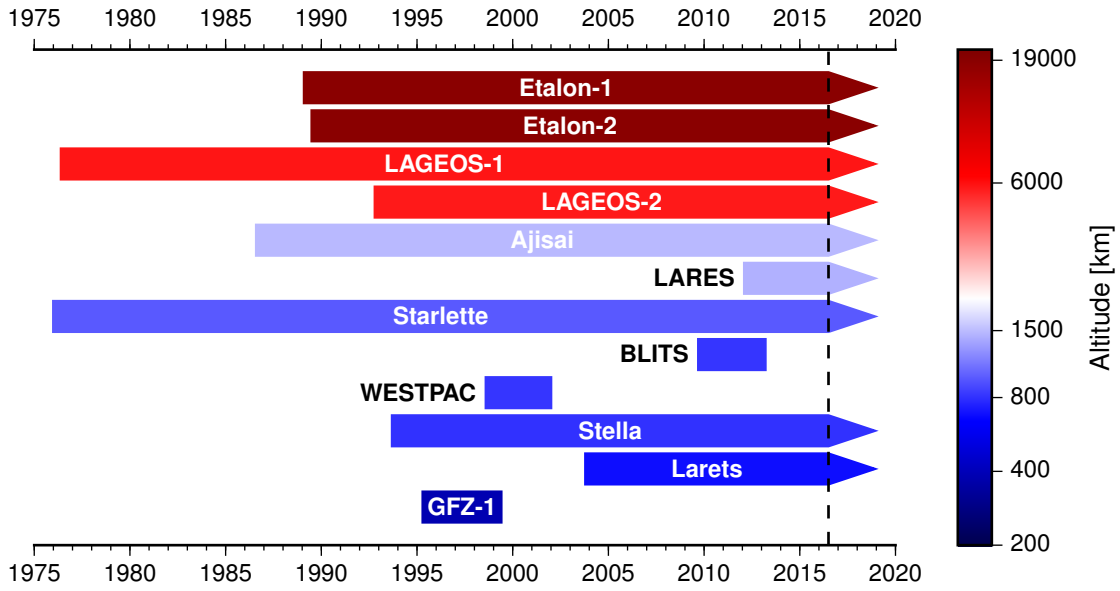

Figure 2.2 Timeline of geodetic satellite launches since 1975

LAGEOS-1 and LAGEOS-2

LAGEOS-1 (Figure 2.3) was launched in a retrograde medium Earth orbit by the United States (US) National Aeronautics and Space Administration (NASA) on 4 May 1976 from the Vandenberg Air Force Base in California. Its follow-up mission, LAGEOS-2, was built by the Italian Space Agency (Agenzia Spaziale Italiana, ASI) based on the design of LAGEOS-1 and launched in a prograde orbit by NASA on 22 October 1992 from

[2] http://ilrs.dgfi.tum.de/fileadmin/data_handling/ILRS_Data_Handling_File.snx

Cape Canaveral, Florida. Each of the two satellites is composed of two hemispherical aluminium shells with brass inner cores, held together by a steel shaft (*Minott et al.*, 1993). The satellites are covered by 426 uncoated CCRs each, 422 of which are made from fused silica for visible and near-infrared ranging. The other four reflectors were manufactured from germanium for infrared laser ranging. At present, the LAGEOS satellites are at the forefront of high-precision laser ranging and represent the main targets for the determination of the TRF and EOPs. They also contribute to the estimation of long-wavelength variations in the Earth's gravity field.

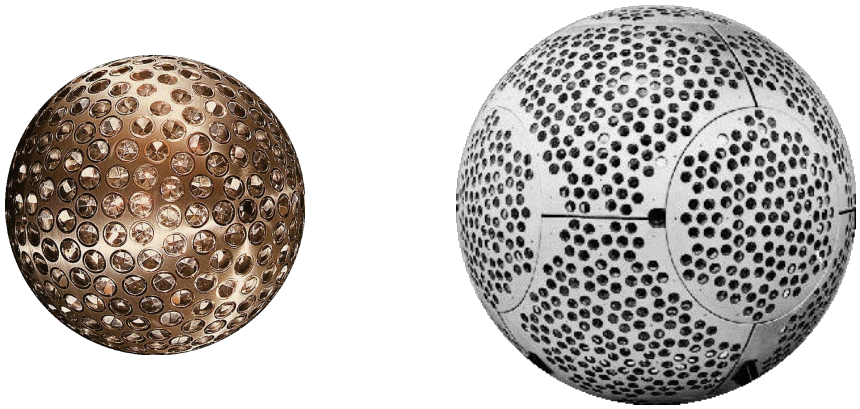

Figure 2.3 The LAGEOS-1 (*left*) and Etalon-1 (*right*) satellites. Image credits: NASA and the Russian Science Research Institute for Precision Instrument Engineering, respectively

Etalon-1 and Etalon-2

The former Soviet Union launched Etalon-1 (Figure 2.3) on 10 January 1989 and Etalon-2 on 31 May 1989 from Baikonur (presently in Kazakhstan), each together with two Global'naya Navigatsionnaya Sputnikovaya Sistema (GLONASS) navigation satellites. The surface of each Etalon satellite is made from an aluminium-titanium alloy and studded with 2146 aluminium coated CCRs irregularly distributed in arrays of seven or six. Only six of the reflectors are made from germanium, whereas all other 2140 are from fused silica. Although the initial objective of the Etalon missions was to estimate SRP for orbital adjustments of GLONASS satellites (*Seeber*, 2003), the two highest-orbiting spherical satellites presently contribute to the determination of the TRF and EOPs.

Starlette and Stella

Starlette (Figure 2.4) was the first passive spherical satellite equipped with retro-reflectors. It was launched by the French Space Agency (Centre National d'Études Spatiales, CNES) on 6 February 1975 from Kourou, French Guiana. The twin satellite of Starlette, named Stella, was launched by CNES in a sun-synchronous orbit on 26 September 1993 as the secondary payload of the remote sensing spacecraft Satellite Pour l'Observation de la Terre (SPOT) 3. The outer surface of each twin satellite is composed of 20 spherical caps with

triangular bases made from a 95% aluminium and 5% magnesium alloy (*Kramer*, 2002). Three CCRs are embedded in each spherical cap. The core is an icosahedron manufactured from uranium-238 and 0.2% vanadium. Due to their low altitudes, Starlette and Stella are well suited for studies of the Earth's gravity field, solid Earth tides and ocean tides.

Ajisai

The Japanese Experimental Geodetic Satellite (EGS), renamed Ajisai (Figure 2.4) after its launch on 12 August 1986 from the Tanegashima Space Center, was inserted in a quasi-circular orbit by the former National Space Development Agency (NASDA), currently part of the Japan Aerospace Exploration Agency (JAXA). Unlike other passive geodetic satellites, Ajisai is a hollow sphere made from fibreglass. In addition to 1436 uncoated CCRs distributed in 120 arrays, the satellite is also equipped with 318 aluminium coated mirrors for optical direction measurements and photometric observations. Being the largest and least dense spherical geodetic satellite, Ajisai is more exposed to accelerations due to non-gravitational forces. The initial objective of the mission was to determine the locations of isolated Japanese islands, but Ajisai presently contributes mainly to the improvement of gravity field models.

Figure 2.4 The Starlette (*left*), Ajisai (*middle*) and LARES (*right*) satellites. Image credits: CNES, JAXA and ASI, respectively

LARES

On 13 February 2012, ASI launched LARES (Figure 2.4) from Kourou, French Guiana on the qualification flight of the Vega launch vehicle belonging to the European Space Agency (ESA). In contrast to all other passive geodetic satellites, LARES is a single-piece sphere manufactured from a tungsten alloy and has a mean density of 15 300 $\mathrm{kg\,m^{-3}}$, the highest of all known objects in the solar system (*Paolozzi and Ciufolini*, 2013). Its favourable area-to-mass ratio, about 2.6 times lower than that of each LAGEOS satellite, significantly reduces the effects of non-conservative forces acting on the satellite's surface. To minimise thermal effects, the 92 CCRs mounted in plastic rings cover only ∼26% of

the total surface area of the satellite, as opposed to ∼43% for each of LAGEOS-1 and 2 (*Ciufolini et al.*, 2012). The main objective of the LARES mission is to contribute to fundamental and gravitational physics, particularly by measuring the frame-dragging (or Lense–Thirring) effect predicted by Einstein's theory of general relativity. Significant contributions to the determination of the Earth's gravity field and potentially of the TRF and EOPs are also expected.

Miscellaneous missions

Larets is the only other spherical geodetic satellite tracked by ILRS stations at present. Its distinctive design with 60 CCRs recessed in the satellite's brass body is intended to ensure single-reflector returns. Another three dedicated laser ranging missions were supported in the past by the ILRS, namely the GeoForschungsZentrum (GFZ) 1, the Western Pacific Laser Tracking Network Satellite (WESTPAC) and the Ball Lens In The Space (BLITS). GFZ-1 (*König et al.*, 1996) was inserted into a low Earth orbit (∼400 km) and contributed to the recovery of long-period gravity field parameters (*König et al.*, 1999) before disintegrating in the atmosphere on 23 June 1999. The tracking of WESTPAC was discontinued in 2002 due to the low energy of return signals caused by the design of the satellite (i.e. retro-reflectors embedded in baffles). BLITS was damaged on 22 January 2013 in a collision with debris from the former Chinese weather satellite Fengyun-1C, destroyed by an anti-satellite missile in 2007.

Table 2.1 Selected orbital parameters of spherical geodetic satellites

Satellite name	a [km]	e	i [°]	$\dot{\omega}$ [°/day]	$\dot{M}$ [°/day]	P_Ω [days]	P_s [days]
LAGEOS-1	12 270.0	0.0044	109.83	−0.214	2299.2	1051.7	559.6
LAGEOS-2	12 162.1	0.0138	52.66	0.437	2330.3	570.1	222.6
Etalon-1	25 503.3	0.0019	64.17	−0.002	767.4	10 600.6	353.1
Etalon-2	25 499.4	0.0017	64.64	−0.003	767.5	10 778.0	353.3
Starlette	7334.6	0.0206	49.82	3.306	4976.3	91.2	73.1
Stella	7175.9	0.0007	98.72	−2.919	5138.5	360.0	24 946.5
Ajisai	7866.5	0.0011	50.01	2.547	4480.1	117.1	88.7
LARES	7820.3	0.0008	69.49	−0.943	4517.7	210.5	133.5

LAGEOS-1 and 2, Etalon-1 and 2, Starlette, Stella, Ajisai and LARES are the eight satellites of interest for this study. Selected orbital parameters of these satellites are listed in Table 2.1. The values of the Keplerian elements a, e and i were extracted from North American Aerospace Defense Command (NORAD) two-line element sets.[3] Larets is omitted due to its similar inclination to that of Stella, larger area-to-mass ratio and lower altitude. These characteristics expose Larets to larger non-gravitational orbital perturbations, particularly due to atmospheric drag. During the 3.5 years in its planned

[3] http://www.celestrak.com/NORAD/elements/

orbit, BLITS also shared a similar inclination with Stella, but had an area-to-mass ratio more than three times larger. As demonstrated by *Bloßfeld et al.* (2015), Larets and BLITS provide much lower contributions to combined solutions compared to the eight satellites considered in this study.

2.3.3 Tracking stations

In mid-2016 the ILRS tracking network comprised 51 stations with a global distribution biased towards the northern and eastern hemispheres (Figure 2.5). Each SLR system includes the following hardware:

- a laser oscillator responsible for the generation of the uplink laser beam,
- a propagation timer controlled by an atomic clock,
- mechanically mounted optical telescopes acting as transmitter and receiver,
- a detector and analyser of the downlink pulses, and
- a computer for system control and data analysis.

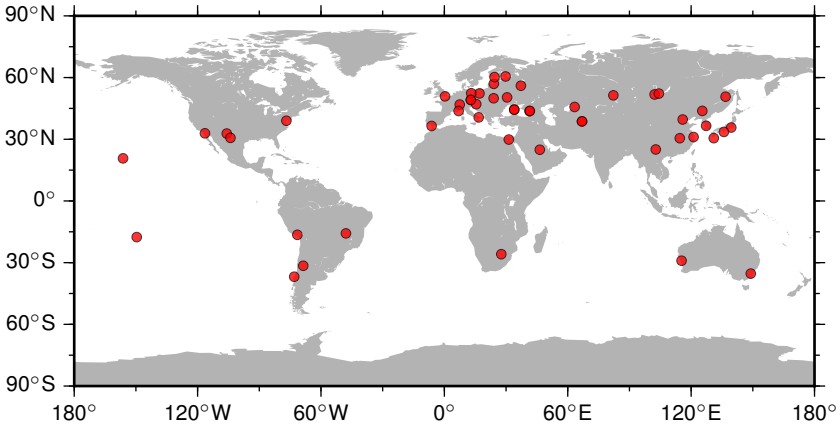

Figure 2.5 The ILRS tracking network in mid-2016

The core component is the laser oscillator. Current systems almost exclusively employ neodymium-doped yttrium aluminium garnet (Nd:YAG) lasers capable of producing narrow pulses at high repetition rates. The telescope mount provides automatic target tracking with a pointing accuracy of 1″ or better, based on pre-calculated orbits. Returning laser pulses are converted to electronic signals by the detector. SLR systems use either micro-channel plate (MCP) or single-photon avalanche diode (SPAD) detectors. All NASA stations employ MCP detectors, which operate at a multi-photon level of return (i.e. ten to several hundred photons) and are configured to be triggered by the leading edge of the returning signal. Stations with SPAD detectors operate at or near a single-photon return level and are thus more capable of observing in unfavourable atmospheric conditions. As shown by *Otsubo and Appleby* (2003), ranges measured by multi-photon systems are typically shorter than those observed by single-photon systems and consequently require larger corrections to refer them to the centre of mass of a satellite.

2.4 Faust updates

The multi-satellite POD software of Newcastle University was named Faust as a tribute to the German mathematician, physicist, astronomer and geodesist Carl Friedrich Gauss (1777–1855), who is believed to have inspired the character from Goethe's version of the classic legend. Originally developed in the 1990s at Aston University using the FORTRAN 77 programming language (*Boomkamp*, 1998; *Moore et al.*, 1999), Faust has since been modified by various researchers at Newcastle University. In the early stages of this research project, it became apparent that some of the models in Faust are obsolete and updates are needed to bring the software in line with the IERS Conventions (2010) and the latest practices in SLR data analysis.

Table 2.2 Faust updates performed during this project

Model type	Previous model	Current model
Precession-nutation	IAU 1976/1980	IAU 2006/2000A
Global geopotential model	EGM96	EGM2008
Conventional mean pole	IERS (2003)	IERS (2010) mean pole model
S_1–S_2 atmospheric pressure loading	–	*Ray and Ponte* (2003)
Ocean pole tide loading	–	*Desai* (2002)
Atmospheric refraction for optical signals	*Marini and Murray* (1973)	*Mendes and Pavlis* (2004) zenith delay; *Mendes et al.* (2002) FCULa mapping function
CoM corrections for spherical geodetic satellites	Constant per satellite	System-dependent for LAGEOS, Etalon and Ajisai (*Otsubo and Appleby*, 2003)

A summary of the main Faust updates performed during the course of this project is given in Table 2.2 for future reference. The IAU 2006/2000A precession-nutation model was implemented using Standards of Fundamental Astronomy (SOFA) routines available at `http://www.iausofa.org`. System-dependent CoM corrections were adopted for LAGEOS-1 and 2, Etalon-1 and 2 and Ajisai based on ILRS supplied tables.[4] Similar tables for Starlette, Stella and LARES (*Otsubo et al.*, 2015) are expected to be released in the near future. Changes not documented in Table 2.2 include the implementation of the kinematic approach for geocentre motion estimation (see Chapter 3), the addition of the NRLMSISE-00 thermospheric model (*Picone et al.*, 2002), editing sections of code for the production of reduced solutions in the SINEX format and the adoption of a priori EOP values consistent with the IAU 2006/2000A precession-nutation model and ITRF2008 (i.e. the IERS EOP 08 C04 long-term series).[5]

[4] `http://ilrs.gsfc.nasa.gov/network/site_information/data_correction.html`
[5] `http://www.iers.org/IERS/EN/DataProducts/EarthOrientationData/eop.html`

Chapter 3

Geocentre motion modelling approaches

3.1 Introduction

Since geocentre motion was first recognised in the 1970s (*Stolz*, 1976a,b), various methods for estimating the phenomenon at seasonal and longer timescales have been proposed. They range from forward modelling using a combination of geophysical fluid models to complex inverse approaches that integrate satellite observations and models. The observation of geocentre motion using satellite geodetic techniques only became feasible in the 1990s, once the techniques matured and their ground networks achieved satisfactory densities. More than two decades later, the reconciliation of model predictions and geodetic estimates of geocentre motion, as well as of measurements obtained using different geodetic techniques, remains challenging. As one of the most demanding applications, geocentre motion observation is at the forefront of geodetic research and may be used as a performance indicator for geodetic techniques.

This chapter reviews the methods used for geocentre motion determination both at seasonal and secular timescales using satellite data and models. Direct satellite tracking approaches are first presented, followed by inverse procedures and forward modelling. The chapter ends with a discussion of the geocentre velocity induced by PDMT and GIA and a summary of the methods.

3.2 Translational approaches

Translational approaches model the geocentre coordinates as translations of the CM frame with respect to the CF frame along the three Cartesian axes. The *dynamic approach* (e.g. *Kar*, 1997) involves the estimation of degree-1 geopotential coefficients, proportional to the three CM–CF translations. The translation parameters can also be determined via seven or six-parameter similarity transformations in a procedure termed the *network shift approach* (e.g. *Dong et al.*, 2003) or directly during POD alongside other parameters using the *kinematic approach* (e.g. *Kang et al.*, 2009).

3.2.1 The dynamic approach

The geocentre vector $\mathbf{r}_{\mathrm{CM-CF}} = \begin{bmatrix} X_{\mathrm{GC}} & Y_{\mathrm{GC}} & Z_{\mathrm{GC}} \end{bmatrix}^T$ contains the Cartesian coordinates of CM in the crust-fixed CF frame, whereas the instantaneous position of a satellite in the CF frame is defined by the vector $\mathbf{r} = \begin{bmatrix} X & Y & Z \end{bmatrix}^T$. The two positions can also be expressed in spherical coordinates (radial distance, latitude and longitude) related to the Cartesian coordinates by

$$\left.\begin{aligned} X_{\mathrm{GC}} &= r_{\mathrm{CM-CF}} \cos\varphi' \cos\lambda' \\ Y_{\mathrm{GC}} &= r_{\mathrm{CM-CF}} \cos\varphi' \sin\lambda' \\ Z_{\mathrm{GC}} &= r_{\mathrm{CM-CF}} \sin\varphi' \end{aligned}\right\}, \qquad \left.\begin{aligned} X &= r \cos\varphi \cos\lambda \\ Y &= r \cos\varphi \sin\lambda \\ Z &= r \sin\varphi \end{aligned}\right\}, \tag{3.1}$$

where the triplets $(r_{\mathrm{CM-CF}}, \varphi', \lambda')$ and (r, φ, λ) are the spherical coordinates in the CF frame of CM and the satellite, respectively (Figure 3.1). The position of the satellite in the CM frame is given by the vector $\mathbf{r}' = \mathbf{r} - \mathbf{r}_{\mathrm{CM-CF}}$ with the magnitude obtained using the law of cosines

$$\begin{aligned} r' &= \left(r^2 + r_{\mathrm{CM-CF}}^2 - 2\, r\, r_{\mathrm{CM-CF}} \cos\psi\right)^{\frac{1}{2}} \\ &= r \left[1 + \left(\frac{r_{\mathrm{CM-CF}}}{r}\right)^2 - 2\left(\frac{r_{\mathrm{CM-CF}}}{r}\right)\cos\psi\right]^{\frac{1}{2}}, \end{aligned} \tag{3.2}$$

where ψ is the angle formed by $\mathbf{r}$ and $\mathbf{r}_{\mathrm{CM-CF}}$.

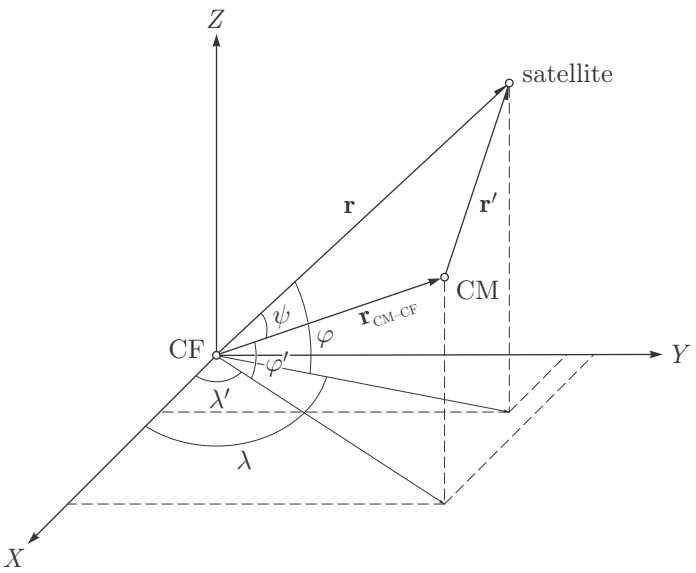

Figure 3.1 Cartesian and spherical coordinates of a satellite and CM in the CF frame

Under the assumption of a homogeneous and spherically symmetric mass distribution, the Earth can be regarded as a point mass with the gravitational potential at the position of the satellite given by

$$V = \frac{GM}{r'}, \tag{3.3}$$

where GM is the geocentric gravitational constant, the product of the universal gravitational constant G and the Earth's mass M. The reciprocal distance $1/r'$ can be expanded in a power series that converges for $r_{\mathrm{CM-CF}} < r$. Arranging the terms of the series expansion according to increasing powers of $r_{\mathrm{CM-CF}}/r$ leads to

$$\frac{1}{r'} = \frac{1}{r}\sum_{n=0}^{\infty}\left(\frac{r_{\mathrm{CM-CF}}}{r}\right)^n P_{n0}\left(\cos\psi\right). \tag{3.4}$$

Inserting (3.4) in (3.3), applying the decomposition formula for the Legendre polynomials $P_{n0}\left(\cos\psi\right)$ and using identities from spherical trigonometry yields

$$\begin{aligned} V = \frac{GM}{r}\Bigg[&\sum_{n=0}^{\infty}\left(\frac{r_{\mathrm{CM-CF}}}{r}\right)^n P_{n0}\left(\sin\varphi\right)C'_{n0}\cos\lambda \\ &+\sum_{n=1}^{\infty}\sum_{m=1}^{n}\left(\frac{r_{\mathrm{CM-CF}}}{r}\right)^n P_{nm}\left(\sin\varphi\right)\left(C'_{nm}\cos m\lambda + S'_{nm}\sin m\lambda\right)\Bigg], \end{aligned} \tag{3.5}$$

where

$$\begin{aligned} C'_{n0} &= P_{n0}\left(\sin\varphi'\right), \\ C'_{nm} &= 2\frac{(n-m)!}{(n+m)!}P_{nm}\left(\sin\varphi'\right)\cos m\lambda', \\ S'_{nm} &= 2\frac{(n-m)!}{(n+m)!}P_{nm}\left(\sin\varphi'\right)\sin m\lambda'. \end{aligned} \tag{3.6}$$

The terms $P_{nm}\left(\sin\varphi'\right)$ represent the associated Legendre functions of degree n and order m. By decomposing the ratio $r_{\mathrm{CM-CF}}/r$ so that

$$\frac{r_{\mathrm{CM-CF}}}{r} = \frac{r_{\mathrm{CM-CF}}}{a_e}\frac{a_e}{r}, \tag{3.7}$$

with a_e the equatorial radius of the Earth, and allowing the harmonic coefficients to absorb the term $r_{\mathrm{CM-CF}}/a_e$, (3.5) can be written as

$$\begin{aligned} V = \frac{GM}{r}\Bigg[&\sum_{n=0}^{\infty}\left(\frac{a_e}{r}\right)^n P_{n0}\left(\sin\varphi\right)\bar{C}_{n0}\cos\lambda \\ &+\sum_{n=1}^{\infty}\sum_{m=1}^{n}\left(\frac{a_e}{r}\right)^n P_{nm}\left(\sin\varphi\right)\left(\bar{C}_{nm}\cos m\lambda + \bar{S}_{nm}\sin m\lambda\right)\Bigg]. \end{aligned} \tag{3.8}$$

Equation (3.8) represents the external gravitational potential of the Earth in terms of zonal and non-zonal spherical harmonic coefficients given by the expressions

$$\begin{aligned} \bar{C}_{n0} &= \left(\frac{r_{\mathrm{CM-CF}}}{a_e}\right)^n P_{n0}\left(\sin\varphi'\right), \\ \bar{C}_{nm} &= \left(\frac{r_{\mathrm{CM-CF}}}{a_e}\right)^n 2\frac{(n-m)!}{(n+m)!}P_{nm}\left(\sin\varphi'\right)\cos m\lambda', \\ \bar{S}_{nm} &= \left(\frac{r_{\mathrm{CM-CF}}}{a_e}\right)^n 2\frac{(n-m)!}{(n+m)!}P_{nm}\left(\sin\varphi'\right)\sin m\lambda'. \end{aligned} \tag{3.9}$$

The corresponding fully normalised coefficients

$$\begin{aligned} C_{n0} &= \frac{1}{\sqrt{2n+1}}\bar{C}_{n0}, \\ C_{nm} &= \sqrt{\frac{(n+m)!}{2\,(2n+1)\,(n-m)!}}\,\bar{C}_{nm}, \\ S_{nm} &= \sqrt{\frac{(n+m)!}{2\,(2n+1)\,(n-m)!}}\,\bar{S}_{nm}, \end{aligned} \tag{3.10}$$

are commonly used in practice.

The conventional (or unnormalised) degree-1 geopotential coefficients obtained from (3.9) are

$$\begin{aligned} \bar{C}_{10} &= \frac{r_{\mathrm{CM-CF}}}{a_e} P_1\left(\sin\varphi'\right), \\ \bar{C}_{11} &= \frac{r_{\mathrm{CM-CF}}}{a_e} P_{11}\left(\sin\varphi'\right)\cos\lambda', \\ \bar{S}_{11} &= \frac{r_{\mathrm{CM-CF}}}{a_e} P_{11}\left(\sin\varphi'\right)\sin\lambda'. \end{aligned} \tag{3.11}$$

Substituting the Legendre polynomial $P_{10}\left(\sin\varphi'\right) = \sin\varphi'$ and the Legendre function $P_{11}\left(\sin\varphi'\right) = \cos\varphi'$ in (3.11) and converting spherical coordinates to Cartesian coordinates using (3.1) leads to the following relations between the degree-1 geopotential coefficients and the geocentre coordinates:

$$\bar{C}_{10} = \frac{Z_{\mathrm{GC}}}{a_e}, \qquad \bar{C}_{11} = \frac{X_{\mathrm{GC}}}{a_e}, \qquad \bar{S}_{11} = \frac{Y_{\mathrm{GC}}}{a_e}. \tag{3.12}$$

The degree-1 harmonic coefficients can also be written as (*Hofmann-Wellenhof and Moritz*, 2006)

$$\bar{C}_{10} = \frac{1}{a_e M}\iiint\limits_{Earth} Z\,dm, \quad \bar{C}_{11} = \frac{1}{a_e M}\iiint\limits_{Earth} X\,dm, \quad \bar{S}_{11} = \frac{1}{a_e M}\iiint\limits_{Earth} Y\,dm, \tag{3.13}$$

where dm is a differential element of mass. The Cartesian coordinates of CM are also known from mechanics to be

$$X_{\mathrm{GC}} = \frac{1}{M}\iiint X\,dm, \quad Y_{\mathrm{GC}} = \frac{1}{M}\iiint Y\,dm, \quad Z_{\mathrm{GC}} = \frac{1}{M}\iiint Z\,dm, \tag{3.14}$$

so that inserting (3.14) in (3.13) leads to (3.12).

Given that the relation between the unnormalised and normalised degree-1 geopotential coefficients is

$$\begin{bmatrix} \bar{C}_{10} \\ \bar{C}_{11} \\ \bar{S}_{11} \end{bmatrix} = \sqrt{3}\begin{bmatrix} C_{10} \\ C_{11} \\ S_{11} \end{bmatrix}, \tag{3.15}$$

Equation (3.12) is equivalent to

$$C_{10} = \frac{Z_{\mathrm{GC}}}{\sqrt{3}\,a_e}, \qquad C_{11} = \frac{X_{\mathrm{GC}}}{\sqrt{3}\,a_e}, \qquad S_{11} = \frac{Y_{\mathrm{GC}}}{\sqrt{3}\,a_e}. \tag{3.16}$$

From (3.12) and (3.16) the geocentre vector is given by

$$\mathbf{r}_{\mathrm{CM-CF}} = a_e \begin{bmatrix} \bar{C}_{11} \\ \bar{S}_{11} \\ \bar{C}_{10} \end{bmatrix} = \sqrt{3}\,a_e \begin{bmatrix} C_{11} \\ S_{11} \\ C_{10} \end{bmatrix}. \tag{3.17}$$

Using $a_e = 6378.137$ km in (3.17), a geocentre offset of 1 cm corresponds to a change in the unnormalised degree-1 geopotential coefficients of $1.568 \cdot 10^{-9}$ and a change in the corresponding normalised coefficients of $0.905 \cdot 10^{-9}$. As shown by (3.9), all geopotential coefficients are perturbed by geocentre motion, not just the degree-1 terms. However, since $a_e \gg r_{\mathrm{CM-CF}}$, the ratio $({}^{r_{\mathrm{CM-CF}}}/_{a_e})^n \approx 10^{-9 \cdot n}$ decreases rapidly with increasing degree n. Thus, harmonics of degree $n \geq 2$ are affected to a negligible degree by geocentre motion and their numerical values pertain across frames. Degree-1 harmonics equal zero only in the CM frame. If coefficients are required in a different frame, higher degree terms need to be complemented by degree-1 terms obtained using (3.12) or (3.16).

The proportionality between the degree-1 geopotential coefficients and the geocentre coordinates has been succinctly mentioned in several textbooks (*Heiskanen and Moritz*, 1967; *Montenbruck and Gill*, 2000; *Hofmann-Wellenhof and Moritz*, 2006; *Torge and Müller*, 2012) and fully elaborated by *Kar* (1997), at a time when the theory of degree-1 deformation was incompletely formalised. This theoretical gap ultimately resulted in neglecting the small differential motion between CF and CE due to the Earth being inhomogeneous (see Section 3.3.2). Consequently, (3.17) actually characterises the motion of CM relative to CE rather than the motion of CM with respect to CF.

In the dynamic approach, which has also been referred to as the gravitational method (*Devoti et al.*, 1999), geopotential coefficients are estimated at regular time intervals during orbit determination and then converted to geocentre coordinates using (3.17). Nevertheless, this approach requires the formulation of the equations of satellite motion in the CF frame, which is non-geocentric and moves about the static CM frame in inertial space. In turn, the force model needs to be complemented by the following *apparent forces* that arise when considering the rotational motion of the non-geocentric frame: the Coriolis force, the centrifugal force and the gyro force (*Reigber*, 1981). Since the accelerations induced by the centrifugal and gyro forces are either zero or negligibly small, accurate modelling of the Coriolis accelerations suffices, but a priori knowledge of the geocentre coordinates is a prerequisite (*Kar*, 1997). Furthermore, errors in the static geopotential model used for orbit determination are likely to alias into the estimates of the degree-1 geopotential coefficients, especially when higher-degree coefficients are not recovered, but this also applies to other methods. These complications hinder the application of the

dynamic approach in practice and led to its sporadic use (e.g. *Pavlis*, 1999; *Devoti et al.*, 1999; *Govind et al.*, 2010; *König et al.*, 2015), occurring predominantly in the incipient stages of geocentre motion observation.

3.2.2 The network shift approach

Epoch reference frames obtained through the analysis of satellite observations spanning regular time intervals (typically one day for GNSS and one week for SLR and DORIS) are theoretically centred at the quasi-instantaneous CM. The origin of multi-year reference frames such as the ITRF follows CF (or CN) at sub-secular timescales. Consequently, the net translation between an epoch reference frame and multi-year frame at the same epoch represents the relative position of CM with respect to CF. Following *Dong et al.* (2003), the estimation of geocentre coordinates as translation parameters of a Helmert transformation is routinely known as the network shift approach. Another occasional designation for the network shift approach is the geometric approach (*Pavlis*, 1999; *Devoti et al.*, 1999; *Govind et al.*, 2010; *König et al.*, 2015). The problem of modelling Coriolis accelerations encountered in the dynamic approach is circumvented by formulating the dynamic equations of motion in the CM frame, the natural frame for modelling satellite dynamics.

For each station i, the linear observation equations of the network shift approach are

$$\begin{bmatrix} X_i^{\mathrm{CF}} - X_i^{\mathrm{CM}} \\ Y_i^{\mathrm{CF}} - Y_i^{\mathrm{CM}} \\ Z_i^{\mathrm{CF}} - Z_i^{\mathrm{CM}} \end{bmatrix} = \begin{bmatrix} t_X \\ t_Y \\ t_Z \end{bmatrix} + d \begin{bmatrix} X_i^{\mathrm{CM}} \\ Y_i^{\mathrm{CM}} \\ Z_i^{\mathrm{CM}} \end{bmatrix} + \begin{bmatrix} 0 & -r_Z & r_Y \\ r_Z & 0 & -r_X \\ -r_Y & r_X & 0 \end{bmatrix} \begin{bmatrix} X_i^{\mathrm{CM}} \\ Y_i^{\mathrm{CM}} \\ Z_i^{\mathrm{CM}} \end{bmatrix}, \tag{3.18}$$

where the meaning of each individual quantity is the following:

X_i^{CF}, Y_i^{CF}, Z_i^{CF}	Cartesian station coordinates in the CF frame, propagated at the epoch of the CM frame,
X_i^{CM}, Y_i^{CM}, Z_i^{CM}	Cartesian station coordinates in a quasi-instantaneous CM frame,
t_X, t_Y, t_Z	translation parameters between the CM frame and the CF frame,
r_X, r_Y, r_Z	rotation parameters between the CM frame and the CF frame,
d	optional scale parameter.

In matrix form, (3.18) can be expressed as

$$\mathbf{l}_i = \mathbf{A}_i \mathbf{x}, \tag{3.19}$$

where the vector of unknown parameters $\mathbf{x}$ is given by

$$\mathbf{x} = \begin{bmatrix} t_X & t_Y & t_Z & d & r_X & r_Y & r_Z \end{bmatrix}^T, \tag{3.20}$$

whereas the design matrix $\mathbf{A}_i$ for each station i reads

$$\mathbf{A}_i = \begin{bmatrix} 1 & 0 & 0 & X_i^{\mathrm{CM}} & 0 & -Z_i^{\mathrm{CM}} & Y_i^{\mathrm{CM}} \\ 0 & 1 & 0 & Y_i^{\mathrm{CM}} & Z_i^{\mathrm{CM}} & 0 & -X_i^{\mathrm{CM}} \\ 0 & 0 & 1 & Z_i^{\mathrm{CM}} & -Y_i^{\mathrm{CM}} & X_i^{\mathrm{CM}} & 0 \end{bmatrix}. \tag{3.21}$$

The $\mathbf{l}_i$ vector contains the observations on the left-hand side of (3.18). Using measurements from $n \gg 3$ stations leads to a redundant system of linear equations $\mathbf{l} + \mathbf{v} = \mathbf{A}\mathbf{x}$, where

$$\begin{aligned} \mathbf{A} &= \begin{bmatrix} \mathbf{A}_1 & \mathbf{A}_2 & \dots & \mathbf{A}_n \end{bmatrix}^T, \\ \mathbf{l} &= \begin{bmatrix} \mathbf{l}_1 & \mathbf{l}_2 & \dots & \mathbf{l}_n \end{bmatrix}^T, \end{aligned} \tag{3.22}$$

and $\mathbf{v}$ is the vector of observation residuals. The weighted least squares solution of the redundant system found by minimising $\mathbf{v}^T\mathbf{W}\mathbf{v}$ is

$$\hat{\mathbf{x}} = \left(\mathbf{A}^T\mathbf{W}\mathbf{A}\right)^{-1}\mathbf{A}^T\mathbf{W}\mathbf{l}, \tag{3.23}$$

where $\mathbf{W} = \mathbf{C}^{-1}$ is the weight matrix, equal to the inverse of the variance-covariance matrix of the observations $\mathbf{C}$. Finally, the geocentre coordinates are the estimates of the translation parameters, so that

$$\mathbf{r}_{\mathrm{CM-CF}} = \begin{bmatrix} X_{\mathrm{GC}} \\ Y_{\mathrm{GC}} \\ Z_{\mathrm{GC}} \end{bmatrix} = \begin{bmatrix} t_X \\ t_Y \\ t_Z \end{bmatrix}. \tag{3.24}$$

With equal weighting of all stations, the geocentre vector can be modelled in a more simplistic way as the translation between the barycentres of the CM and the CF frames

$$\mathbf{r}_{\mathrm{CM-CF}} = \frac{1}{n}\sum_{i=1}^{n}\left(\mathbf{p}_i - \mathbf{p}'_i\right), \tag{3.25}$$

with $\mathbf{p}_i = \begin{bmatrix} X_i^{\mathrm{CF}} & Y_i^{\mathrm{CF}} & Z_i^{\mathrm{CF}} \end{bmatrix}^T$ and $\mathbf{p}'_i = \begin{bmatrix} X_i^{\mathrm{CM}} & Y_i^{\mathrm{CM}} & Z_i^{\mathrm{CM}} \end{bmatrix}^T$ the positions of station i in the CF and CM frames, respectively.

Traditionally, the network shift approach has been the most widely used procedure for determining geocentre motion from SLR (*Bouillé et al.*, 2000; *Crétaux et al.*, 2002; *Moore and Wang*, 2003; *Feissel-Vernier et al.*, 2006; *Collilieux et al.*, 2009), GPS (*Blewitt et al.*, 1992; *Heflin and Watkins*, 1999; *Dong et al.*, 2003; *Ferland and Piraszewski*, 2009; *Collilieux et al.*, 2011) and DORIS (*Bouillé et al.*, 2000; *Crétaux et al.*, 2002; *Feissel-Vernier et al.*, 2006; *Kuzin et al.*, 2010) tracking data. Nevertheless, to date only SLR has proven capable of providing reliable geocentre motion estimates using this approach, whereas GPS (*Meindl et al.*, 2013; *Rebischung et al.*, 2014) and DORIS (*Willis et al.*,

2006; *Gobinddass et al.*, 2009a,b) solutions are of lower quality due to orbit modelling errors and large correlations between parameters.

The scale factor d from (3.18) is typically estimated when investigating biases between reference frames realised by different satellite geodetic techniques. The inclusion of a scale parameter in the network shift approach is though a debatable matter (e.g. *Tregoning and van Dam*, 2005; *Lavallée et al.*, 2006; *Collilieux et al.*, 2012; *Wu et al.*, 2015) since it has the potential to exacerbate the aliasing of loading signals and degrade the quality of the translation estimates.

3.2.3 The kinematic approach

In the topocentric tangential coordinate system whose origin is at the location of the ground station described by the geodetic latitude φ and longitude λ, the position vector $\mathbf{q}$ of a satellite at an arbitrary time t may be expressed as

$$\mathbf{q} = \mathbf{R}\left(\mathbf{r}' - \mathbf{p} + \mathbf{r}_{\mathrm{CM-CF}}\right), \tag{3.26}$$

where

$$\mathbf{R} = \begin{bmatrix} -\sin\lambda & \cos\lambda & 0 \\ -\sin\varphi\cos\lambda & -\sin\varphi\sin\lambda & \cos\varphi \\ \cos\varphi\cos\lambda & \cos\varphi\sin\lambda & \sin\varphi \end{bmatrix} \tag{3.27}$$

is the matrix describing the rotation from geocentric to topocentric coordinates, $\mathbf{r}'$ is the position vector of the satellite in the CM frame, $\mathbf{p}$ is the station position vector in the CF frame and $\mathbf{r}_{\mathrm{CM-CF}}$ is the geocentre vector (Figure 3.2). If the topocentric position vector $\mathbf{q}$ is expressed in an Earth-centred, Earth-fixed frame such as the ITRF, $\mathbf{R}$ vanishes from (3.26).

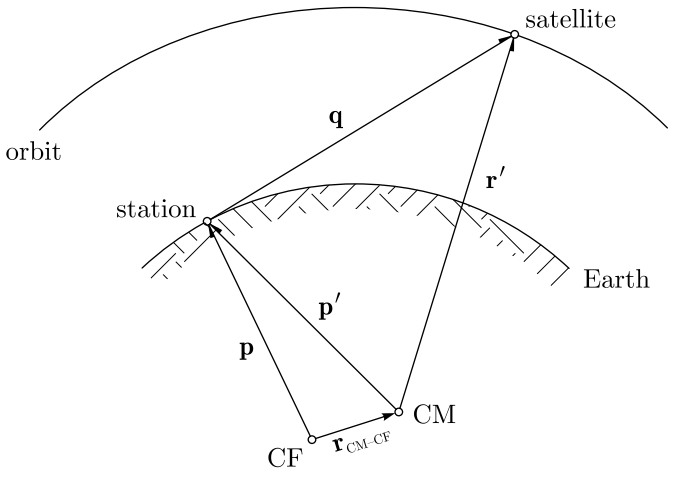

Figure 3.2 Observation geometry of the geocentre vector in the kinematic approach

By neglecting technique-specific light-time corrections, signal propagation effects and modelling errors, the first order approximation of the geometric station-satellite range ρ

is given by

$$\rho = \|\mathbf{r}' - \mathbf{p} + \mathbf{r}_{\mathrm{CM-CF}}\| \,. \tag{3.28}$$

The partial derivatives of the range ρ with respect to the geocentre coordinates in the Earth-centred, Earth-fixed frame are obtained as

$$\frac{\partial \rho}{\partial \mathbf{r}_{\mathrm{CM-CF}}} = \frac{\partial q}{\partial \mathbf{r}_{\mathrm{CM-CF}}} = \frac{\mathbf{q}^T}{q}, \tag{3.29}$$

where $\frac{\mathbf{q}^T}{q}$ is the normalised topocentric position vector of the satellite and $q = \|\mathbf{q}\|$. Analogously, the partial derivatives

$$\frac{\partial \rho}{\partial \mathbf{p}} = \frac{\partial q}{\partial \mathbf{p}} = -\frac{\mathbf{q}^T}{q} \tag{3.30}$$

with respect to the station coordinates can be derived. They are equal with opposite sign to the partial derivatives (3.29) when the geocentre vector is directed from CF towards CM, as assumed throughout this thesis. Conversely, when the geocentre vector is defined from CM towards CF, the partial derivatives of the range with respect to the geocentre coordinates and the station coordinates are equal. Due to this redundancy, the station coordinates $\mathbf{p}$ are typically held fixed for all or a selection of stations in the kinematic approach. For example, *Vigue et al.* (1992) and *Malla et al.* (1993) fixed the positions of three stations to constrain the orientation and scale of the frame to the a priori reference frame and determined positions only for non-fiducial sites. Alternatively, when explicitly estimating geocentre coordinates using (3.29) in the design matrix, a no-net-translation (NNT) condition can be introduced to eliminate the net-translation between the estimated and a priori frames.

Kuang et al. (2015) referred to the kinematic approach as the *fiducial solution*. The method was used by *Kang et al.* (2009) to determine geocentre motion from space-borne GPS tracking data acquired by the receivers aboard the twin GRACE satellites. Unlike the network shift approach, the kinematic approach takes into account the correlations between the geocentre coordinates and other parameters. However, by fixing the station coordinates, the origin of the underlying frame used for orbit determination is closer to CF (or CN) rather than the quasi-instantaneous CM. This origin inconsistency leads to orbital errors due to neglected displacements at individual stations.

3.3 Deformation approaches

Deformation approaches use geodetic observations of surface displacements to infer geocentre motion through the degree-1 elastic deformation of the solid Earth and degree-1 load Love numbers (*Farrell*, 1972; *Blewitt*, 2003). The *degree-1 deformation approach* (*Blewitt et al.*, 2001) models the translational aspect of the network of ground stations using surface displacements in the CF frame, whereas the *CM method* (*Lavallée et al.*,

2006) considers both the translation and the deformation of the network with surface displacements expressed in the CM frame. Alternatively, satellite observations can be expressed as functions of surface mass coefficients in a *rigorous parameter combination* (*Rülke et al.*, 2008; *Fritsche et al.*, 2010) that allows the estimation of geocentre motion simultaneously with station positions and Earth orientation parameters.

3.3.1 Geopotential and surface mass

The Earth's gravity field is represented by the gravity potential W, the sum of the gravitational potential V due to Earth's mass and the centrifugal potential Φ induced by the Earth's rotation. The gravitational potential at a point on or external to the Earth's surface is expressed using spherical harmonics as

$$V(r,\varphi,\lambda) = \frac{GM}{r}\sum_{n=0}^{\infty}\sum_{m=0}^{n}\left(\frac{a_e}{r}\right)^n P_{nm}(\sin\varphi)\left(C_{nm}\cos m\lambda + S_{nm}\sin m\lambda\right), \tag{3.31}$$

where

r, φ, λ	spherical geocentric coordinates (radial distance, latitude, longitude),
GM	geocentric gravitational constant,
n, m	degree, order of the spherical harmonic expansion,
a_e	equatorial radius of the Earth,
P_{nm}	fully normalised associated Legendre functions, and
C_{nm}, S_{nm}	fully normalised spherical harmonic (Stokes) coefficients.

In theory, the summation over n in equation (3.31) runs from 0 to ∞. By assuming mass conservation in the Earth system $C_{00} = 1$ and the adopted GM value is preserved. Additionally, the degree-1 coefficients vanish in the CM frame. The expansion is generally truncated to a degree $\bar{n}$ which defines the spatial resolution of a given gravity field model (or geopotential model). Apart from $(\bar{n}+1)^2$ spherical harmonic coefficients, any geopotential model contains numerical values of GM and a_e that serve as scaling parameters.

The geopotential is commonly referenced to a best-fitting ellipsoid that closely approximates the geoid (i.e. the equipotential surface coinciding with the undisturbed mean sea level). The difference in height between the geoid and the reference ellipsoid measured along the ellipsoidal normal is known as the geoid height (or geoid undulation). As a first-order approximation, the geoid height N is related to the gravitational potential V through Bruns' theorem (*Hofmann-Wellenhof and Moritz*, 2006):

$$N = \frac{V - V_0}{\gamma} = \frac{T}{\gamma}, \tag{3.32}$$

where V_0 is the (normal) gravitational potential of the ellipsoid,

$$T(r,\varphi,\lambda) = \frac{GM}{r}\sum_{n=0}^{\infty}\sum_{m=0}^{n} P_{nm}(\sin\varphi)\left(\delta C_{nm}\cos m\lambda + \delta S_{nm}\sin m\lambda\right) \tag{3.33}$$

represents the anomalous potential, and γ is normal gravity on the ellipsoid. The residual harmonic coefficients δC_{nm} and δS_{nm} represent differences between the actual and the normal gravity field coefficients, but the δ notation is dropped hereinafter for simplicity. With $\gamma = \frac{GM}{r^2}$ in spherical approximation, using (3.32) and (3.33) the geoid height expressed in terms of surface spherical harmonics is

$$N(\varphi,\lambda) = a_e\sum_{n=0}^{\infty}\sum_{m=0}^{n} P_{nm}(\sin\varphi)\left(C_{nm}\cos m\lambda + S_{nm}\sin m\lambda\right). \tag{3.34}$$

Time variations in N due to mass redistribution in the Earth system can be represented through variations, ΔC_{nm} and ΔS_{nm}, of the spherical harmonic coefficients either between two epochs or with respect to a reference value (e.g. time average), thus

$$\Delta N(\varphi,\lambda) = a_e\sum_{n=0}^{\infty}\sum_{m=0}^{n} P_{nm}(\sin\varphi)\left(\Delta C_{nm}\cos m\lambda + \Delta S_{nm}\sin m\lambda\right). \tag{3.35}$$

The coefficients ΔC_{nm} and ΔS_{nm} contain contributions from both the gravitational attraction of the surface loads and the elastic deformation of the solid Earth due to mass loading. Under the assumption that on short timescales mass transport occurs within a thin fluid envelope above the Earth's crust, the total change in geopotential coefficients is given by the surface integral (*Wahr et al.*, 1998)

$$\left\{\begin{array}{c}\Delta C_{nm}\\ \Delta S_{nm}\end{array}\right\} = \frac{3}{4\pi a_e\rho_e}\frac{1+k_n}{2n+1}\iint \Delta\sigma(\varphi,\lambda)\,P_{nm}(\sin\varphi)\left\{\begin{array}{c}\cos m\lambda\\ \sin m\lambda\end{array}\right\}\sin\varphi\,d\varphi\,d\lambda, \tag{3.36}$$

where $\rho_e = \frac{3M}{4\pi a_e^3}$ is the mean density of the Earth ($= 5514\ \mathrm{kg\,m^{-3}}$) and k_n represents the load Love number of degree n (*Farrell*, 1972). The change in surface mass density, $\Delta\sigma(\varphi,\lambda)$, expressed in units of mass per area is described by

$$\Delta\sigma(\varphi,\lambda) = a_e\rho_w\sum_{n=0}^{\infty}\sum_{m=0}^{n} P_{nm}(\sin\varphi)\left(\Delta\tilde{C}_{nm}\cos m\lambda + \Delta\tilde{S}_{nm}\sin m\lambda\right), \tag{3.37}$$

where ρ_w denotes the density of sea water ($= 1025\ \mathrm{kg\,m^{-3}}$), so that the mass coefficients $\Delta\tilde{C}_{nm}$ and $\Delta\tilde{S}_{nm}$ are dimensionless and changes $\Delta\sigma/\rho_w$ are expressed in units of equivalent water height (EWH, i.e. the height of a column of sea water). The conversion between mass coefficients and geopotential coefficients is performed via

$$\left\{\begin{array}{c}\Delta C_{nm}\\ \Delta S_{nm}\end{array}\right\} = \frac{3\rho_w}{\rho_e}\frac{1+k_n}{2n+1}\left\{\begin{array}{c}\Delta\tilde{C}_{nm}\\ \Delta\tilde{S}_{nm}\end{array}\right\} \tag{3.38}$$

or, conversely,

$$\left\{ \begin{array}{c} \Delta\tilde{C}_{nm} \\ \Delta\tilde{S}_{nm} \end{array} \right\} = \frac{\rho_e}{3\rho_w} \frac{2n+1}{1+k_n} \left\{ \begin{array}{c} \Delta C_{nm} \\ \Delta S_{nm} \end{array} \right\}. \tag{3.39}$$

Inserting (3.39) in (3.37) leads to the relation

$$\Delta\sigma\left(\varphi,\lambda\right) = \frac{a_e\rho_e}{3} \sum_{n=0}^{\infty} \sum_{m=0}^{n} \frac{2n+1}{1+k_n} P_{nm}\left(\sin\varphi\right) \left(\Delta C_{nm}\cos m\lambda + \Delta S_{nm}\sin m\lambda\right), \tag{3.40}$$

which expresses the surface mass density anomaly in terms of changes in the geopotential coefficients. Likewise, using (3.38) in (3.35) yields the geoid height change as a function of mass coefficient variations

$$\Delta N\left(\varphi,\lambda\right) = \frac{3a_e\rho_w}{\rho_e} \sum_{n=0}^{\infty} \sum_{m=0}^{n} \frac{1+k_n}{2n+1} P_{nm}\left(\sin\varphi\right) \left(\Delta\tilde{C}_{nm}\cos m\lambda + \Delta\tilde{S}_{nm}\sin m\lambda\right). \tag{3.41}$$

The degree-0 term in (3.41) is proportional to the invariant mass of the Earth, including its fluid envelope, and vanishes unless contributions of individual surface layer components to the geoid are treated separately. A non-zero $\Delta\tilde{C}_{00}$ reflects the exchange of mass between different components, but does not result in a degree-0 response of the solid Earth (i.e. $k_0 = 0$ for an incompressible Earth model).

At a point on the Earth's crust, the load-induced elastic deformation expressed in the local topocentric frame (east, north, radial) is given by the spherical harmonic expansions (*Farrell*, 1972; *Lavallée et al.*, 2006)

$$\begin{aligned} s_e\left(\varphi,\lambda\right) &= \frac{3a_e\rho_w}{\rho_e} \sum_{n=1}^{\infty} \sum_{m=0}^{n} \frac{l_n}{2n+1} \frac{P_{nm}\left(\sin\varphi\right)}{\cos\varphi} \\ &\quad \cdot \left(-m\Delta\tilde{C}_{nm}\sin m\lambda + m\Delta\tilde{S}_{nm}\cos m\lambda\right), \\ s_n\left(\varphi,\lambda\right) &= \frac{3a_e\rho_w}{\rho_e} \sum_{n=1}^{\infty} \sum_{m=0}^{n} \frac{l_n}{2n+1} \frac{\partial P_{nm}\left(\sin\varphi\right)}{\partial\varphi} \left(\Delta\tilde{C}_{nm}\cos m\lambda + \Delta\tilde{S}_{nm}\sin m\lambda\right), \\ s_u\left(\varphi,\lambda\right) &= \frac{3a_e\rho_w}{\rho_e} \sum_{n=1}^{\infty} \sum_{m=0}^{n} \frac{h_n}{2n+1} P_{nm}\left(\sin\varphi\right) \left(\Delta\tilde{C}_{nm}\cos m\lambda + \Delta\tilde{S}_{nm}\sin m\lambda\right), \end{aligned} \tag{3.42}$$

where h_n and l_n are degree-n load Love numbers. Equation (3.42) can also be written as

$$\begin{aligned} s_e\left(\varphi,\lambda\right) &= \frac{3a_e\rho_w}{\rho_e} \sum_{n=1}^{\infty} \sum_{m=0}^{n} \frac{l_n}{2n+1} \frac{1}{\cos\varphi} \left[\Delta\tilde{C}_{nm} \frac{\partial Y^C_{nm}\left(\varphi,\lambda\right)}{\partial\lambda} + \Delta\tilde{S}_{nm} \frac{\partial Y^S_{nm}\left(\varphi,\lambda\right)}{\partial\lambda}\right], \\ s_n\left(\varphi,\lambda\right) &= \frac{3a_e\rho_w}{\rho_e} \sum_{n=1}^{\infty} \sum_{m=0}^{n} \frac{l_n}{2n+1} \left[\Delta\tilde{C}_{nm} \frac{\partial Y^C_{nm}\left(\varphi,\lambda\right)}{\partial\varphi} + \Delta\tilde{S}_{nm} \frac{\partial Y^S_{nm}\left(\varphi,\lambda\right)}{\partial\varphi}\right], \\ s_u\left(\varphi,\lambda\right) &= \frac{3a_e\rho_w}{\rho_e} \sum_{n=1}^{\infty} \sum_{m=0}^{n} \frac{h_n}{2n+1} \left[\Delta\tilde{C}_{nm} Y^C_{nm}\left(\varphi,\lambda\right) + \Delta\tilde{S}_{nm} Y^S_{nm}\left(\varphi,\lambda\right)\right], \end{aligned} \tag{3.43}$$

where

$$\begin{aligned} Y^C_{nm}\left(\varphi,\lambda\right) &= P_{nm}\left(\sin\varphi\right)\cos m\lambda, \\ Y^S_{nm}\left(\varphi,\lambda\right) &= P_{nm}\left(\sin\varphi\right)\sin m\lambda, \end{aligned} \tag{3.44}$$

are spherical harmonic basis functions, which are orthogonal on the unit sphere (i.e. the surface integral of the product of any two different functions equals zero).

3.3.2 The degree-1 deformation approach

Theory of degree-1 deformation

The degree-1 load Love numbers are frame dependent (*Blewitt*, 2003) and their choice is determined by the frame in which the observations (i.e. station displacements or geopotential coefficients) are provided. Regardless of the frame, using (3.38) the relation between degree-1 geopotential coefficients and degree-1 mass coefficients is given by

$$\begin{bmatrix} \Delta C_{10} \\ \Delta C_{11} \\ \Delta S_{11} \end{bmatrix} = \frac{\rho_w}{\rho_e} (1 + k_1) \begin{bmatrix} \Delta \tilde{C}_{10} \\ \Delta \tilde{C}_{11} \\ \Delta \tilde{S}_{11} \end{bmatrix} \tag{3.45}$$

or, alternatively,

$$\begin{bmatrix} \Delta \tilde{C}_{10} \\ \Delta \tilde{C}_{11} \\ \Delta \tilde{S}_{11} \end{bmatrix} = \frac{\rho_e}{\rho_w} \frac{1}{1 + k_1} \begin{bmatrix} \Delta C_{10} \\ \Delta C_{11} \\ \Delta S_{11} \end{bmatrix}. \tag{3.46}$$

The load-driven motion between CM and a frame F (i.e. any of CE, CF, CL, CH) obtained by surface integration of (3.42) is (*Trupin et al.*, 1992)

$$\mathbf{r}_{\mathrm{CM}-F} = \sqrt{3}\, a_e \frac{\rho_w}{\rho_e} \left([\alpha_{\mathrm{CM}}]_{\mathrm{CE}} + [\alpha_{\mathrm{CE}}]_F \right) \begin{bmatrix} \Delta \tilde{C}_{11} \\ \Delta \tilde{S}_{11} \\ \Delta \tilde{C}_{10} \end{bmatrix}, \tag{3.47}$$

where $[\alpha_{\mathrm{CE}}]_F = [k_1]_F$ is an *isomorphic parameter* characterising the average solid Earth deformation that causes a translation between CE and frame F (*Blewitt*, 2003). The term $[\alpha_{\mathrm{CM}}]_{\mathrm{CE}} = 1$ is constant, whereas the factor $\sqrt{3}$ is included in (3.47) to convert normalised to conventional (or unnormalised) mass coefficients of degree-1. Table 3.1 lists the numerical values the degree-1 load Love numbers computed by *Blewitt* (2003) for the spherically symmetric, radially layered and elastic Earth used by *Farrell* (1972). Similar values were obtained for the commonly used preliminary reference Earth model (PREM; *Dziewonski and Anderson*, 1981) by *Grafarend et al.* (1997) and *Métivier et al.* (2006) and for more recent Earth models by *Wang et al.* (2012). For the CF frame $[\alpha_{\mathrm{CE}}]_{\mathrm{CF}} = -\frac{1}{3} \left([h_1]_{\mathrm{CE}} + 2\, [l_1]_{\mathrm{CE}} \right) = [k_1]_{\mathrm{CF}}$, thus the motion between CM and CF is

$$\mathbf{r}_{\mathrm{CM}-\mathrm{CF}} = \begin{bmatrix} X_{\mathrm{GC}} \\ Y_{\mathrm{GC}} \\ Z_{\mathrm{GC}} \end{bmatrix} = \sqrt{3}\, a_e \frac{\rho_w}{\rho_e} \left(1 - \frac{[h_1]_{\mathrm{CE}} + 2\, [l_1]_{\mathrm{CE}}}{3} \right) \begin{bmatrix} \Delta \tilde{C}_{11} \\ \Delta \tilde{S}_{11} \\ \Delta \tilde{C}_{10} \end{bmatrix} \tag{3.48}$$

or, alternatively,

$$\mathbf{r}_{\mathrm{CM-CF}} = \sqrt{3}\, a_e \frac{\rho_w}{\rho_e} \left(1 + [k_1]_{\mathrm{CF}}\right) \begin{bmatrix} \Delta\tilde{C}_{11} \\ \Delta\tilde{S}_{11} \\ \Delta\tilde{C}_{10} \end{bmatrix}. \tag{3.49}$$

Analogously, the motion of CM relative to CE is given by

$$\mathbf{r}_{\mathrm{CM-CE}} = \sqrt{3}\, a_e \frac{\rho_w}{\rho_e} \begin{bmatrix} \Delta\tilde{C}_{11} \\ \Delta\tilde{S}_{11} \\ \Delta\tilde{C}_{10} \end{bmatrix}. \tag{3.50}$$

From (3.46) and (3.50), the following relation between the vector directed from CE towards CM and the degree-1 geopotential coefficients is obtained:

$$\mathbf{r}_{\mathrm{CM-CE}} = \sqrt{3}\, a_e \begin{bmatrix} \Delta C_{11} \\ \Delta S_{11} \\ \Delta C_{10} \end{bmatrix}, \tag{3.51}$$

which is identical to (3.17) derived in Section 3.2.1.

Table 3.1 Numerical values of degree-1 load Love numbers for different reference frames

Frame F	$[h_1]_F$	$[l_1]_F$	$[k_1]_F$
CE	−0.290	0.113	0
CF	−0.269	0.134	0.021
CM	−1.290	−0.887	−1
CL	−0.403	0	−0.113
CH	0	0.403	0.290

The relative position of CE with respect to CF is given by

$$\mathbf{r}_{\mathrm{CE-CF}} = \sqrt{3}\, a_e \frac{\rho_w}{\rho_e} [k_1]_{\mathrm{CF}} \begin{bmatrix} \Delta\tilde{C}_{11} \\ \Delta\tilde{S}_{11} \\ \Delta\tilde{C}_{10} \end{bmatrix} = [k_1]_{\mathrm{CF}}\, \mathbf{r}_{\mathrm{CM-CE}}. \tag{3.52}$$

Inserting (3.50) in (3.49) yields the relation

$$\mathbf{r}_{\mathrm{CM-CE}} = \frac{1}{1 + [k_1]_{\mathrm{CF}}} \mathbf{r}_{\mathrm{CM-CF}}, \tag{3.53}$$

which can be substituted in (3.52) to obtain

$$\mathbf{r}_{\mathrm{CE-CF}} = \frac{[k_1]_{\mathrm{CF}}}{1 + [k_1]_{\mathrm{CF}}} \mathbf{r}_{\mathrm{CM-CF}} \approx 0.021 \cdot \mathbf{r}_{\mathrm{CM-CF}}. \tag{3.54}$$

As (3.54) shows, the motion between CE and CF represents only about 2% of the geocentre motion CM–CF, which quantifies to less than 0.2 mm. Although both $\mathbf{r}_{\mathrm{CM-CE}}$

and $\mathbf{r}_{\mathrm{CM-CF}}$ constitute possible definitions of the geocentre vector, the adoption of the latter is supported by the practical realisation of the ITRF origin via networks of stations attached to the Earth's crust.

The degree-1 geopotential coefficients vanish in the CM frame since $[k_1]_{\mathrm{CM}} = -1$ in equation (3.45). Hence satellite missions such as GRACE that deliver observations in this particular frame are inherently insensitive to geocentre motion. In situ hydrological observations and outputs of geophysical loading models are given in the CF frame. To represent mass variations from GRACE in the CF frame, the geopotential coefficients of degree $n \geq 2$ need to be complemented by degree-1 terms derived from alternative datasets or data combinations, an approach often employed in recent studies of mass variability from GRACE (e.g. *Baur et al.* 2013; *Schrama et al.* 2014).

Determination of geocentre motion

Surface mass coefficients can be estimated using observations of load-induced deformations from a dense and well-distributed network of permanent GNSS stations. For each station i, the observation equations are as follows:

$$\begin{aligned}\begin{bmatrix} X_i^{\mathrm{CF}} - X_i^{\mathrm{CM}} \\ Y_i^{\mathrm{CF}} - Y_i^{\mathrm{CM}} \\ Z_i^{\mathrm{CF}} - Z_i^{\mathrm{CM}} \end{bmatrix} &= \begin{bmatrix} t_X \\ t_Y \\ t_Z \end{bmatrix} + \begin{bmatrix} 0 & -r_Z & r_Y \\ r_Z & 0 & -r_X \\ -r_Y & r_X & 0 \end{bmatrix} \begin{bmatrix} X_i^{\mathrm{CM}} \\ Y_i^{\mathrm{CM}} \\ Z_i^{\mathrm{CM}} \end{bmatrix} \\ &\quad + \frac{a_e \rho_w}{\rho_e} \mathbf{R}_i^T \mathbf{L}_{\mathrm{CF}} \mathbf{R}_i \begin{bmatrix} \Delta\tilde{C}_{11} \\ \Delta\tilde{S}_{11} \\ \Delta\tilde{C}_{10} \end{bmatrix} + \frac{3 a_e \rho_w}{\rho_e} \mathbf{R}_i^T \mathbf{Y}_i \begin{bmatrix} \Delta\tilde{C}_{20} \\ \Delta\tilde{C}_{21} \\ \vdots \\ \Delta\tilde{S}_{\bar{n}\bar{n}} \end{bmatrix}, \end{aligned} \tag{3.55}$$

where $\mathbf{R}_i$ is the rotation matrix (3.27) from the geocentric frame to the local topocentric frame (east, north, radial), $\mathbf{L}_{\mathrm{CF}} = \mathrm{diag}\left([l_1]_{\mathrm{CF}}, [l_1]_{\mathrm{CF}}, [h_1]_{\mathrm{CF}}\right)$ is a diagonal matrix containing the degree-1 load Love numbers in the CF frame, $[l_1]_{\mathrm{CF}}$ and $[h_1]_{\mathrm{CF}}$, and

$$\mathbf{Y}_i = \begin{bmatrix} \frac{l_2}{5} \frac{1}{\cos\varphi_i} \frac{\partial Y_{20}^C(\varphi_i,\lambda_i)}{\partial\lambda} & \frac{l_2}{5} \frac{1}{\cos\varphi_i} \frac{\partial Y_{21}^C(\varphi_i,\lambda_i)}{\partial\lambda_i} & \cdots & \frac{l_{\bar{n}}}{2\bar{n}+1} \frac{1}{\cos\varphi_i} \frac{\partial Y_{\bar{n}\bar{n}}^S(\varphi_i,\lambda_i)}{\partial\lambda_i} \\ \frac{l_2}{5} \frac{\partial Y_{20}^C(\varphi_i,\lambda_i)}{\partial\varphi_i} & \frac{l_2}{5} \frac{\partial Y_{21}^C(\varphi_i,\lambda_i)}{\partial\varphi_i} & \cdots & \frac{l_{\bar{n}}}{2\bar{n}+1} \frac{\partial Y_{\bar{n}\bar{n}}^S(\varphi_i,\lambda_i)}{\partial\varphi_i} \\ \frac{h_2}{5} Y_{20}^C(\varphi_i,\lambda_i) & \frac{h_2}{5} Y_{21}^C(\varphi_i,\lambda_i) & \cdots & \frac{h_{\bar{n}}}{2\bar{n}+1} Y_{\bar{n}\bar{n}}^S(\varphi_i,\lambda_i) \end{bmatrix}. \tag{3.56}$$

The other quantities in (3.55) have the following meaning:

$X_i^{\mathrm{CF}}, Y_i^{\mathrm{CF}}, Z_i^{\mathrm{CF}}$	Cartesian station coordinates in the CF frame, propagated at the epoch of the CM frame,
$X_i^{\mathrm{CM}}, Y_i^{\mathrm{CM}}, Z_i^{\mathrm{CM}}$	Cartesian station coordinates in a quasi-instantaneous CM frame with secular deformations (i.e. due to plate tectonics and GIA) removed,
t_X, t_Y, t_Z	translation parameters between the CM frame and the CF frame,

r_X, r_Y, r_Z rotation parameters between the CM frame and the CF frame,
$\bar{n}$ truncation degree of the deformation field.

The removal of long-term deformations ensures that the coordinate differences $X_i^{\mathrm{CF}} - X_i^{\mathrm{CM}}$, $Y_i^{\mathrm{CF}} - Y_i^{\mathrm{CM}}$, $Z_i^{\mathrm{CF}} - Z_i^{\mathrm{CM}}$ represent the inverted field of non-linear deformations supposedly due exclusively to elastic loading of the solid Earth. The estimation of translation parameters imposes the use of CF frame degree-1 load Love numbers, so that the load-induced deformations are expressed in the CF frame.

Using (3.48), the observation equations (3.55) can be expressed as functions of the geocentre coordinates using

$$\begin{aligned}\begin{bmatrix} X_i^{\mathrm{CF}} - X_i^{\mathrm{CM}} \\ Y_i^{\mathrm{CF}} - Y_i^{\mathrm{CM}} \\ Z_i^{\mathrm{CF}} - Z_i^{\mathrm{CM}} \end{bmatrix} &= \begin{bmatrix} t_X \\ t_Y \\ t_Z \end{bmatrix} + \begin{bmatrix} 0 & -r_Z & r_Y \\ r_Z & 0 & -r_X \\ -r_Y & r_X & 0 \end{bmatrix} \begin{bmatrix} X_i^{\mathrm{CM}} \\ Y_i^{\mathrm{CM}} \\ Z_i^{\mathrm{CM}} \end{bmatrix} \\ &\quad + \frac{1}{\sqrt{3}} \left(1 - \frac{[h_1]_{\mathrm{CE}} + 2\,[l_1]_{\mathrm{CE}}}{3} \right)^{-1} \mathbf{R}_i^T \mathbf{L}_{\mathrm{CF}} \mathbf{R}_i \begin{bmatrix} X_{\mathrm{GC}} \\ Y_{\mathrm{GC}} \\ Z_{\mathrm{GC}} \end{bmatrix} \\ &\quad + \frac{3 a_e \rho_w}{\rho_e} \mathbf{R}_i^T \mathbf{Y}_i \begin{bmatrix} \Delta\tilde{C}_{20} \\ \Delta\tilde{C}_{21} \\ \vdots \\ \Delta\tilde{S}_{\bar{n}\bar{n}} \end{bmatrix}. \end{aligned} \tag{3.57}$$

The parameter vector of the degree-1 deformation approach is

$$\mathbf{x} = \begin{bmatrix} t_X & t_Y & t_Z & r_X & r_Y & r_Z & \mathbf{r}_{\mathrm{CM-CF}}^T & \Delta\tilde{C}_{20} & \Delta\tilde{C}_{21} & \dots & \Delta\tilde{S}_{\bar{n}\bar{n}} \end{bmatrix}^T. \tag{3.58}$$

The least squares design matrix for each station i is given by

$$\mathbf{A}_i = \begin{bmatrix} \mathbf{I}_3 & \mathbf{B}_i & \frac{1}{\sqrt{3}} \left(1 - \frac{[h_1]_{\mathrm{CE}} + 2[l_1]_{\mathrm{CE}}}{3} \right)^{-1} \mathbf{R}_i^T \mathbf{L}_{\mathrm{CF}} \mathbf{R}_i & \frac{3 a_e \rho_w}{\rho_e} \mathbf{R}_i^T \mathbf{Y}_i \end{bmatrix}, \tag{3.59}$$

where $\mathbf{I}_3 = \mathrm{diag}\,(1,\, 1,\, 1)$ is the 3×3 identity matrix and

$$\mathbf{B}_i = \begin{bmatrix} 0 & -Z_i^{\mathrm{CM}} & Y_i^{\mathrm{CM}} \\ Z_i^{\mathrm{CM}} & 0 & -X_i^{\mathrm{CM}} \\ -Y_i^{\mathrm{CM}} & X_i^{\mathrm{CM}} & 0 \end{bmatrix}. \tag{3.60}$$

The term $\frac{3 a_e \rho_w}{\rho_e} \mathbf{R}_i^T \mathbf{Y}_i$ contains the partial derivatives of (3.42) with respect to mass coefficients of degree $n \in [2, \bar{n}]$, transformed by the rotation matrix $\mathbf{R}_i^T$ in the geocentric frame.

When first proposed by *Blewitt et al.* (2001), the method only included the estimation of degree-1 mass coefficients with the associated geocentre coordinates, hence the name of degree-1 deformation approach. However, *Wu et al.* (2002) found that neglecting higher-

degree elastic deformation components by omitting the last term in (3.57) may lead to the aliasing of truncated coefficients into the estimated geocentre coordinates. The severity of the aliasing depends on the station distribution and may be more pronounced for sparse networks. Simultaneously estimating geocentre coordinates and mass coefficients of higher degrees mitigates the aliasing problem (*Blewitt and Clarke*, 2003; *Dong et al.*, 2003; *Wu et al.*, 2003). The truncation degree $\bar{n}$ can be varied over time to account for changes in network size (e.g. *Fritsche et al.*, 2010).

Subsequent refinements of the degree-1 deformation approach focused predominantly on mitigating the lack of observations over oceanic regions. *Blewitt and Clarke* (2003) forced the solution over the ocean domain to follow an equipotential surface consistent with the distribution of continental mass and taking into account the mass exchange between oceans and land. The limited variability in oceanic mass compared to continental mass was constrained by *Kusche and Schrama* (2005) via a regularisation matrix. To avoid oceanic constraints, *Clarke et al.* (2007) proposed modified basis functions, as an alternative to the spherical harmonic basis functions given by (3.44). Unlike approaches that employ oceanic smoothing, the modified basis functions implicitly conserve mass globally and allow significant continental mass variability while preserving a smooth oceanic domain, which responds gravitationally to continental mass. As a trade-off between the methods of *Blewitt and Clarke* (2003) and *Kusche and Schrama* (2005), *Rietbroek et al.* (2014) adopted a regularisation technique that forces the ocean surface to approach an equipotential surface without strictly following it.

3.3.3 The CM method

The direct satellite tracking approaches described in Section 3.2 model the net translation of the network of ground stations in the CF frame. Conversely, the degree-1 deformation approach discussed in Section 3.3.2 models only the deformation of the network in the CF frame due to the estimation of nuisance translation parameters. To address the conceptual limitations of previous approaches, *Lavallée et al.* (2006) proposed a unified procedure named the *CM method* that models both the translational and the deformation signatures of the network on geocentre motion in the CM frame.

Using the same notations as in Section 3.3.2, the observation equations for each station i can be expressed in terms of the geocentre coordinates as

$$\begin{aligned}\begin{bmatrix} X_i^{\mathrm{CF}} - X_i^{\mathrm{CM}} \\ Y_i^{\mathrm{CF}} - Y_i^{\mathrm{CM}} \\ Z_i^{\mathrm{CF}} - Z_i^{\mathrm{CM}} \end{bmatrix} &= \begin{bmatrix} 0 & -r_Z & r_Y \\ r_Z & 0 & -r_X \\ -r_Y & r_X & 0 \end{bmatrix} \begin{bmatrix} X_i^{\mathrm{CM}} \\ Y_i^{\mathrm{CM}} \\ Z_i^{\mathrm{CM}} \end{bmatrix} \\ &+ \frac{1}{\sqrt{3}} \left(1 - \frac{[h_1]_{\mathrm{CE}} + 2\,[l_1]_{\mathrm{CE}}}{3} \right)^{-1} \mathbf{R}_i^T \mathbf{L}_{\mathrm{CM}} \mathbf{R}_i \begin{bmatrix} X_{\mathrm{GC}} \\ Y_{\mathrm{GC}} \\ Z_{\mathrm{GC}} \end{bmatrix} \\ &+ \frac{3 a_e \rho_w}{\rho_e} \mathbf{R}_i^T \mathbf{Y}_i \begin{bmatrix} \Delta\tilde{C}_{20} \\ \Delta\tilde{C}_{21} \\ \vdots \\ \Delta\tilde{S}_{\bar{n}\bar{n}} \end{bmatrix}, \end{aligned} \tag{3.61}$$

where $\mathbf{L}_{\mathrm{CM}} = \mathrm{diag}\left([l_1]_{\mathrm{CM}}, [l_1]_{\mathrm{CM}}, [h_1]_{\mathrm{CM}}\right)$ contains the degree-1 load Love numbers $[l_1]_{\mathrm{CM}}$ and $[h_1]_{\mathrm{CM}}$ in the CM frame. The differences between (3.61) and the observation equations (3.57) from the degree-1 deformation approach consist in the omission of the translation vector and the use of degree-1 Love numbers in the CM frame.

In the CM method, the parameter vector is

$$\mathbf{x} = \begin{bmatrix} r_X & r_Y & r_Z & \mathbf{r}_{\mathrm{CM-CF}}^T & \Delta\tilde{C}_{20} & \Delta\tilde{C}_{21} & \cdots & \Delta\tilde{S}_{\bar{n}\bar{n}} \end{bmatrix}^T, \tag{3.62}$$

whereas the station-specific design matrix reads

$$\mathbf{A}_i = \begin{bmatrix} \mathbf{B}_i & \frac{1}{\sqrt{3}} \left(1 - \frac{[h_1]_{\mathrm{CE}} + 2[l_1]_{\mathrm{CE}}}{3} \right)^{-1} \mathbf{R}_i^T \mathbf{L}_{\mathrm{CM}} \mathbf{R}_i & \frac{3 a_e \rho_w}{\rho_e} \mathbf{R}_i^T \mathbf{Y}_i \end{bmatrix}. \tag{3.63}$$

The CM method performs more robustly than direct satellite tracking and the degree-1 deformation approach when a fully populated covariance matrix is employed to appropriately adjust the contributions of network translation and network deformation to the estimated geocentre coordinates (*Lavallée et al.*, 2006). When using a diagonal or block diagonal covariance matrix, the network translation considerably outweighs the deformation and the CM approach supplies identical results to the network shift approach.

3.3.4 Rigorous parameter combination

As an alternative to the a posteriori determination of geocentre motion and surface mass coefficients from station displacements $\mathbf{s}$ given by (3.42), *Rülke et al.* (2008) and *Fritsche et al.* (2010) suggested the simultaneous estimation of station positions and velocities $\mathbf{p}$, Earth orientation parameters and orbital parameters $\mathbf{o}$ and surface mass coefficients $\boldsymbol{\sigma}$

from satellite observations $\mathbf{l}$. The parameter vector reads

$$\mathbf{x} = \begin{bmatrix} \mathbf{p} & \mathbf{o} & \boldsymbol{\sigma} \end{bmatrix}^T \tag{3.64}$$

and the design matrix is

$$\mathbf{A} = \begin{bmatrix} \frac{\partial \mathbf{l}}{\partial \mathbf{p}} & \frac{\partial \mathbf{l}}{\partial \mathbf{o}} & \frac{\partial \mathbf{l}}{\partial \boldsymbol{\sigma}} \end{bmatrix}. \tag{3.65}$$

The partial derivatives of the observations with respect to the mass coefficients $\Delta\tilde{C}_{nm}$ and $\Delta\tilde{S}_{nm}$ forming the vector $\boldsymbol{\sigma}$ can be expressed as

$$\frac{\partial \mathbf{l}}{\partial \boldsymbol{\sigma}} = \frac{\partial \mathbf{l}}{\partial \mathbf{p}} \frac{\partial \mathbf{p}}{\partial \boldsymbol{\sigma}} = \frac{\partial \mathbf{l}}{\partial \mathbf{p}} \operatorname{diag}\left(\mathbf{R}_1^T, \mathbf{R}_2^T, \ldots, \mathbf{R}_k^T\right) \frac{\partial \mathbf{s}}{\partial \boldsymbol{\sigma}}, \tag{3.66}$$

where $\partial\mathbf{s}/\partial\boldsymbol{\sigma}$ are the partial derivatives of the station displacements with respect to the mass coefficients, which can be obtained from (3.42) and $\mathbf{R}_{i=1,k}$ are the geocentric to topocentric rotation matrices (3.27) for each station i.

Denoting the weight matrix by $\mathbf{W}$, the normal matrix $\mathbf{N}$ reads

$$\begin{aligned} \mathbf{N} = \mathbf{A}^T\mathbf{W}\mathbf{A} &= \begin{bmatrix} \mathbf{N}_{\mathbf{pp}} & \mathbf{N}_{\mathbf{po}} & \mathbf{N}_{\mathbf{p\sigma}} \\ \cdots & \mathbf{N}_{\mathbf{oo}} & \mathbf{N}_{\mathbf{o\sigma}} \\ \cdots & \cdots & \mathbf{N}_{\boldsymbol{\sigma\sigma}} \end{bmatrix} \\ &= \begin{bmatrix} \frac{\partial \mathbf{l}}{\partial \mathbf{p}}^T \mathbf{W} \frac{\partial \mathbf{l}}{\partial \mathbf{p}} & \frac{\partial \mathbf{l}}{\partial \mathbf{p}}^T \mathbf{W} \frac{\partial \mathbf{l}}{\partial \mathbf{o}} & \frac{\partial \mathbf{l}}{\partial \mathbf{p}}^T \mathbf{W} \frac{\partial \mathbf{l}}{\partial \boldsymbol{\sigma}} \\ \cdots & \frac{\partial \mathbf{l}}{\partial \mathbf{o}}^T \mathbf{W} \frac{\partial \mathbf{l}}{\partial \mathbf{o}} & \frac{\partial \mathbf{l}}{\partial \mathbf{o}}^T \mathbf{W} \frac{\partial \mathbf{l}}{\partial \boldsymbol{\sigma}} \\ \cdots & \cdots & \frac{\partial \mathbf{l}}{\partial \boldsymbol{\sigma}}^T \mathbf{W} \frac{\partial \mathbf{l}}{\partial \boldsymbol{\sigma}} \end{bmatrix} \end{aligned} \tag{3.67}$$

and the right-hand side $\mathbf{b}$ of the normal equations system is

$$\mathbf{b} = \mathbf{A}^T\mathbf{W}\mathbf{l} = \begin{bmatrix} \mathbf{b}_{\mathbf{p}} & \mathbf{b}_{\mathbf{o}} & \mathbf{b}_{\boldsymbol{\sigma}} \end{bmatrix}^T = \begin{bmatrix} \frac{\partial \mathbf{l}}{\partial \mathbf{p}}^T \mathbf{W}\mathbf{l} & \frac{\partial \mathbf{l}}{\partial \mathbf{o}}^T \mathbf{W}\mathbf{l} & \frac{\partial \mathbf{l}}{\partial \boldsymbol{\sigma}}^T \mathbf{W}\mathbf{l} \end{bmatrix}^T. \tag{3.68}$$

Using (3.66), the elements of $\mathbf{N}$ and $\mathbf{b}$ containing the partial derivatives $\partial\mathbf{l}/\partial\boldsymbol{\sigma}$ can be decomposed as follows:

$$\begin{aligned} \mathbf{N}_{\mathbf{p\sigma}} &= \frac{\partial \mathbf{l}}{\partial \mathbf{p}}^T \mathbf{W} \frac{\partial \mathbf{l}}{\partial \mathbf{p}} \frac{\partial \mathbf{p}}{\partial \boldsymbol{\sigma}} = \mathbf{N}_{\mathbf{pp}} \frac{\partial \mathbf{p}}{\partial \boldsymbol{\sigma}}, \\ \mathbf{N}_{\mathbf{o\sigma}} &= \frac{\partial \mathbf{l}}{\partial \mathbf{o}}^T \mathbf{W} \frac{\partial \mathbf{l}}{\partial \mathbf{p}} \frac{\partial \mathbf{p}}{\partial \boldsymbol{\sigma}} = \mathbf{N}_{\mathbf{po}}^T \frac{\partial \mathbf{p}}{\partial \boldsymbol{\sigma}}, \\ \mathbf{N}_{\boldsymbol{\sigma\sigma}} &= \frac{\partial \mathbf{p}}{\partial \boldsymbol{\sigma}}^T \frac{\partial \mathbf{l}}{\partial \mathbf{p}}^T \mathbf{W} \frac{\partial \mathbf{l}}{\partial \mathbf{p}} \frac{\partial \mathbf{p}}{\partial \boldsymbol{\sigma}} = \frac{\partial \mathbf{p}}{\partial \boldsymbol{\sigma}}^T \mathbf{N}_{\mathbf{pp}} \frac{\partial \mathbf{p}}{\partial \boldsymbol{\sigma}}, \\ \mathbf{b}_{\boldsymbol{\sigma}} &= \frac{\partial \mathbf{p}}{\partial \boldsymbol{\sigma}}^T \frac{\partial \mathbf{l}}{\partial \mathbf{p}}^T \mathbf{W}\mathbf{l} = \frac{\partial \mathbf{p}}{\partial \boldsymbol{\sigma}}^T \mathbf{b}_{\mathbf{p}}. \end{aligned} \tag{3.69}$$

When considering mean station positions valid over a certain time period, the partial derivatives $\partial\mathbf{p}/\partial\boldsymbol{\sigma}$ are constant. This characteristic permits the introduction of the mass coefficients at the normal equation level rather than at the observation level. However,

the simultaneous estimation of station positions, station velocities and mass coefficients leads to additional singularities. Station coordinates are able to compensate any surface deformation pattern represented by the mass coefficients. Similarly, station velocities can absorb any linear rate of change in the mass coefficients. To remove these singularities, additional constraint conditions are imposed so that the mean and the linear trend of each mass coefficient equal zero over the entire period of the analysis (*Rülke et al.*, 2008). The effect of secular deformations due to plate tectonics and GIA is also implicitly removed in this manner.

The estimation of mass coefficients via either of the functional models (3.57) and (3.61) was called the *coordinate residual approach* by *Fritsche et al.* (2010) because it uses coordinate differences between a secular reference frame and an epoch reference frame as observations. In contrast to the degree-1 deformation and CM approaches, the rigorous parameter combination has the advantage of taking into consideration the correlations between mass coefficients and other parameters.

3.4 Forward modelling

Forward modelling of geocentre variations using geophysical fluid models has been performed for almost four decades (*Stolz*, 1976a,b; *Dong et al.*, 1997; *Chen et al.*, 1999; *Bouillé et al.*, 2000; *Crétaux et al.*, 2002; *Moore and Wang*, 2003; *Feissel-Vernier et al.*, 2006; *Collilieux et al.*, 2009; *Dong et al.*, 2014). In the absence of a complete system model encompassing all fluids of the Earth's surface layer, geocentre motion predictions rely on the combination of individual model outputs. The change in surface mass density, $\Delta\sigma(\varphi,\lambda)$, due to each load component can be computed and expanded into mass spherical harmonics by surface integration via the formula

$$\left\{ \begin{array}{c} \Delta\tilde{C}_{nm} \\ \Delta\tilde{S}_{nm} \end{array} \right\} = \frac{1}{4\pi a_e \rho_w} \iint \Delta\sigma(\varphi,\lambda)\, P_{nm}(\sin\varphi) \left\{ \begin{array}{c} \cos m\lambda \\ \sin m\lambda \end{array} \right\} \sin\varphi\, d\varphi\, d\lambda, \tag{3.70}$$

obtained by substituting (3.39) in (3.36). The geocentre coordinates can then be derived by inserting the values of the degree-1 mass coefficients in (3.48).

Variations in atmospheric mass are ordinarily modelled using outputs of surface pressure from atmospheric general circulation models, which are designed for forecasting weather and do not usually assimilate in situ observations of surface pressure. The most commonly employed global atmospheric models are the Integrated Forecasting System (IFS) developed by the European Centre for Medium-Range Weather Forecasts (ECMWF) and the Global Forecast System (GFS) produced by US National Centers for Environmental Prediction (NCEP). Both organisations operationally provide atmospheric surface pressure fields (Figure 3.3) with a maximum temporal resolution of six hours, along with other parameters such as geopotential height, air temperature and relative humidity. Differences between the two models occur predominantly on short

timescales, in particular over polar regions, the Southern Ocean and Asia (*Salstein et al.*, 2008), where atmospheric observations are sparse or lacking.

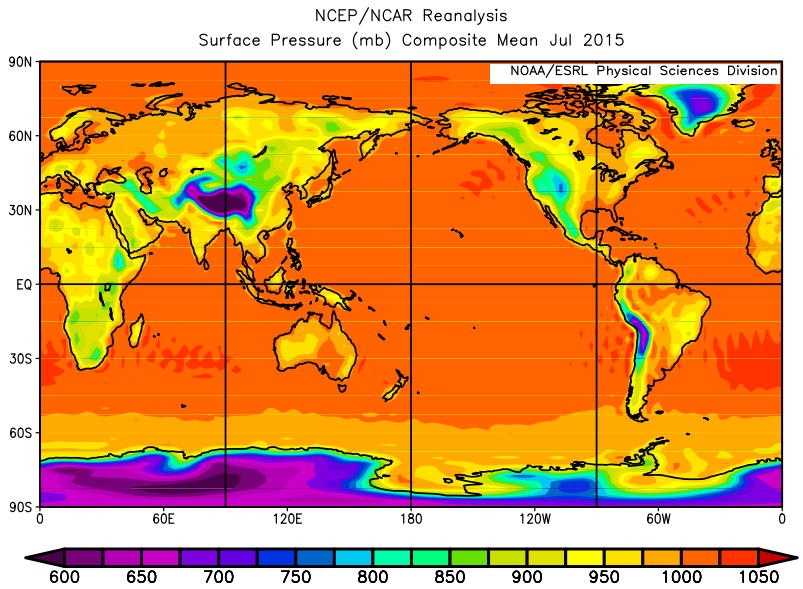

Figure 3.3 Average atmospheric surface pressure in July 2015 derived from the NCEP/NCAR reanalysis. Figure produced using the visualisation tools available at `http://www.esrl.noaa.gov/psd/products/display/`

According to *Wahr et al.* (1998), surface mass density changes can be derived from variations in surface pressure, ΔP, by

$$\Delta\sigma\left(\varphi,\lambda\right)=\frac{\Delta P\left(\varphi,\lambda\right)}{\bar{\gamma}}, \tag{3.71}$$

where $\bar{\gamma}$ is the mean value of surface gravity ($\approx 9.798\ \mathrm{m\,s^{-2}}$). The inverted barometer (IB) assumption (e.g. *Wunsch and Stammer*, 1997) is generally adopted to describe the oceanic response to fluctuations in atmospheric pressure. According to the IB theory, over periods longer than a few days, an increase of 1 hPa in atmospheric pressure results in a depression of 1 cm of the ocean surface and thus zero total mass change in the integrated oceanic and atmospheric mass column. Oceanic mass redistribution due to atmospheric pressure variations is implicitly admitted by choosing $\Delta\sigma = 0$ over oceans (*Wahr et al.*, 1998).

Seasonal geocentre motion predictions derived from ECMWF and NCEP surface pressure data display similar amplitudes and phases (*Bouillé et al.*, 2000; *Crétaux et al.*, 2002; *Dong et al.*, 2014) when the adopted oceanic response is identical, i.e. either IB or non-inverted barometer (NIB). However, *Dong et al.* (2014) showed that predictions made under the NIB assumption have approximately double amplitudes compared to the IB solutions using either of the atmospheric models. Linear trends and inter-annual oscillations are unaltered.

The contribution of the hydrosphere to geocentre motion is generally modelled as a sum of individual inputs from oceans, continental hydrology and occasionally from ice sheets

and glaciers (i.e. the cryosphere). Non-tidal oceanic mass variations can be derived either via outputs of ocean bottom pressure (OBP) from oceanic general circulation models (OGCM) or from altimeter observations. The latter need to be corrected for the steric contribution to sea level variations by means of temperature and salinity observations from the Argo network of floats or using equivalent data from a world ocean atlas.

Two of the most widely used OGCMs are the Ocean Model for Circulation and Tides (OMCT; *Thomas*, 2002) and the Estimating the Circulation and Climate of the Ocean (ECCO; *Wunsch et al.*, 2009). As many other OGCMs, both employ the Boussinesq approximation to conserve oceanic volume rather than the total mass. ECCO benefits from finer horizontal and vertical resolutions, but only spans the latitudes between 80°N and 80°S, a shortcoming that is addressed by the ECCO2 reanalysis in addition to reducing grid spacing (*Azaneu et al.*, 2014). OMCT forcing is based on various parameters from the ECMWF operational analyses and lacks real data constraints. In contrast, ECCO is obtained by iteratively fitting a general circulation model to both ground and satellite observations. OBP exhibits greater variability in OMCT, which tends to perform worse than ECCO when comparing predicted and measured OBP at a limited number of sites where observations are available (*Quinn and Ponte*, 2011). Another source of OBP is the Finite Element Sea Ice–Ocean Model (FESOM; *Timmermann et al.*, 2009).

Mass conservation can be enforced in OGCMs through a global adjustment of the ocean height by a uniform and time dependent parameter (*Greatbatch*, 1994; *Moore and Wang*, 2003). In analogy to (3.71), changes in surface mass density due to the redistribution of oceanic mass can be obtained as a ratio of the adjusted OBP, as a result of the mass conservation constraint, and the mean surface gravity. The variability in oceanic mass is arguably better modelled at present than continental mass variations.

The land water stored in any of its states above or below the Earth's surface represents the TWS, which plays a major role in the global hydrological cycle. Before the launch of the GRACE mission, consistent monitoring of the TWS at global scale was impractical. Among the components of the TWS, groundwater is the most inaccessible to conventional observation techniques. Due to the lack of vertical resolution, GRACE detects the integrated water content of all components. This constitutes a barrier for constraining large-scale hydrological models using GRACE observations, since models represent water storage in a modular way through various state variables. By subtracting the contributions of surface water, snow and ice, soil moisture and canopy water from the GRACE hydrological signature, variations in groundwater storage can be readily obtained, but results strongly depend on the adopted hydrological model (e.g. *Jin and Feng*, 2013).

Hydrological models developed for scales ranging from continental to global can be separated in water balance models (WBMs), used primarily for offline studies, and land surface models (LSMs), which employ an energy balance approach and are often coupled to atmospheric general circulation models. WBMs operate at longer timescales and finer spatial resolutions than LSMs and invoke a detailed representation of terres-

trial hydrological processes to close the water balance. Well-known WBMs include the Macro-scale–Probability-Distributed Moisture model (Mac-PDM; *Arnell*, 1999; *Gosling and Arnell*, 2011), WBM (*Fekete et al.*, 2002), the WaterGAP Global Hydrology Model (WGHM; *Döll et al.*, 2003) and the Water And Snow balance Modeling system–Macro-scale (WASMOD-M; *Widén-Nilsson et al.*, 2007). Despite the complex parameterisation of water and energy fluxes at the land–atmosphere boundary, the majority of LSMs have coarse vertical resolution, neglect water transport and are uncalibrated to observations (*Güntner*, 2008). Prominent models from this category are the Variable Infiltration Capacity (VIC) model (*Liang et al.*, 1994; *Nijssen et al.*, 2001), the Land Dynamics (LaD) model (*Milly and Shmakin*, 2002), PCR-GLOBWB (*van Beek et al.*, 2011) and its derivative PCR-GLOBWB-MOD (*Sutanudjaja et al.*, 2011), the land surface components of general circulation models, the Global Land Data Assimilation System (GLDAS; *Rodell et al.*, 2004) and the Land Surface Discharge Model (LSDM; *Dill*, 2008; *Dill and Dobslaw*, 2013). LSDM operates in near real-time, in close link to ECMWF atmospheric fields and OMCT to close the global water cycle and cover a large extent of the spectrum of mass transport within the fluid envelope.

Difficulties in quantifying groundwater storage variations led to incomplete assessments of the total contribution of continental hydrology to geocentre motion. Analyses are generally limited to the use of parameters routinely provided by hydrological models such as soil moisture and snow depth (*Chen et al.*, 1999; *Bouillé et al.*, 2000; *Crétaux et al.*, 2002; *Moore and Wang*, 2003; *Dong et al.*, 2014). These variables are often supplied in units of EWH, so that variations in surface mass density can be inferred from net changes in soil moisture and snow depth, ΔH, by

$$\Delta\sigma\left(\varphi,\lambda\right) = \Delta H\left(\varphi,\lambda\right)\rho_a, \tag{3.72}$$

where ρ_a is the density of water ($\approx 1000\ \mathrm{kg\,m^{-3}}$). The redistribution of canopy water induces negligible geocentre motion (*Dong et al.*, 2014). Despite the restrictions imposed by data scarcity, independent studies agree that the continental hydrological cycle is the primary driving force of geocentre variations in the axial direction.

Variations in ice mass from ice sheets and glaciers occur over long timescales and, along with other mass trends and GIA, give rise to secular geocentre motion (see Section 3.6). Published mass balance estimates for the Antarctic and Greenland ice sheets from satellite altimetry, gravimetry and interferometry display clear inconsistencies and large formal errors (*Zwally and Giovinetto*, 2011; *Hanna et al.*, 2013). A recent reanalysis performed by *Shepherd et al.* (2012) employing uniform modelling over common temporal and spatial domains produced reconciled estimates of mass balance with reduced uncertainties. Nevertheless, the amount of mass loss from the two major ice sheets and the corresponding contributions to global mean sea level rise and geocentre motion are still poorly constrained. The integrated effect of ice mass loss from Antarctica and Greenland

on the geocentre velocity along the Z Cartesian axis is small due to the geographical locations of the two ice sheets in opposite Earth hemispheres.

The total count of glaciers outside Antarctica and Greenland stands at more than 200,000, but glaciological data are presently available for only 54% of the total glaciated area. The primary data source is the two data centres of the World Glacier Inventory (WGI) project, namely the World Glacier Monitoring Service in Zürich, Switzerland, and the National Snow and Ice Data Center in Boulder, Colorado, USA (*Ohmura*, 2010). The second major source of glaciological data is the Global Land Ice Measurements from Space (GLIMS) project (*Raup et al.*, 2007). About 26% of the total surface area of glaciers is covered by both WGI and GLIMS. Despite representing only approximately 3% of the glaciated area and less than 0.35% of the total ice volume, land glaciers affect the trend of geocentre motion to a similar extent as Antarctica and Greenland (*Dong et al.*, 2014). The three commonly used methods for quantifying glacier mass balance, known as stake, geodetic and hydrological (see, e.g., *Ohmura*, 2011), often yield inconsistent results due to insufficient data constraints. *Schrama et al.* (2014) applied a mascon approach to assess glacier mass balance from GRACE data with a reported high level of certainty.

Table 3.2 Common fluid models and parameters used for forward modelling of seasonal and inter-annual geocentre motion

Fluid	Parameter(s)	Model	Reference
Atmosphere	Surface pressure	ECMWF ERA-Interim	*Dee et al.* (2011)
		NCEP/NCAR reanalysis	*Kalnay et al.* (1996)
Oceans	OBP	OMCT	*Thomas* (2002)
		ECCO	*Wunsch et al.* (2009)
Continental hydrology	Soil moisture, snow depth	GLDAS	*Rodell et al.* (2004)
		LSDM	*Dill* (2008)

The development of a model that encompasses all geophysical fluids, conserves mass, replicates mass exchange between individual components and allows changes in the state of matter remains a long-term ambition. Until a full Earth system model tailored for geodetic applications becomes available, forward modelling of geocentre motion will be confined to optimum combinations of individual loading models and uncertainty calibrations based on comparisons between model predictions. Mass conservation can only be simulated in such analyses by permitting globally uniform or gravitationally consistent changes in ocean volume (e.g. *Clarke et al.*, 2005). *Dong et al.* (2014) estimated that the mass conservation assumption induces a net geocentre velocity of approximately $-0.08\ \mathrm{mm\,yr^{-1}}$. Table 3.2 provides a non-exhaustive list of fluid models used for geocentre motion prediction.

3.5 Inverse modelling

The determination of geocentre motion through the degree-1 deformation constitutes in essence an inverse problem. It is, nevertheless, treated separately because of its pioneering role in geocentre motion observation. New horizons for the monitoring of surface mass variability with unprecedented accuracy and resolution were opened with the launch of the GRACE gravity mission in March 2002. The insensitivity of GRACE to degree-1 surface mass variations has prompted efforts to combine multiple datasets to recover the full spectrum of low frequency mass variability, including geocentre motion. The integration of GRACE and GNSS is particularly appealing to circumvent both the paucity of GNSS data over oceans and the potentially large GRACE errors at low spherical harmonic degrees (see, e.g., *Chen and Wilson*, 2008). *Kusche and Schrama* (2005) showed that in joint inversions, GRACE is expected to contribute less than GPS at degrees 2 to 4. Nevertheless, GRACE data facilitates the separation of degree-1 mass coefficients from the other parameters (*Rietbroek et al.*, 2009). OBP estimates are also frequently assimilated in inversion schemes and have been appraised to contribute more than GPS owing to their low uncertainties and high spatial density (*Jansen et al.*, 2009).

Joint inversion schemes generally seek to minimise an objective function of the form

$$\mathcal{S} = \sum_i \omega_i \left(\mathbf{A}_i\mathbf{x} - \mathbf{l}_i\right)^T \mathbf{W}_i \left(\mathbf{A}_i\mathbf{x} - \mathbf{l}_i\right), \tag{3.73}$$

where i represents the three types of observations contained in the vectors $\mathbf{l}_i$, namely GPS-derived elastic deformations, GRACE geopotential coefficients and OBP estimates. The design matrices and weight matrices are designated by $\mathbf{A}_i$ and $\mathbf{W}_i$, respectively. The artificial weights ω_i determine the contribution of each dataset to the determination of the unknowns $\mathbf{x}$ by weighted least squares. When $\omega_i > 0$ for each data type, a general GPS–GRACE–OBP inversion is conducted (*Wu et al.*, 2006; *Rietbroek et al.*, 2009, 2012a, 2014), whereas in GPS–only inversions $\omega_{\mathrm{GPS}} = 1$ and the artificial weights of GRACE and OBP are zero. GPS–OBP ($\omega_{\mathrm{GPS}} > 0$, $\omega_{\mathrm{GRACE}} = 0$, $\omega_{\mathrm{OBP}} > 0$) and GRACE–OBP ($\omega_{\mathrm{GPS}} = 0$, $\omega_{\mathrm{GRACE}} > 0$, $\omega_{\mathrm{OBP}} > 0$) integrations have also been performed (*Kusche and Schrama*, 2005; *Jansen et al.*, 2009). Less frequently employed setups include GPS–GRACE ($\omega_{\mathrm{GPS}} = 1$, $\omega_{\mathrm{GRACE}} \gg 1$, $\omega_{\mathrm{OBP}} = 0$), as used by *Munekane* (2007) to mitigate spatial aliasing, and GPS–OBP ($\omega_{\mathrm{GPS}} = 1$, $\omega_{\mathrm{GRACE}} = 0$, $\omega_{\mathrm{OBP}} \gg 1$), which may augment GPS–only inversions with oceanic constraints.

Some benefits of the combined estimation of mass variations from GPS and GRACE were outlined by *Davis et al.* (2004). *Munekane* (2007) demonstrated the use of differences between elastic deformations from GPS data and GRACE-inferred deformations for degrees $n \geq 2$ to recover geocentre motion. In addition to satellite data, *Wu et al.* (2006) also incorporated OBP in the inversion for mass coefficients up to degree and order 50 using the method of least squares with reduced a priori information. The information

content of GPS, GRACE, and OBP datasets was discussed by *Jansen et al.* (2009), who found that the accuracy of joint inversions for mass variations is up to five times higher than that of GRACE–only solutions, particularly at low degrees. Issues of relative data weighting were also recently addressed in progressively refined GPS–GRACE–OBP inversions (*Rietbroek et al.*, 2009, 2012a, 2014). In particular, *Rietbroek et al.* (2014) applied variance component estimation to determine the relative contributions of each dataset to a benchmark solution used to assess the potential of GPS-inferred surface mass variability to fill the anticipated observational gap between the GRACE mission and its follow-on, planned to be launched in 2017.

The inverse method of *Swenson et al.* (2008) is particularly appealing for GRACE users since it allows the estimation of degree-1 mass coefficients compatible with the coefficients of degree $n \geq 2$ provided by GRACE, which lack atmospheric and oceanic contributions. Assuming knowledge of the mass coefficients of degree $n \geq 2$ (e.g. from GRACE) and the degree-1 oceanic mass coefficients, $\Delta\tilde{C}_{10}^{oc}, \Delta\tilde{C}_{11}^{oc}, \Delta\tilde{S}_{11}^{oc}$ (e.g. from an OGCM), the degree-1 mass coefficients can be obtained using the formula

$$\begin{bmatrix} \Delta\tilde{C}_{10} \\ \Delta\tilde{C}_{11} \\ \Delta\tilde{S}_{11} \end{bmatrix} = \begin{bmatrix} I_{10C}^{10C} & I_{11C}^{10C} & I_{11S}^{10C} \\ I_{10C}^{11C} & I_{11C}^{11C} & I_{11S}^{11C} \\ I_{10C}^{11S} & I_{11C}^{11S} & I_{11S}^{11S} \end{bmatrix}^{-1} \begin{bmatrix} \Delta\tilde{C}_{10}^{oc} - G_{10C} \\ \Delta\tilde{C}_{11}^{oc} - G_{11C} \\ \Delta\tilde{S}_{11}^{oc} - G_{11S} \end{bmatrix}, \tag{3.74}$$

where the superscript and subscript in the notation

$$I_{10C}^{10C} = \frac{a_e \rho_w}{4\pi} \iint P_{10}(\cos\theta)\, \vartheta(\theta,\lambda)\, P_{10}(\cos\theta)\, d\theta\, d\lambda \tag{3.75}$$

indicate the Legendre polynomials or functions to the left and right, respectively, of the ocean function ϑ defined as

$$\vartheta(\theta,\lambda) = \begin{Bmatrix} 1 & \text{over oceans} \\ 0 & \text{over land} \end{Bmatrix}, \tag{3.76}$$

$\theta = 90° - \varphi$ is colatitude and G_{10C} is given by

$$G_{10C} = \frac{1}{4\pi} \iint P_{10}(\cos\theta)\, \vartheta(\theta,\lambda)\, \Delta\sigma(\theta,\lambda)\, d\theta\, d\lambda\,. \tag{3.77}$$

The summation in the surface mass density anomaly $\Delta\sigma(\theta,\lambda)$ starts at degree $n = 2$. The expressions of G_{11C} and G_{11S}, as well as of the other elements of the $\mathbf{I}$ matrix are omitted here, but can be derived analogously to G_{10C} and I_{10C}^{10C} (see *Swenson et al.*, 2008). Following the estimation of degree-1 mass coefficients, the geocentre coordinates can be computed using (3.48). For consistency, the degree-1 oceanic mass coefficients and the higher-degree GRACE coefficients used in (3.74) should contain contributions from the same components of the fluid envelope.

Swenson et al. (2008) derived both degree-1 surface mass variations compatible with GRACE (i.e. with atmospheric and oceanic contributions removed) and total geocentre coordinates using a combination of GRACE data and degree-1 oceanic coefficients from OMCT and ECCO. The method of *Swenson et al.* (2008) was tested under several scenarios by *Bergmann-Wolf et al.* (2014), who also proposed a modification by which the required degree-1 oceanic terms are determined exclusively from GRACE data using the methodology of *Chambers et al.* (2004) and an a priori annual geocentre motion model. The approach of *Bergmann-Wolf et al.* (2014) includes the derivation of an empirical model of eustatic sea-level variability, assumed to be globally homogeneous, as an alternative to correcting OBP estimates for the eustatic signal, also present in the GRACE geopotential coefficients.

The time series of geocentre coordinates obtained via inverse modelling using multiple datasets generally contain less high frequency noise and smaller seasonal oscillations than direct satellite estimates. This may be occasionally due to the omission of contributions from specific fluid envelope components. Inverse approaches incorporating detrended series of elastic deformations from GNSS are unable to recover long-term trends in geocentre motion.

3.6 Secular geocentre motion

The derivations presented in Section 3.3.1 assumed the Earth is an elastic body, which deforms instantaneously under loading and restores its initial (pre-loading) shape immediately after unloading. The theory of elastic solid Earth deformation proposed by *Farrell* (1972) is applicable for relatively short timescales (i.e. sub-daily to decadal). Over longer periods of thousands to several hundred thousand years, however, the deformation of the solid Earth is viscoelastic in nature and has two primary contributors: GIA and PDMT.

The secular process of GIA is characterised by localised surface displacements, predominantly in the radial direction and geographically confined mostly to regions covered by major ice sheets during the last glacial period. GIA-induced surface displacements change at a constant rate over time in the present day and are accompanied by secular changes in the geoid height (*Wu et al.*, 2010). The second major contributor to the geoid trend is the PDMT. Both GIA and PDMT also cause linear drifts between CM and CF, which are known collectively as *geocentre velocity* or *secular geocentre motion* and represented by the time derivative, $\dot{\mathbf{r}}_{\mathrm{CM-CF}}$, of the geocentre vector.

The secular rate of change in the geoid height due to the integrated effect of GIA and PDMT can be written as

$$\dot{N}(\varphi,\lambda) = \frac{3a_e\rho_w}{\rho_e}\sum_{n=1}^{\infty}\sum_{m=0}^{n}\frac{1}{2n+1}\left[\dot{C}^k_{nm}\,Y^C_{nm}(\varphi,\lambda) + \dot{S}^k_{nm}\,Y^S_{nm}(\varphi,\lambda)\right], \tag{3.78}$$

where each of the coefficients

$$\begin{aligned} \dot{C}^{k}_{nm} &= (1+k_n)\,\dot{C}^{e}_{nm} + \dot{C}^{v,k}_{nm}, \\ \dot{S}^{k}_{nm} &= (1+k_n)\,\dot{S}^{e}_{nm} + \dot{S}^{v,k}_{nm}, \end{aligned} \tag{3.79}$$

contains an elastic component due to PDMT, indicated by the superscript e, and a viscoelastic component due to GIA, marked by the superscript v. Thus, the time derivatives (i.e. rates of change) of the mass coefficients $\Delta\tilde{C}_{nm}$ and $\Delta\tilde{S}_{nm}$ represent a sum of elastic and viscoelastic signatures. The superscript k in the notations of the viscoelastic components, $\dot{C}^{v,k}_{nm}$ and $\dot{S}^{v,k}_{nm}$, is used to indicate GIA potential coefficients, to be distinguished from the horizontal and vertical GIA velocity coefficients introduced later.

The surface velocities in the east, north and radial directions are given by the expressions

$$\begin{aligned} \dot{s}_e(\varphi,\lambda) &= \frac{3a_e\rho_w}{\rho_e}\sum_{n=1}^{\infty}\sum_{m=0}^{n}\frac{1}{2n+1}\frac{1}{\cos\varphi} \\ &\quad\cdot\left[\left(l_n\,\dot{C}^{e}_{nm}+\dot{C}^{v,l}_{nm}\right)\frac{\partial Y^{C}_{nm}(\varphi,\lambda)}{\partial\lambda}+\left(l_n\,\dot{S}^{e}_{nm}+\dot{S}^{v,l}_{nm}\right)\frac{\partial Y^{S}_{nm}(\varphi,\lambda)}{\partial\lambda}\right], \\ \dot{s}_n(\varphi,\lambda) &= \frac{3a_e\rho_w}{\rho_e}\sum_{n=1}^{\infty}\sum_{m=0}^{n}\frac{1}{2n+1} \\ &\quad\cdot\left[\left(l_n\,\dot{C}^{e}_{nm}+\dot{C}^{v,l}_{nm}\right)\frac{\partial Y^{C}_{nm}(\varphi,\lambda)}{\partial\varphi}+\left(l_n\,\dot{S}^{e}_{nm}+\dot{S}^{v,l}_{nm}\right)\frac{\partial Y^{S}_{nm}(\varphi,\lambda)}{\partial\varphi}\right], \\ \dot{s}_u(\varphi,\lambda) &= \frac{3a_e\rho_w}{\rho_e}\sum_{n=1}^{\infty}\sum_{m=0}^{n}\frac{1}{2n+1} \\ &\quad\cdot\left[\left(h_n\,\dot{C}^{e}_{nm}+\dot{C}^{v,h}_{nm}\right)Y^{C}_{nm}(\varphi,\lambda)+\left(h_n\,\dot{S}^{e}_{nm}+\dot{S}^{v,h}_{nm}\right)Y^{S}_{nm}(\varphi,\lambda)\right], \end{aligned} \tag{3.80}$$

where $\dot{C}^{v,l}_{nm}$ and $\dot{S}^{v,l}_{nm}$ represent horizontal GIA velocity coefficients and $\dot{C}^{v,h}_{nm}$ and $\dot{S}^{v,h}_{nm}$ designate vertical GIA velocity coefficients. The GIA coefficients $\dot{C}^{v,i}_{nm}$ and $\dot{S}^{v,i}_{nm}$ with $i = k,l,h$ are functions of the ice load history and the viscoelastic relaxation modes characterising the Earth's viscoelastic response to loading (see, e.g., *Mitrovica and Peltier*, 1989). For Antarctica and Greenland, independent of the distribution of surface loads, the rates of horizontal elastic deformation are lower by a factor of approximately three than vertical elastic deformation rates and the viscoelastic contributions to surface velocities are likely to be several times larger than the elastic rates (*Wahr et al.*, 1995). Despite containing errors at low degrees, the following approximation proposed by *Wahr et al.* (2000):

$$\begin{Bmatrix} \dot{C}^{v,k}_{nm} \\ \dot{S}^{v,k}_{nm} \end{Bmatrix} \approx \frac{2}{2n+1}\begin{Bmatrix} \dot{C}^{v,h}_{nm} \\ \dot{S}^{v,h}_{nm} \end{Bmatrix} \tag{3.81}$$

can be used in (3.78) to express the geoid trend as a function of the vertical GIA velocity coefficients with reasonable fidelity for any ice load model and viscosity profile. This allows, for example, the estimation of GIA vertical velocities from secular changes in the

geoid height inferred from GRACE, assuming that the elastic and viscoelastic signatures can be well separated.

The velocity between CM and CF also contains elastic and viscoelastic components, so that

$$\dot{\mathbf{r}}_{\mathrm{CM-CF}} = \dot{\mathbf{r}}_{\mathrm{CM-CE}} - \dot{\mathbf{r}}_{\mathrm{CF-CE}} = \dot{\mathbf{r}}^{e}_{\mathrm{CM-CE}} - \dot{\mathbf{r}}^{e}_{\mathrm{CF-CE}} + \dot{\mathbf{r}}^{v}_{\mathrm{CM-CE}} - \dot{\mathbf{r}}^{v}_{\mathrm{CF-CE}}, \tag{3.82}$$

where $\dot{\mathbf{r}}_{\mathrm{CM-CE}}$ and $\dot{\mathbf{r}}_{\mathrm{CF-CE}}$ are the velocities of CM and CF, respectively, expressed in the CE frame. The velocity of CM with respect to CE due to GIA, $\dot{\mathbf{r}}^{v}_{\mathrm{CM-CE}}$, is likely to be lower than 0.034 mm yr^{-1} (*Argus*, 2007) and can be neglected in (3.82). GIA does not actively cause mass redistribution in the fluid envelope. The passive response of the fluid envelope to GIA-induced crustal motion and changing gravitational potential can be considered part of PDMT. Surface integration of (3.80) yields the following geocentre velocity:

$$\dot{\mathbf{r}}_{\mathrm{CM-CF}} = \sqrt{3}\, a_e \frac{\rho_w}{\rho_e} \left\{ \left(1 - \frac{[h_1]_{\mathrm{CE}} + 2\,[l_1]_{\mathrm{CE}}}{3} \right) \begin{bmatrix} \dot{C}^{e}_{11} \\ \dot{S}^{e}_{11} \\ \dot{C}^{e}_{10} \end{bmatrix} - \begin{bmatrix} \dot{C}^{v,h}_{11} \\ \dot{S}^{v,h}_{11} \\ \dot{C}^{v,h}_{10} \end{bmatrix} \right\}. \tag{3.83}$$

Forward modelling of the GIA-induced geocentre velocity independently performed by *Greff-Lefftz* (2000) and *Klemann and Martinec* (2011) revealed a strong dependence on the adopted Earth model parameters and the deglaciation history. In particular, the lower-mantle viscosity and the time evolution of the deglaciation have a much greater influence on predictions of secular geocentre motion than the upper-mantle viscosity and the lithospheric thickness. Due to the large uncertainties in GIA models, the net geocentre velocity is poorly constrained with lower and upper bounds of -1 and -0.1 mm yr^{-1}, respectively, when considering the results of both aforementioned studies. The negative geocentre velocity (i.e. the velocity of CF relative to CM) was, nevertheless, robustly found by *Klemann and Martinec* (2011) to be directed towards the north-east of Hudson Bay, Canada. Apart from GIA, the contribution of other Earth internal processes to secular geocentre motion estimated from theoretical models is small enough to be neglected (*Greff-Lefftz et al.*, 2010).

Using observations of contemporary ice mass loss from Antarctica, Greenland and major glaciers, *Métivier et al.* (2010) obtained geocentre velocities between -0.8 and -0.3 mm yr^{-1} and noticed a potential recent acceleration, correlated with the increase in ice melting reported by several studies quantifying ice mass balance. Similarly, *Dong et al.* (2014) estimated the secular geocentre motion due to ice melting to be -0.1 mm yr^{-1} over the period 1983–2008 and almost double during the decade 1998–2008, particularly in the Z direction. The same study reported that PDMT contributes -0.3 mm yr^{-1} to the net geocentre velocity. Both *Métivier et al.* (2010) and *Dong et al.* (2014) support the theory that the PDMT-induced non-linearity of geocentre motion may only partially explain the

large Z translation rate between the origins of ITRF2005 and ITRF2000 (*Altamimi et al.*, 2007) and systematic analysis errors may have also corrupted the ITRF2000 origin, given the good agreement between the origins of ITRF2008 and ITRF2005 (*Altamimi et al.*, 2011).

The individual contributions of GIA and PDMT are indistinguishable in geocentre velocity estimates obtained from satellite tracking observations. Further complications arise due to the approximation of CF by various CNs (i.e. the network effect) and the uncertainty in the ITRF origin realisation. In particular, the drift error of the ITRF origin currently stands at the level of 0.5–1 $\mathrm{mm\,yr^{-1}}$ (*Wu et al.*, 2011; *Argus*, 2012), a similar amplitude to the expected geophysical signal. Quantitative appraisals of the effects of GIA and PDMT on the velocity between CF and CN are lacking, but trends can arise due to the ever-changing geometry of the SLR network.

Inverse modelling approaches to secular geocentre motion are able to separate the fingerprints of GIA and PDMT using complementary datasets. *Swenson et al.* (2008) derived PDMT-induced secular geocentre motion by combining GRACE data with OBP estimates from OMCT and ECCO corrected for eustatic fluctuations due to mass transport in the Earth system, which are neglected in uncoupled OGCMs. *Schrama et al.* (2014) modelled the surface of the oceans by a rotationally and gravitationally consistent solution of the sea level equation (SLE) forced by Antarctic, Greenland and continental mass fluxes to infer geocentre motion estimates in good agreement with those of *Swenson et al.* (2008). In both studies, the GIA signatures were first removed from the GRACE data using the model of *Paulson et al.* (2007), based on the ICE-5G deglaciation history and a two-layer mantle viscosity profile derived from VM2 (*Peltier*, 2004). To circumvent the propagation of potentially large GIA modelling errors in the estimates of secular geocentre motion and allow the separation of GIA and PDMT signatures, *Wu et al.* (2010) combined GRACE gravity data, OBP and surface velocities from GNSS. PDMT signatures are present in all data types, whereas only GRACE and the surface velocities contain GIA signals. The a priori values and covariance matrix of GIA parameters were computed from an average of the ICE-5G and IJ05 (*Ivins and James*, 2005) ice load models and the VM2 viscosity profile. *Rietbroek et al.* (2012b) demonstrated the potential of a combined analysis of GRACE gravimetry and Jason-1 altimetry data to produce independent estimates of GIA and PDMT-induced geocentre velocities.

3.7 Summary

Geocentre motion can be estimated from geodetic observations, loading models or combinations of observations and models. A wide range of methods are available for the geodetic determination of the geocentre coordinates at seasonal and secular timescales. They exploit the proportionality between the geocentre coordinates, the degree-1 geopotential coefficients and the degree-1 surface mass coefficients and seek to estimate one of

these triplets. The determination of regularly spaced degree-1 geopotential coefficients through the dynamic approach raises methodological issues associated with the modelling of orbital dynamics in a non-inertial frame. Errors due to the approximation of CF by various CNs corrupt the translational estimates of the geocentre position obtained via the network shift approach and the kinematic approach. Furthermore, the current definition of the ITRF origin as a linear function of time and the limited origin stability reduce the value of secular geocentre motion obtained from satellite tracking data. Linear trends in such geocentre motion time series may be attributed to data reduction errors. *Wu et al.* (2015) proposed an alternative TRF formulation based on GNSS, SLR, DORIS and VLBI weekly time series of station positions combined using a Kalman filter and Rauch–Tung–Striebel smoother that promises to improve the TRF origin accuracy and stability.

The determination of geocentre motion via deformation approaches is complicated by the data scarcity over oceanic regions and the potential aliasing of mass coefficients of degree $n \geq 2$ into degree-1 estimates. When omitting higher-degree coefficients, the geocentre coordinates are likely to be lumped sums of several low degree coefficients. This problem is satisfactorily addressed by estimating higher-degree coefficients, but the results depend on the truncation degree dictated by data coverage. Inverse approaches attempt to address the deficiencies of geodetic geocentre motion estimates by assimilating GRACE gravity data and OBP model estimates to account for oceanic gaps and provide more robust results, in reasonable agreement with SLR at the annual frequency. The dissociation of PDMT and GIA footprints on the geocentre velocity may also be performed by inverse approaches (*Wu et al.*, 2010; *Rietbroek et al.*, 2012b). In the lack of a complete system model, geophysical predictions of geocentre motion are highly dependent on the choice of individuals fluid models and typically serve for the validation of geodetic and inverse results.

Of the satellite geodetic techniques, only SLR provides a direct measure of the station-satellite range ρ. In contrast, the absolute distance information in GNSS observations is greatly reduced by the estimation of transmitter and receiver clock corrections, equivalent to double differencing four simultaneous range measurements (*Meindl et al.*, 2013; *Kuang et al.*, 2015). The discrepancies between the origins of the IGS AC solutions can reach a few cm.[1] It is therefore necessary to reconcile the origins by estimating translations between the individual AC solutions and subsequently fixing the estimates in the final IGS combination (*Rebischung and Garayt*, 2013) or, alternatively, by reparameterising the unconstrained normal equations to isolate the apparent geocentre coordinates (*Rebischung et al.*, 2016). In the former approach, the coordinates of the apparent geocentre are obtained by aligning the combined solution to the latest IGS reference frame, currently IGb08 – an update of IGS08 (*Rebischung et al.*, 2012), through a seven-parameter

[1] http://webigs.ign.fr/en/tfcc/geocenter/

similarity transformation. Both routines are far from ideal and limit the value of IGS apparent geocentre product.

The degree-1 mode of elastic deformation is present in all geometric observations acquired by geodetic techniques, including baselines determined by the non-satellite technique VLBI (*Lavallée and Blewitt*, 2002). To date, however, only GNSS (GPS in particular) proved capable of providing reliable determinations of surface mass variability, despite poor coverage of the oceanic domain. The other continuously operating technique, DORIS, benefits from the most geographically balanced network (including reasonable coverage over the oceans), but trails GNSS, VLBI and SLR in terms of positioning accuracy due to difficulties in modelling the orbits of the complex spacecrafts equipped with DORIS receivers (*Willis et al.*, 2006; *Gobinddass et al.*, 2009a,b; *Štěpánek et al.*, 2014). VLBI and SLR provide the most unambiguous observations, but both operate intermittently and have sparse networks owing to the costly instrumentation and labour-intensive operation.

Important barriers for the production of a seasonal geocentre motion model from all four space geodetic techniques akin to the IGS apparent geocentre are the infrequently surveyed local ties at co-located sites and the questionable quality of these measurements, which display large discrepancies with respect to inter-system differences derived from satellite tracking data (*Altamimi et al.*, 2011). The substitution of ground local ties by space ties (or satellite co-locations) has been investigated (*Thaller et al.*, 2011, 2014), particularly in GNSS–SLR combinations, but this approach poses its own challenges. Particularly problematic is the determination of relative position vectors for the various instruments on board the satellites enabled for multi-technique tracking.

Chapter 4

Collinearity assessment of geocentre coordinates

4.1 Introduction

Traditionally, the LAGEOS-1 and 2 and Etalon-1 and 2 MEOs have been used for TRF determination with SLR. The combined solution submitted by the ILRS for the computation of ITRF2008 resulted from the analysis of LAGEOS-1 data spanning the period 1983.0–1992.8, LAGEOS-1 and 2 data from 1992.8 to 2002.5 and a combination of LAGEOS-1 and 2 and Etalon-1 and 2 observations over the period 2002.5–2009.0.[1] Etalon data dating back to the beginning of 1993 was included in the latest ILRSA combination (*Luceri et al.*, 2015), supplied for the development of ITRF2014.

The LEOs Starlette, Stella and Ajisai have been predominantly used, in conjunction with LAGEOS-1 and 2, for recovering low degree and order (d/o) geopotential coefficients (*Cheng et al.*, 1997; *Cheng and Tapley*, 1999; *Moore et al.*, 2005; *Maier et al.*, 2012; *Sośnica et al.*, 2015; *Bloßfeld et al.*, 2015). Recent studies (*Cheng et al.*, 2013a; *Sośnica et al.*, 2014) reported geocentre coordinates from combined LAGEOS–LEO data, but no conclusive evidence that multi-satellite solutions improve the observability of the geocentre coordinates compared to LAGEOS-1 and 2 solutions has been provided. The higher sensitivity of LEOs to the long-wavelength harmonics of the gravity field and the quasi-polar orbit of Stella are often speculatively quoted as arguments for the potentially superior quality of geocentre motion time series derived from multi-satellite data (*Angermann and Müller*, 2008; *Sośnica et al.*, 2014). LARES data analysis results have yet to be widely reported due to the short tracking history of the satellite launched on 13 February 2012, but its inclusion in ILRS products is envisaged for the near future.[2]

Using simulated observations sampled every 5 minutes to two LAGEOS–like satellites and an ideal network of 100 stations, *Rebischung et al.* (2014) concluded that the SLR

[1] http://ilrs.gsfc.nasa.gov/docs/ILRS_contribution_to_ITRF2008.pdf

[2] http://ilrs.gsfc.nasa.gov/docs/2014/Minutes_ILRS_AWG_19th_ILW_2014.10.26_Meeting.pdf

geocentre determination is free of major collinearity issues, especially for the equatorial geocentre coordinates. In this chapter, the analysis is extended to sparse and asymmetric real networks acquiring measurements at irregular time intervals to provide an indication of the current capability of SLR to sense geocentre motion. Additionally, the potential of Etalon and LEO observations to strengthen the tie of the SLR-derived TRF origin to CM, and thus improve the accuracy of the ITRF origin, is also assessed. Various satellite combinations and solution parameterisations are investigated. The conclusions of this chapter apply exclusively to the network shift approach for geocentre motion determination.

4.2 Collinearity diagnosis in geodetic data analysis

The problem of perfect collinearity among the parameters of a least squares problem arises when linear dependencies exist between the parameters. This issue translates to a rank deficient design matrix $\mathbf{A}$ (i.e. at least one linear function of its columns equals the zero vector) and a singular normal matrix $\mathbf{N}$, a ubiquitous occurrence in geodetic analyses in the absence of a priori information. When $\mathbf{N}$ is near to singularity rather than singular, a unique but very unstable solution of the normal equations system can be determined. This latter complication is known as the collinearity (or multicollinearity) problem. In its presence, even minor changes in the data or in the functional model (e.g. the addition or removal of parameters) severely affect parameters suffering collinearity issues. Nearly collinear parameters are poorly determined from observational data and have large associated variances.

Collinearity can have dramatic effects on parameter estimation (*Rawlings et al.*, 1998; *Montgomery et al.*, 2012). Analysis of correlations between parameters can uncover pairwise near-linear dependencies, but it is unsuitable and inefficient for identifying severe non-orthogonality among several parameters. Proper detection and handling of collinearity problems are crucial for the estimation of geophysically meaningful and unbiased geodetic parameters. This section summarises the procedure developed by *Rebischung et al.* (2014) for diagnosing the collinearity of geodetic parameters in general and, in particular, the collinearity of geocentre coordinates obtained through the network shift approach.

To reduce the rank defect r of the design matrix $\mathbf{A}$, it is customary in geodesy to augment the normal equations with minimum (or inner) constraints (*Blaha*, 1982), leading to the following system of conditional equations:

$$\begin{bmatrix} \mathbf{N} & \mathbf{C} \\ \mathbf{C}^T & \mathbf{0} \end{bmatrix} \begin{bmatrix} \mathbf{x} \\ \mathbf{k} \end{bmatrix} = \begin{bmatrix} \mathbf{b} \\ \mathbf{0} \end{bmatrix}, \tag{4.1}$$

where $\mathbf{C}$ is a $u \times r$ constraint matrix, $\mathbf{x}$ a vector of u unknown parameters, $\mathbf{k}$ a vector of r Lagrange multipliers and $\mathbf{b}$ the right-hand side of the normal equations system. The

constraint matrix for station coordinates has a standard form (e.g *Rebischung et al.*, 2014). It removes the three orientation singularities by imposing a NNR condition with respect to the a priori reference frame and a fourth singularity stemming from the correlation between UT1–UTC and the longitudes of the orbital ascending nodes by fixing UT1–UTC to a known value.

The network shift approach for geocentre motion determination involves the computation of six or seven-parameter similarity transformations between successive CM-centred epoch reference frames and a secular frame such as ITRF2008. The average global displacement of the entire network forming an epoch reference frame is equated to the translation vector between the origins of the epoch frame and the secular frame. Geocentre information is inherently contained in the station coordinates estimated in the CM frame. The geocentre coordinates are therefore implicit parameters realised via station coordinates. Simultaneous estimation of geocentre coordinates and station coordinates may cause collinearity problems since the two interdependent parameter types represent similar information in different forms.

The signature (or effect of a unit variation) of an implicit parameter y on the observation vector $\mathbf{l}$ can be expressed as

$$\mathbf{s}_y = \frac{\partial \mathbf{l}}{\partial y} = \mathbf{A}\boldsymbol{\lambda}, \tag{4.2}$$

where $\boldsymbol{\lambda} = {}^{\partial \mathbf{x}}/_{\partial y}$ contains the partial derivatives of the explicit parameters $\mathbf{x}$ with respect to the implicit parameter y. The signatures of the three geocentre coordinates on station-satellite ranges are as follows:

$$\begin{aligned}
\mathbf{s}_X &= \mathbf{A}\left[\delta p, 0, 0, \delta p, 0, 0, \ldots, \delta p, 0, 0, 0, 0, 0, 0, \ldots, 0\right]^T, \\
\mathbf{s}_Y &= \mathbf{A}\left[0, \delta p, 0, 0, \delta p, 0, \ldots, 0, \delta p, 0, 0, 0, 0, 0, \ldots, 0\right]^T, \\
\mathbf{s}_Z &= \mathbf{A}\left[\underbrace{0, 0, \delta p, 0, 0, \delta p, \ldots, 0, 0, \delta p}_{\text{station coordinates}}, \underbrace{0, 0, 0, 0, \ldots, 0}_{\text{other parameters}}\right]^T,
\end{aligned} \tag{4.3}$$

where δp is the geocentre offset, assumed here to be identical along all three axes for simplicity. A positive geocentre offset along any axis has the effect of lengthening the ranges to satellites orbiting in the positive hemisphere of the axis and shortening the ranges to satellites in the negative hemisphere.

The first step for diagnosing the collinearity of a particular geocentre coordinate with the other parameters consists in introducing a fictitious geocentre offset (e.g. $\delta p = 1$ cm) and calculating $\boldsymbol{\lambda}_c$ from the system

$$\begin{bmatrix} \mathbf{N} & \mathbf{C} \\ \mathbf{C}^T & \mathbf{0} \end{bmatrix} \begin{bmatrix} \boldsymbol{\lambda}_c \\ \mathbf{k} \end{bmatrix} = \begin{bmatrix} \mathbf{N}\boldsymbol{\lambda} \\ \mathbf{0} \end{bmatrix}. \tag{4.4}$$

The partial derivatives $\boldsymbol{\lambda}_c$ represent the variations (under minimum constraints) of the explicit parameters due to a change in the implicit parameter.

In the second stage, the following system of equations is solved:

$$\begin{bmatrix} \mathbf{N} & \mathbf{C} & \boldsymbol{\lambda}_c \\ \mathbf{C}^T & \mathbf{0} & \mathbf{0} \\ \boldsymbol{\lambda}_c^T & \mathbf{0} & \mathbf{0} \end{bmatrix} \begin{bmatrix} \mathbf{x}_c \\ \mathbf{k} \\ \mathbf{k}' \end{bmatrix} = \begin{bmatrix} \mathbf{0} \\ \mathbf{0} \\ \boldsymbol{\lambda}_c^T \boldsymbol{\lambda}_c \end{bmatrix}. \tag{4.5}$$

Its solution is $\mathbf{x}_c = \boldsymbol{\lambda}_c - \boldsymbol{\gamma}_{y,c}$, where the term $-\boldsymbol{\gamma}_{y,c}$ represents the optimum response of the system to account for the artificially introduced offset $\boldsymbol{\lambda}_c$. Examination of $-\boldsymbol{\gamma}_{y,c}$ can reveal which explicit parameters are most affected by variations of the implicit parameter y and thus responsible for its potential collinearity problems.

The final step of the collinearity diagnosis consists in computing the variance inflation factor (VIF) of y using the formula

$$V_{y,c} = \frac{\|\mathbf{s}_y\|^2}{\|\mathbf{s}_{y,c}^p\|^2} = \frac{\|\mathbf{A}\boldsymbol{\lambda}_c\|^2}{\|\mathbf{A}\mathbf{x}_c\|^2}, \tag{4.6}$$

where $\mathbf{s}_{y,c}^p$ is the observable component of $\mathbf{s}_y$, known as the proper signature of y. If the full design matrix is unavailable, $\mathbf{A}\boldsymbol{\lambda}_c$ and $\mathbf{A}\mathbf{x}_c$ can be obtained by successively evaluating the functional model at the a priori parameters $\mathbf{x}_0$, $\mathbf{x}_0 + \boldsymbol{\lambda}_c$ and $\mathbf{x}_0 + \mathbf{x}_c$ and pairwise differencing the observational residuals.

The VIF is one of the most commonly used indicators of collinearity. It represents the ratio of the actual variance, $1/\|\mathbf{s}_{y,c}^p\|^2$, of a parameter and the theoretical variance, $1/\|\mathbf{s}_y\|^2$, of the same parameter unaffected by collinearity problems. In an ideal case when the VIF equals unity, the investigated parameter is free of collinearity issues. A maximum value of 10 is generally considered admissible, but, as *Rebischung et al.* (2014) suggested, this value is most likely unsuitable for geodetic problems involving hundreds to tens of thousands of parameters. Numerical VIF values vary logarithmically due to their quotient nature. To facilitate interpretation, each VIF value can be accompanied by a percentage value obtained from

$$R_{y,c} = \sqrt{1 - \frac{1}{V_{y,c}}}, \tag{4.7}$$

where $R_{y,c}$ represents the multiple correlation coefficient of y with the other parameters.

Collinearity diagnosis provides a platform for investigating the observability of parameters. The VIF, however, is defined as the ratio of two variances and thus lacks absolute meaning. Relative comparisons of VIFs are only meaningful when their values are derived from the same set of observations since the signature norm $\|\mathbf{s}_y\|$ and, implicitly, the variance $1/\|\mathbf{s}_y\|^2$ of a parameter are constant when varying the analysis settings alone. The formal error $1/\|\mathbf{s}_{y,c}^p\|$ is generally a better measure of observability and has the advantage of being readily interpretable. Of particular interest for the observability of a parameter is how the formal error $1/\|\mathbf{s}_{y,c}^p\|$ compares to the required level of accuracy.

4.3 Satellite data and processing strategy

4.3.1 Data, network and conventions

Normal point observations to eight spherical geodetic satellites (i.e. LAGEOS-1 and 2, Etalon-1 and 2, Starlette, Stella, Ajisai and LARES) were homogeneously processed using an updated version of the precise orbit determination software Faust (*Moore et al.*, 1999). The data used in this study span 52 weeks from 30 December 2012 to 28 December 2013 and represent a combined data set retrieved from the two ILRS data centres, namely the Crustal Dynamics Data Information System (CDDIS; *Noll*, 2010) and the EUROLAS Data Center (EDC). Satellite arcs, with a standard length of seven days, were simultaneously analysed in a multi-step iterative parameter estimation process. Four types of solutions involving different data combinations were generated in this study, namely (1) LAGEOS-1 and 2 solutions (which will be referred to as type A solutions), (2) LAGEOS-1 and 2 and Etalon-1 and 2 solutions (type B), (3) LAGEOS-1 and 2, Starlette, Stella and Ajisai solutions (type C), and (4) LAGEOS-1 and 2 and LARES solutions (type D).

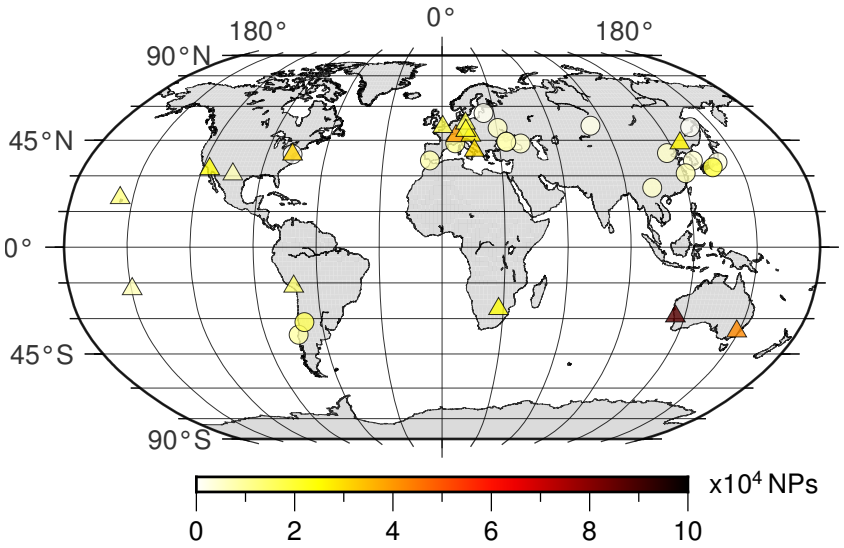

Figure 4.1 The SLR network during the period 30 December 2012 – 28 December 2013. Core stations are represented by *triangles* and non-core stations by *circles*. The colour scale shows the total number of NPs to LAGEOS-1 and 2, Etalon-1 and 2, Starlette, Stella, Ajisai and LARES

A total of 34 SLR stations contribute to the analysed data set. Their spatial distribution and contributions to the data set are depicted in Figure 4.1, which clearly illustrates the prevalence of stations located in the northern hemisphere of the Earth. The core network comprises 16 stations, 12 of which were chosen in accordance with ILRS recommendations for the time span of the data set.[3] Monument Peak (7110), Tahiti (7124), Arequipa (7403) and Wettzell (8834) are the four additional stations part of the core network used in this study. The core set of stations serves as a reference network for the application of minimum constraints.

[3] http://ilrs.dgfi.tum.de/fileadmin/data_handling/ILRS_Discontinuities_File.snx

The SLR network is dynamic by nature due to several limiting factors. In contrast to GNSS, only one satellite can be observed by an SLR station at any moment of time. Furthermore, weather dependency prohibits the acquisition of regularly spaced observations over time. Finally, the complex equipment installed at SLR stations is susceptible to failures leading to interruptions in data collection and provision. An exemplification of the dynamic nature of the SLR network is given in Figure 4.2, which depicts the percentages of stations situated in the positive X, Y and Z hemispheres as a function of time for solutions of types A and C. In LAGEOS–only solutions, the network is biased towards the positive hemispheres and the incorporation of Starlette, Stella and Ajisai data further degrades the distribution along the X and Z axes. Figure 4.3 illustrates the variations over time in the number of stations and the number of NPs in solutions of types A, C and D. The contribution of the Etalon satellites is limited and therefore omitted from Figure 4.3. Conversely, the addition of LEO data to LAGEOS data inflates the network size, but more significantly the number of measurements.

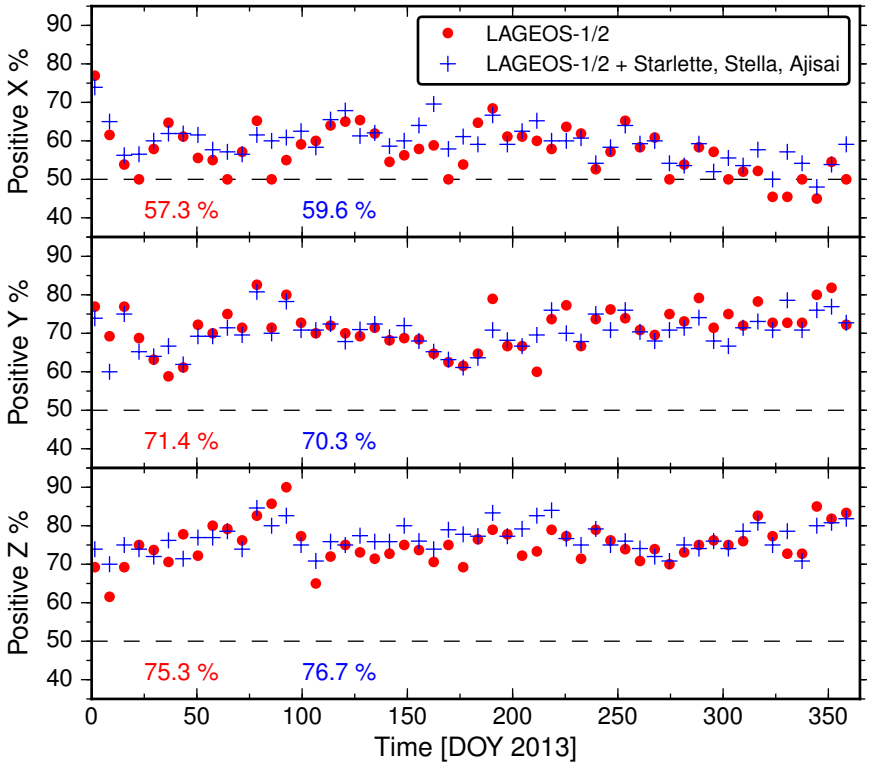

Figure 4.2 Percentages of stations located in the hemispheres defined by the positive X, Y and Z Cartesian axes in LAGEOS-1 and 2 (type A) and LAGEOS–Starlette–Stella–Ajisai (type C) weekly solutions. Printed numerical values represent average percentages over the entire time span

The geographical coverage of LAGEOS-1 and 2 observations is restricted mainly to continental regions and displays polar gaps (Figure 4.4). On the other hand, Starlette, Stella, Ajisai and LARES NPs have a much more confined spatial extent owing to the lower altitudes of the satellites. Overall, the distribution of NPs is biased towards the northern hemisphere, despite the fact that the two most prolific stations in terms of data

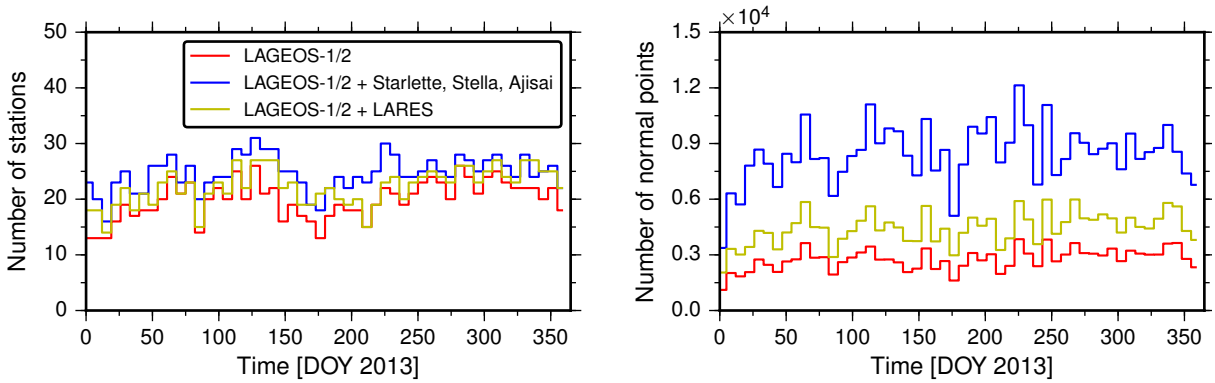

Figure 4.3 Number of stations with more than 20 NPs (*left*) and number of NPs (*right*) in LAGEOS-1 and 2 (type A), LAGEOS–Starlette–Stella–Ajisai (type C) and LAGEOS–LARES (type D) weekly solutions

yield for the eight spherical geodetic satellites considered in this study are situated in the southern hemisphere (i.e. 7090 – Yarragadee and 7825 – Mount Stromlo, both in Australia). Together, 7090 and 7825 provide nearly one quarter of the data set. The third most prolific station is Zimmerwald (7810), Switzerland.

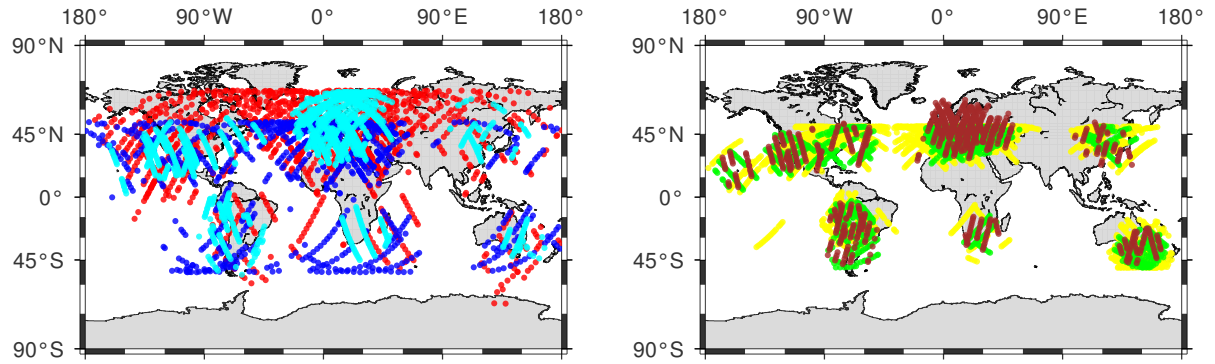

Figure 4.4 Observed ground tracks of LAGEOS-1 (*red circles*), LAGEOS-2 (*blue circles*) and LARES (*cyan circles*) during the week 28 July – 3 August, 2013 (*left*). Observed ground tracks of Starlette (*green circles*), Stella (*brown circles*) and Ajisai (*yellow circles*) over the same time period (*right*)

The main characteristics of the selected satellites are summarised in Table 4.1. All satellites, with the exception of Ajisai, are characterised by small area-to-mass ratios which reduce non-gravitational perturbations such as SRP and atmospheric drag. In particular, the area-to-mass ratio of LARES is approximately 2.6 times lower than that of each LAGEOS satellite, making LARES the densest known object in the Solar System (*Paolozzi and Ciufolini*, 2013). Apart from atmospheric drag, the non-gravitational perturbations experienced by the orbit of LARES are typically the smallest in magnitude among all satellites. In contrast to LAGEOS-1 and 2, LARES is constructed of a solid single-piece sphere of smaller diameter and higher thermal conductivity. These particular physical characteristics minimise the thermal effects on LARES.

Ajisai contributes approximately 29% to the data set used in this study, more than the combined contribution of both LAGEOS satellites (∼27%). The 1436 large CCRs aboard

Table 4.1 Selected physical parameters of spherical geodetic satellites

Satellite name	Diameter [cm]	Mass [kg]	Area-to-mass [$cm^2\,kg^{-1}$]	Standard CoM corr. [mm]	SRP coeff.
LAGEOS-1	60	406.965	6.948	251	1.130
LAGEOS-2	60	405.380	6.975	251	1.130
Etalon-1	129.4	1 415	9.294	576	1.240
Etalon-2	129.4	1 415	9.294	576	1.280
Starlette	24	47.294	9.565	75	1.134
Stella	24	48	9.425	75	1.131
Ajisai	215	685.2	52.985	1 010	1.035
LARES	36.4	386.8	2.690	133	1.125

Ajisai ensure a high return rate of photons which, in conjunction with the favourable inclination for low and mid-latitude tracking and longer satellite passes compared to Starlette and Stella, explains the prevalence of Ajisai NPs. Despite being the second largest targets and having the highest number of retro-reflectors, the contribution of the Etalon satellites amounts to less than 3% of the data set. Owing to their nearly equal inclinations, Starlette and Ajisai have similar perturbation spectra (*Cheng et al.*, 1997). Ajisai and LARES exhibit less sensitivity than Starlette and Stella to variations in the Earth's gravity field due to their higher altitudes. The quasi-polar orbit of Stella was thought to positively influence the determination of the Z geocentre coordinate (*Sośnica et al.*, 2014), but *Kuang et al.* (2015) showed that the orbital inclination of 90° is the least favourable for the observability of the Z geocentre coordinate due to the poor information content of the tracking data in the axial direction.

Starlette, Stella, Ajisai and LARES are placed in low Earth orbits, which allow most SLR stations to track them on a regular basis. Despite their long tracking histories, Starlette, Stella and Ajisai are absent from the contributions submitted by the ILRS ACs for the computation of the ITRF. The prime justifications for their omission are the large orbital perturbations related to temporal changes in the Earth's gravity field and the necessity to model atmospheric drag acting as a deceleration force on LEO orbits, mainly in the along-track direction. The drag force is a function of the atmospheric density at the satellite's position. Even though various thermospheric density models of different complexity are available (see, e.g., *Montenbruck and Gill*, 2000), atmospheric density modelling remains a challenge in orbit determination since limited progress has been achieved over the past few decades. NRLMSISE-00 (*Picone et al.*, 2002) is the model of choice in the current study.

Table 4.2 describes the models and conventions adopted for orbit determination and parameter estimation. These are in general agreement with the IERS Conventions (2010) (*Petit and Luzum*, 2010) and the current processing standards of the ILRS ACs. System-dependent CoM corrections (*Otsubo and Appleby*, 2003) were applied for the LAGEOS, Etalon and Ajisai satellites, whereas for Starlette and Stella the value of 78 mm recom-

Table 4.2 Data processing standards, models and conventions

Measurement models	
Observation weighting	Station-dependent standard deviations: 10-50 cm Satellite-dependent scale factors: 1.0 LAGEOS, 0.44 Etalon, 0.16 Starlette and Stella, 0.11 Ajisai, 0.25 LARES
Elevation cut-off angle	10°
Data editing	5 cm window outlier rejection Minimum of 20 NPs per station per week
Troposphere	Mendes–Pavlis zenith delay (*Mendes and Pavlis*, 2004) Mendes–Pavlis FCULa mapping function (*Mendes et al.*, 2002)
Relativity	Light-time corrections
Satellite CoM corrections	System-dependent for LAGEOS, Etalon and Ajisai (*Otsubo and Appleby*, 2003), 78 mm for Starlette and Stella (*Ries*, 2008), 133 mm for LARES
Force models	
Geopotential	EGM2008 (*Pavlis et al.*, 2012) Static terms up to d/o 60 for MEOs and d/o 120 for LEOs
Tidal forces	Solid Earth tides: IERS Conventions (2010) Solid Earth pole tide and ocean pole tide: IERS Conventions (2010) Ocean tides: FES2004 (*Lyard et al.*, 2006)
Third-body	Planets: Earth's Moon, Sun, Venus, Jupiter, Mars, Mercury Ephemeris: JPL DE403 (*Standish et al.*, 1995)
Solar radiation pressure	Direct, albedo and Earth thermal radiation applied
Atmospheric drag	Modelled for Starlette, Stella, Ajisai and LARES Thermospheric density model: NRLMSISE-00 (*Picone et al.*, 2002)
Relativity	Schwarzschild effect
Numerical integration	
Integrator	Gauss–Jackson 8th order predictor-corrector
Step size	60 s
Arc length	7 days
Reference frames	
Inertial	J2000.0
Terrestrial	SLRF2008[a] (a priori station coordinates and velocities) Solid Earth tides: IERS Conventions (2010) Ocean loading: Bos and Scherneck model[b] based on FES2004 including centre of mass correction Atmospheric pressure loading: diurnal S_1 and semidiurnal S_2 (*Ray and Ponte*, 2003) including centre of mass correction Pole tide: IERS Conventions (2010) Ocean pole tide loading: *Desai* (2002) model
Interconnection	Precession-nutation: IAU 2006/2000A Celestial pole offsets: IERS Conventions (2010) Earth Orientation Parameters: IERS EOP 08 C04 (IAU2000A) a priori

[a] ftp://cddis.gsfc.nasa.gov/slr/products/resource/SLRF2008_150928_2015.09.28.snx
[b] http://holt.oso.chalmers.se/loading/

mended by *Ries* (2008) was adopted rather than the standard value of 75 mm. A recent independent study (*Otsubo et al.*, 2015) also reported an average Starlette and Stella CoM correction of 78–79 mm for the current SLR network. The standard CoM correction of 133 mm was applied to LARES range observations.

The chosen satellite-dependent scale factors (see Table 4.2) are equivalent to assigning a priori standard deviations of 1 cm to LAGEOS data, 1.5 cm to Etalon, 2.5 cm to Starlette and Stella, 3 cm to Ajisai and 2 cm to LARES. This weighting strategy was selected based on the typical post-fit root mean square (RMS) of the observation residuals in an unweighted case. The RMS of n residuals v_i is given by

$$\mathrm{RMS} = \sqrt{\frac{\sum_{i=1}^{n} v_i^2}{n}}. \tag{4.8}$$

Downweighting LEO data is also desirable to counterbalance their dominance over MEO observations.

4.3.2 Standard parameterisation

The orbital parameterisations for MEOs and LEOs are described in Table 4.3, along with the estimated global parameters. The minimal set of parameters was sequentially supplemented by additional parameters to study the effects of various parameterisations on the observability of the geocentre coordinates, as described in Section 4.4. The only difference between LEO and MEO orbits consists in the estimation of drag coefficients for LEO orbits in place of empirical along-track acceleration parameters. These two types of parameters are modelled using piecewise linear functions in Faust (see Section 4.3.3).

Table 4.3 Estimated orbital and global parameters in standard solutions

Parameter	Spacing	
Orbital parameters	*MEOs*	*LEOs*
Initial position and velocity	Weekly	Weekly
Drag coefficients	–	Weekly
Empirical along-track accelerations	Weekly	–
Empirical OPR along-track accelerations	Weekly	Weekly
Empirical OPR cross-track accelerations	Weekly	Weekly
Global parameters		
Station coordinates	Weekly	
Pole coordinates	Daily	
Excess length of day	Daily	
Range biases for selected stations	Weekly	

Unmodelled thermal drag forces acting on LAGEOS (*Rubincam*, 1988, 1990) and the other satellites, as well as deficiencies in the modelling of direct and indirect SRP are accounted for by empirical along-track accelerations. The mismodelling of other non-

conservative forces is compensated by OPR acceleration parameters in the along-track (S_s, S_c) and cross-track (W_s, W_c) directions. The cross-track OPR parameters also compensate for unmodelled variations in the Earth's gravity field and the mismodelled part of ocean tide constituents. There is a lack of consensus in the SLR community on the spacing of empirical parameters over time. ILRS ACs routinely parameterise LAGEOS solutions with either one or two sets of along-track and OPR along-track and cross-track accelerations per week.

In the current practice of the ILRS ACs, SRP coefficients are fixed to best-fit satellite-dependent values. Most ACs apply a value of 1.13 for both LAGEOS-1 and 2, but recent studies (*Sośnica*, 2014; *Zelensky et al.*, 2014) indicated that a lower value of 1.10–1.11 better characterises the optical properties of LAGEOS-2, which may have changed since the launch of the satellite (*Lucchesi et al.*, 2004). In agreement with the practice of the ACs, the SRP coefficients were fixed to the values listed in Table 4.1 in the standard parameterisation.

Pole coordinates and excess LOD were estimated at noon of each day, whereas the UT1–UTC differences were fixed at noon to values obtained by linear interpolation of midnight offsets published by the IERS. Range biases were only estimated for certain stations suggested by the ILRS.[4] The orientations of the estimated CM-centred frames were aligned with respect to the Satellite Laser Ranging Frame (SLRF) 2008 through NNR conditions applied over the core network in each weekly solution. Both orbital and global parameters were freely estimated.

4.3.3 Drag coefficient modelling

The modelling of drag coefficients is briefly addressed due to the different approach implemented in Faust compared to other POD programs, which may affect the results of this study to some extent. The acceleration due to drag is modelled in the conventional way (e.g. *Montenbruck and Gill*, 2000), but Faust adopts a piecewise linear parameterisation of a satellite arc with drag coefficients.

Drag coefficients account mainly for the lack of precise knowledge of the atmospheric density in the upper atmosphere and are usually solved for as a piecewise constant function (Figure 4.5 *left*), which assumes a constant drag coefficient C_D over each of the time intervals composing an arc. The time stamp t_i attached to parameter C_{D_i} marks either the start or the end of the validity period of C_{D_i}. Unlike the piecewise constant function, the piecewise linear model employed in Faust (Figure 4.5 *right*) is continuous. The tag t_i corresponds to the time at which the value of parameter C_{D_i} pertains. At any given time $t \in [t_i, t_{i+1})$, the value of the drag coefficient $C_D(t)$ is found by linear interpolation

[4] http://ilrs.dgfi.tum.de/fileadmin/data_handling/ILRS_Data_Handling_File.snx

between the successive scale factors C_{D_i} and $C_{D_{i+1}}$, that is

$$C_D(t) = C_{D_i} + \frac{t - t_i}{t_{i+1} - t_i} \left(C_{D_{i+1}} - C_{D_i} \right). \tag{4.9}$$

Compared to the piecewise constant model, one additional parameter is required since each time interval is delimited by two drag coefficients, one at each end. The first and last coefficients in an arc are determined by data from only one interval, whereas the middle parameters are constrained by data from adjacent intervals. Thus, the shorter the time intervals are, the less information is used to determine the first and the last drag coefficients. An overparameterisation of an arc with unconstrained drag coefficients may lead to unrealistic negative values of the coefficients at the two ends. Parameterising a standard seven-day arc with only a pair of drag coefficients is equivalent to modelling C_D as a linear function of time (i.e. drag, drag rate). Hereinafter, this practice will be referred to as weekly estimation of drag coefficients.

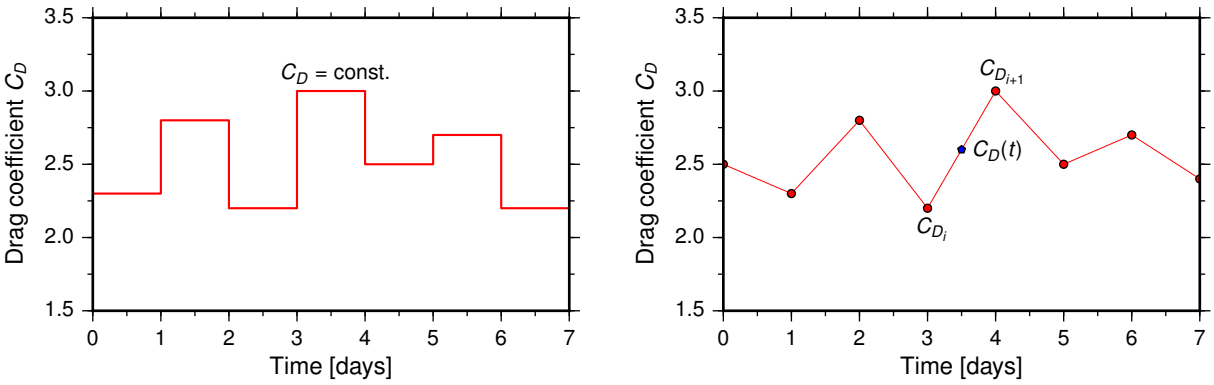

Figure 4.5 Parameterisation of a seven-day satellite arc with drag coefficients using two different models: piecewise constant function (*left*) and piecewise linear function (*right*)

It is customary to set up daily (*Cheng and Tapley*, 1999; *Moore et al.*, 2005; *Maier et al.*, 2012; *Sośnica et al.*, 2014) or even 12-hourly (*Lejba and Schillak*, 2011; *Cheng et al.*, 2013a) drag coefficients for LEO orbits to reduce the RMS of the observation residuals and hence improve the orbital fit. Solving for a high number of drag coefficients does, however, lead to increased correlations between parameters and potential collinearity issues. Despite lowering the residuals RMS, such a routine casts doubt on the quality of the determined orbit and even the fidelity of the model with respect to physical reality. Using the RMS as a measure of the absolute quality of a solution is problematic, although it does offer insight into the relative difference in quality between two solutions.

4.4 Results

The simulations carried out by *Rebischung et al.* (2014) using a synthetic SLR network yielded VIF values of 1.04 (20.4%), 1.04 (19.1%) and 8.6 (94.0%) for the X, Y and Z geocentre coordinates, respectively. A 100-station uniformly distributed network with

simulated observations every 5 minutes over 7 days to two LAGEOS–like satellites was used. However, this idealised network geometry and observation schedule are unrealistic for SLR. In this section, the analysis is extended to the actual SLR network and real data by introducing a 1 cm geocentre offset along each axis and applying the collinearity diagnostic procedure described in Section 4.2. To facilitate a direct comparison of the observability of the geocentre coordinates derived from different solution types, formal error values are provided in the following sections instead of VIFs. The formal error $1/\|\mathbf{s}_y\|$ represents the theoretical uncertainty of each geocentre coordinate estimated in isolation of other parameters, whereas $1/\|\mathbf{s}^p_{y,c}\|$ is the actual uncertainty of each geocentre coordinate under independent parameter variations. The squared ratio of $1/\|\mathbf{s}^p_{y,c}\|$ and $1/\|\mathbf{s}_y\|$ gives the VIF value.

4.4.1 LAGEOS-1 and 2 solutions

Seven solutions labelled A1 to A7 were produced for the LAGEOS-1 and 2 combination. The differences in parameterisation with respect to the standard solution described in Table 4.3 are as follows:

- A1: no differences,
- A2: two sets of empirical along-track and OPR along-track and cross-track accelerations,
- A3: geopotential coefficients up to d/o 2,
- A4: geopotential coefficients up to d/o 3,
- A5: geopotential coefficients up to d/o 3 and no OPR accelerations,
- A6: geopotential coefficients up to d/o 3 and two sets of empirical accelerations, and
- A7: geopotential coefficients up to d/o 4.

Only geopotential coefficients up to a maximum of degree 4 (excluding degree 1) were recovered given the insensitivity of LAGEOS-1 and 2 to harmonics of degree 5 and above (*Cheng et al.*, 1997; *Moore et al.*, 2005).

Weekly values of the formal errors were computed for each geocentre coordinate. Fluctuations in the values of the formal errors occur due to changes in network configuration, as well as variations in data coverage, quantity and quality. Table 4.4 contains the median formal errors over the considered 52-week time frame for each of the seven LAGEOS-1 and 2 solutions. The median values offer insight into the actual capability of the SLR technique to observe geocentre motion under different parameterisations. As shown in the next sections, the parameterisation can indeed affect the observability of the geocentre coordinates in SLR solutions, just as in the case of the GNSS geocentre determination.

Solutions A1 and A2 closely follow the processing standards of the ILRS ACs. The mean RMS of observation residuals is 9.1 mm for LAGEOS-1 and 9.2 mm for LAGEOS-2 in solution A1, whereas in solution A2 the mean RMS is 8.5 mm for each of the two

Table 4.4 Median formal errors of the geocentre coordinates derived from LAGEOS-1 and 2 (type A), LAGEOS–Etalon (type B), LAGEOS–Starlette–Stella–Ajisai (type C) and LAGEOS–LARES (type D) solutions

Solution	Median formal error $1/\|\mathbf{s}_y\|$ [mm]			Median formal error $1/\|\mathbf{s}^p_{y,c}\|$ [mm]		
	X	Y	Z	X	Y	Z
A1	0.357	0.352	0.300	1.407	1.195	3.541
A2	0.358	0.352	0.300	1.443	1.177	3.503
A3	0.357	0.352	0.300	1.482	1.172	3.368
A4	0.357	0.352	0.300	1.529	1.216	3.493
A5	0.372	0.365	0.312	1.400	1.247	3.355
A6	0.357	0.352	0.300	1.528	1.238	3.722
A7	0.357	0.352	0.300	1.794	1.495	3.696
B1	0.342	0.335	0.284	1.354	1.161	3.442
B2	0.342	0.335	0.285	1.434	1.188	3.600
C1	0.224	0.225	0.196	0.821	0.724	1.932
C2	0.220	0.223	0.194	0.807	0.689	1.887
C3	0.221	0.223	0.195	0.811	0.715	1.874
C4	0.256	0.261	0.220	0.832	0.832	2.066
C5	0.222	0.222	0.194	1.629	1.010	3.547
C6	0.244	0.248	0.214	0.806	0.767	1.934
C7	0.243	0.245	0.214	0.871	0.817	2.069
C8	0.243	0.245	0.213	0.848	0.771	2.098
D1	0.282	0.280	0.238	6.594	5.148	15.902
D2	0.282	0.280	0.238	0.887	0.841	2.580
D3	0.282	0.280	0.238	0.910	0.892	2.582
D4	0.280	0.279	0.236	0.978	0.912	2.737
D5	0.280	0.279	0.236	1.037	0.888	2.801
D6	0.280	0.279	0.236	1.027	0.911	2.633
D7	0.280	0.279	0.236	1.110	0.940	2.873

LAGEOS satellites. In addition to the improved orbital fit, the estimation of two sets of empirical accelerations per week instead of one set results in a reduced scatter of formal errors at the expense of only a minor increase in median formal error $1/\|\mathbf{s}^p_{y,c}\|$ of the X geocentre coordinate. If geopotential coefficients are additionally recovered, the formal errors $1/\|\mathbf{s}^p_{y,c}\|$ of the equatorial geocentre coordinates are slightly amplified, particularly when OPR accelerations are also estimated (cf. solutions A4, A5 and A6). When geopotential coefficients beyond degree 3 are determined, the formal errors $1/\|\mathbf{s}^p_{y,c}\|$ increase progressively, most likely due to the reduced sensitivity of the LAGEOS satellites to higher-degree harmonics and the increased correlations between geopotential coefficients and OPR accelerations.

In solution A1, the parameters that experience the largest variations $-\boldsymbol{\gamma}_{y,c}$ in response to imposing a geocentre offset of 1 cm along any axis are, in order of magnitude, the following:

- the satellite initial state vectors, particularly the velocity components,
- OPR accelerations, mainly in the cross-track direction (W_s, W_c), and
- station coordinates and range biases to similar extents.

When determining geopotential coefficients, however, the OPR accelerations are the most affected parameters (W_s and W_c in solution A3; S_s and W_c in solutions A4 and A7). The ability of OPR accelerations to absorb the signature of the geocentre offset increases with increasing degree of estimated harmonics. Nevertheless, OPR accelerations appear to play a minor role in LAGEOS–only solutions since neither their removal (solution A5) nor their increase in number (solution A6) greatly alter the formal error values.

Compared to the simulations conducted by *Rebischung et al.* (2014), range biases were additionally estimated for selected stations in this study. The LAGEOS-1 and 2 data was also processed using the standard parameterisation but without solving for range biases. The median formal errors $1/\|\mathbf{s}^p_{y,c}\|$ decreased by 5, 3 and 10% for the X, Y and Z geocentre coordinates, respectively, with respect to solution A1. This result highlights the importance of both rigorous calibrations of tracking systems and system-dependent CoM corrections. The application of well-established range biases at the pre-processing level and of system-dependent CoM corrections for all spherical geodetic satellites may allow the removal of range biases from the estimated parameters and, thus, a more accurate determination of geocentre motion and potentially other parameters.

4.4.2 LAGEOS–Etalon combined solutions

The Etalon satellites are inserted in GNSS–like orbits which complicate their tracking and limit their sensitivity to temporal variations in the Earth's gravity field. In the current study, only 27 of the 34 contributing stations provided Etalon data. Despite being sparsely tracked, the Etalon satellites contribute to the definition of the ITRF origin. For completeness, they are thus included here to appraise their effect on the observability of the geocentre coordinates.

Two LAGEOS–Etalon combined solutions were generated with the following differences with respect to the standard parameterisation:

- B1: no differences, and
- B2: geopotential coefficients up to d/o 3.

In solution B1, the mean RMS of observation residuals is 12.2 mm for Etalon-1 and 11.8 mm for Etalon-2, whereas in solution B2 the orbital fits are 12 mm for Etalon-1 and 11.7 mm for Etalon-2. Table 4.4 lists the obtained median formal errors of the geocentre coordinates. Comparing solutions B1 to A1 and B2 to A4 reveals that the addition of

Etalon observations to LAGEOS data has a limited effect on the observability of the geocentre coordinates. Etalon-1 and 2 provide beneficial information for the determination of the geocentre location only when geopotential coefficients are omitted. The limited sensitivity of the Etalon satellites to time-varying gravity signals is reflected by the typically higher spreads of formal errors $1/\|\mathbf{s}^p_{y,c}\|$ in solution B2 relative to solutions A3–A7 and a degraded observability of the Z geocentre coordinate. Due to their low contribution of questionable quality, Etalon data were not included in the MEO–LEO combined solutions described in the following two sections.

4.4.3 LAGEOS–Starlette–Stella–Ajisai combined solutions

The orbits of low Earth satellites Starlette, Stella and Ajisai are subject to large non-gravitational perturbations due to atmospheric drag, which pose difficulties for orbit modelling and restrict its accuracy. With the exception of geopotential coefficients, the geodetic products derived from Starlette, Stella and Ajisai data are typically of lower quality than their LAGEOS–derived equivalents (e.g. *Lejba and Schillak*, 2011), but recent LAGEOS–Starlette–Stella–Ajisai data combinations involving complex modelling of LEO orbits yielded promising results (*Cheng et al.*, 2013a; *Sośnica et al.*, 2014). However, to compensate for the effects of non-conservative forces and to improve the orbital fit to LAGEOS–like values, a large number of empirical parameters need to be solved for. Such parameters may also absorb geophysical signals in addition to modelling errors.

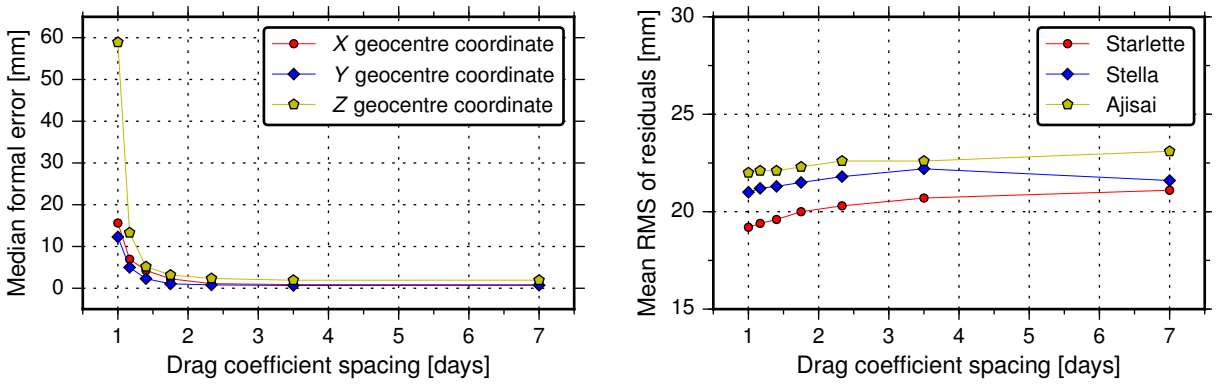

Figure 4.6 Median formal errors $1/\|\mathbf{s}^p_{y,c}\|$ of the three geocentre coordinates as a function of drag coefficient spacing (*left*). Mean RMS of Starlette, Stella and Ajisai observation residuals as a function of drag coefficient spacing (*right*)

The orbits of Starlette, Stella and Ajisai are routinely parameterised with daily drag coefficients. To assess the consequences of such a practice on the observability of the geocentre coordinates in LAGEOS–Starlette–Stella–Ajisai combinations, solutions with temporal spacing of drag coefficients ranging from one day to one week were derived. As Figure 4.6 (*left*) shows, median formal errors $1/\|\mathbf{s}^p_{y,c}\|$ increase exponentially as the number of drag coefficients increases. For each geocentre coordinate, over 98.8% of the variability in median formal errors $1/\|\mathbf{s}^p_{y,c}\|$ can be explained by an exponential function of the type

$a \exp(-bx) + c$ with coefficients a, b and c. On the other hand, the orbital fit for Starlette, Stella and Ajisai is characterised by a gradual but limited improvement with increasing number of drag coefficients, as illustrated in Figure 4.6 (*right*). The average differences in the RMS of the observation residuals between the solution with weekly drag coefficients and the solution with daily drag coefficients are 1.9, 0.5 and 1.1 mm for Starlette, Stella and Ajisai, respectively. Weekly differences are generally within 5 mm and sensibly lower for Ajisai (Figure 4.7). The mean RMS of LAGEOS-1 and 2 observation residuals is at the level of 1 cm, irrespective of the drag coefficient spacing.

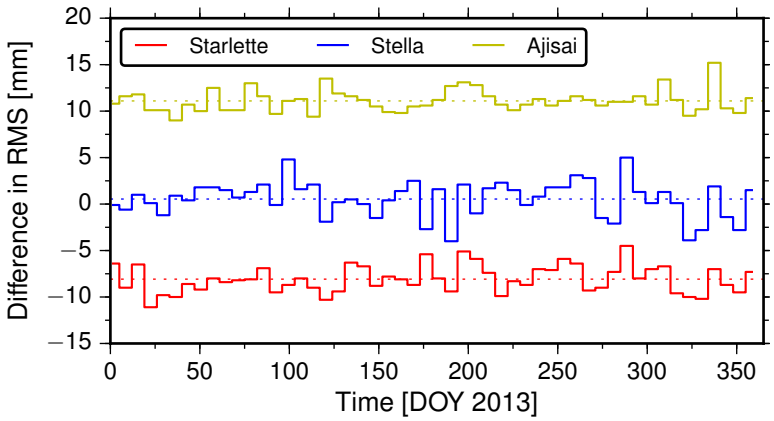

Figure 4.7 Differences in the RMS of observation residuals between the solution with weekly drag coefficients and the solution with daily drag coefficients (weekly minus daily) for Starlette, Stella and Ajisai. Starlette and Ajisai values are shifted by −10 mm and +10 mm, respectively. *Dotted lines* represent average differences

In LAGEOS–Starlette–Stella–Ajisai combined solutions, the independent parameters most affected by the artificial geocentre offset are drag coefficients. The variations $-\boldsymbol{\gamma}_{y,c}$ inflate with increasing number of drag coefficients and a progressively larger proportion of the geocentre offset signatures on the observed ranges are absorbed by drag coefficients. Additionally, the first or first few drag coefficients are moderately to strongly correlated with the elements of the initial state vectors, which are the second most affected parameters by the introduced geocentre offset if geopotential coefficients are not estimated. These correlations also increase as the number of drag coefficients increases and play an important but secondary role in the collinearity issues of the geocentre coordinates with the other parameters in LAGEOS–Starlette–Stella–Ajisai solutions.

These findings led to the decision to parameterise Starlette, Stella and Ajisai orbits with weekly drag coefficients in the remainder of the analysis to isolate the collinearity problems induced by drag coefficients. To investigate the influence of other parameters on the observability of the geocentre coordinates, eight solutions labelled C1 to C8 were produced. They display the following differences with respect to the standard parameterisation:

- C1: no differences,
- C2: two sets of empirical along-track and OPR along-track and cross-track accelerations for LAGEOS orbits and two sets of OPR along-track and cross-track accelerations for LEO orbits,
- C3: geopotential coefficients up to d/o 2,
- C4: geopotential coefficients up to d/o 2 and no OPR accelerations for LEO orbits only,
- C5: geopotential coefficients up to d/o 3,
- C6: geopotential coefficients up to d/o 3 and no OPR accelerations for LEO orbits only,
- C7: geopotential coefficients up to d/o 4 and no OPR accelerations for LEO orbits only, and
- C8: geopotential coefficients up to d/o 5 and no OPR accelerations for LEO orbits only.

Starlette, Stella and Ajisai are sensitive to harmonic coefficients beyond degree 20 (*Cheng et al.*, 1997; *Moore et al.*, 2005). The analysis was, however, restricted to degree 5 following the conclusion of *Maier et al.* (2012) that the estimation of geopotential coefficients above degree 5 leads to ill-conditioned systems of normal equations.

The computed median formal errors of the three geocentre coordinates are given in Table 4.4. In addition to the lower spread of values, the median formal error $1/\|\mathbf{s}^p_{y,c}\|$ of any geocentre coordinate is typically smaller by 40–45% in LAGEOS–Starlette–Stella–Ajisai solutions compared to LAGEOS–only. Since the source of the improvement is not an ameliorated station distribution (see Figure 4.2) and the formal errors $1/\|\mathbf{s}^p_{y,c}\|$ are only weakly correlated with the network size and moderately correlated with the number of observations, the intrinsic sensitivity of Starlette, Stella and Ajisai to geocentre motion is partly responsible for the enhanced observability of the geocentre coordinates. Unlike the formal errors $1/\|\mathbf{s}^p_{y,c}\|$, the values of $1/\|\mathbf{s}_y\|$ are very strongly correlated with the size of the data set. The direction of the correlation is negative in both cases.

As previously mentioned, drag coefficients exhibit the largest variations $-\boldsymbol{\gamma}_{y,c}$ following the introduction of an artificial geocentre offset of 1 cm along any Cartesian axis. In solution C3, the second most affected parameters are the OPR acceleration components W_c, whereas in solution C5 both S_s and W_c experience large variations. Increasing the degree of estimated geopotential coefficients inflates the variations of drag coefficients and OPR accelerations, thus enhancing their ability to jointly compensate the geocentre offsets (see, e.g., solution C5). Nevertheless, omitting the OPR accelerations for the Starlette, Stella and Ajisai when estimating geopotential coefficients greatly reduces the collinearity problems of the geocentre coordinates, as illustrated by solutions C6, C7 and C8. Hence, the simultaneous determination of OPR accelerations for Starlette, Stella and Ajisai and geopotential coefficients above degree 2 reduces the observability of the geocentre coor-

dinates in LAGEOS–Starlette–Stella–Ajisai solutions due to the correlations between the OPR terms, mainly in the cross-track direction, and the geopotential coefficients.

An alternative parameterisation to C1 with weekly drag coefficients fixed to the widely used value of 2.2 (see, e.g., *Cook*, 1965) and weekly empirical along-track accelerations was performed, but resulted in only a small improvement (∼5%) in the formal errors $1/\|\mathbf{s}^p_{y,c}\|$ over solution C1. Using such a parameterisation, however, the RMS of the observation residuals can be reduced for Starlette, Stella and Ajisai by reasonably increasing the number of empirical accelerations, without the risk of compromising the observability of the geocentre coordinates when geopotential coefficients are omitted.

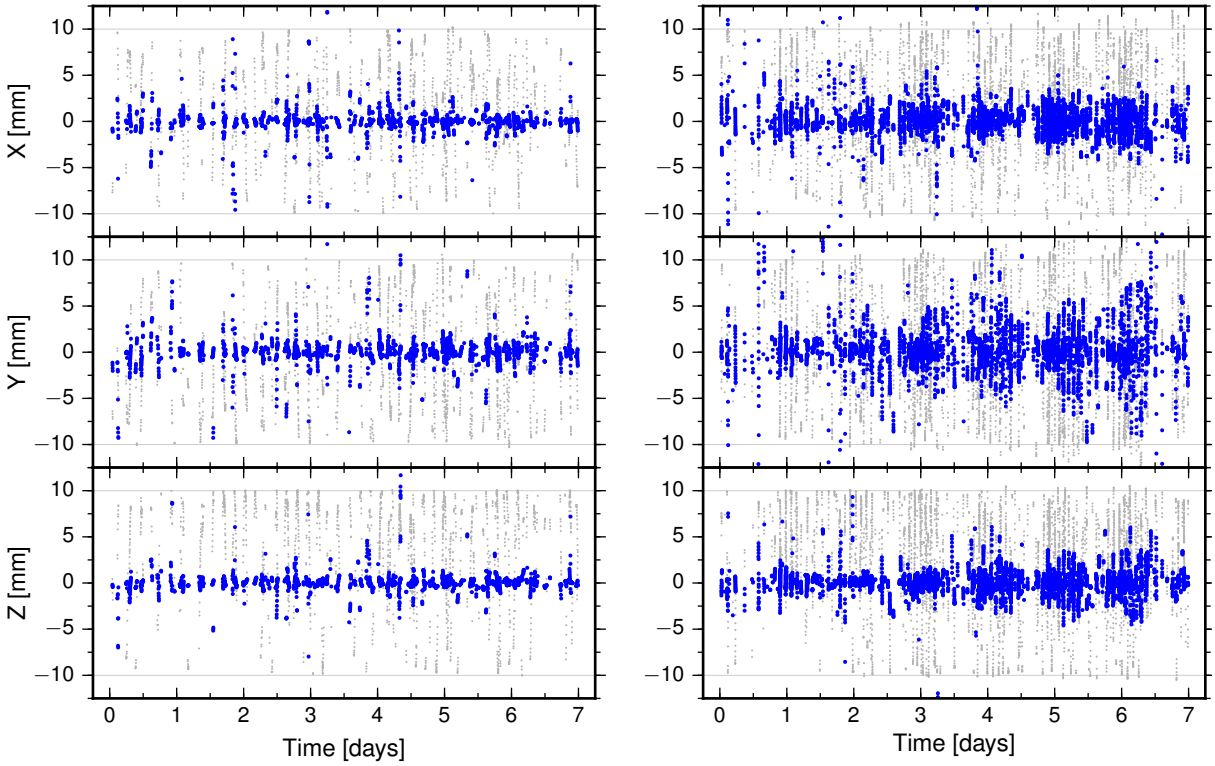

Figure 4.8 Signature $\mathbf{s}_y$ (*grey circles*) and proper signature $\mathbf{s}^p_{y,c}$ (*blue circles*) of a 1 cm geocentre offset along each axis on ranges to LAGEOS-1 and 2 (*left*) and ranges to Starlette, Stella and Ajisai (*right*). Plotted data are for the arcs spanning the week 28 July – 3 August, 2013 and solution C1

Independent parameter variations are less able to absorb the signature of the geocentre offset on ranges to Starlette, Stella and Ajisai than on ranges to LAGEOS-1 and 2. Figure 4.8 presents the case of the weekly combined solution with the lowest formal errors $1/\|\mathbf{s}^p_{y,c}\|$ for all three geocentre coordinates. The spatial coverage of NPs during the same week is shown in Figure 4.4. In all weekly solutions of type C, with the exception of C5, the proper signature is larger for Starlette, Stella and Ajisai ranges than for LAGEOS-1 and 2 ranges. This constitutes evidence of the higher sensitivity of LEOs to geocentre motion.

Observations to Starlette, Stella and Ajisai were also separately integrated with LAGEOS-1 and 2 data to appraise the relative contribution of each LEO to combined so-

lutions. The standard parameterisation was adopted for both LAGEOS and LEO orbits. The combination of Starlette with LAGEOS-1 and 2 provides the most stable results (i.e. the lowest spread of formal errors $1/\|\mathbf{s}^p_{y,c}\|$). Ajisai appears to contribute the most to the observability of the Z geocentre coordinate rather than Stella, as argued by *Sośnica et al.* (2014). This result is partly due to the large number of Ajisai observations, but confirms through real data analysis the finding of *Kuang et al.* (2015) that a polar orbit is the least favourable for the determination of the Z geocentre coordinate. *Kuang et al.* (2015) obtained this result using synthetic SLR data from a network of 40 stations tracking a single box-wing LEO and estimating an SRP coefficient, which is strongly correlated with the Z component of the geocentre vector (see, e.g., *Meindl et al.*, 2013). For polar orbits, the Z geocentre vector component lies in the orbital plane and can be compensated by the in-plane (i.e. radial and along-track) periodic orbital perturbations induced by SRP. This study shows that this statement holds even when the SRP coefficients are fixed, since Stella has an insignificant contribution to the observability of the geocentre coordinates compared to Starlette, despite the similar construction and altitudes of the two satellites. The quasi-polar orbit of Stella also hampers its tracking by the current SLR network that abounds in stations located at low and medium latitudes.

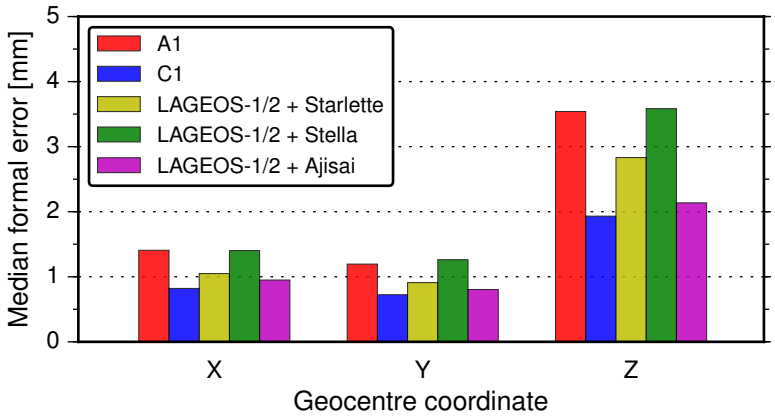

Figure 4.9 Median formal errors $1/\|\mathbf{s}^p_{y,c}\|$ of the three geocentre coordinates in solutions A1, C1 and separate combinations of Starlette, Stella and Ajisai with LAGEOS-1 and 2

The observability of the geocentre coordinates is improved by combining LAGEOS-1 and 2 with Starlette or Ajisai, whereas Stella fails to contribute significantly. No single LEO can fully explain the reduction in formal errors $1/\|\mathbf{s}^p_{y,c}\|$ and their spread from solution A1 to C1 (Figure 4.9). Important factors for the uncertainty reduction are the larger number of observations and the higher sensitivity of LEOs to geocentre motion.

4.4.4 LAGEOS–LARES combined solutions

Among the LEOs considered in this study, LARES is arguably the most suitable target for TRF determination given its favourable design features. As the inclusion of LARES in the ILRS operational products is imminent, seven LAGEOS–LARES solutions were derived

to investigate the potential benefits of incorporating LARES data for the origin of the TRF. The seven solutions display the following differences with respect to the standard parameterisation:

- D1: no differences,
- D2: one set of empirical along-track accelerations for LARES orbits instead of drag coefficients,
- D3: two sets of empirical along-track and OPR along-track and cross-track accelerations for all orbits,
- D4: one set of empirical along-track accelerations for LARES orbits and geopotential coefficients up to d/o 2,
- D5: one set of empirical along-track accelerations for LARES orbits and geopotential coefficients up to d/o 3,
- D6: one set of empirical along-track accelerations for LARES orbits and geopotential coefficients up to d/o 4, and
- D7: one set of empirical along-track accelerations for LARES orbits and geopotential coefficients up to d/o 5.

The mean RMS of LARES observation residuals improves from 18.8 mm in solutions D1 and D2 to 13.1 mm in solution D7, whereas the orbital fits of LAGEOS-1 and 2 observations lie in the confined interval 8.5–9.7 mm, with the lowest value in solution D7. Table 4.4 contains the computed median formal errors of the geocentre coordinates in solutions of type D.

In solution D1, drag coefficients vary the most among all parameters after the introduction of a 1 cm geocentre offset along any axis. The variations are larger than in type C solution and can compensate the artificial geocentre offset to a great extent, even when drag coefficients are estimated weekly rather than daily. The orbital perturbations due to atmospheric drag are smaller in magnitude for LARES than for any other LEO included in this study. This allows the efficient modelling of atmospheric drag effects on LARES using a single set of empirical along-track acceleration parameters instead of drag coefficients, as illustrated in Figure 4.10 by the small differences in the RMS of observations residuals between the alternative parameterisations D1 and D2 and a solution with daily drag coefficients for LARES orbits. The next most affected parameters in solution D1 after drag coefficients are the velocity components of the initial state vectors, followed by station coordinates.

The parameters displaying the largest variations $-\boldsymbol{\gamma}_{y,c}$ in solution D2 are the same as in solution A1, namely the satellite initial state vectors, the OPR acceleration parameters W_s and W_c, station coordinates and range biases. Similar to LAGEOS–only solutions, when geopotential coefficients are also estimated, the OPR accelerations are the most affected parameters (W_c in solution D4; S_s and W_c in solutions D5, D6 and D7), followed by the satellite velocity components. Unlike in type C solutions, the observability of the geocentre

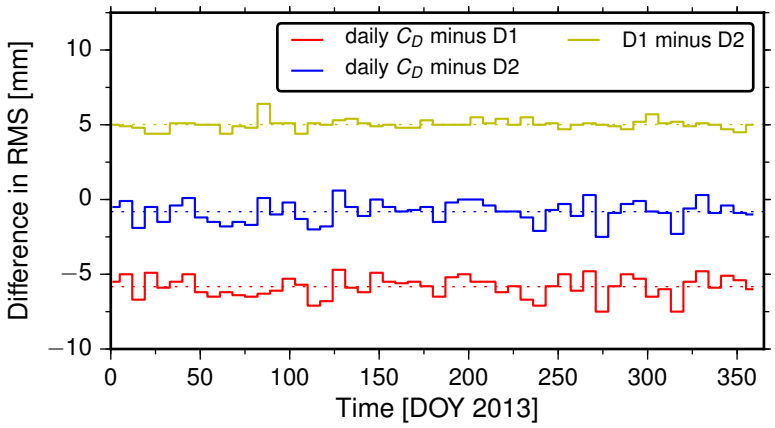

Figure 4.10 Differences in the RMS of LARES observation residuals between the solution with daily drag coefficients (designated as daily C_D) and solutions D1 and D2. Daily C_D minus D1 and D1 minus D2 values are shifted by −5 mm and +5 mm, respectively. *Dotted lines* represent average differences

coordinates is unaffected by the simultaneous determination of OPR accelerations for LARES and geopotential coefficients beyond degree 2 (cf. solutions C5 and D5). In an alternative solution to D1 and D2 with weekly drag coefficients fixed to the value of 2.2 for LARES and weekly empirical along-track accelerations, the orbital fits are identical to solutions D1 and D2 for all three satellites, whereas the observability of the geocentre vector is largely unaffected.

The median formal errors $1/\|\mathbf{s}^p_{y,c}\|$ of the geocentre coordinates are generally smaller by 20–35% in LAGEOS–LARES solutions relative to LAGEOS–only and LAGEOS–Etalon. Given the low altitude of LARES, the estimation of geopotential coefficients in LAGEOS–LARES solutions may be necessary to account for unmodelled and mismodelled long-wavelength variations in the Earth's gravity field. For the sake of an accurate determination of the geocentre location, a maximum truncation degree of 4 is preferable. The degraded observability of the geocentre coordinates in LAGEOS–LARES solutions with estimated geopotential coefficients beyond degree 4 (see solution D7) can be attributed to the insensitivity of LAGEOS-1 and 2 to these harmonics.

In combination with LAGEOS and other LEOs, LARES may also contribute to the separation of correlated geopotential coefficients. Preliminary analyses performed by *Ciufolini et al.* (2012) demonstrated a significant reduction in the uncertainties of geopotential coefficients determined from LARES data compared to observations of other spherical geodetic satellites. More recent studies (*Bloßfeld et al.*, 2015; *Sośnica et al.*, 2015) also reported promising results.

4.4.5 Effects of solar radiation pressure modelling

Direct SRP represents the dominant source of non-gravitational perturbations for the orbits of Ajisai, LARES and satellites at higher altitudes. Atmospheric drag may exert larger perturbations than direct SRP on the orbits of Starlette and Stella. For spherical

geodetic satellites, the acceleration due to direct SRP is more accurately modelled than the acceleration due to atmospheric drag owing to the lower uncertainty of the SRP force model components (see, e.g., *Milani et al.*, 1987). In addition, *Gobinddass et al.* (2009a) and *Meindl et al.* (2013) showed that the effects of SRP mismodelling on the estimated geocentre coordinates are much less problematic for laser ranging to spherical geodetic satellites than for DORIS and GNSS. In SLR analyses, SRP coefficients are commonly held fixed to satellite-specific a priori values, as done throughout this study. SRP introduces periodic orbital perturbations only in the radial and along-track directions. The along-track OPR acceleration parameters S_s and S_c are correlated with the SRP coefficients and can compensate the mismodelled part of SRP to a large extent. SRP modelling deficiencies are typically reflected in the power spectra of the geocentre coordinates by anomalous harmonics occurring at periods corresponding to the draconitic years of the spherical geodetic satellites, as well as at multiples of the draconitic frequencies.

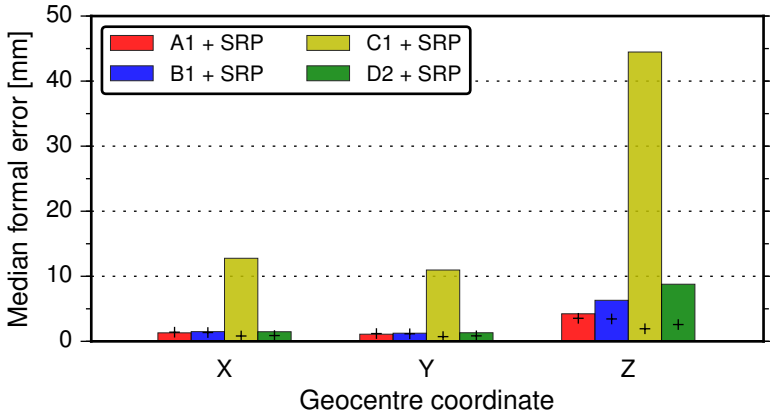

Figure 4.11 Median formal errors $1/\|\mathbf{s}^p_{y,c}\|$ of the three geocentre coordinates when the SRP coefficients of all satellites are estimated instead of being fixed in solutions A1, B1, C1 and D2. The median formal errors of the geocentre coordinates in solutions A1, B1, C1 and D2 are plotted as *black pluses* for comparison

To investigate the effects of the correlation between SRP coefficients and along-track OPR acceleration parameters on the observability of the geocentre coordinates, the parameterisations from solutions A1, B1, C1 and D2 were adopted, but an SRP coefficient for each satellite was freely estimated. As illustrated in Figure 4.11 via median formal errors $1/\|\mathbf{s}^p_{y,c}\|$, SRP coefficients and along-track OPR acceleration parameters have the potential to absorb the fictitious geocentre offset and thus reduce the observability of the geocentre vector, in particular of the Z component. The reduction in observability is more prominent in multi-satellite combinations (especially LAGEOS–Starlette–Stella–Ajisai) due to the larger variations of the SRP coefficients of LEOs. Fixing the SRP coefficients to a priori values can alleviate this collinearity issue without significant compromise in orbital fit. Omitting the estimation of along-track OPR terms is another but less justifiable option.

4.4.6 Comparison of solutions

Although not theoretically expected, variations in the formal error $1/\|\mathbf{s}_y\|$ among solutions of the same type (see Table 4.4) are due to the different number of accepted observations following the rejection of outliers. Low values of $1/\|\mathbf{s}_y\|$ are indicative of a high acceptance rate and vice versa. Solving for a high number of empirical parameters typically increases the acceptance rate (cf. solutions C3 and C4, also C5 and C6). A similar effect of the number of accepted observations on the formal error $1/\|\mathbf{s}^p_{y,c}\|$ is expected, but the statistical relationships between parameters are the main driver of fluctuations in $1/\|\mathbf{s}^p_{y,c}\|$ numerical values.

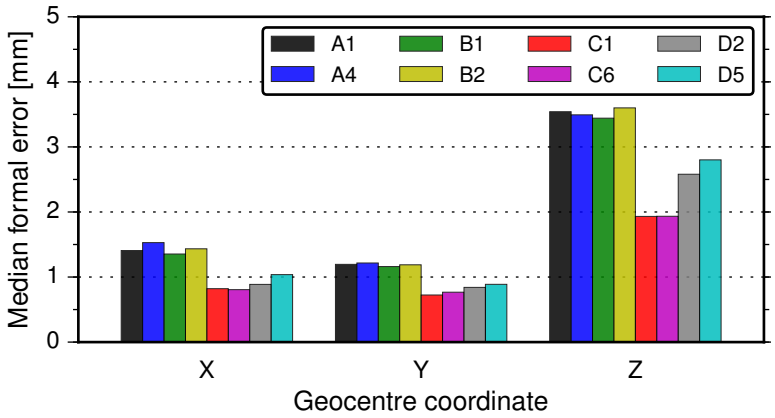

Figure 4.12 Comparison of the median formal errors $1/\|\mathbf{s}^p_{y,c}\|$ obtained for the three geocentre coordinates in eight different solutions of types A (LAGEOS-1 and 2), B (LAGEOS–Etalon), C (LAGEOS–Starlette–Stella–Ajisai) and D (LAGEOS–LARES)

The median formal errors $1/\|\mathbf{s}^p_{y,c}\|$ obtained for the geocentre coordinates in eight of the most representative solutions of types A, B, C and D are compared in Figure 4.12. In LAGEOS–Etalon combinations, median formal errors are marginally lower than in LAGEOS–only solutions, except for the formal error of the Z geocentre coordinates when geopotential coefficients are also recovered. Combining LAGEOS-1 and 2 with Starlette, Stella and Ajisai or only with LARES significantly reduces the median formal errors, particularly for the Z geocentre coordinate. By using only observations acquired by the core network shown in Figure 4.1 and the standard parameterisation, the median formal errors $1/\|\mathbf{s}^p_{y,c}\|$ are largely unaltered for any data combination. This approach results in improved network distributions at the expense of greatly diminished network sizes and data coverage.

The box plots of the Z coordinate formal errors $1/\|\mathbf{s}^p_{y,c}\|$ shown in Figure 4.13 illustrate the differences in the observability of this component in the eight solutions compared in Figure 4.12. Solutions A1 and D2 contain outliers which notably shift the arithmetic means away from the medians. Estimating geopotential coefficients in LAGEOS–only and LAGEOS–LARES solutions reduces the scatter of formal errors, but a similar effect can be achieved by doubling the number of empirical acceleration parameters. The relative

improvement in observability from solutions of types A–B to solutions of types C–D is indicated by the lower placement of the box plots for the latter. The distribution of formal errors is generally skewed towards large values, which explains the larger averages compared to the medians.

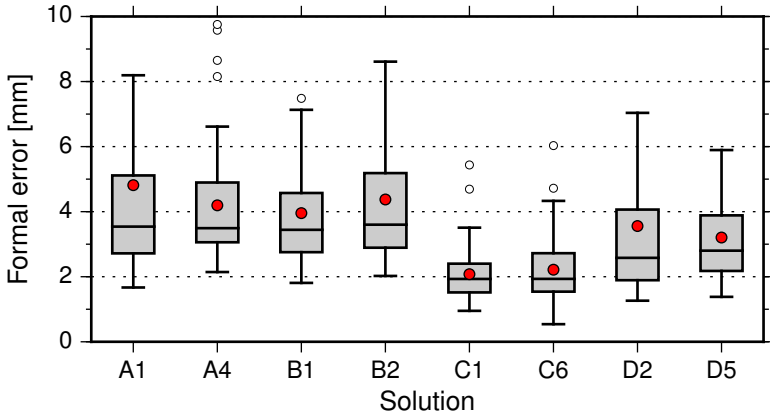

Figure 4.13 Box plots displaying the 25th (Q_1), 50th (median) and 75th (Q_3) percentiles and the 1.5 interquartile ranges (IQR $= Q_3 - Q_1$) of the formal errors $1/\|\mathbf{s}^p_{y,c}\|$ computed for the Z geocentre coordinate in eight different solutions. Mean formal errors are represented by *red circles* and outlying formal errors (i.e. larger than $Q_1 + 1.5 \cdot \mathrm{IQR}$ in this case) are plotted as *hollow circles*

Among the two equatorial components of the geocentre vector, X is less observable in SLR data analyses involving any combination of observations to spherical geodetic satellites, potentially due to its higher sensitivity to network effects (*Collilieux et al.*, 2009). The considerably stronger collinearity of the Z coordinate with other parameters engenders an increase of its formal error by a factor of 2–3 compared to the formal errors of the X and Y geocentre coordinates. The geocentre coordinates are typically more observable in LAGEOS–LEO combinations than in LAGEOS–only solutions due to both the higher sensitivity of LEOs to geocentre motion and the larger number of observations.

To validate the inferences from the analysis of formal errors, time series of geocentre coordinates were derived from the eight solutions compared in Figure 4.12 using the network shift approach with no scale factors estimated between weekly CM-centred frames and the SLRF2008. Figure 4.14 depicts the unfiltered series from the LAGEOS–only, LAGEOS–Starlette–Stella–Ajisai and LAGEOS–LARES solutions. Due to their similarity with the LAGEOS–only series and to avoid clutter, the LAGEOS–Etalon series are omitted from Figure 4.14. The RMS of the differences between the LAGEOS–only and LAGEOS–Etalon series derived from solutions with identical parameterisation varies between 0.9 mm and 1.6 mm, depending on the geocentre coordinate. This casts further doubt on the value added by Etalon data in LAGEOS–Etalon combinations.

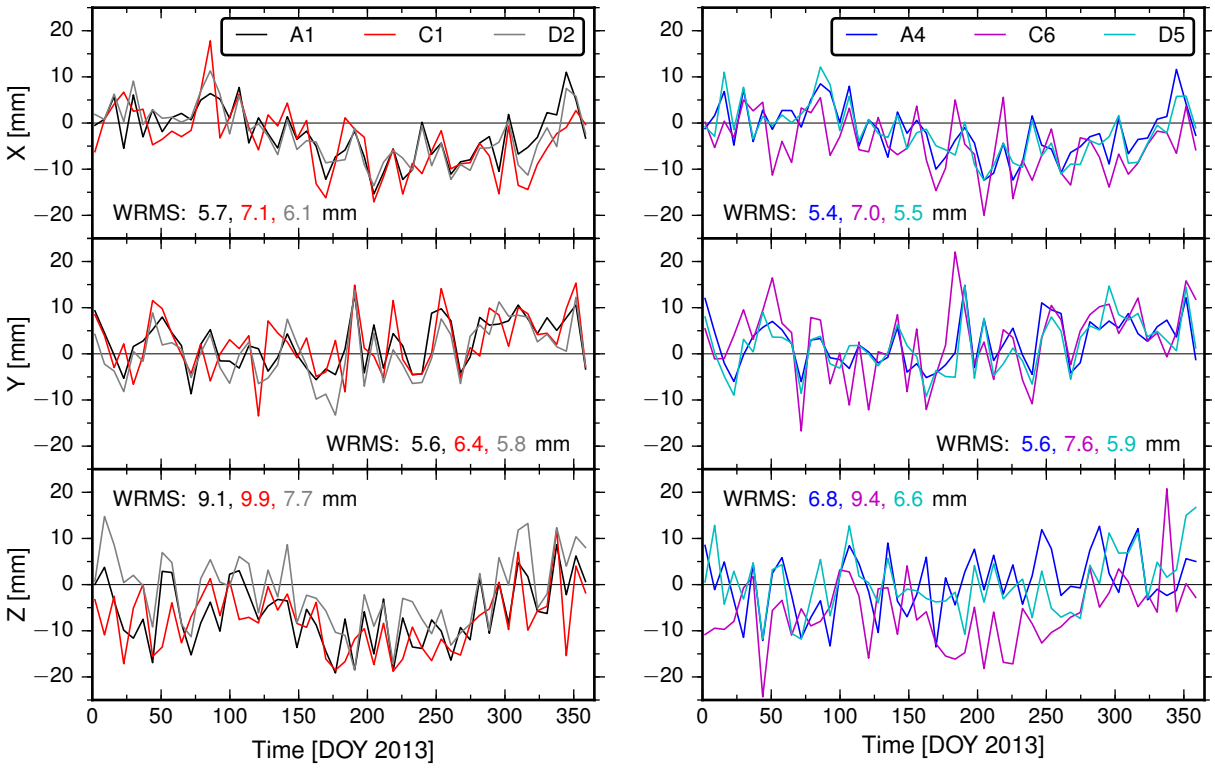

Figure 4.14 Unfiltered geocentre coordinates obtained via the network shift approach from solutions A1, C1 and D2 (*left*) and solutions A4, C5 and D5 (*right*). Six parameters (i.e. three translations and three rotations) were estimated weekly with respect to the SLRF2008

The scatter of the geocentre motion series can be quantified through the weighted root mean square (WRMS) of the geocentre coordinates defined as

$$\mathrm{WRMS} = \sqrt{\frac{\sum_{i=1}^{n} w_i \, y_i^2}{\sum_{i=1}^{n} w_i}}, \tag{4.10}$$

where y_i $(i = 1, 2, \ldots, n)$ are the values of each geocentre coordinate with the associated errors σ_i and $w_i = {}^1\!/_{\sigma_i^2}$ are the corresponding weights. The time series derived from solutions with estimated geopotential coefficients are typically characterised by a lower scatter. This is particularly true for the Z geocentre coordinate, which experiences a reduction in scatter of up to 26% in LAGEOS–only solutions. However, the annual variation of the axial geocentre motion component appears to be absorbed by the estimated geopotential coefficients, possibly due to Z being exclusively determined by orbital perturbations due to the geopotential (*Angermann and Müller*, 2008). Both the geopotential and Earth rotation affect the equatorial geocentre coordinates.

The LAGEOS–Starlette–Stella–Ajisai series exhibit the largest high-frequency variations and consequently have the largest scatter. Orbit modelling deficiencies may have contaminated the geocentre coordinates estimated from type C solutions given the simplistic force modelling applied for Starlette, Stella and Ajisai to circumvent collinearity issues. Despite the strong collinearity of the geocentre coordinates, the solution with daily drag coefficients estimated for Starlette, Stella and Ajisai (not shown in Figure 4.14) is

very similar to solution C1, but still noisier than other types of solutions. Without significant advances in surface force modelling, a beneficial contribution of Starlette, Stella and Ajisai to the definition of the ITRF origin appears unlikely, despite the improved observability of the geocentre coordinates.

The estimates of the equatorial geocentre coordinates from LAGEOS–only and LAGEOS–LARES solutions are in good agreement, despite the marginally larger scatter of the LAGEOS–LARES series. The WRMS of the Z geocentre coordinates is, nevertheless, lower in LAGEOS–LARES solutions, suggesting a potential improvement relative to LAGEOS-1 and 2 solutions. More conclusive evidence should be provided by the analysis of longer time series.

4.5 Summary

By means of collinearity diagnosis, this chapter set out to determine the actual current capability of SLR to sense geocentre motion and whether observations to the Etalon satellites and the LEOs Starlette, Stella, Ajisai and LARES can improve the observability of the geocentre coordinates with respect to standard LAGEOS-1 and 2 solutions. The processing of LAGEOS and Etalon NP data closely followed the standards of the ILRS ACs and the IERS Conventions (2010) (*Petit and Luzum*, 2010). Numerous solutions involving various data combinations were generated to investigate the effect of different parameterisations on the collinearity of the geocentre coordinates with the other parameters in the analyses.

Under ideal conditions, the determination of the X and Y geocentre coordinates from simulated observations to LAGEOS–like satellites is free of collinearity issues, whereas the determination of the Z coordinate suffers minor collinearity issues. This study showed that under real world conditions, the determination of the X and Y coordinates also suffers minor collinearity problems, whereas the Z coordinate is less observable by a factor of 2–3. The collinearity problems of the geocentre coordinates obtained from real SLR data are largely attributable to network effects and the unevenly spaced and imperfect observations of heterogeneous quality. The estimation of geopotential coefficients beyond degree and order 3 further amplifies the collinearity issues in LAGEOS–only solutions.

The combination of LAGEOS observations with Etalon data has a marginally positive effect on the observability of the geocentre coordinates only when geopotential coefficients are omitted. One reason for this result is that, in LAGEOS–Etalon solutions, the doubling of the number of orbital parameters (leading to increased correlations between parameters) is only accompanied by an increase of a few percent ($\sim$10%) in the size of data set. The incorporation of Etalon data in SLR analyses for the purpose of geocentre motion determination using the network shift approach is questionable.

Observations to the low altitude satellites Starlette, Stella and Ajisai can potentially improve the ties of the SLR-derived weekly TRFs to the CM frame subject to two pa-

rameterisation constraints. First, the parameterisation of orbital arcs of Starlette, Stella and Ajisai with frequent (i.e. sub-weekly) drag coefficients has a detrimental effect on the observability of the geocentre coordinates in LAGEOS–Starlette–Stella–Ajisai combined solutions. Second, the simultaneous estimation of OPR acceleration parameters for Starlette, Stella and Ajisai and geopotential coefficients above degree 2 also negatively affects the determination of geocentre motion, but on a smaller scale than frequently spaced drag coefficients. A third parameterisation constraint applies to all satellite combinations, but especially to LAGEOS–Starlette–Stella–Ajisai. The concurrent determination of SRP coefficients and along-track OPR acceleration parameters increases the formal errors of the geocentre coordinates due to the well-known correlations between the two types of parameters. Despite these collinearity issues, the real geophysical signal is expected to be recoverable in multi-satellite solutions involving LEOs.

The larger proper signature on Starlette, Stella and Ajisai ranges compared to LAGEOS ranges constitutes evidence of the higher sensitivity of LEOs to geocentre motion. The Z component of geocentre motion benefits most in an absolute sense from the combination of LAGEOS and LEO data. However, the geocentre coordinates estimated from LAGEOS–Starlette–Stella–Ajisai solutions are likely to be contaminated by force modelling errors that cannot be accommodated using a simplistic modelling strategy required to avoid collinearity issues. Until a satisfactory compromise between minimising orbital errors and circumventing collinearity issues is found, the exploitation of the high sensitivity of Starlette and Ajisai to geocentre motion appears unlikely. The sensitivity of Stella is lower due to its quasi-polar orbit, which also negatively affects the tracking of the satellite by the current SLR network.

Drag coefficients are predominantly used to absorb errors in atmospheric density modelling. Thus, an obvious path to more accurate geocentre motion estimates from LAGEOS–Starlette–Stella–Ajisai combinations is significant improvements of atmospheric models. Such developments would, in turn, allow the routine estimation of a low number of drag coefficients without major compromises in orbital quality. Parameterisations involving a high number of empirical parameters for the sake of deceptively small observation residuals can corrupt the geophysical significance of SLR-determined parameters.

The lower bound uncertainty of the equatorial geocentre coordinates determined from LAGEOS–Etalon data is around 1.5 mm and 4 mm for the Z coordinate, higher than the target of 1 mm geocentre vector accuracy pursued by GGOS (*Gross et al.*, 2009). Primarily designed to test fundamental and gravitational physics, LARES may prove a useful addition to the solutions derived by the ILRS ACs for TRF determination. The modelling of non-conservative forces acting on LARES is greatly simplified by the very low area-to-mass ratio of this satellite. An average improvement of 25–30% in the observability of the geocentre coordinates can be achieved by combining LAGEOS-1 and 2 with LARES data. Future ITRF releases following ITRF2014 will directly benefit from this improvement and edge closer towards meeting the stringent origin accuracy and stability

requirements imposed by highly demanding scientific applications such as the monitoring of sea level change.

The differences in the median formal errors reported in this study for different parameterisation are primarily driven by the strengths of statistical relationships between parameters. Collinearity diagnosis is particularly useful for identifying the effect of correlations between several parameters on the observability of the geocentre coordinates and provides optimistic formal error values that do not account for modelling errors. As argued by *Kuang et al.* (2015), the observability of a parameter and the contamination level of its estimate by modelling errors are distinct matters since models, including surface force models, are subject to refinements. Modelling errors do not constitute an inherent limitation for the sensitivity of satellite geodetic techniques to geophysical parameters. The main factors that govern the observability are rather the intrinsic quality, the quantity and spatial distribution of observations, along with the orbital configuration. Modelling errors can, however, alias into the estimates of parameters, particularly parameters affected by collinearity issues. Strongly collinear parameters may still be satisfactorily determined if their proper signatures on the observations are considerably larger than the modelling errors.

Chapter 5

Network shift estimates of geocentre coordinates

5.1 Introduction

The observability of the geocentre coordinates determined using the network shift approach was shown to be affected by the parameterisation of SLR solutions in Chapter 4. Important parameterisation constraints were determined and are used in the current chapter to generate geocentre motion time series spanning a maximum of 20 years from identical solution types to those in Chapter 4. Such time series have been conventionally analysed using ordinary least squares regression under the assumption of uncorrelated successive data points. Nevertheless, stochastic independence was proven an unrealistic supposition for various types of geophysical data (e.g. *Langbein and Johnson*, 1997; *Zhang et al.*, 1997; *Mao et al.*, 1999; *Williams et al.*, 2004; *Hughes and Williams*, 2010; *Bos et al.*, 2014; *Moore and Williams*, 2014; *Williams et al.*, 2014) and can have serious implications for the interpretation of deterministic parameters estimated from geophysical time series. Maximum likelihood estimation (MLE) provides the means to account for temporal correlations and determine realistic parameter uncertainties, but has yet to be applied to the analysis of geocentre motion time series, which may indeed contain temporally correlated noise.

This chapter commences with a brief review of the functional and stochastic models used in the analysis of geodetic time series and the estimation of model parameters by maximum likelihood. The analysed 20-year SLR data set is then described, together with the parameterisations of the four types of generated solutions. Subsequently, geocentre motion time series obtained via the network shift approach from the SLR solutions are analysed in the frequency and time domains to check for periodicities, aliasing errors and temporal correlations. Aided by model-selection statistics, the optimal functional-stochastic model is selected for each series and checked by comparing the modelled power spectra with the power spectra of the geocentre coordinate residuals. The extent to which

the geocentre coordinates are affected by variations in the SLR network distribution is assessed using a sub-network of notably reliable stations. Relevant parameter estimates from the various time series are compared before concluding the chapter with a summary of the findings.

5.2 Model parameter estimation

5.2.1 Functional model

A time series of geodetic parameters taking the values y_i at times t_i $(i = 1, 2, \ldots, n)$ can typically be fitted by the model

$$y_i = a + b\,(t_i - t_0) + \frac{1}{2}\,c\,(t_i - t_0)^2 + \sum_{j=1}^{m} A_j \cos(2\pi f_j t_i - \phi_j) + \varepsilon_i, \tag{5.1}$$

containing an intercept (or bias) a at epoch t_0, a linear trend (or rate) b, an acceleration (or quadratic) term c, m periodic signals of amplitude A_j and phase ϕ_j representing harmonics of the frequency f_j and the error term ε_i that accounts for noise in the time series. For data points sampled at equal time intervals of length Δt, the highest detectable frequency known as the *Nyquist frequency* is $1/2\Delta t$. Meaningful information may be extracted from a time series for any frequency between the lowest frequency $1/n\Delta t$ and the Nyquist frequency.

The value of the linear term b in (5.1) depends on the choice of the reference epoch t_0 when b and the quadratic term c are simultaneously recovered (*Moore and Williams*, 2014). If c is omitted, b is independent of t_0. Using the notations

$$p_j = A_j \sin\phi_j, \qquad q_j = A_j \cos\phi_j \tag{5.2}$$

Equation (5.1) can be written as

$$y_i = a + b\,(t_i - t_0) + \frac{1}{2}\,c\,(t_i - t_0)^2 + \sum_{j=1}^{m} \left[p_j \sin(2\pi f_j t_i) + q_j \cos(2\pi f_j t_i)\right] + \varepsilon_i. \tag{5.3}$$

If omitting the quadratic coefficient c and retaining only annual and semi-annual signals (i.e. $f = 1, 2$ cpy), (5.3) simplifies to

$$\begin{aligned} y_i = a + b\,(t_i - t_0) + p_1 \sin(2\pi t_i) + q_1 \cos(2\pi t_i) \\ + p_2 \sin(4\pi t_i) + q_2 \cos(4\pi t_i) + \varepsilon_i. \end{aligned} \tag{5.4}$$

It is worth noting that in the sine and cosine terms of (5.4), t_i is typically defined as a decimal year offset with respect to 1 January of each year. The matrix representation of (5.4) is

$$\mathbf{y} - \mathbf{v} = \mathbf{A}\mathbf{x}, \tag{5.5}$$

where

$$\begin{aligned}
\mathbf{y} &= \begin{bmatrix} y_1 & y_2 & \dots & y_n \end{bmatrix}^T, \\
\mathbf{v} &= \begin{bmatrix} v_1 & v_2 & \dots & v_n \end{bmatrix}^T, \\
\mathbf{A} &= \begin{bmatrix} 1 & t_1 - t_0 & \sin(2\pi t_1) & \cos(2\pi t_1) & \sin(4\pi t_1) & \cos(4\pi t_1) \\ 1 & t_2 - t_0 & \sin(2\pi t_2) & \cos(2\pi t_2) & \sin(4\pi t_2) & \cos(4\pi t_2) \\ \vdots & \vdots & \vdots & \vdots & \vdots & \vdots \\ 1 & t_n - t_0 & \sin(2\pi t_n) & \cos(2\pi t_n) & \sin(4\pi t_n) & \cos(4\pi t_n) \end{bmatrix}, \\
\mathbf{x} &= \begin{bmatrix} a & b & p_1 & q_1 & p_2 & q_2 \end{bmatrix}^T
\end{aligned} \tag{5.6}$$

are the vector of observations, the vector of observation residuals, the design matrix and the vector of unknown parameters, respectively.

5.2.2 Stochastic model

Under the assumption that the error term ε_i comprises only independent and identically distributed random variables w_i, the variance-covariance matrix $\mathbf{C}$ of the observations equals either the unit matrix $\mathbf{I}$ scaled by the variance a_w^2 (i.e. $\mathbf{C} = a_w^2\mathbf{I}$) in the case of classical white noise or, for time-variable white noise, a diagonal matrix that contains individual variances σ_i^2 for all data points, thus

$$\mathbf{C} = \operatorname{diag}\left(\sigma_1^2, \sigma_2^2, \dots, \sigma_n^2\right). \tag{5.7}$$

However, several studies (*Langbein and Johnson*, 1997; *Zhang et al.*, 1997; *Mao et al.*, 1999; *Williams et al.*, 2004; *Amiri-Simkooei et al.*, 2007; *Hackl et al.*, 2011; *Santamaría-Gómez et al.*, 2011; *Bogusz and Klos*, 2015) demonstrated the presence in geodetic time series of temporally correlated errors that follow the power-law f^κ, where f is the temporal frequency and κ represents the *spectral index*, equal to the slope of the PSD in a log-log plot of f versus PSD. This power-law process is a one-dimensional stochastic process with the power spectrum (e.g. *Agnew*, 1992)

$$P(f) = P_0 \left(\frac{f}{f_0}\right)^\kappa \tag{5.8}$$

where P_0 and f_0 are normalising constants. The values of the spectral index typically fall in the range $[-3, 1]$, with lower values indicative of larger correlations and more power at low frequencies. Classical white noise is characterised by $\kappa = 0$, whereas $\kappa = -1$ designates flicker noise (or pink noise). Random walk (i.e. $\kappa = -2$) and flicker walk (i.e. $\kappa = -3$) are other common noise types.

The neglect of temporally correlated noise, also referred to as coloured noise, may lead to an underestimation of model parameter uncertainties, particularly of the linear trend uncertainty, by up to a factor of 11 (*Mao et al.*, 1999; *Santamaría-Gómez et al.*, 2011). For a combination of white noise with amplitude a_w and power-law noise with amplitude

a_κ, the covariance matrix of the observations may be expressed as (*Zhang et al.*, 1997; *Williams*, 2003)

$$\mathbf{C} = a_w^2 \mathbf{I} + a_\kappa^2 \mathbf{J}_\kappa, \tag{5.9}$$

where $\mathbf{J}_\kappa = \mathbf{T}\mathbf{T}^T$ is the covariance matrix of the power-law noise derived using the transformation matrix

$$\mathbf{T} = \begin{bmatrix} \psi_0 & 0 & 0 & \cdots & 0 \\ \psi_1 & \psi_0 & 0 & \cdots & 0 \\ \psi_2 & \psi_1 & \psi_0 & \cdots & 0 \\ \vdots & \vdots & \vdots & \ddots & \vdots \\ \psi_n & \psi_{n-1} & \psi_{n-2} & \cdots & \psi_0 \end{bmatrix}, \tag{5.10}$$

with

$$\psi_n = \frac{-\frac{\kappa}{2}\left(1-\frac{\kappa}{2}\right)\left(2-\frac{\kappa}{2}\right)\cdots\left(n-1-\frac{\kappa}{2}\right)}{n!}. \tag{5.11}$$

For uniformly spaced data, the transformation matrix $\mathbf{T}$ is sometimes scaled by $\Delta t^{-\kappa/4}$, where Δt is expressed in years, before the computation of the covariance matrix $\mathbf{J}_\kappa$. Using the notations $a_w = r\cos\varphi$ and $a_\kappa = r\sin\varphi$, where r is a scalar known as innovation noise and φ is an angle, *Williams* (2008) provided the following alternative formulation of the covariance matrix:

$$\mathbf{C} = r^2\left(\cos^2\varphi\,\mathbf{I} + \sin^2\varphi\,\mathbf{J}_\kappa\right). \tag{5.12}$$

This allows a reduction of one in dimensionality since r can be explicitly estimated for a given angle φ determining the ratio of white noise and power-law noise. The stochastic model can be extended with other noise models such as autoregressive noise, band-pass-filtered noise and generalised Gauss–Markov noise (*Langbein*, 2004), which may occasionally be preferred to the standard white noise and power-law noise combination.

5.2.3 Maximum likelihood estimation

The weighted least squares estimate of the parameter vector $\mathbf{x}$ from (5.5) is given by

$$\hat{\mathbf{x}} = \left(\mathbf{A}^T\mathbf{C}^{-1}\mathbf{A}\right)^{-1}\mathbf{A}^T\mathbf{C}^{-1}\mathbf{y} \tag{5.13}$$

and the covariance matrix of the estimated parameters $\mathbf{C}_{\hat{\mathbf{x}}}$ equals the inverse of the normal equation matrix, that is

$$\mathbf{C}_{\hat{\mathbf{x}}} = \left(\mathbf{A}^T\mathbf{C}^{-1}\mathbf{A}\right)^{-1}. \tag{5.14}$$

The post-fit observation residuals can be obtained as

$$\hat{\mathbf{v}} = \mathbf{y} - \mathbf{A}\hat{\mathbf{x}}. \tag{5.15}$$

MLE yields the most likely estimates of the parameter vector $\mathbf{x}$ and of the noise model components given the observations $\mathbf{y}$ by maximising the probability function (*Langbein and Johnson*, 1997; *Williams*, 2008)

$$\mathcal{L}(\hat{\mathbf{v}}, \mathbf{C}) = \frac{1}{(2\pi)^{n/2} (\det \mathbf{C})^{1/2}} \exp\left(-\frac{1}{2}\hat{\mathbf{v}}^T \mathbf{C}^{-1} \hat{\mathbf{v}}\right) \tag{5.16}$$

or, equivalently, the log-likelihood

$$\ln\left[\mathcal{L}(\hat{\mathbf{v}}, \mathbf{C})\right] = -\frac{1}{2}\left[n \ln(2\pi) + \ln(\det \mathbf{C}) + \hat{\mathbf{v}}^T \mathbf{C}^{-1} \hat{\mathbf{v}}\right] \tag{5.17}$$

for improved numerical stability. Alternatively, the negative of the log-likelihood function may be minimised using an algorithm such as the downhill simplex method (see, e.g., *Press et al.*, 1992). Starting from a priori values, the noise parameters are iteratively varied until a predefined convergence criterion is met.

The optimal functional and stochastic models for a particular time series may be selected by evaluating two widely used model-selection statistics know as the Akaike Information Criterion (AIC; *Akaike*, 1974) and the Bayesian Information Criterion (BIC; *Schwarz*, 1978), which can be obtained as

$$\begin{aligned} \mathrm{AIC} &= -2 \ln \mathcal{L} + 2u, \\ \mathrm{BIC} &= -2 \ln \mathcal{L} + u \ln n, \end{aligned} \tag{5.18}$$

where u denotes the number of estimated parameters. The goodness-of-fit term $-2 \ln \mathcal{L}$ is identical in both criteria, but due to its more stringent penalty term (i.e. $u \ln n$ exceeds $2u$ for $n \geq 8$), the BIC favours models with a smaller number of parameters. Nevertheless, among a finite number of models, the preferred one is that corresponding to the minimum value of the AIC or BIC. Throughout this study, the BIC is given preference over the AIC when the two criteria disagree, as recommended by *Faraway and Chatfield* (1998).

Create and Analyse Time Series (CATS; *Williams*, 2008) and Hector (*Bos et al.*, 2013) are two software packages that employ the MLE algorithm and include a wide range of noise models. While CATS is more widely known and offers additional noise models, Hector is faster by a factor of 10–100 due to the use of fast matrix operations under the assumption that only stationary noise (i.e. with constant mean and variance) is present in the time series. For non-stationary series (i.e. $\kappa \leq -1$), stationarity can typically be attained by first-order differencing (e.g. *Bos et al.*, 2008). Both CATS and Hector are able to cope with missing data.

5.3 Data statistics and processing strategy

5.3.1 Network and satellite data

The analysed data set consists of NP observations to LAGEOS-1 and 2, Etalon-1 and 2, Starlette, Stella, Ajisai and LARES spanning the time interval 1995.0–2015.0, with LARES data available from 2012.1. As the archives of the two ILRS data centres (i.e. CDDIS and EDC) differ slightly, a merged data set was derived to maximise the number of observations. The 20-year data set includes approximately 9.3 million NPs acquired by a total of 89 stations, many of which have been decommissioned, replaced or repositioned in the case of mobile tracking systems. Consequently, only 34 stations have a tracking history of more than 10 years over the two decades considered. The data combinations corresponding to the four types of generated solutions are identical to those in Chapter 4, namely (1) LAGEOS–only, (2) LAGEOS–Etalon, (3) LAGEOS–Starlette–Stella–Ajisai, and (4) LAGEOS–LARES.

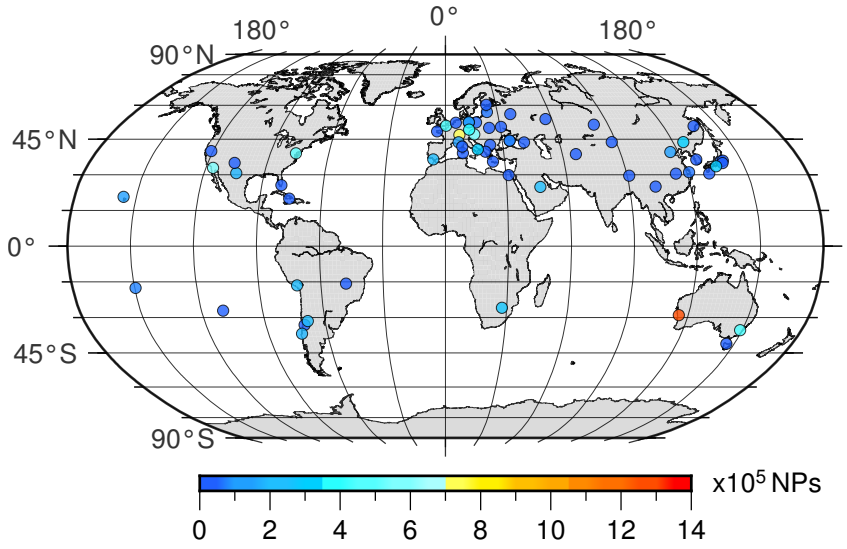

Figure 5.1 The SLR network during the period 1995.0–2015.0. The *colour scale* shows the total number of NPs to LAGEOS-1 and 2, Etalon-1 and 2, Starlette, Stella, Ajisai and LARES

Figure 5.1 shows the geographical distribution of the SLR stations. The majority of stations are situated at mid-latitudes, in the eastern and northern hemispheres of the Earth and thus on the positive Y and Z Cartesian axes of the geocentric reference frame. This is further illustrated in Figure 5.2, which depicts the temporal variability in network distribution along the three Cartesian axes. The time series were smoothed using a Butterworth low-pass filter with a cut-off frequency of 1.25 cpy to allow the investigation of seasonal and long-period variations. Significant annual variability with minima in the northern hemisphere winters and maxima in summers can be observed along the X axis, which displays the most balanced distribution among the Cartesian axes. Since laser beams are unable to penetrate clouds and most stations with positive X geocentric coordinates are clustered in Europe, the sinusoidal pattern in the X direction is likely to

mirror seasonal variations in cloud cover and precipitation over Europe. Inter-seasonal variations are discernible in all three directions, as well as occasional offsets occurring due to stations being decommissioned or added to the network. For example, the addition of San Juan (7406), Argentina in February 2006 rendered the distributions in the Y and Z directions closer to the ideal value of 50%. Although not shown in Figure 5.2, the combination of LAGEOS-1 and 2 with Starlette, Stella and Ajisai observations results in degraded distributions along the X, Y and Z axes by averages of 0.8, 0.5 and 1 percentage points, respectively.

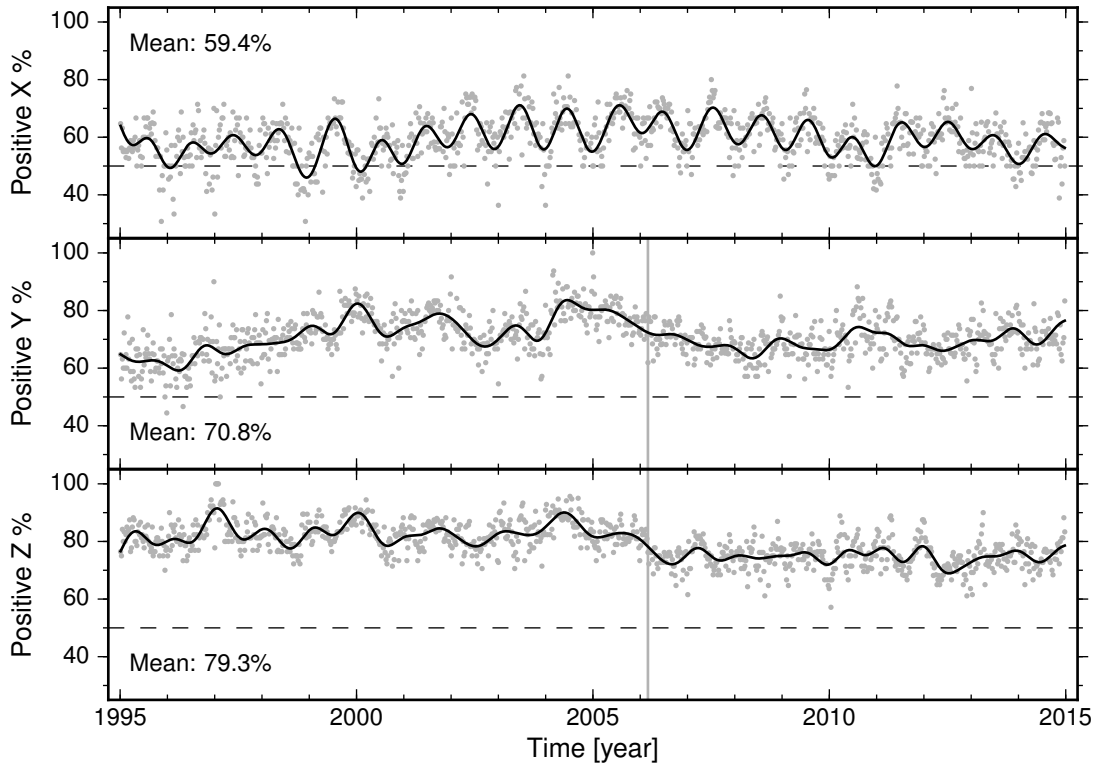

Figure 5.2 Percentages of stations located in the hemispheres defined by the positive X, Y and Z Cartesian axes in LAGEOS-1 and 2 weekly solutions (*grey circles*) and smoothed percentages using a sixth-order Butterworth low-pass filter with a cut-off frequency of 1.25 cpy (*black curve*). The vertical *grey line* at 2006.16 marks an offset in the Y and Z time series due to the addition of station San Juan (7406) to the network

LAGEOS-1 and 2 were tracked by 84 stations, whereas Etalon-1 and 2 only by 54 stations. The most frequently tracked satellite was Ajisai with more than 33% of the data set, roughly identical to the combined contribution of the two LAGEOS satellites. LARES is only surpassed by Ajisai in terms of average number of observations per year. Yarragadee (7090), Australia was the most productive station with approximately 14% of the total number of observations, followed by Zimmerwald (7810), Switzerland and Monument Peak (7110), US. Nevertheless, Herstmonceux (7840), United Kingdom had the third highest LAGEOS-1 and 2 data yield, trailing Yarragadee and Zimmerwald.

The temporal variability in the number of stations and the number of NPs in three solution types is illustrated in Figure 5.3. Following an increase in the late 1990s, the weekly

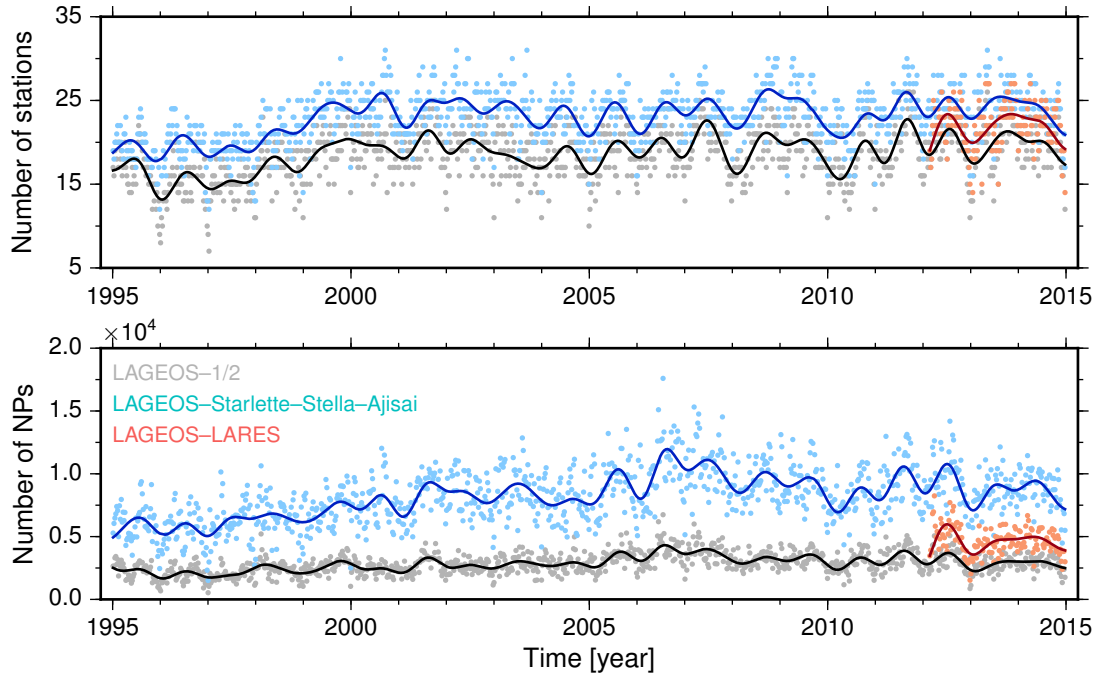

Figure 5.3 Number of stations with more than 20 NPs (*top*) and number of NPs (*bottom*) in LAGEOS-1 and 2, LAGEOS–Starlette–Stella–Ajisai and LAGEOS–LARES weekly solutions. The solid curves were obtained using a sixth-order Butterworth low-pass filter with a cut-off frequency of 1.25 cpy

network size has stabilised at an average of 19 stations in the LAGEOS–only solution and 24 stations in the LAGEOS–Starlette–Stella–Ajisai solution, disregarding seasonal variations due to weather conditions. The LAGEOS–LARES solution lies between the two, with an average of 22 stations per week. The variations in the number of observations follow a similar pattern, but several stations appear to have increased their data yields over the last decade.

5.3.2 Analysis strategy

The data were processed in seven-day batches starting each Sunday using an updated version of the POD software Faust (*Moore et al.*, 1999). The computational models employed for orbit determination (see Table 4.2) closely follow the IERS Conventions (2010) (*Petit and Luzum*, 2010), whereas the data analysis strategy is consistent with the recommendations of the ILRS Analysis Working Group (AWG) for ACs contributing to ITRF2014 (*Luceri et al.*, 2015). Stations were assigned a priori standard deviations (SDs) ranging from 10 cm for core stations to 50 cm for low-performing stations. The threshold for including a particular station in a weekly solution was set to 20 NPs with residuals lower in absolute value than the rejection criterion of 5 cm. Station-specific CoM corrections proposed by *Otsubo and Appleby* (2003) were applied to LAGEOS-1 and 2, Etalon-1 and 2 and Ajisai ranges. Following *Ries* (2008), the CoM correction adopted for Starlette and Stella was 78 mm, whereas the standard value of 133 mm was used for LARES.

Geocentre motion estimates are highly dependent on the quality of the underlying TRF used for orbit determination. The a priori TRF adopted in this study is the SLRF2008, which contains a revised set of station positions and velocities of all SLR stations, including historical stations omitted from ITRF releases. The SLRF2008 is consistent with the ITRF2008, but regularly updated to include new stations and account for discontinuities in the position time series following, for example, seismic events. It is thus an invaluable resource for the analysis of SLR data acquired outside the temporal coverage of the latest ITRF.

The findings from Chapter 4 served as guidelines for the optimal parameterisation of satellite orbits. Two sets of OPR along-track and cross-track acceleration parameters were estimated for LAGEOS-1 and 2 and all LEOs, whereas the Etalon-1 and 2 orbits were parameterised with a single set of OPR accelerations due to the lack of sufficient observations to physically justify the estimation of more OPR terms. Similarly, empirical along-track acceleration parameters were adjusted weekly for the Etalon satellites and every 3.5 days for the LAGEOS and LARES satellites. Starlette, Stella and Ajisai orbits were parameterised with weekly drag coefficients rather than empirical along-track acceleration parameters. Initial state vectors were determined once per week for all considered satellites.

Table 5.1 A priori and estimated SRP coefficients for the spherical geodetic satellites

Satellite	A priori C_R	Mean estimated C_R	Time span
LAGEOS-1	1.130	1.137 ± 0.004	1995.0–2015.0
LAGEOS-2	1.130	1.111 ± 0.004	1995.0–2015.0
Etalon-1	1.240	1.239 ± 0.002	2003.0–2015.0
Etalon-2	1.280	1.276 ± 0.001	2003.0–2015.0
Starlette	1.134	1.137 ± 0.010	1995.0–2015.0
Stella	1.131	1.133 ± 0.001	1995.0–2015.0
Ajisai	1.035	1.055 ± 0.004	1995.0–2015.0
LARES	1.125	1.123 ± 0.005	2012.1–2015.0

As shown in Section 4.4.5, the concurrent estimation of SRP coefficients and OPR along-track acceleration parameters reduces the observability of the geocentre coordinates due to the correlations between the two types of parameters. A viable solution is to fix the SRP coefficient C_R of each satellite to a predetermined value which optimally characterises the reflective properties of the satellite's surface. Due to the large spread of values reported in the literature and the temporal dependence of the SRP coefficients, it was decided to estimate mean SRP coefficients valid for the time span of the current analysis starting with the a priori values listed in Table 4.1 and an uncertainty of 0.1 to allow for reasonable variability in the adjusted SRP coefficients. Table 5.1 lists the mean C_R value obtained for each satellite and its 95% confidence interval. The largest differences with respect to the a priori values occur for Ajisai and LAGEOS-2. However, the LAGEOS-2 mean C_R value

of 1.111 is equal to that used by *Zelensky et al.* (2014) and similar to the value of 1.11 employed by the Center of Space Research (CSR) of the University of Texas at Austin for operational products.[1] For the SRP coefficient of Ajisai, CSR adopted a value of 1.051, which lies within the uncertainty range of the estimate in this study. Consequently, the SRP coefficients were fixed to the mean values from Table 5.1 for the generation of all subsequent solutions.

Table 5.2 Estimated global parameters and their a priori standard deviations

Parameter	Spacing	Uncertainty
Station coordinates	Weekly	1 m
Pole coordinates	Daily	35 mas
Excess length of day	Daily	3 ms
Range biases for selected stations	Weekly	1 m

In contrast to the minimally constrained solutions described in Chapter 4, a priori station coordinates were assigned large uncertainties of 1 m to generate loosely constrained solutions akin to those derived by ILRS ACs. Loose constraints tie the estimated frame to the a priori frame, but preserve the geometry of the network polyhedron. The a priori pole coordinates and excess LOD values published by IERS were also attached large standard deviations (see Table 5.2). Range biases were estimated starting from a priori values of zero only for selected stations listed in the ILRS data handling file.[2] All other mandatory corrections documented in the ILRS data handling file were applied at the pre-processing stage.

5.4 Geocentre motion time series

After processing the data and storing the weekly analysis results in the SINEX format, geocentre coordinates were estimated using the network shift approach without a scale parameter. The next four sections are dedicated to the analysis of the geocentre motion time series obtained for each data combination. The implications of estimating a scale parameter for the geocentre coordinates are also investigated.

5.4.1 LAGEOS-1 and 2 solution

Most SLR-derived estimates of geocentre motion are based on LAGEOS-1 and 2 data, as the orbits of these MEOs can be modelled with high accuracy and are adequate for the establishment of reliable reference frames. In the LAGEOS–only solution, the mean RMS of observation residuals is 8.6 mm for LAGEOS-1 and 8.2 mm for LAGEOS-2 (Figure 5.4). These values are similar to those obtained by *Zelensky et al.* (2014) over the 19.5-year span

[1] ftp://cddis.gsfc.nasa.gov/slr/products/ac/csr.dsc
[2] http://ilrs.dgfi.tum.de/fileadmin/data_handling/ILRS_Data_Handling_File.snx

from 1993.0 to 2012.5 using the GEODYN II Orbit Determination and Geodetic Parameter Estimation Program (*Pavlis et al.*, 2013) and different analysis settings, including the use of standard CoM corrections for both satellites and the modelling of non-tidal atmospheric pressure loading effects. The negative trend in the RMS up to around 1997 is attributable to improvements in data quality, whereas the positive trend from 1997 to 2005 is an effect of the gradual increase in the number of NPs (see Figure 5.3).

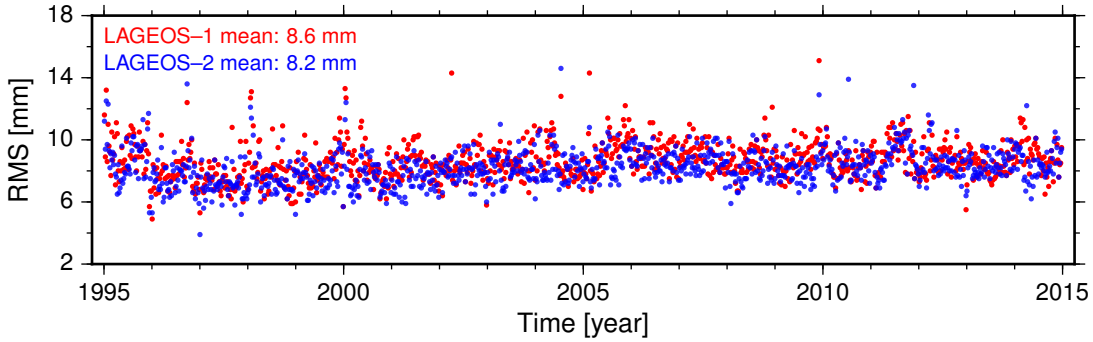

Figure 5.4 Weekly RMS of observation residuals for LAGEOS-1 (*red circles*) and LAGEOS-2 (*blue circles*) in the LAGEOS–only solution

Figure 5.5 displays both the raw geocentre coordinates obtained from the LAGEOS-1 and 2 solution and the smoothed coordinates using a sixth-order Butterworth low-pass filter with a cut-off frequency of 3 cpy, designed to attenuate high-frequency noise. The Butterworth filter (*Butterworth*, 1930) was preferred over the commonly employed moving average (or boxcar) filter due to its maximally flat frequency response, that is, without ripples that cause undesired oscillations or *ringing* within the filtered signal. The chosen filter order represents a trade-off between a sharp frequency cut-off attainable for high orders and lower ringing. A regular seasonal variation with larger oscillations in the years preceding 2000 is discernible in the time series of the equatorial components. In line with the findings of previous studies (e.g. *Collilieux et al.*, 2009; *Cheng et al.*, 2013a; *Luceri et al.*, 2015), the Z component is considerably noisier and exhibits approximately 50% larger variability than the X and Y coordinates, as quantified via the RMS of the series.

The ILRSA solution supplied for the computation of ITRF2014 (*Luceri et al.*, 2015) contains two distinctive features, namely a previously observed trend reversal around 1997 in the axial geocentre coordinate (*Altamimi et al.*, 2007, 2011) and an offset in the Y geocentre coordinate occurring in the second half of 2010. The latter feature has yet to be explained, but may be a modelling artefact as it is absent from both the LAGEOS-1 and 2 solution derived in this study and related solutions computed by CSR with larger sampling periods.[3] Figure 5.5 shows an apparent trend reversal in the Z component potentially induced by the 18.6-year tide (see, e.g., *Cheng et al.*, 2013b for a discussion of the 18.6-year variation in the Earth's oblateness coefficient J_2), but the pre-1997 time span of only two years is insufficient to make a credible inference of long-period variations.

[3] ftp://ftp.csr.utexas.edu/pub/slr/geocenter/

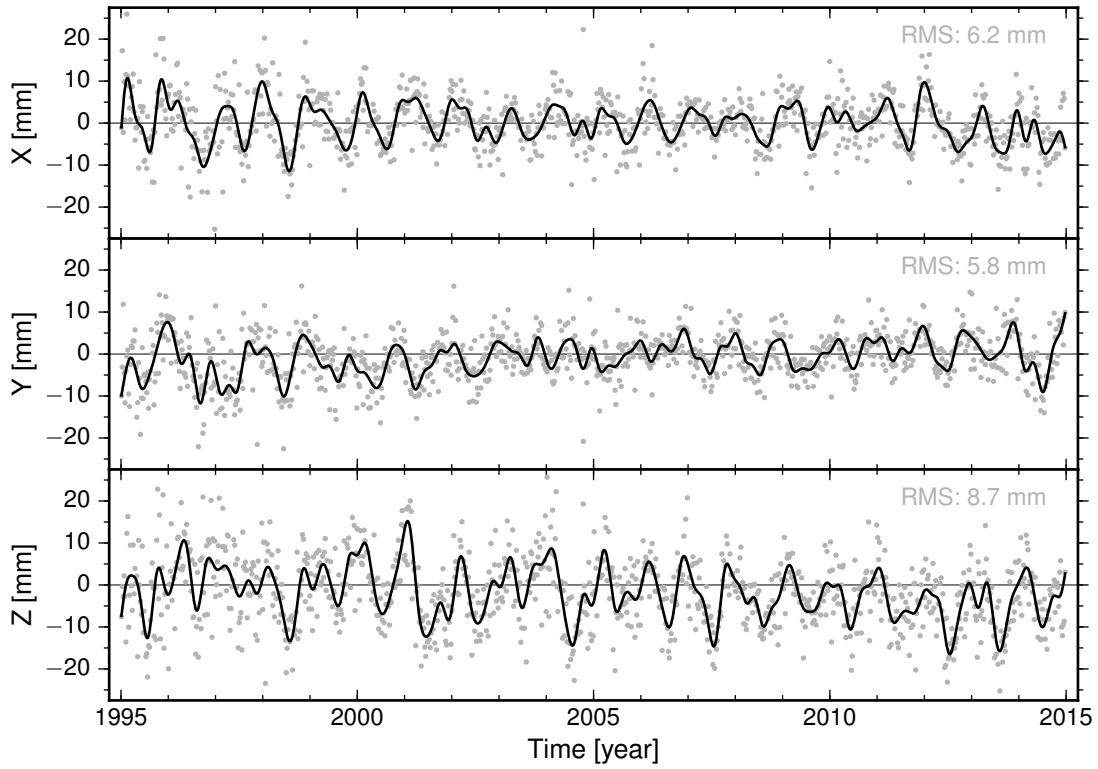

Figure 5.5 Geocentre coordinates obtained via the network shift approach from LAGEOS-1 and 2 data (*grey circles*) and smoothed geocentre coordinates using a sixth-order Butterworth low-pass filter with a cut-off frequency of 3 cpy (*black curve*)

Considerable inter-annual variability is only visible in the Z geocentre vector component, which displays a pronounced negative linear rate post-1997, also found in CSR solutions.

Spectral analysis

The LAGEOS-derived geocentre motion time series were detrended and analysed in the frequency domain using the Lomb–Scargle method (*Lomb*, 1976; *Scargle*, 1982). Common to the three amplitude spectra shown in Figure 5.6 are the sharp peaks at 1 cpy that confirm the presence of seasonality, as identified in Figure 5.5. Annual cycles are associated with seasonal mass transport between opposite Earth hemispheres and are also present in the spectra of SLR and GPS station position estimates (e.g. *Ray et al.*, 2008). A semi-annual cycle is only detectable in the Z component and to a lesser extent in the X component. Semi-annual variations are either absent from the Y geocentre vector component or engulfed in noise. The Z geocentre coordinate shows evidence of considerable inter-annual variability, but most of the power in all components is at low frequencies.

Overlaid on the amplitude spectrum of the Z geocentre coordinate in Figure 5.6 are vertical dashed lines at some fractions and integer multiples of the draconitic frequencies of LAGEOS-1 (∼0.65 cpy) and LAGEOS-2 (∼1.64 cpy). The spectral peaks detectable at such frequencies or in their proximity are likely to be artefacts caused by SRP modelling deficiencies. In particular, the sinusoidal component with a frequency of 3.27 cpy and an approximate amplitude of 0.91 mm may arise through the superposition of the fifth

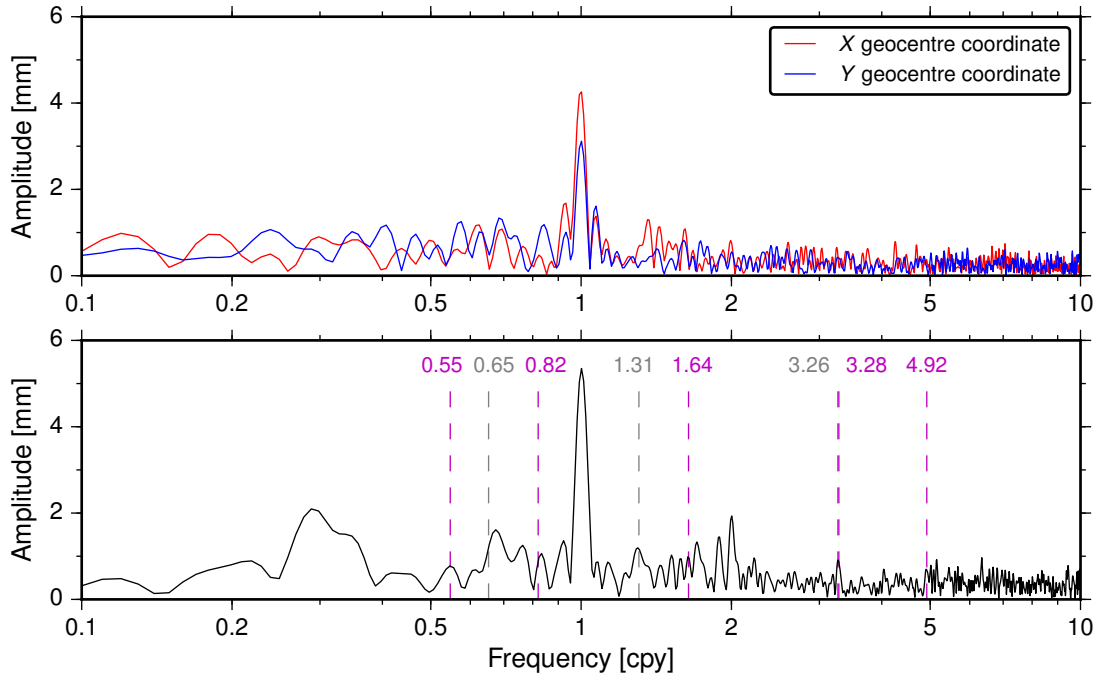

Figure 5.6 Amplitude spectra of the detrended X and Y geocentre coordinates (*top*) and of the detrended Z geocentre coordinate (*bottom*) obtained using the Lomb–Scargle method for the LAGEOS-1 and 2 solution. The vertical dashed lines mark fractions and integer multiples of the LAGEOS-1 (*grey*) and LAGEOS-2 (*magenta*) draconitic frequencies

draconitic harmonic of LAGEOS-1 (∼3.26 cpy) and the second draconitic harmonic of LAGEOS-2 (∼3.28 cpy). A similar component with a frequency of 3.29 cpy was detected by *Lavallée et al.* (2010) in the spectrum of SLR-derived J_2 series and regarded as a technique-specific error of unexplained origin.

The LAGEOS-1 and 2 draconitic frequencies generate a beat with a frequency of 0.99 cpy or a period of 369.6 days and variations at 2.29 cpy or every 159.3 days. The frequency separation of 0.01 cpy between the beat and the annual sinusoidal components is less than the frequency resolution of ∼0.05 cpy, equal to the reciprocal of the time series length. Consequently, the beat and annual sinusoids cannot be well separated and are likely to alias giving rise to broadband annual peaks merely discernible in Figure 5.6.

Model identification

To date, the standard practice in the analysis of geocentre motion time series has been to fit a functional model containing a bias at a reference epoch, a linear term and periodic terms of annual and occasionally semi-annual frequencies. In addition, the residuals $\hat{\mathbf{v}}$ obtained by subtracting the fitted model from the observations using (5.15) were assumed purely random (i.e. uncorrelated and identically distributed). This assumption has yet to be tested and attempts to find optimal functional and stochastic models for SLR-derived geocentre motion time series are lacking. Hereinafter, functional models containing a bias, a linear trend plus annual and semi-annual components will be referred to as linear models, whereas models that additionally incorporate an acceleration will be designated as

quadratic. Unless otherwise specified, annual and semi-annual components are considered included when referring to linear and quadratic functional models.

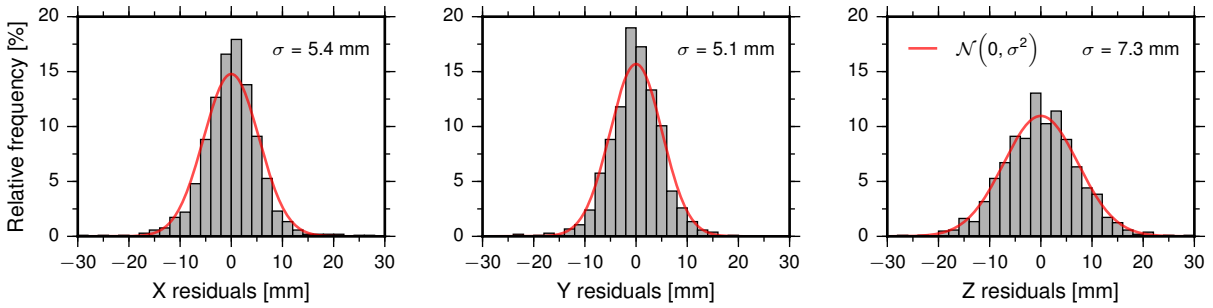

Figure 5.7 Histograms of the geocentre coordinate residuals from the LAGEOS-1 and 2 solution. Superimposed are normal distributions with zero mean and the variances of the residuals

To check for temporal correlations in the LAGEOS-1 and 2 geocentre motion time series, a linear model was first fitted by ordinary least squares using a white noise stochastic model. The distributions of the residuals along the three axes are approximately centred about zero and resemble normal distributions with the standard deviations of the residuals along each axes (Figure 5.7), characteristics which may indicate stationarity. The Z geocentre coordinate residuals have a larger scatter and therefore a flatter distribution with two peaks. Most of the residuals are lower than 20 mm in absolute value.

A useful graphical tool for assessing the randomness of residuals is the *correlogram*, also known as the *autocorrelation plot*. The correlogram is a plot of the sample autocorrelation coefficients at varying time lags that can aid the process of choosing the most appropriate model for a given time series. Autocorrelation coefficients are dimensionless measures of correlations between observations separated in time by a varying interval k called *lag* and take values between -1 and 1. The autocorrelation coefficient at lag $k = 0$ is unity. When testing for randomness, confidence intervals for the sample autocorrelation coefficients r_k ($k = 1, 2, \ldots, m;\ m \ll n$) can be obtained as (e.g. *Brockwell and Davis*, 2002)

$$-\frac{z_{1-\alpha/2}}{\sqrt{n}} \leq r_k \leq \frac{z_{1-\alpha/2}}{\sqrt{n}} \tag{5.19}$$

with $100\,(1-\alpha)\%$ confidence, where $z_{1-\alpha/2}$ is the normal random variable of the standard normal distribution $\mathcal{N}(0,1)$ for the significance level α and n is the sample size. Using $\alpha = 0.05$, the autocorrelation coefficients lying outside the bounds $\pm 1.96/\sqrt{n}$ are significantly different from zero at 95% level of confidence. White noise is characterised by a flat correlogram with all autocorrelation coefficients at non-zero lags approximately equal to zero (*Chatfield*, 2003), but spurious non-zero autocorrelation coefficients can occasionally be present in the correlogram of random time series.

Figure 5.8 shows the correlograms of the X, Y and Z geocentre coordinate residuals from the LAGEOS-1 and 2 solution. Any residual larger in absolute value than the sum of the median and three times the interquartile range was regarded an outlier and discarded

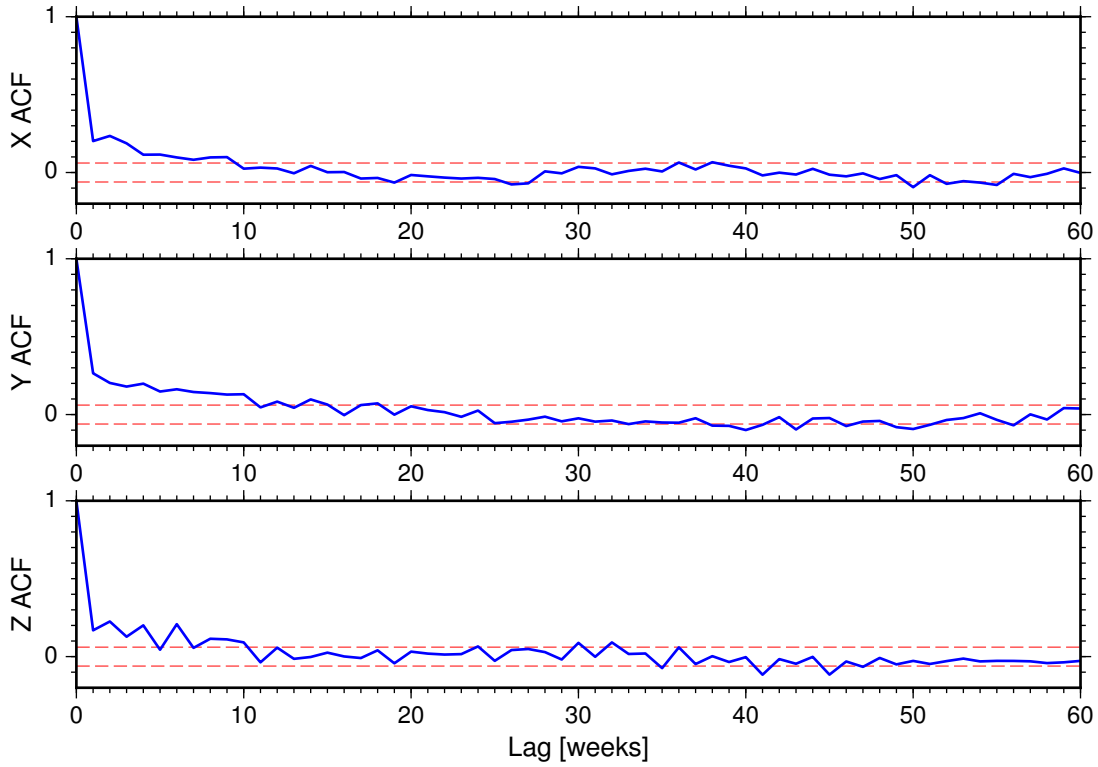

Figure 5.8 Correlograms of the geocentre coordinate residuals from the LAGEOS-1 and 2 solution. The *red dashed lines* represent 95% confidence bands

prior to the computation of autocorrelation coefficients. For each of the three Cartesian components, the sample autocorrelation function (ACF) exhibits a rapid exponential decay, characteristic of an autoregressive (AR) process rather than a purely random process. With few exceptions, the autocorrelation coefficients up to lag 10 are significant for each component. Other apparently significant values are probably fabricated since they occur at arbitrary lags. This implies that the residuals exhibit short-term temporal correlations and a white noise stochastic models is unlikely to be the best fit for the LAGEOS-1 and 2 series of geocentre coordinates. Ignoring temporal correlations may lead to an underestimation of the model parameter uncertainties.

With the advent of software such as CATS and Hector, a variety of noise models can be effortlessly fitted to the residuals. Therefore, the main challenge consists in the identification of the optimal model rather than its estimation. The AIC and BIC model-selection statistics given by (5.18) can help in choosing between a number of competing models by identifying the most parsimonious model (i.e. the most explanatory model with the least amount of parameters) through the lowest AIC and BIC values, albeit disagreements between the two criteria can occur. The stochastic models considered in this study are white noise (WN), power-law (PL) noise, AR noise of order p designated as AR(p), generalised Gauss–Markov (GGM) noise and the combinations PL plus WN and AR(1) plus WN. AR processes of progressively higher order were fitted and the best explanatory AR model was chosen based on the AIC and BIC. The PSD of GGM noise emulates the flat PSD of WN at low and high frequencies and the sloping PSD of

power-law noise at intermediate frequencies (*Langbein*, 2004). The GGM noise model is therefore likely to perform similarly to the PL plus WN combination. AR($p \geq 2$) plus WN model pairs were also initially considered, but discarded due to high AIC and BIC values. Functional models only differed in the omission or inclusion of a quadratic term, whereas annual and semi-annual periodic terms were always included.

Table 5.3 Percent reductions in AIC and BIC values computed for each functional-stochastic model with respect to a linear and WN functional-stochastic model fitted to the LAGEOS-1 and 2 time series of network shift geocentre motion estimates. The largest values identify the preferred model pair for each geocentre coordinate and are italicised

Model	*X*		*Y*		*Z*	
	ΔAIC	ΔBIC	ΔAIC	ΔBIC	ΔAIC	ΔBIC
Quadratic, WN	0.090	0.090	0.023	0.023	0.026	0.026
Linear, PL	1.296	1.217	1.888	1.809	1.004	0.934
Quadratic, PL	1.310	1.231	1.891	1.812	1.012	0.942
Linear, AR(4)	1.489	1.173	1.840	1.523	1.314	1.032
Quadratic, AR(4)	1.517	1.201	1.846	1.529	*1.324*	1.042
Linear, GGM	1.294	1.136	1.893	1.735	0.999	0.859
Quadratic, GGM	1.316	1.158	1.899	1.740	1.010	0.869
Linear, PL + WN	1.289	1.131	1.884	1.725	1.039	0.898
Quadratic, PL + WN	1.297	1.139	1.886	1.727	1.045	0.904
Linear, AR(1) + WN	1.502	1.345	2.055	1.896	1.234	1.094
Quadratic, AR(1) + WN	*1.522*	*1.364*	*2.059*	*1.900*	1.244	*1.103*

Using the MLE implementation in Hector, the stochastic and functional model parameters were simultaneously solved for. For PL noise, the spectral index was estimated instead of being fixed to integer values that imply the presence of particular noise types. Table 5.3 shows the percent reductions in AIC and BIC values obtained for each model fitted to the geocentre motion time series derived using the network shift approach from the LAGEOS-1 and 2 solution. The functional-stochastic model relative to which the percent reductions are calculated is the standard linear and WN. Higher values in Table 5.3 indicate a better fit.

Despite containing an additional parameter, quadratic functional models are consistently favoured over linear models by both the AIC and BIC. Among the stochastic models, PL, PL plus WN and GGM perform comparably well, but the preferred model is AR(1) plus WN, although for the *Z* geocentre coordinate the AIC indicates a preference for AR(4). Due to the two additional stochastic parameters contained in AR(4) compared to AR(1) plus WN, the BIC favours the latter model. The linear and WN model pair almost exclusively employed in the analysis of geocentre motion time series provides the poorest fit, whereas the optimal functional-stochastic model for the LAGEOS-1 and 2 weekly series of geocentre coordinates comprises a quadratic functional model and the AR(1) plus WN stochastic model. This model is preferred by all three geocentre vector components.

Model estimation and validation

The AR(1) plus WN stochastic model may be expressed as

$$\varepsilon_i = \alpha\, \varepsilon_{i-1} + w_i, \tag{5.20}$$

where α is the AR coefficient and w_i are uncorrelated and identically distributed random variables with zero mean and variance $a_w^2 = r^2 \cos^2 \varphi$. The scale factor r and the angle φ that determines the fractions of AR noise and WN were defined in Section 5.2.2. Aside from the functional model quantities, the two stochastic parameters required to be determined by MLE are φ and α. Outlying data points were removed from the time series prior to the estimation of model parameters by fitting a linear model and discarding residuals larger in absolute value than the median plus three times the interquartile range, as described before.

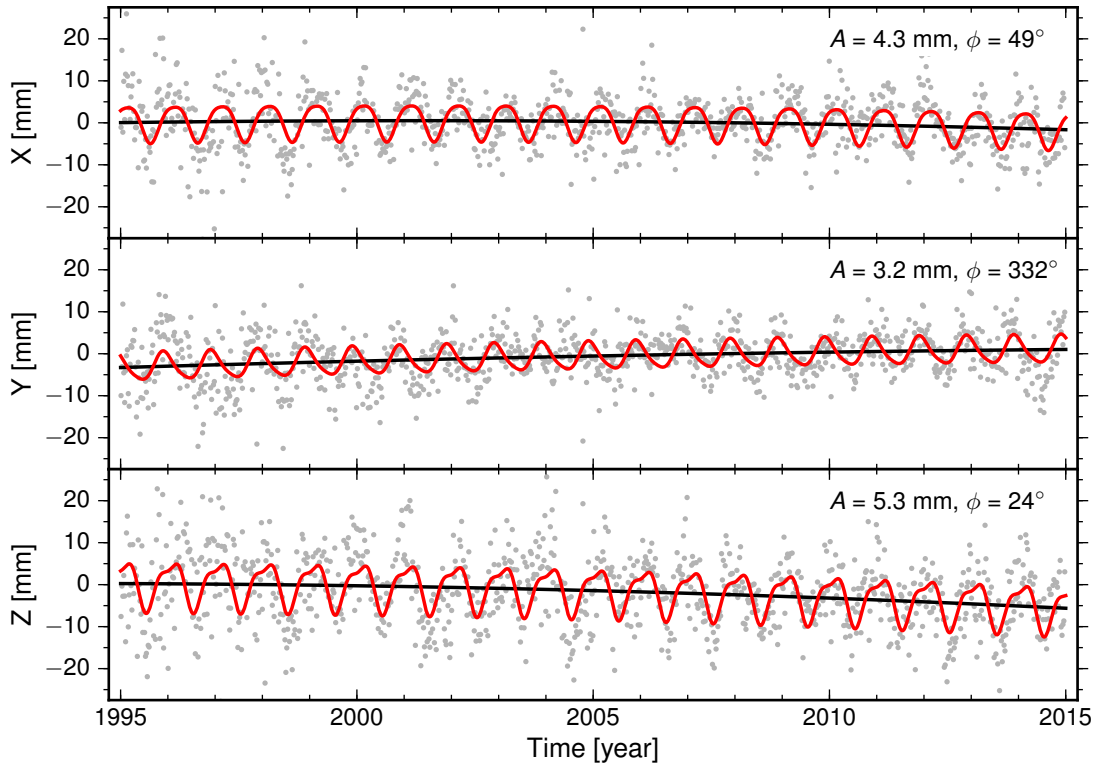

Figure 5.9 Quadratic (*black curve*) and quadratic plus annual and semi-annual (*red curve*) fits to the geocentre motion time series derived from LAGEOS-1 and 2 data. The annual amplitude A and annual phase ϕ are defined according to the convention $A\cos[2\pi(t - t_0) - \phi]$, where t is time expressed in decimal years and $t_0 = \texttt{int}(t)$ represents 1 January of a particular year

The quadratic, annual and semi-annual components of the model fitted to the LAGEOS-1 and 2 geocentre motion time series are shown in Figure 5.9. The Z component exhibits the largest annual oscillations which peak in January and a prominent negative trend. Since they are expected to reflect seasonal mass transport, annual amplitudes and phases are of particular interest and are the most frequently used parameters to compare geocentre motion models. The linear trends and the accelerations along the three Cartesian

axes have received less attention for reasons that will be discussed in Section 5.6.2. A comparison of the annual amplitudes and phases determined in this study with other recent estimates will be undertaken in *Chapter 6*.

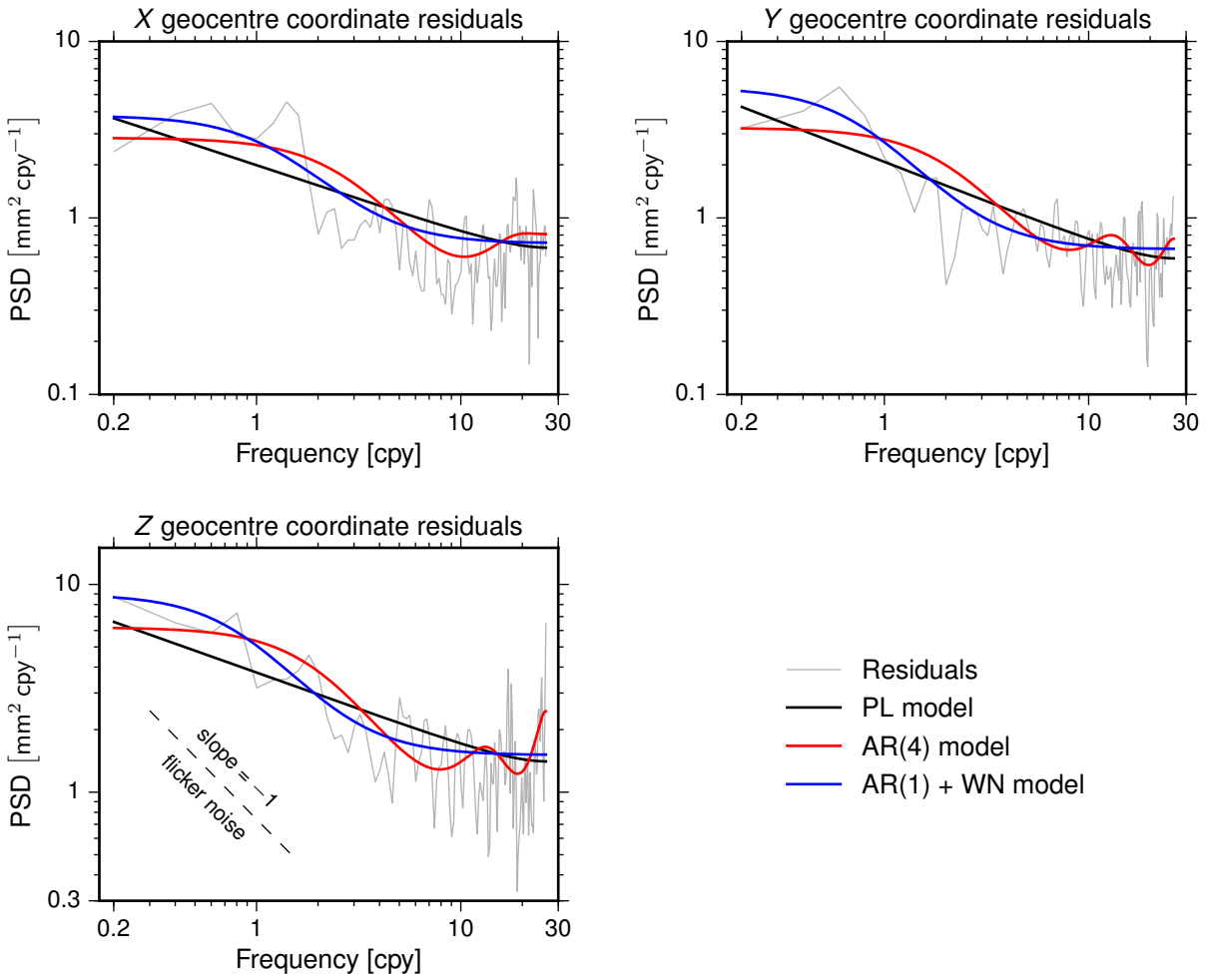

Figure 5.10 Power spectra of the geocentre coordinate residuals obtained from the LAGEOS-1 and 2 solution and power spectra of three best-fit noise models. The *black dashed line* with a slope of −1 illustrates the spectral behaviour of flicker noise

To confirm that the chosen functional-stochastic model adequately describes the data, the PSDs of the geocentre coordinate residuals are plotted in Figure 5.10, along with the PSDs of three noise models, including AR(1) plus WN. The one-sided power spectra of the geocentre coordinates were obtained using the method of *Welch* (1967) with seven segments and 50% overlap between adjacent segments. The PSDs clearly deviate from the constant PSD of WN, particularly at low frequencies. Nevertheless, the slopes of the PSDs are less pronounced than the slope of flicker noise, which suggests that the practice of fixing the spectral index to −1, as exercised by *Argus* (2012), should be avoided despite the additional computational effort with software such as CATS.

Analysing weekly translation time series of the SLR input solution to ITRF2008 with respect to ITRF2008, *Argus* (2012) adopted a flicker noise plus WN stochastic model to determine the linear trend uncertainty using CATS, quoting evidence from previous stud-

ies on noise in GPS station position estimates. However, *Ray et al.* (2008) demonstrated the predominance of WN in SLR station position estimates, particularly at high frequencies in the radial component and across the entire power spectra in the east and north components. In this study, the estimated spectral indices using a PL plus WN model are −0.58, −0.68 and −0.74 for the X, Y and Z geocentre coordinates, respectively, markedly different from the −1 spectral index of flicker noise. In addition, the AIC and BIC indicate that PL noise with the estimated spectral indices −0.38, −0.45 and −0.35 for the three geocentre coordinates better describes the stochastic characteristics of the LAGEOS-1 and 2 geocentre motion time series, which are similar to those analysed by *Argus* (2012). The effects of adopting an inadequate stochastic model on the rate uncertainty will be discussed in Section 5.6.2.

Effects of estimating a scale parameter

Several authors advocated the omission of the scale parameter when estimating geocentre motion using the network shift approach (*Tregoning and van Dam*, 2005; *Lavallée et al.*, 2006; *Collilieux et al.*, 2012; *Wu et al.*, 2015). Since the terrestrial scale is physically defined by the geocentric gravitational constant and the speed of light in a vacuum, there is insufficient substantiation for adjusting the scale when the geocentre coordinates are of primary interest rather than the assessment of biases between reference frames. For a dense GNSS network, adjusting the scale has small effects on the translation estimates (*Collilieux et al.*, 2012), which may not be the case for the much sparser SLR network.

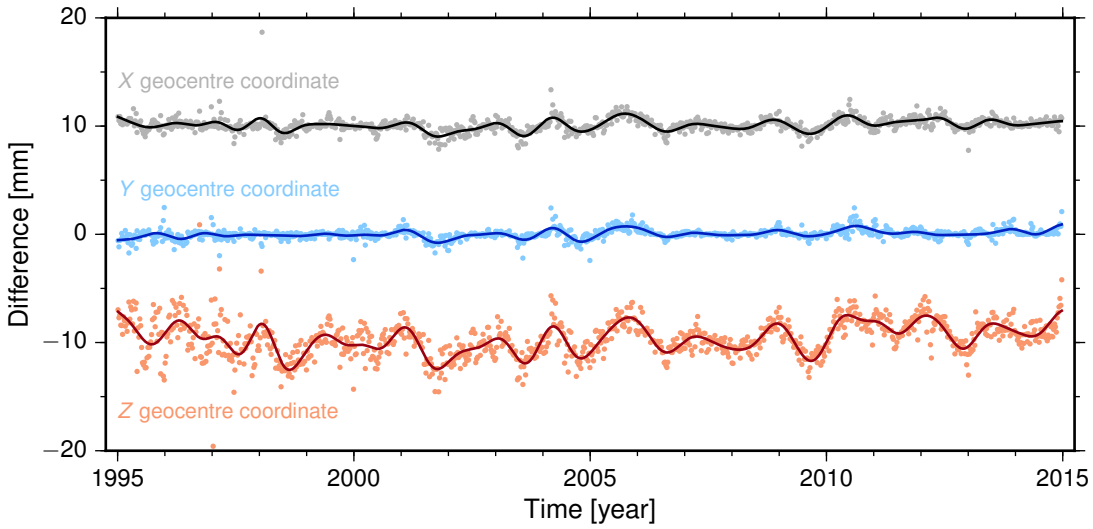

Figure 5.11 Differences between the geocentre coordinates estimated without and alongside a scale parameter from the LAGEOS-1 and 2 solution using the network shift approach. X and Z values are shifted by +10 mm and −10 mm, respectively. The solid curves were obtained using a sixth-order Butterworth low-pass filter with a cut-off frequency of 1.25 cpy

Figure 5.11 illustrates the differences between the geocentre coordinates derived from the LAGEOS-1 and 2 solution via the network shift approach without and with a scale factor. The RMS values of the differences are 0.6, 0.5 and 1.8 mm for the X, Y and Z axes,

respectively. Apart from exhibiting the largest long-term variability, the differences in the Z direction contain an annual cycle with an amplitude of approximately 0.5 mm, largely absent from both of the equatorial components. This implies that the Z translation is correlated with the scale parameter, which can partly absorb the annual variation in the Z geocentre coordinate, potentially due to the unbalanced SLR network. Moreover, the amplitude spectrum of the Z differences contains a sinusoidal component with a frequency of ∼0.65 cpy, roughly equal to the draconitic frequency of LAGEOS-1, and an approximate amplitude of 1 mm. This is the largest spectral peak and is also present in the spectra of the X and Y differences, but has considerably lower amplitudes.

Collilieux et al. (2009) opted for the estimation of the scale parameter, arguing that the translation estimates are not altered to a level that justifies the omission of the scale parameter. However, omitting the scale factor caused an increase of 1.4 mm in the annual amplitude of the Z geocentre coordinate and an improved agreement in both annual amplitude and phase with respect to independent estimates. In this study, the LAGEOS-1 and 2 geocentre motion time series obtained by adjusting the scale prefer the same noise model as when the scale parameter is omitted, namely AR(1) plus WN. Additionally, the Z annual amplitude decreases by only 0.3 mm, but the artefactual spectral peak at 0.65 cpy is considerably amplified. It thus appears reasonable to conclude that the estimation of a scale parameter may lead to the aliasing of SLR-specific errors in the translation estimates. All other solutions presented in this chapter were obtained without scale adjustments.

5.4.2 LAGEOS–Etalon combined solution

The LAGEOS–Etalon solution spans the period 2003.0–2015.0 since insufficient Etalon observations were available in the years preceding 2003 to complement LAGEOS-1 and 2 weekly data. The mean orbital fits are 12.3 mm for Etalon-1 and 12 mm for Etalon-2. Over the common time span of the LAGEOS–only and LAGEOS–Etalon geocentre motion time series, the latter exhibit marginally lower scatter in the Y and Z components. The RMS values of the differences between the time series are 1, 1.2 and 1.5 mm for the X, Y and Z geocentre coordinates, respectively. Visual inspection of the correlogram and the amplitude spectra of the differences revealed that they are purely random and lack seasonal components of geophysical interest. Despite the potentially insignificant contribution of Etalon data, an analysis of the LAGEOS–Etalon geocentre motion time series was performed since they span the least noisy period of the LAGEOS–derived series illustrated in Figure 5.5. However, Etalon data will be neglected throughout the rest of the chapter.

Similar features to those in Figure 5.6 were detected in the amplitude spectra of the detrended LAGEOS–Etalon geocentre motion time series. The main discrepancies are smaller amplitudes of the annual sinusoidal components and typically more pronounced aliasing of LAGEOS-1 and 2 draconitic errors, particularly into the Z geocentre coordinate. These differences arise due to the shorter length of the series (leading to lower

frequency resolution and more broadband spectral peaks) rather than the addition of Etalon data.

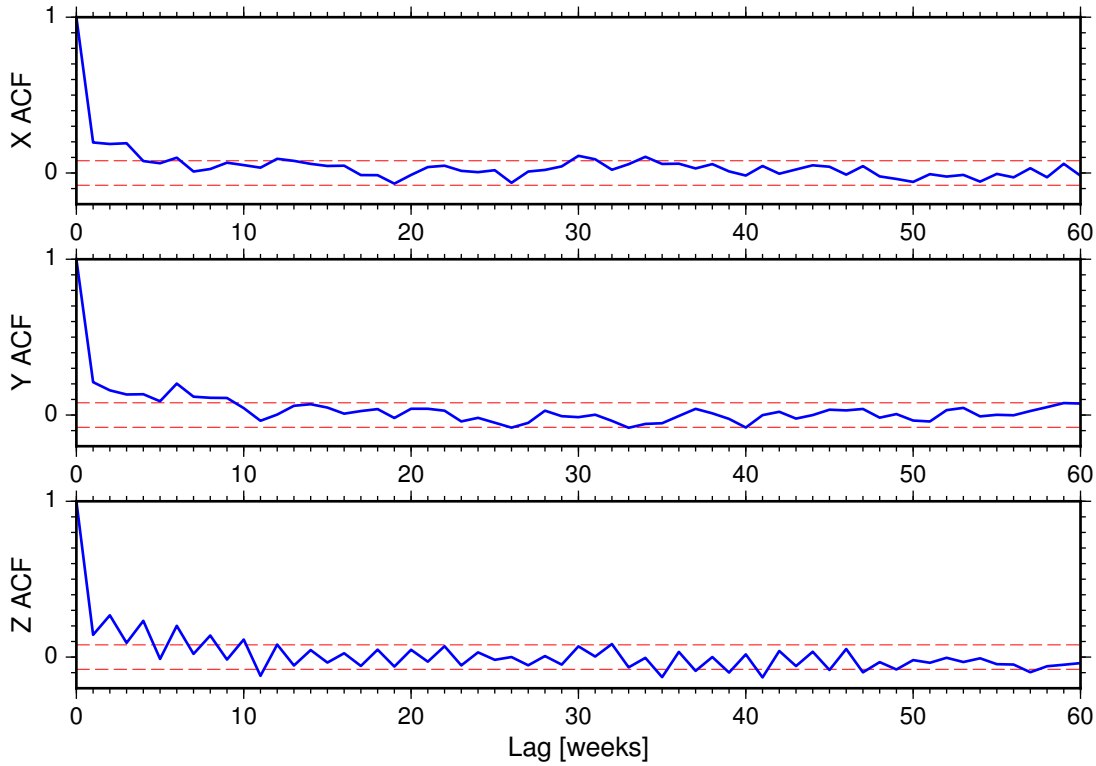

Figure 5.12 Correlograms of the geocentre coordinate residuals from the LAGEOS–Etalon solution. The *red dashed lines* represent 95% confidence bands

Short-term serial correlations are present in the geocentre coordinate residuals, as illustrated by the correlograms in Figure 5.12. Additionally, an alternating pattern can be distinguished in the correlogram of the Z geocentre coordinate residuals. This alternation of the autocorrelation coefficients is due to successive residuals lying on opposite sides of the mean value. The Y component displays the largest correlations, but all components exhibit less correlation than in the longer LAGEOS–only solution (cf. Figure 5.12 and Figure 5.8).

Similar to the LAGEOS–only solution, quadratic functional models are always preferred, irrespective of the noise model. For the equatorial geocentre coordinates, the AIC and BIC disagree on the preferred stochastic model. The AIC indicated a preference for AR(1) plus WN, whereas PL is the best explanatory stochastic model based on the BIC. Since the BIC is the model-selection statistic favoured in this study, PL is the chosen stochastic model for the equatorial geocentre coordinates. For the Z geocentre coordinate, the optimal stochastic model indicated by both the AIC and BIC is AR(4), followed by AR(1) plus WN. Figure 5.13 depicts the quadratic, annual and semi-annual fits to the LAGEOS–Etalon geocentre motion time series. Compared to the LAGEOS–only solution (see Figure 5.9), the estimated amplitudes of the annual X, Y and Z signals are 0.5, 0.4 and 0.3 mm lower, respectively, due to the absence of the pre-2003 noisier values from the LAGEOS–Etalon series.

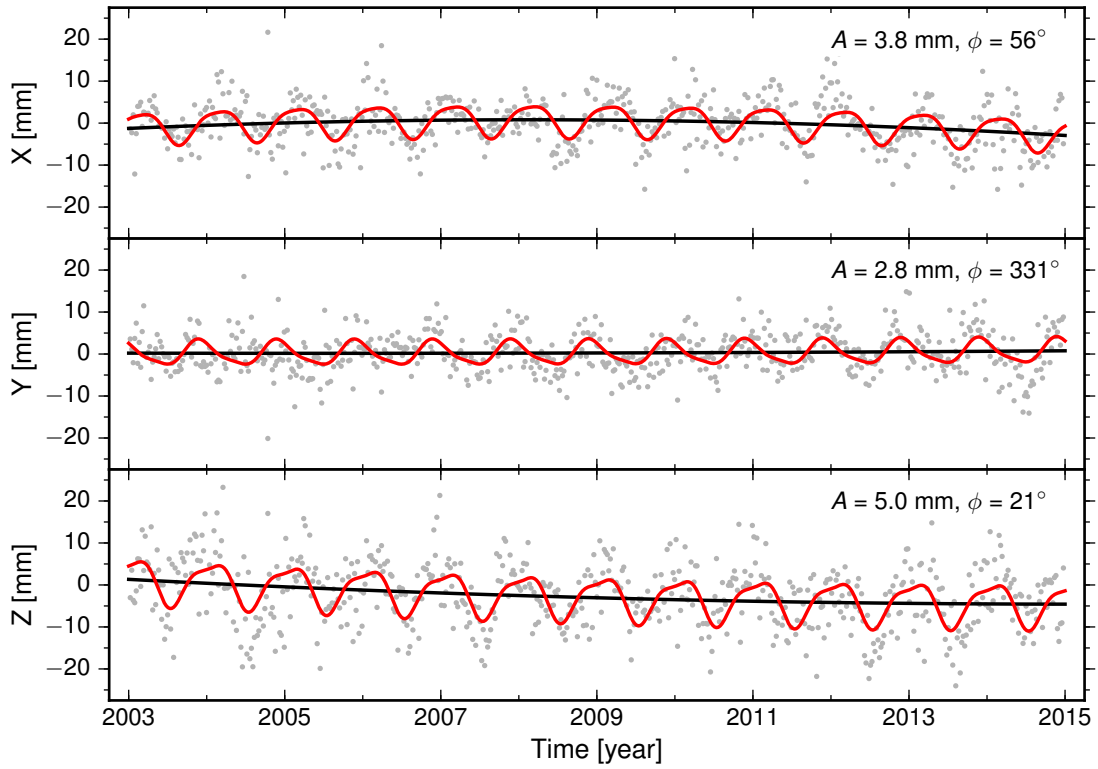

Figure 5.13 Quadratic (*black curve*) and quadratic plus annual and semi-annual (*red curve*) fits to the geocentre motion time series derived from the LAGEOS–Etalon solution. The annual amplitude A and annual phase ϕ are defined according to the convention $A\cos[2\pi(t-t_0)-\phi]$, where t is time expressed in decimal years and $t_0 = \texttt{int}(t)$ represents 1 January of a particular year

The AR(4) stochastic model preferred by the Z geocentre coordinate is given by

$$\varepsilon_i = \sum_{j=1}^{4} \alpha_j \, \varepsilon_{i-j} + w_i, \tag{5.21}$$

where α_j $(j = 1, 2, 3, 4)$ are AR coefficients and w_i is a purely random process with zero mean and variance a_w^2. To validate this model after its estimation using Hector, the following transformation can be applied to the residual estimates $\hat{v}_i$ obtained using (5.15):

$$\tilde{v}_i = \hat{v}_i - \sum_{j=1}^{4} \hat{\alpha}_j \, \hat{v}_{i-j}, \tag{5.22}$$

where $\hat{\alpha}_j$ are the maximum likelihood estimates of the AR coefficients. As shown in Figure 5.14, the correlogram of the filtered residuals $\tilde{v}_i$ of the Z geocentre coordinate is predominantly flat, with only a few statistically significant autocorrelation coefficients. This suggests that the AR(4) model is effective in modelling the temporal correlations present in the series. Consequently, the filtered residuals resemble WN and are often designated as *whitened residuals*.

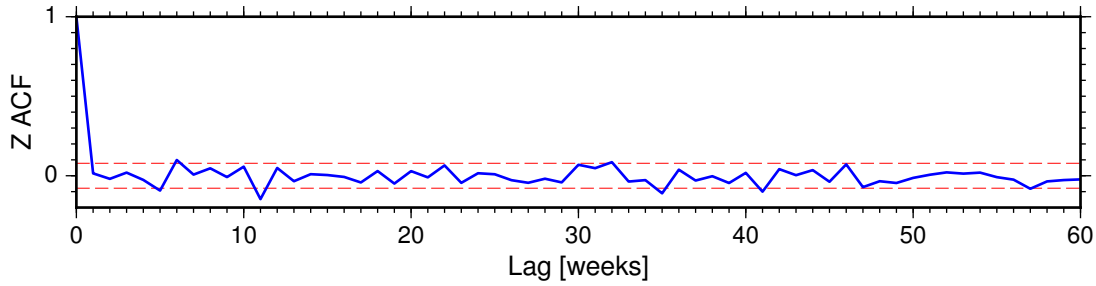

Figure 5.14 Correlogram of the Z geocentre coordinate whitened residuals from the LAGEOS–Etalon solution. The *red dashed lines* represent 95% confidence bands

5.4.3 LAGEOS–Starlette–Stella–Ajisai combined solution

Due to the larger gravitational and non-gravitational perturbations experienced by Starlette, Stella and Ajisai orbits compared to LAGEOS-1 and 2 orbits, the three LEOs have been rightfully neglected for the determination of the ITRF. The geocentre coordinates are, however, proportional to the longest-wavelength harmonics of the gravity field and incorporating LEO observations alongside LAGEOS-1 and 2 data can theoretically benefit the determination of geocentre motion if orbital errors are sufficiently reduced, as demonstrated in Chapter 4. This section assesses the quality of geocentre motion estimates derived from the LAGEOS–Starlette–Stella–Ajisai solution spanning the period 1995.0–2015.0. The mean RMS of observation residuals is 19.6 mm for Starlette, 19.9 mm for Stella and 21.7 mm for Ajisai.

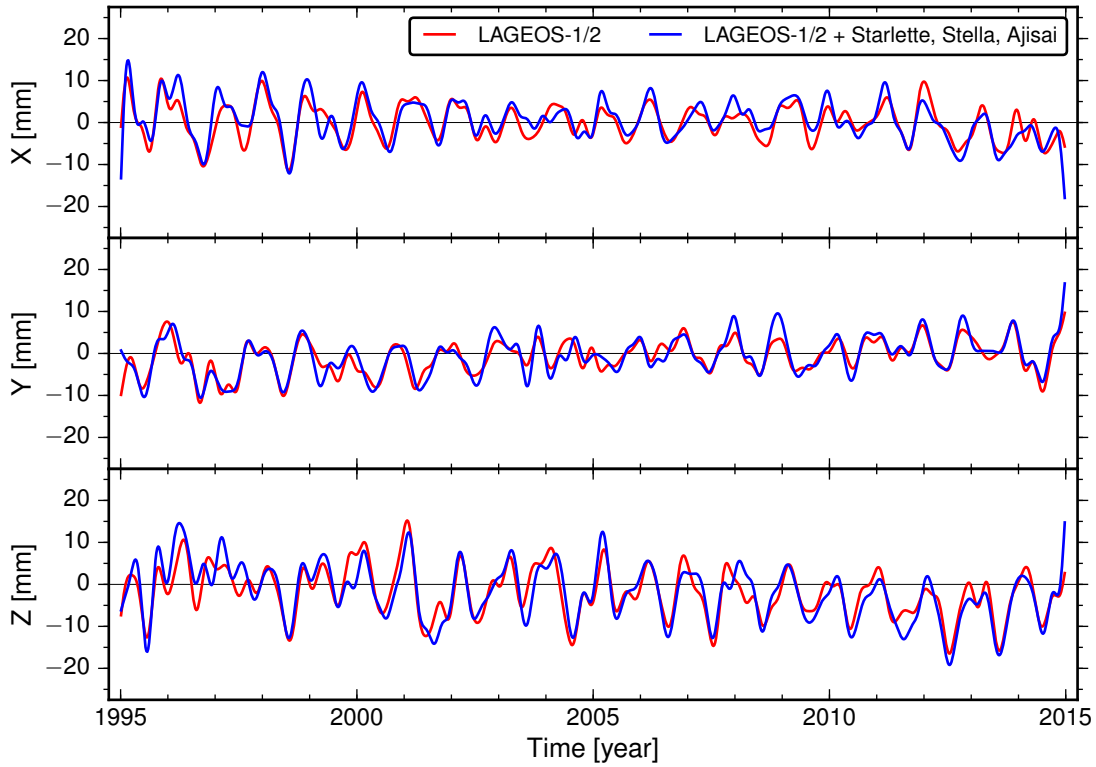

Figure 5.15 LAGEOS–only and LAGEOS–Starlette–Stella–Ajisai geocentre motion time series smoothed using a sixth-order Butterworth low-pass filter with a cut-off frequency of 3 cpy

The smoothed LAGEOS–Starlette–Stella–Ajisai geocentre motion time series are similar to the smoothed LAGEOS–only series, but appear to exhibit larger annual variability (Figure 5.15). An apparent positive offset is also discernible in the Z component between 1996 and 1998, potentially attributable to data noise. The RMS values of the raw X, Y and Z geocentre coordinates are 7.4, 6.8 and 9.5 mm, respectively, 1 mm larger on average than the scatter of LAGEOS–only series (see Figure 5.5). This is a strong indication that Starlette, Stella and Ajisai orbital errors may have aliased in the geocentre motion estimates and degraded their quality.

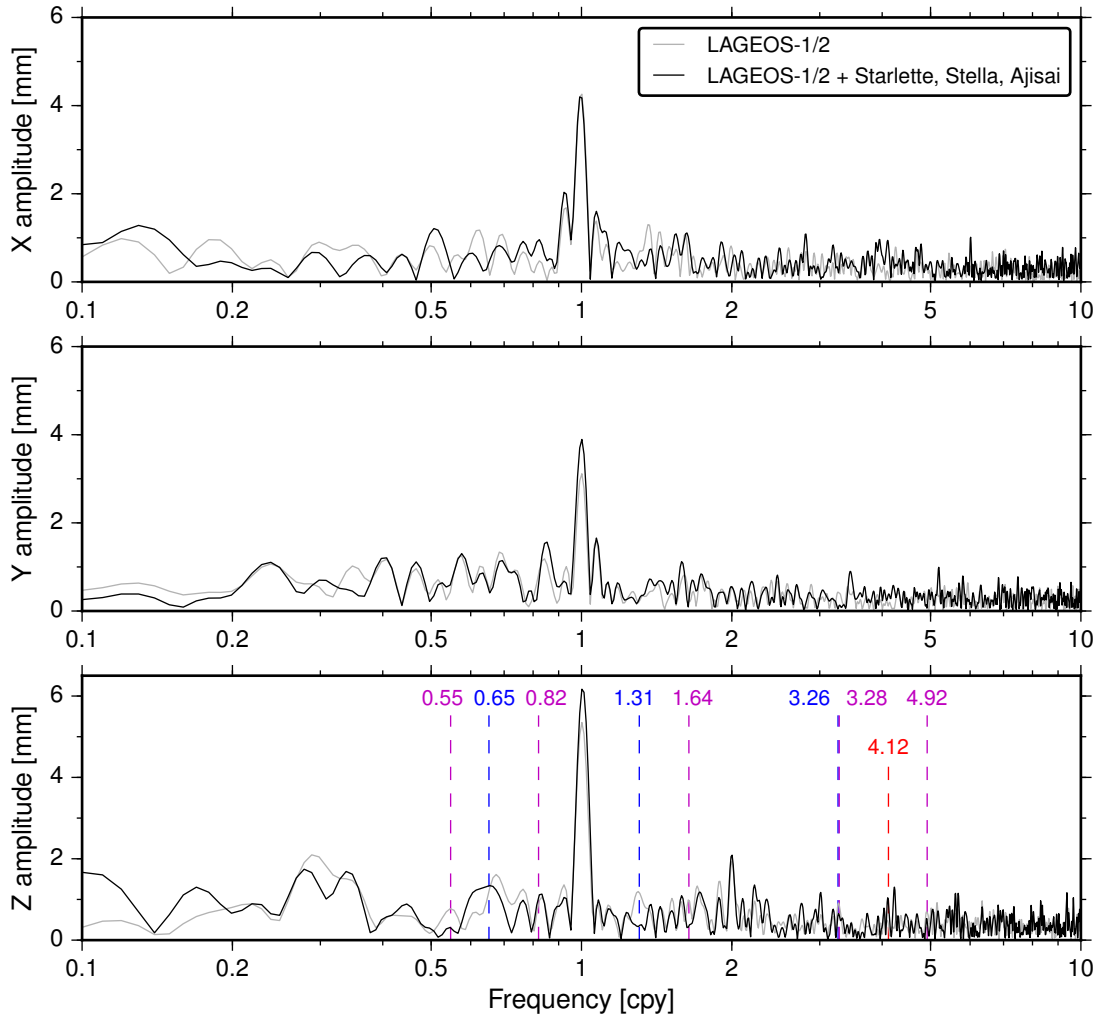

Figure 5.16 Amplitude spectra of the detrended geocentre coordinates obtained using the Lomb–Scargle method for the LAGEOS–Starlette–Stella–Ajisai solution and the LAGEOS-1 and 2 solution. The vertical dashed lines mark fractions and integer multiples of the LAGEOS-1 (*blue*), LAGEOS-2 (*magenta*) and Ajisai (*red*) draconitic frequencies

An important benefit of supplementing LAGEOS-1 and 2 data with Starlette, Stella and Ajisai observations is the reduced aliasing of LAGEOS-1 and 2 draconitic errors into the geocentre coordinates, manifested particularly through the attenuation of the spurious spectral peaks at 0.55, 1.31, 1.64 and 3.27 cpy in the amplitude spectrum of the Z geocentre coordinate (Figure 5.16). Nevertheless, spurious peaks at the draconitic frequency of Ajisai ($\sim$4.12 cpy) are discernible in the X and Z amplitude spectra, in addition to more

high-frequency noise in all components. There is insufficient evidence that Starlette draconitic errors contaminate the LAGEOS–Starlette–Stella–Ajisai geocentre motion time series, whereas due to its sun-synchronous orbit, Stella's draconitic frequency approaches zero.

To identify the optimal functional-stochastic model, a linear functional model including annual and semi-annual sinusoids was first fitted to the LAGEOS–Starlette–Stella–Ajisai geocentre motion time series assuming a WN stochastic model. The residuals from the linear model display short-term temporal dependencies akin to those in the LAGEOS–only solution (see Figure 5.8). Based on the AIC and BIC values, quadratic functional models are consistently favoured over linear models. According to the BIC, the X and Z geocentre vector components prefer a PL noise model ahead of AR(1) plus WN, which has lower AIC values and may constitute an equally good explanatory model. Both the AIC and BIC indicate that AR(1) plus WN is the optimal stochastic model for the Y component. The quadratic, annual and semi-annual fits to the LAGEOS–Starlette–Stella–Ajisai geocentre motion time series are shown in Figure 5.17.

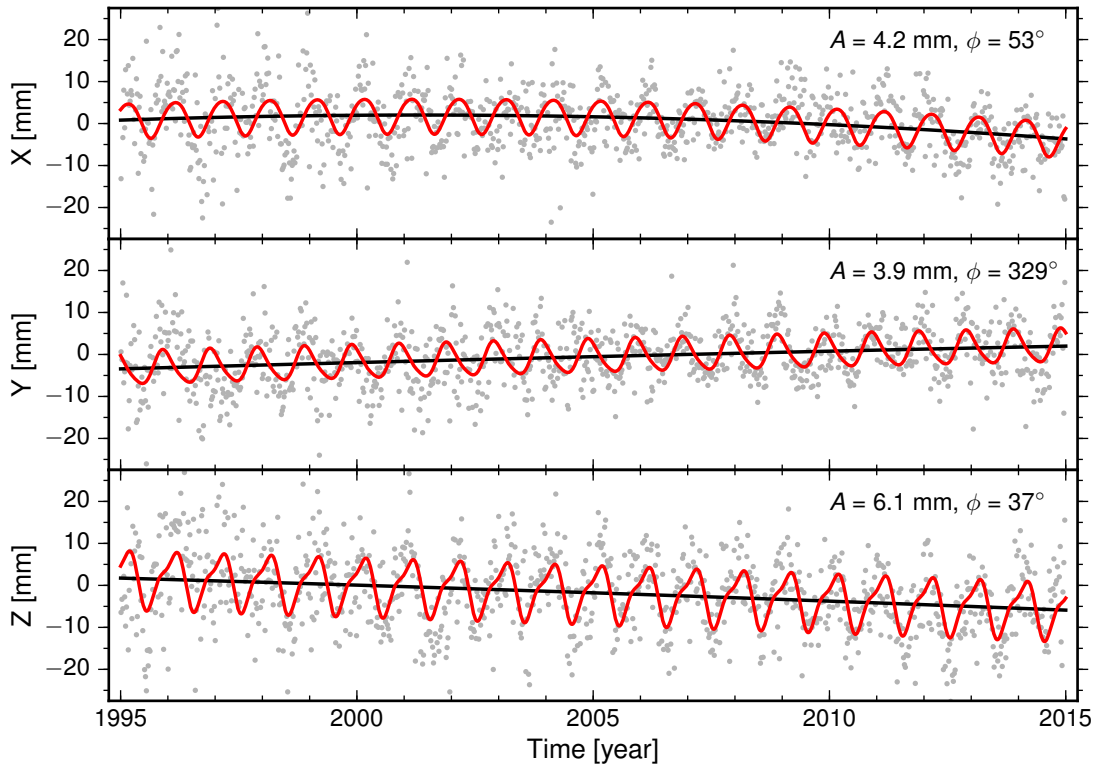

Figure 5.17 Quadratic (*black curve*) and quadratic plus annual and semi-annual (*red curve*) fits to the geocentre motion time series derived from the LAGEOS–Starlette–Stella–Ajisai solution. The annual amplitude A and annual phase ϕ are defined according to the convention $A\cos[2\pi(t - t_0) - \phi]$, where t is time expressed in decimal years and $t_0 = \texttt{int}(t)$ represents 1 January of a particular year

Figure 5.18 illustrates the PSDs of the geocentre coordinate residuals and of three of the best-fit stochastic models. There is clear evidence of additional WN at high frequencies relative to the power spectra of the LAGEOS–derived geocentre coordinate residuals

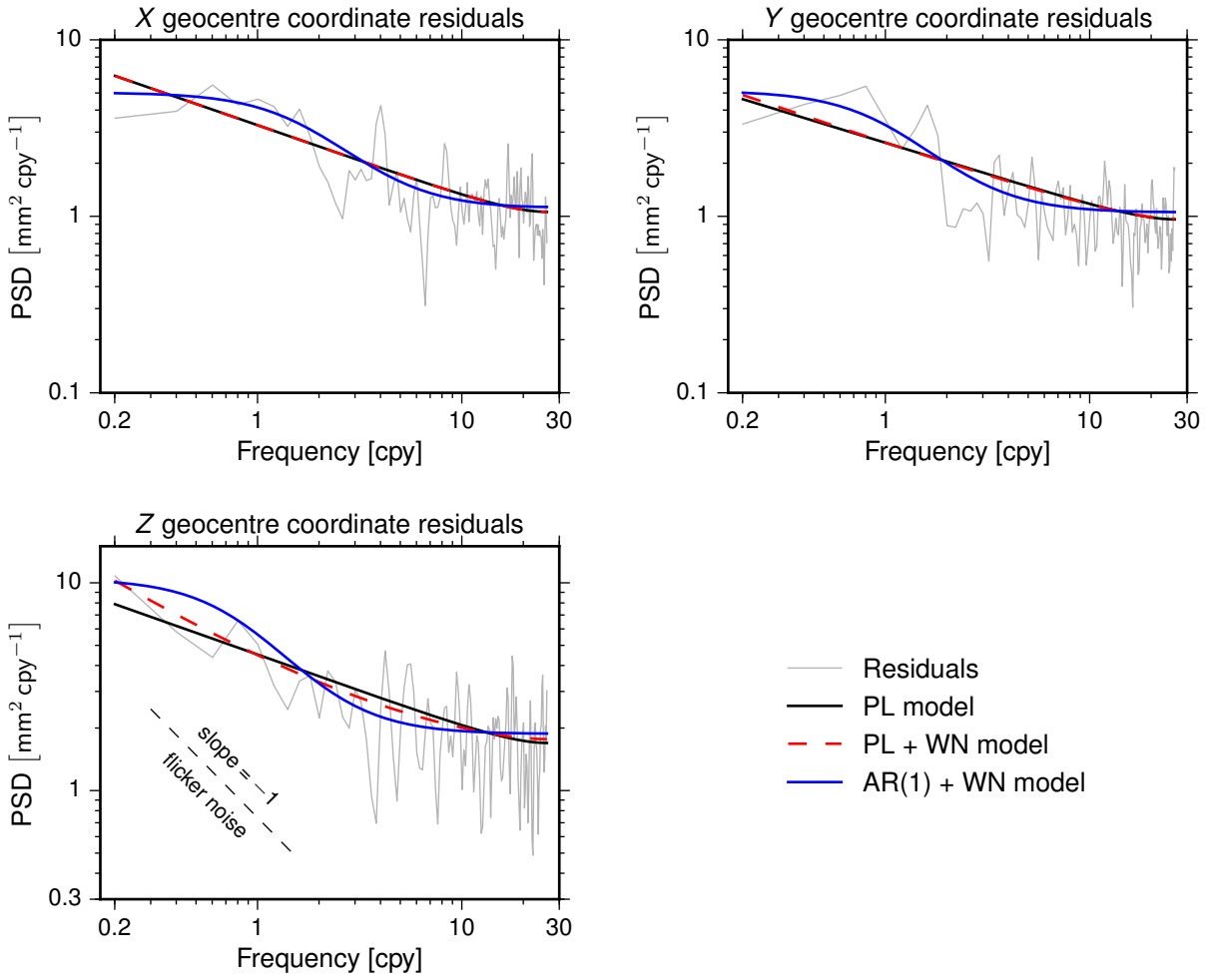

Figure 5.18 Power spectra of the geocentre coordinate residuals obtained from the LAGEOS–Starlette–Stella–Ajisai solution and power spectra of three best-fit noise models. The *black dashed line* with a slope of −1 illustrates the spectral behaviour of flicker noise

(cf. Figure 5.18 and Figure 5.10). For the equatorial geocentre coordinates, the PL and PL plus WN stochastic models perform similarly, but the former is favoured by model-selection criteria due to its lower number of parameters. The spectral index estimates using a PL noise model are −0.4, −0.35 and −0.35 for the X, Y and Z geocentre coordinates, respectively. These values are similar to those obtained for the LAGEOS-1 and 2 geocentre motion time series and again considerably different from the −1 spectral index of flicker noise.

Since time-varying gravity signals are coarsely modelled in the geopotential model employed for orbit determination, long-wavelength geopotential coefficients may also be estimated in LAGEOS–Starlette–Stella–Ajisai combinations to better account for the larger gravitational perturbations of LEO orbits. When estimating geopotential coefficients up to degree and order 3 and omitting OPR acceleration parameters for Starlette, Stella and Ajisai to mitigate collinearity problems, the orbital fits of the LEOs degrade by approximately 2.5 mm. Moreover, this parameterisation results in noisier geocentre motion time series with RMS values of 7.7, 7.3 and 9.8 mm for the X, Y and Z components, respectively. The amplitudes of the annual signals are, however, smaller by up to 0.6 mm

than in the solution without geopotential coefficients. This suggests that, when inappropriately modelled, gravity signals of degree 2 and beyond leak into the geocentre motion estimates, which should be accordingly interpreted as lumped sums of several low-degree and order geopotential coefficients.

5.4.4 LAGEOS–LARES combined solution

As demonstrated in Section 4.4.4, the simultaneous processing of LARES data and LAGEOS-1 and 2 observations promises to improve the accuracy of the geocentre location determination by a maximum of 35% with respect to standard LAGEOS–only solutions. Additionally, the very favourable design features of LARES allow the accurate modelling of its orbit in a similar manner to LAGEOS-1 and 2 orbits, without the need to explicitly model atmospheric drag. In the LAGEOS–LARES solution derived in this study, which spans 149 weeks from 2012.1 to 2015.0, the mean RMS of LARES observation residuals is 17.1 mm.

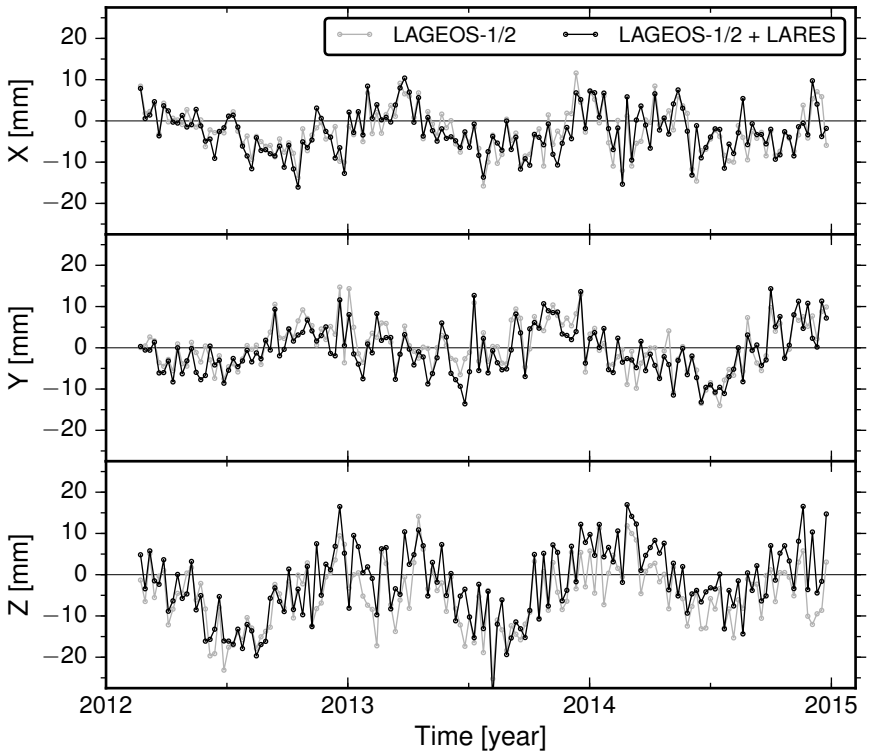

Figure 5.19 Unfiltered geocentre coordinates obtained via the network shift approach from the LAGEOS–only and LAGEOS–LARES solutions spanning the period 2012.1–2015.0

Figure 5.19 depicts the unfiltered geocentre coordinates obtained from the LAGEOS–LARES solution, overlaid on the LAGEOS–derived geocentre coordinates. The agreement between the series is striking for the equatorial geocentre coordinates, despite the marginally larger variability in the LAGEOS–LARES solution (Table 5.4). The inclusion of LARES shifts the geocentre variations along the Z axis by an average of 3 mm, thus improving the alignment of CM-centred frames with respect to the SLRF2008 over the

Table 5.4 Summary statistics of the unfiltered geocentre coordinates obtained from the LAGEOS–only and LAGEOS–LARES solutions spanning the period 2012.1–2015.0

Solution	X [mm]			Y [mm]			Z [mm]		
	Mean	SD	RMS	Mean	SD	RMS	Mean	SD	RMS
LAGEOS-1 and 2	−2.5	5.2	5.8	0.4	5.6	5.6	−5.1	7.5	9.1
LAGEOS–LARES	−2.6	5.4	6.0	−0.7	5.8	5.8	−2.1	8.8	9.0
LAGEOS–LARES 3×3	−2.6	5.2	5.8	0.6	5.6	5.6	−1.4	9.3	9.4

considered time frame. Given its improved centring about zero, the Z component also has a lower RMS in the LAGEOS–LARES solution. The differences between the LAGEOS–only and LAGEOS–LARES time series approximate WN and have RMS values of 3.2, 3.3 and 5.5 mm for the X, Y and Z geocentre coordinates, respectively.

Due to the short time span of the LAGEOS–LARES solution, only periodic terms with frequencies in the range 0.35 to 26 cpy may be resolved. Additionally, the spectral peaks discernible in Figure 5.20 are broadband due to the coarse frequency resolution of ∼0.35 cpy, which explains the crude delineation of the annual and semi-annual sinusoidal components. However, the incorporation of LARES data alongside LAGEOS-1 and 2 observations appears to diminish the aliasing of the LAGEOS-1 and 2 draconitic harmonics into the Z geocentre motion estimates, although the amplitudes of the annual signals increase for all geocentre vector components with respect to the LAGEOS–only solution. There is no evidence that LARES draconitic errors contaminate the geocentre motion estimates.

The autocorrelation structures of the LAGEOS–LARES geocentre coordinate residuals indicate that the dominant noise source is WN, since only a limited number of autocorrelation coefficients lie outside the 95% confidence limits (Figure 5.21). This fact is confirmed by the AIC and BIC, based on which the three geocentre vector components prefer a functional-stochastic model composed of a linear trend, an acceleration, annual and semi-annual terms with superimposed purely random noise. The fits to the LAGEOS–LARES time series have large uncertainties and are omitted here. As the tracking history of LARES increases, the power spectra of the LAGEOS–LARES geocentre coordinate residuals will widen at low frequencies and the preferred noise models will likely change.

A LAGEOS–LARES solution that included the recovery of geopotential coefficients up to degree and order 3 was also generated to assess the effects of this parameterisation on the geocentre motion estimates. Descriptive statistics of this solution designated as LAGEOS–LARES 3×3 are also included in Table 5.4. As already noted in Section 4.4.6, the annual variations of the Z geocentre coordinate seem to be absorbed by the estimated geopotential coefficients, particularly over the period 2013–2015, whereas the equatorial geocentre coordinates are largely unaffected. The mean RMS of the LARES observation residuals does, however, decrease in the LAGEOS–LARES 3×3 solution to 13.2 mm.

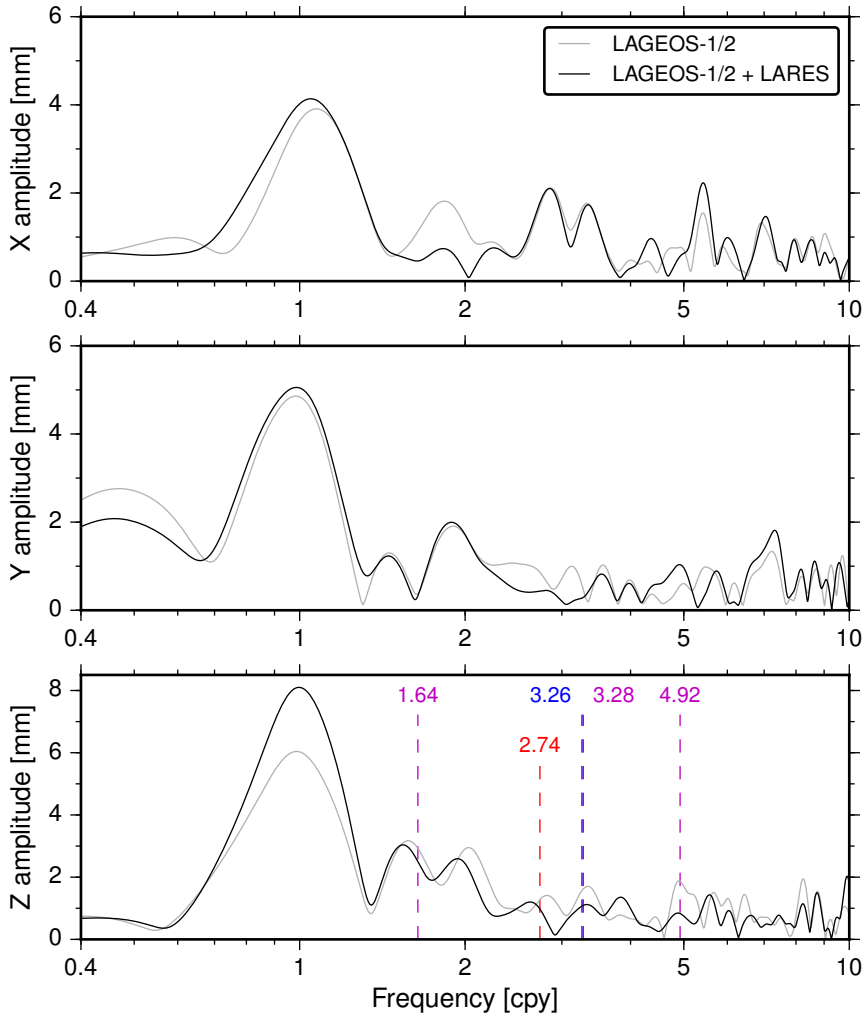

Figure 5.20 Amplitude spectra of the detrended geocentre coordinates obtained using the Lomb–Scargle method for the LAGEOS–LARES solution and the LAGEOS-1 and 2 solution. The vertical dashed lines mark integer multiples of the LAGEOS-1 (*blue*), LAGEOS-2 (*magenta*) and LARES (*red*) draconitic frequencies

5.5 Effects of network geometry changes

Due to restrictive weather conditions, inhomogeneous laser technologies and inconsistent management and operation of ground instrumentation, SLR stations intermittently acquire data of variable quality across the network. Despite being downgraded in all solutions presented in this study, low-performing stations still contributed to the determination of satellite orbits and global parameters, including the geocentre coordinates. One option to minimise the effects of low-performing stations on the geocentre motion estimates is to downweight their geocentric coordinates or ignore them altogether when computing the similarity transformation parameters. An alternative approach that involves analysing only data from a sub-network of high-performing stations shown in Figure 5.22 was adopted instead. The 31 stations forming the sub-network were selected based on ILRS system performance reports and include 22 stations with tracking histories longer

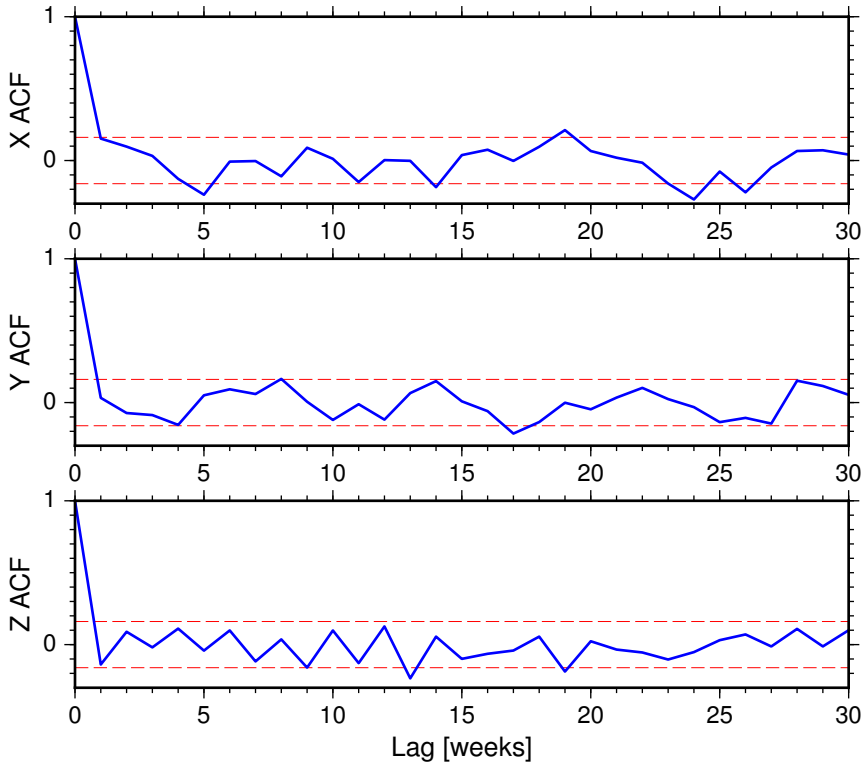

Figure 5.21 Correlograms of the geocentre coordinate residuals from the LAGEOS–LARES solution. The *red dashed lines* represent 95% confidence bands

than 10 years, 18 of which are core stations over certain periods of the 20-year time span. Only LAGEOS-1 and 2 observations were analysed.

Compared to the full network, the sub-network provides a more stable configuration, with less variability in network size and an improved distribution, at the expense of the number of observations. The average sub-network size is 15 stations per week, just 4 below the average size of the full network. The average percentages of stations located in the hemispheres defined by the positive X, Y and Z Cartesian axes are 2.0, 3.1 and 4.5 percentage points lower, respectively, than the values displayed in Figure 5.2. However, the general distribution patterns pertain, including the strong annual variation along the X axis. Given the reduction in data set size, the mean orbital fits of LAGEOS-1 and 2 marginally improved to 8.5 and 8.1 mm RMS, respectively.

The raw and the Butterworth–filtered geocentre coordinates obtained using the sub-network in Figure 5.22 are shown in Figure 5.23. The equatorial geocentre vector components are considerably less scattered, particularly in the years preceding 2000, whereas the Z geocentre coordinate exhibits comparable variability to the estimates obtained with the entire network (cf. Figure 5.23 and Figure 5.5). Although the 1997 trend reversal in the axial component is more distinguishable, evidence of a 2010 offset in the Y component is still lacking, in contradiction with the finding of *Luceri et al.* (2015). In the frequency domain, using the sub-network results in generally reduced draconitic errors, but the power at periods larger than two years increases for the Z component in particular.

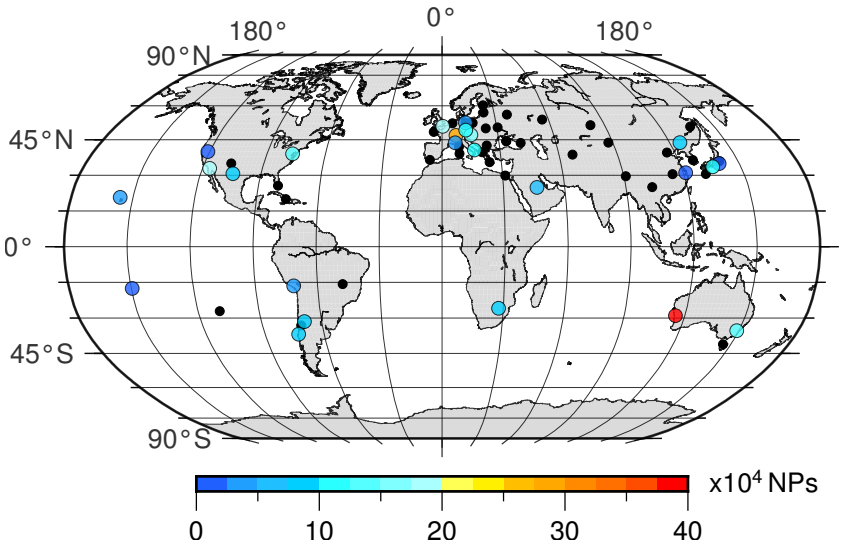

Figure 5.22 The SLR stations included in the sub-network used for the estimation of geocentre motion from LAGEOS-1 and 2 data (*coloured circles*). The *colour scale* shows the total number of NPs to LAGEOS-1 and 2 during the period 1995.0–2015.0. Discarded stations are also shown as *black circles* of smaller diameter

Similar autocorrelation structures to the full network results were identified in the geocentre coordinate residuals, but with generally larger autocorrelation coefficients presumably due to the reduction in WN. The Y geocentre coordinate residuals display more correlation than the X and Z residuals. Unsurprisingly, the AIC and BIC indicate a preference for the AR(1) plus WN stochastic model. Quadratic functional models are also consistently preferred, regardless of the noise model. Using the optimal functional-stochastic model, the amplitudes of the annual signals are 0.7, 0.5 and 0.6 mm lower for the X, Y and Z geocentre coordinates, respectively, compared to the full network case (Table 5.5). The phases of the annual signals agree within the one-sigma uncertainties.

Relative motion between CF and CN caused by the ever-changing SLR network polyhedron leads to the aliasing of loading signals into geocentre motion estimates. *Collilieux et al.* (2009) evaluated the geocentre motion biases due to aliasing, collectively called the network effect, as the difference between synthetic translation estimates and degree-1 surface mass coefficients converted to geocentre motion. The synthetic translations were derived by adding surface displacements predicted by a GPS-derived inverse model and a forward loading model to the SLR station positions in ITRF2005 and performing seven-parameter similarity transformations with respect to the stacked frame. The degree-1 surface mass coefficients were also obtained from the two models used for the estimation of synthetic translations. Strong annual variability with approximately double the annual amplitude of the Y network effect term was found in the X and Z components. The results in this study support the findings of *Collilieux et al.* (2009), as the X and Z annual cycle estimates decrease by the largest amounts when restricting the network to only a subset of reliable stations with marginally improved global distribution. In addition to partially mitigating the network effect, using a reliable sub-network also reduces the

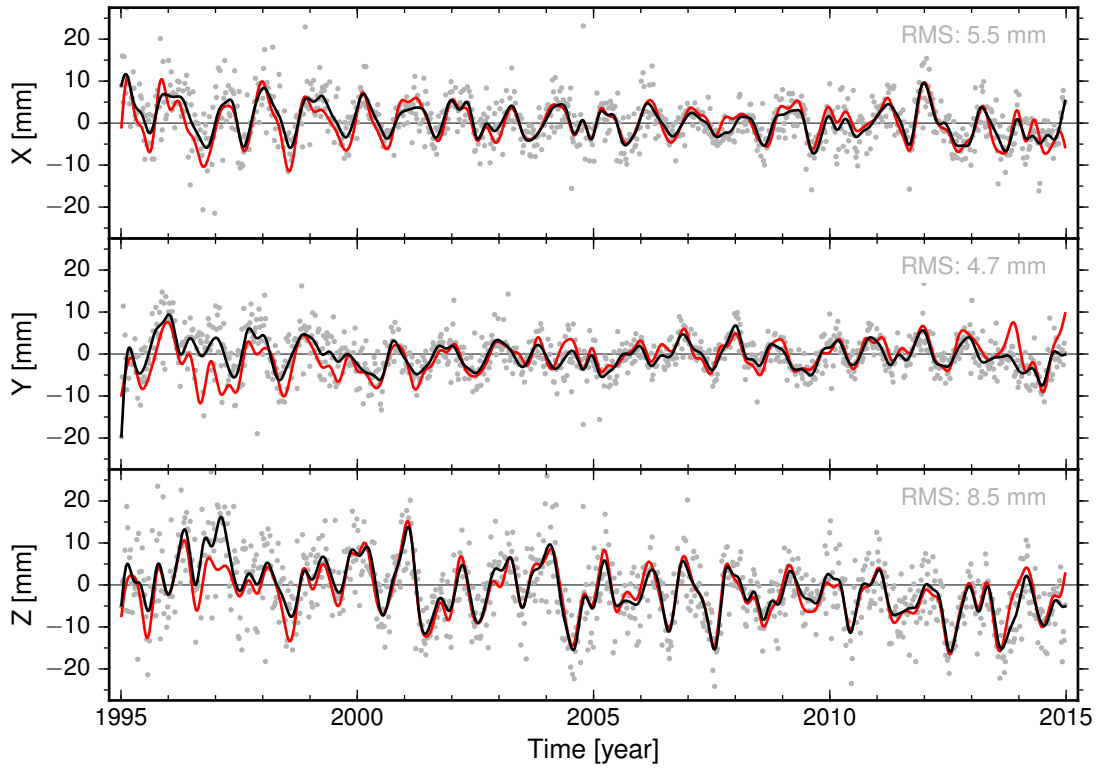

Figure 5.23 Geocentre coordinates obtained from LAGEOS-1 and 2 data using the sub-network depicted in Figure 5.22 (*grey circles*) and smoothed geocentre coordinates using a sixth-order Butterworth low-pass filter with a cut-off frequency of 3 cpy (*black curve*). The full network smoothed estimates shown in Figure 5.5 (*red curve*) are also plotted for comparison

risk of corrupting the geocentre coordinates by systematic observational errors. *Collilieux et al.* (2012) showed that a similar strategy applied to GPS networks is reasonably efficient in alleviating aliasing problems, despite the inability to fully reconcile GPS position time series and loading model predictions at the annual frequency.

5.6 Comparisons

In this section, the annual signals and the secular components of the geocentre motion estimates presented in the previous sections are compared. The effects of adopting an incorrect stochastic model on the estimates are also discussed. Comparisons between the most robust solutions from this study and results of other studies will be performed in Chapter 6.

5.6.1 Annual signals

Geocentre motion models are most commonly compared using the amplitudes and phases of the annual signals in the three Cartesian components. To facilitate comparisons, the solutions generated in this chapter are designated as follows: LAGEOS-1 and 2 obtained using the full SLR network as solution A1, LAGEOS-1 and 2 obtained using the sub-network displayed in Figure 5.22 as solution A2, LAGEOS–Etalon as solution B and,

finally, LAGEOS–Starlette–Stella–Ajisai as solution C. Solutions B and C were computed using all available data. The annual geocentre motion estimates obtained using the preferred functional-stochastic models are listed in Table 5.5 for each solution. The amplitude A and phase ϕ are defined according to the convention $A\cos[2\pi(t - t_0) - \phi]$, where t is time expressed in decimal years and $t_0 = \texttt{int}(t)$ represents 1 January of a particular year. Using this convention, the phase of each annual component is interpretable as the day of peak oscillation within a year. The uncertainties given in Table 5.5 are one-sigma, as estimated using the preferred stochastic models.

Table 5.5 Amplitude A and phase ϕ of annual geocentre motion estimated using the network shift approach from different solutions

Solution	X		Y		Z		Time span
	A [mm]	ϕ [°]	A [mm]	ϕ [°]	A [mm]	ϕ [°]	
A1	4.3 ± 0.4	49 ± 5	3.2 ± 0.4	332 ± 6	5.3 ± 0.5	24 ± 5	1995.0–2015.0
A2	3.6 ± 0.3	57 ± 5	2.8 ± 0.3	322 ± 6	4.7 ± 0.6	27 ± 7	1995.0–2015.0
B	3.8 ± 0.3	56 ± 5	2.8 ± 0.3	331 ± 7	5.0 ± 0.6	21 ± 7	2003.0–2015.0
C	4.2 ± 0.4	53 ± 6	3.9 ± 0.4	329 ± 6	6.1 ± 0.5	37 ± 4	1995.0–2015.0

All amplitude and phase estimates agree within their two-sigma formal errors. The best agreement is between the 20-year solution A2 derived using the sub-network and solution B spanning the least noisy period of 12 years. This indicates that the strategy of using a sub-network is efficient in mitigating the network effect and yields more reliable geocentre motion estimates. The noisier pre-2003 segment of the time series amplifies the annual amplitudes of all three components (cf. solutions A1 and B). Solution C shows the largest Y and Z annual amplitudes and a positive phase shift along the Z axis relative to the other three solutions. This is likely due to both orbit modelling deficiencies and the aliasing of higher-degree geopotential coefficients into the degree-1 estimates proportional to the geocentre coordinates.

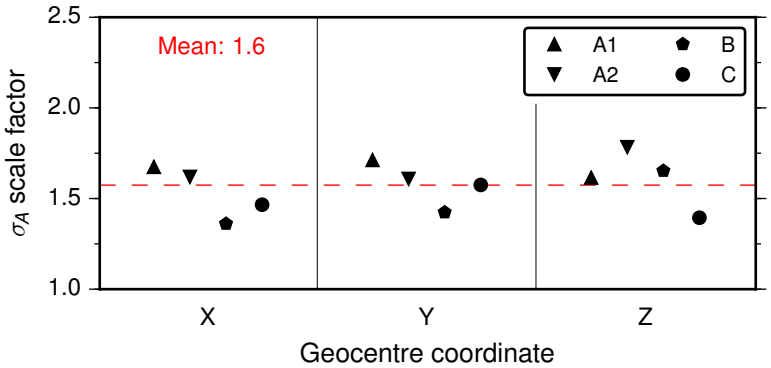

Figure 5.24 Scale factors for the uncertainties of the geocentre motion annual amplitudes obtained from different solutions under the stochastic assumption of WN only. The *red dashed line* represents the average factor computed for all solutions and geocentre coordinates

Neglecting serial correlations among geocentre coordinate residuals leads to the underestimation of the annual amplitude and phase uncertainties by an average factor of 1.6 (Figure 5.24). This numerical value represents the multiplication factor that needs to be applied to the amplitude and phase formal errors derived using the assumption of purely random noise, which has been almost unanimously adopted in previous studies. Parameter estimates are merely affected by the choice of noise model and their scaling is unnecessary.

5.6.2 Velocities and accelerations

Due to the parameterisation of station positions as piecewise linear functions in the ITRF, direct satellite tracking estimates of geocentre motion are expected to exhibit predominantly non-linear motions, including accelerations and seasonal components. Since the ITRF origin is constrained by the ILRS input solution, linear trends contained in SLR-derived geocentre motion time series are attributable to errors in the ITRF origin realisation, believed to have affected ITRF2000 and previous releases (*Altamimi et al.*, 2011), deficiencies in SLR data analysis or most likely the coupling of both error sources. Geocentre motion estimates outside the span of the latest ITRF are particularly vulnerable to potentially inaccurate station velocities and undetected offsets in position estimates.

Table 5.6 Estimated geocentre velocities and accelerations obtained from different solutions using the network shift approach

Solution	Velocity $[\mathrm{mm\,yr^{-1}}]$			Acceleration $[\mathrm{mm\,yr^{-2}}]$		
	X	Y	Z	X	Y	Z
A1	-0.08 ± 0.05	0.22 ± 0.06	-0.29 ± 0.08	-0.02 ± 0.02	-0.01 ± 0.02	-0.03 ± 0.03
A2	-0.21 ± 0.04	0.09 ± 0.06	-0.49 ± 0.09	0.02 ± 0.02	0.01 ± 0.02	0.00 ± 0.03
B	-0.14 ± 0.12	0.05 ± 0.11	-0.49 ± 0.14	-0.16 ± 0.06	0.01 ± 0.06	0.08 ± 0.09
C	-0.22 ± 0.10	0.27 ± 0.06	-0.38 ± 0.10	-0.06 ± 0.03	0.00 ± 0.02	-0.01 ± 0.04

Table 5.6 contains the estimated linear and quadratic terms for the geocentre motion time series derived from solutions A1, A2, B and C. All solutions are consistent in the sign of the linear drifts, although the magnitudes vary significantly across solutions. The most reasonable agreement is again between solutions A2 and B, despite the shorter temporal coverage of the latter reflected in higher uncertainties which render the X and Y velocities not statistically significant at 95% confidence level. At the same level of confidence, the only statistically significant acceleration is along the X axis in solution B, but generally there is no indication of accelerated geocentre motion in any direction despite the preference for quadratic functional models in all solutions.

Velocity and acceleration uncertainties are underestimated by a factor of 2.2–2.3 under the assumption of WN only (Figure 5.25). Motivated by findings on the prevalent noise types in GPS station position time series, *Argus* (2012) inadequately adopted a flicker

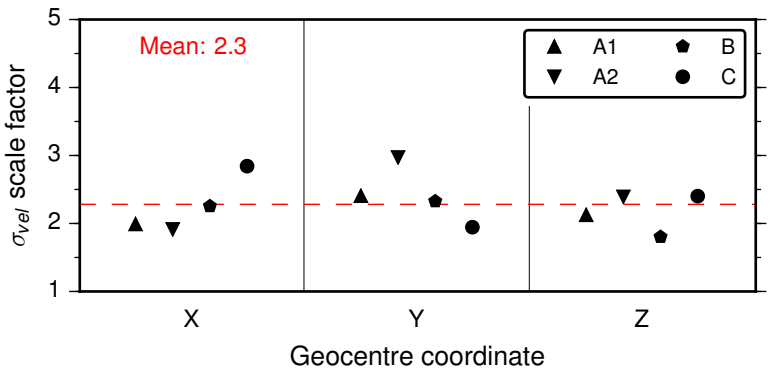

Figure 5.25 Scale factors for the uncertainties of the geocentre velocities obtained from different solutions under the stochastic assumption of WN only. The *red dashed line* represents the average factor computed for all solutions and geocentre coordinates

noise plus WN stochastic model to quantify the ITRF2008 origin stability based on the ILRS geocentre motion time series analysed using CATS. To validate the choice of noise model, *Argus* (2012) employed a PL plus WN stochastic model and estimated the spectral indices -0.6, -0.7 and -1 for the X, Y and Z geocentre coordinates, respectively. These values are similar to those obtained in Section 5.4.1 for solution A1 using Hector. For the same time series and stochastic model, CATS yields the spectral index values -0.62, -0.72 and -0.77, respectively. However, when estimating the spectral indices using CATS the linear trend uncertainties decrease by an average factor of 1.6 compared to the case of adopting a flicker noise plus WN stochastic model. This indicates that *Argus* (2012) has overestimated the linear trend uncertainties by inappropriately fixing the spectral index to -1 and thus the ITRF2008 origin may actually exhibit greater stability than initially thought.

The PL plus WN stochastic model trails both AR(1) plus WN and PL in the rankings of preferred models by solution A1 (see Table 5.3) and produces the velocity estimates -0.11 ± 0.10, 0.20 ± 0.11 and -0.25 ± 0.16 for the three geocentre motion components, respectively. With respect to the optimal AR(1) plus WN model, PL plus WN overestimates the linear trend and acceleration formal errors by average factors of 1.8 and 1.5, respectively, while also marginally underestimating the annual amplitude and phase uncertainties. These results urge caution when interpreting geocentre velocity uncertainties as measures of the ITRF origin stability, given their strong dependence on the choice of noise model.

5.7 Summary

Similar to other geodetic parameters, geocentre coordinates exhibit temporal correlations that should be accounted for to avoid biasing the interpretation of functional model parameters estimated from geocentre motion time series. Temporal correlations can be modelled by appropriately choosing the stochastic model with the aid of model-selection

criteria and simultaneously solving for stochastic and functional model parameters using MLE. Four types of SLR solutions involving different satellite data combinations were analysed in this chapter to establish a framework for the analysis of geocentre motion time series derived from satellite tracking data.

For weekly SLR solutions spanning at least 12 years, functional models that include a quadratic parameter were always preferred for the geocentre coordinates, although the accelerations estimated using optimal noise models are generally not statistically significant even at 68% level of confidence. In most situations, AR(1) plus WN and PL are comparably good explanatory models of stochastic variations, but other noise models may be better suited for geocentre motion time series with different sampling periods or time spans. For instance, the stochastic assumption of uncorrelated data points holds for the LAGEOS–LARES time series spanning almost three years. The analysis of such short series is, however, unjustified for the determination of reliable geocentre motion models. Despite some promising signs, the quantitative assessment of the contribution of LARES to the determination of geocentre motion is currently inconclusive.

Solutions based on LAGEOS-1 and 2 data provide the most reliable geocentre motion time series. Despite attenuating spurious harmonics of the LAGEOS-1 and 2 draconitic frequencies in a combined solution, the incorporation of Starlette, Stella and Ajisai appears questionable with the currently achievable orbit modelling accuracies. Estimating low-degree and order geopotential coefficients may be justifiable to improve orbital fits, but is unlikely to benefit the geocentre coordinates, which show degraded repeatability. Including Etalon-1 and 2 data in combined solutions has negligible effects on the geocentre coordinates.

The omission of the scale parameter from the functional model of the network shift approach can reduce the aliasing of SLR-specific draconitic errors into the translation estimates. Restricting the SLR network to well-distributed and high-performing stations further mitigates systematic errors and consequently improves the determination of geocentre motion, particularly in the years preceding 2000. The use of a sub-network is, nevertheless, a less viable option for the already small SLR network compared to the much denser GNSS network. Accurate modelling of data biases, CoM corrections and other systematic effects is more desirable.

By modelling the temporal dependencies found in the SLR-derived geocentre motion time series, the uncertainties of the annual amplitude and phase estimates increased by an average factor of 1.6. The formal errors of the linear trend and acceleration estimates were amplified by an even larger factor of 2.2–2.3. Geocentre velocity uncertainties are the most affected parameters by an incorrect choice of noise model from a selection that excludes WN. The effects on the annual amplitude and phase formal errors are relatively small.

Since computationally inexpensive implementations of MLE are available and model-selection statistics such as the AIC and BIC can support decision making, choosing noise

models based on previous studies to occasionally reduce the computation time is unwarranted. As demonstrated for various types of global data (*Williams et al.*, 2004; *Hughes and Williams*, 2010; *Bos et al.*, 2014; *Moore and Williams*, 2014; *Williams et al.*, 2014; *Bogusz and Klos*, 2015), stochastic model preferences and noise parameter estimates exhibit spatial dependencies that a single model is unable to appropriately capture. Additionally, stochastic properties also depend on the length and sampling period of the analysed time series, which govern the frequency range that requires fitting. Despite being poorly determined, the bulk of power lying at low frequencies is responsible for the amplification of functional model parameter uncertainties. Neglecting temporal correlations or adopting incorrect noise models can lead to biased inferences. Notorious examples that have stirred considerable debate are ice mass change and sea level change estimates.

Chapter 6

Kinematic estimates of geocentre coordinates

6.1 Introduction

The network shift approach employed in Chapter 5 has historically been the most popular of the translational procedures for geocentre motion determination, but it involves two computational steps, unless the estimation of similarity parameters between quasi-instantaneous CM frames and a secular frame is embedded in the orbit determination program. A less computationally expensive choice is the kinematic approach which permits the simultaneous recovery of geocentre coordinates and other parameters of interest through the analysis of satellite tracking data. Initially applied to GPS data more than two decades ago (*Vigue et al.*, 1992; *Malla et al.*, 1993), the kinematic approach has recently attracted increasing attention from the geodetic community (*Kang et al.*, 2009; *Cheng et al.*, 2013a; *Sośnica et al.*, 2013, 2014; *Kuang et al.*, 2015). However, amid valid concerns of correlations between station coordinates and the geocentre coordinates, the question of whether station positions should be estimated or fixed in the secular frame remains unanswered.

This chapter investigates the relationship between network shift and kinematic estimates of geocentre motion and the circumstances under which a near one-to-one correspondence is attainable using the network shift results from the previous chapter for validation purposes. Geocentre motion time series derived using the kinematic approach are seasonally filtered and smoothed in the spectral domain to assess the level of contamination by aliasing errors in the absence of the dominating annual signals. The effects of estimating range biases for all SLR stations and permitting only a sub-network to contribute to the determination of the geocentre coordinates are also considered. Finally, a comparison of results from the current and other studies is performed before recapitulating the main findings.

6.2 Validation of the processing strategy

Since the early 1990s, the kinematic approach has been applied in different variants for the determination of geocentre motion from GPS and SLR data. The differences between implementations of the kinematic approach relate to the choice of the datum parameters defining the underlying TRF (i.e. three translations describing the origin, one scale factor, three rotation parameters describing the orientation and their rates of change). Space geodetic observations are insensitive to a number of datum parameters that equals the rank defect of the design matrix, also called the *datum defect*. In particular, satellite tracking observations lack information about the orientation of the TRF, whereas VLBI observations are additionally insensitive to the origin.

To remove the datum defect and generate TRF solutions, certain parameters need to be fixed or constrained using supplementary information (i.e. pseudo-observations), typically in the form of either minimum constraints or loose constraints. Minimally constrained solutions are obtained by fixing datum parameters to particular values, generally zeros for rotations (i.e. NNR condition) and translations (i.e. NNT condition). Minimum constraints can be applied over the entire network of stations or, more commonly, over a subset of well-distributed and reliable stations chosen empirically or using optimisation techniques (*Coulot et al.*, 2010, 2015). On the other hand, in loosely constrained solutions the a priori station positions are attached large uncertainties ≥ 1 m and equivalent constraints are applied to the EOPs. Additional details on the types of constraints employed in space geodesy are provided by *Sillard and Boucher* (2001) and *Altamimi et al.* (2002).

In early applications of the kinematic approach, the positions of three GPS stations were fixed in the a priori TRF to constrain mainly the orientation and scale, whereas the geocentric coordinates of non-fiducial stations were freely estimated (*Vigue et al.*, 1992; *Malla et al.*, 1993). This strategy produced results in reasonable agreement with network shift estimates. In later studies (*Kar*, 1997; *Kang et al.*, 2009; *Cheng et al.*, 2013a; *Kuang et al.*, 2015), all station coordinates were held fixed to fully constrain the origin to CF (or CN) and estimate the translational offset of CM with respect to CF due to elastic Earth deformation. However, as recognised by *Blewitt* (2003) and *Kuang et al.* (2015), not allowing for individual station displacements leads to orbital errors that ultimately corrupt the determination of geocentre motion. The aliasing of neglected station-specific loading signals into the geocentre motion estimates is also possible, particularly for inhomogeneous networks. An alternative approach to the datum definition is to apply NNR and NNT conditions with respect to the a priori TRF and simultaneously solve for station positions and geocentre coordinates (*Thaller et al.*, 2011, 2014; *Meindl et al.*, 2013; *Sośnica et al.*, 2013, 2014). The NNR condition removes the three orientation singularities and it suffices when estimating only station coordinates, whereas the NNT condition is only necessary when the displacement of CM with respect to CF is explicitly modelled.

Recent kinematic geocentre motion estimates were obtained from SLR data either by fixing all station coordinates (*Cheng et al.*, 2013a) or by applying NNR and NNT conditions over the core SLR network (*Sośnica et al.*, 2013, 2014). Geocentre motion time series derived using the two alternative datum definitions have yet to be compared and benchmarked against network shift results over frequencies other than the annual. To achieve this objective, LAGEOS-1 and 2 data spanning the period 1995.0–2015.0 were analysed in weekly batches first by fixing station coordinates in the SLRF2008 and freely estimating weekly geocentre coordinates and second by concurrently solving for station positions and unconstrained geocentre coordinates. The solutions were loosely constrained using the uncertainties given in Table 5.2 and the orbital parameterisation was as described in Section 5.3.2 to allow an impartial comparison of network shift and kinematic estimates.

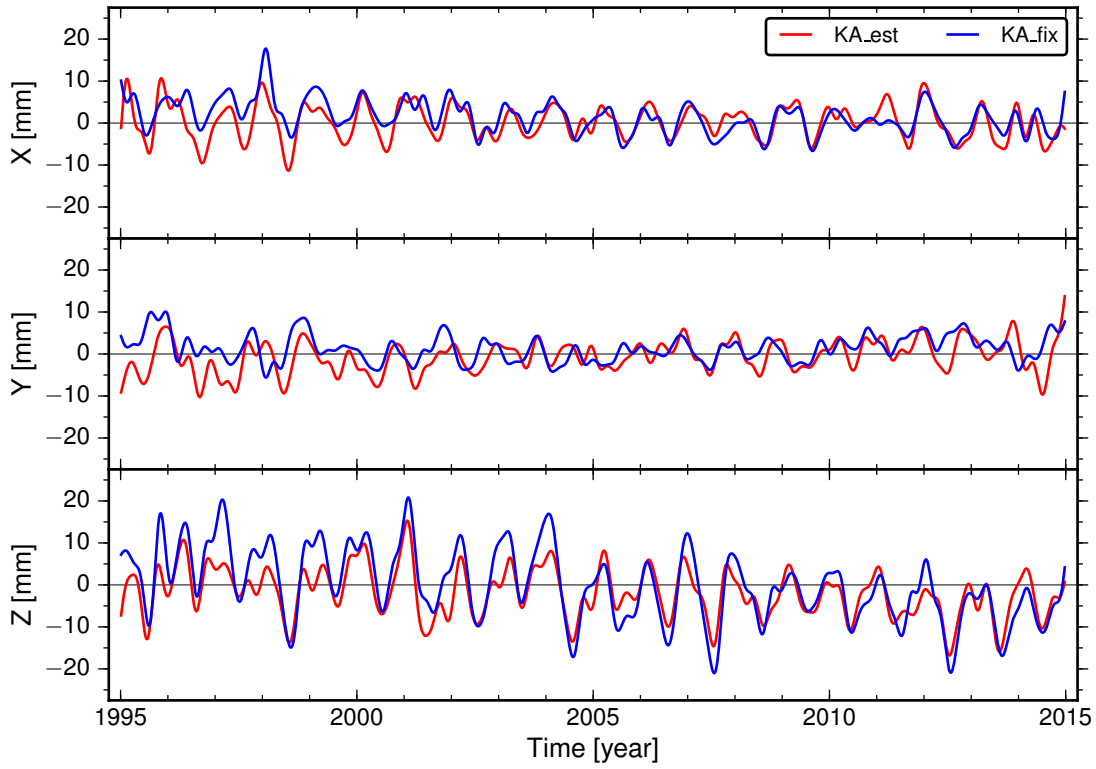

Figure 6.1 LAGEOS–only geocentre motion time series obtained using the kinematic approach by estimating station coordinates (KA_est) and by fixing station coordinates (KA_fix). The time series were smoothed using a sixth-order Butterworth low-pass filter with a cut-off frequency of 3 cpy

As illustrated in Figure 6.1, the time series obtained using the two alternative datum definitions show notable differences, especially in the early years of the analysis when larger data noise levels are likely. The equatorial geocentre coordinates exhibit less scatter in the solution with fixed station coordinates, but clear inter-annual variations are also discernible. In contrast, larger seasonal variability is observed along the Z axis when fixing station positions, in addition to more pronounced negative drift from 1997 onwards.

Comparisons with network shift results should provide insight into the reliability of each of the two solutions.

Given their historical dependability, network shift geocentre motion estimates represent an appropriate baseline for benchmarking kinematic results, assuming the use of similar processing standards in generating the solutions. Coherence spectra and phase spectra can be used to perform pairwise comparisons of identically sampled and equal-length time series over their entire frequency range. The *coherence-squared function* or *squared coherency* represents a measure of the squared linear correlation between two time series as a function of frequency. Squared coherency estimates are obtained as the ratio of the squared cross-spectrum and the product of the autospectra and take values in the interval 0 to 1. Two signals are considered coherent at frequency f if the squared coherency estimate lies above an established confidence limit and the phase lag is near zero. Convenient bounds for the phase lag are $\pm\Delta t$ degrees, where Δt denotes the sampling period of the series (*Kuehne and Wilson*, 1991). Following *Thomson and Emery* (2014), the $100\,(1-\alpha)\%$ confidence limit for the squared coherency estimates can be obtained as

$$c^2_{1-\alpha} = 1 - \alpha^{1/(\mathrm{EDoF}-1)}, \tag{6.1}$$

where α is the significance level and the equivalent degrees of freedom, designated as EDoF, depend on the smoothing applied to spectral estimates. Without spectral smoothing the coherence spectrum equals unity at all frequencies.

To improve the statistical significance of squared coherency estimates by block averaging, the method of *Welch* (1967) was adopted for conducting the coherence analysis. The geocentre motion time series were partitioned in five segments overlapping 50%, each tapered using a Hanning window to reduce the leakage of spectral power between frequency bands. For frequencies above 6.5 cpy, where the signal to noise ratio is lower, seven segments with 50% overlap were used for additional smoothing. The trade-off is a loss of spectral resolution, which is unlikely to be problematic in this analysis given the main purpose of determining the overall agreement between the time series. For the Hanning window, the EDoF value equals $^{8n}/_{3m}$, where n represents the number of data points in the time series and m is half of the window width.

The one-sided coherence spectra and phase spectra computed for the pairs (1) network shift estimates (NS) versus kinematic estimates obtained by estimating station coordinates (KA_est) and (2) NS versus kinematic estimates obtained by fixing station coordinates (KA_fix) are shown in Figure 6.2. The NS and KA_est series are highly coherent and in phase across the entire range of frequencies along all three axes. Conversely, the KA_fix series are relatively less coherent with the NS estimates, particularly for the equatorial geocentre coordinates. The Y annual component of the KA_fix series trails its counterpart from the NS time series by $\sim 41°$, but better agreement is observed in the X

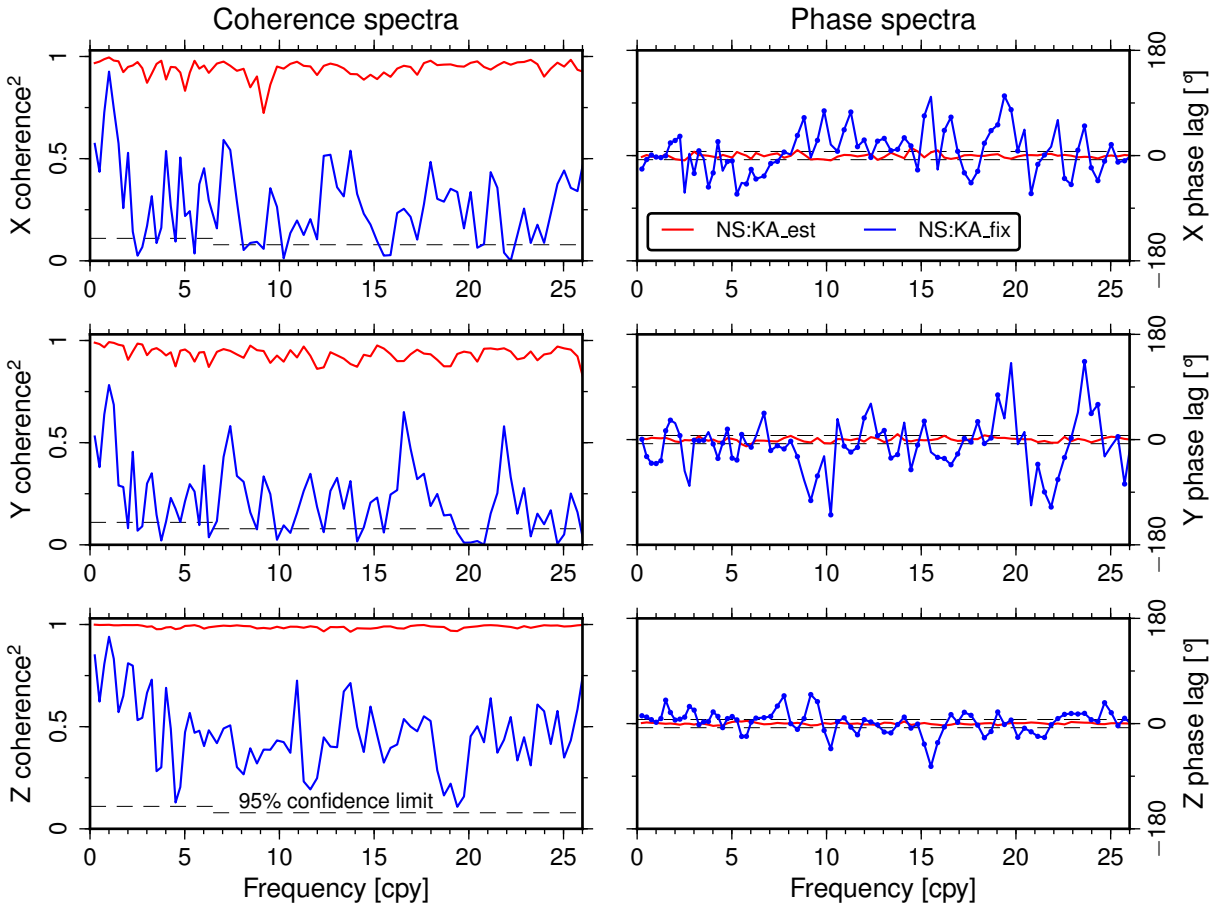

Figure 6.2 One-sided coherence spectra (*left*) and phase spectra (*right*) between detrended network shift (NS) geocentre motion estimates and kinematic geocentre motion estimates obtained (1) simultaneously with station coordinates (KA_est, *red curve*) and (2) by fixing the datum (KA_fix, *blue curve*). The *blue circles* in the phase spectra mark reliable phase estimates at frequencies where the coherency amplitudes lie above the 95% confidence levels. The *red dashed lines* drawn at ±7° in the phase spectra represent empirical bounds outside which the phase lags are significantly different from zero. Additional smoothing has been applied at frequencies above 6.5 cpy

and Z directions at the annual frequency. The NS and KA_fix series also lack coherence along the Y axis at 2 cpy.

The striking similarity between the NS and KA_est series is additionally emphasised through the summary statistics listed in Table 6.1. Descriptive statistics of the network shift estimates derived by simultaneously estimating a scale parameter are also included for comparison under the denomination NS_scl. The KA_est series also exhibit a high level of coherence with the NS_scl series, but to a lower extent than with NS estimates, especially in the Z direction. As the Z geocentre coordinate was shown in Section 5.4.1 to be the most affected by the concurrent estimation of a scale factor, the higher coherence between the NS and KA_est series along the Z axis represents a supplementary incentive to omit the scale parameter when estimating geocentre motion with the network shift approach.

Table 6.1 Summary statistics of the unfiltered network shift and kinematic geocentre motion estimates obtained from LAGEOS-1 and 2 data spanning the period 1995.0–2015.0

Solution	X [mm]			Y [mm]			Z [mm]		
	Mean	SD	RMS	Mean	SD	RMS	Mean	SD	RMS
NS	−0.4	6.2	6.2	−0.8	5.7	5.8	−1.8	8.5	8.7
NS_scl	−1.0	6.2	6.2	−0.8	5.7	5.7	−2.1	8.5	8.7
KA_est	0.2	6.0	6.0	−0.7	5.6	5.6	−1.9	8.5	8.7
KA_fix	1.5	5.2	5.4	1.3	4.4	4.6	−0.1	10.4	10.4

The assessment conducted in this section demonstrates the feasibility of simultaneously estimating geocentre coordinates and station positions using loose constraints applied to station coordinates, EOPs and range biases. With this approach, the station coordinates are expressed in a frame whose origin coincides with that of the a priori frame, since the translations between the two origins are explicitly modelled. The collinearity between station coordinates and the geocentre coordinates invoked, for instance, by *Cheng et al.* (2013a) does not affect the separability of the two types of parameters. This is confirmed by the high coherence and phase agreement between the kinematic geocentre motion estimates obtained simultaneously with station coordinates and the network shift results described in Chapter 5. Consequently, the majority of kinematic solutions discussed in the current chapter have been obtained by concurrently determining station coordinates and the geocentre coordinates.

6.3 Geocentre motion time series

Due to the similarities between network shift geocentre motion estimates and kinematic results obtained simultaneously with station positions, the general conclusions drawn in Chapter 5 also apply to the current chapter for all solution types. Thus, in view of avoiding repetition, a series of other LAGEOS-1 and 2 analyses will be presented to give further insight into the differences between the network shift and kinematic approaches and discuss the errors contaminating SLR-derived geocentre motion time series in more detail. Kinematic geocentre motion estimates obtained with fixed station coordinates are first analysed.

6.3.1 Kinematic estimates with fixed datum

Fixing station coordinates predictably degrades the LAGEOS-1 and 2 orbital fits to the level of $\sim$ 1 cm. The KA_fix time series display an apparent pre-2002 offset in all components with respect to the KA_est series, in addition to more pronounced irregularities in annual variations (Figure 6.1). The RMS values of the differences between the KA_est and KA_fix series equal 5.7, 6.1 and 7.3 mm for the X, Y and Z geocentre coordinates,

respectively. Considerable inter-annual patterns and strong annual cycles along the Y and Z axes were found in the time series of the differences, illustrative of the systematic biases between the two solutions. Spurious long-period variations can be induced by inaccuracies in the a priori station velocities used to linearly map station positions at the epochs of interest. The KA_fix solution is more vulnerable to such inaccuracies since the linearly mapped station coordinates are considered errorless.

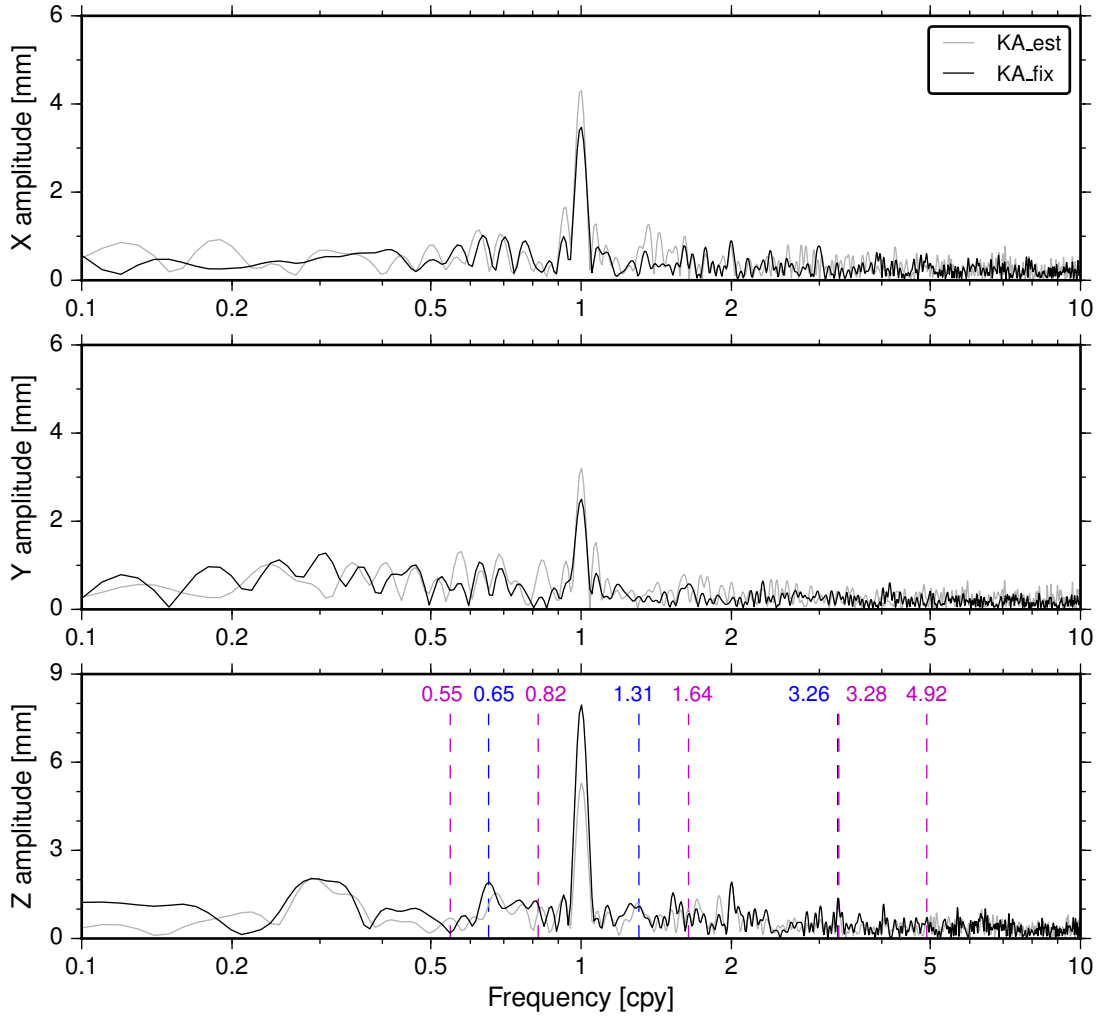

Figure 6.3 Amplitude spectra of the detrended geocentre coordinates obtained using the Lomb–Scargle method for the KA_fix and KA_est solutions. The vertical dashed lines mark fractions and integer multiples of the LAGEOS-1 (*blue*) and LAGEOS-2 (*magenta*) draconitic frequencies

Figure 6.3 depicts the overlaid amplitude spectra of the detrended KA_fix and KA_est series. The annual peaks are less prominent in the KA_fix series for the equatorial geocentre coordinates, but considerably larger for the axial component. Although the mechanism causing these differences is unclear, one possibility is the asymmetric aliasing of unmodelled loading displacements into the geocentre coordinates due to the unbalanced SLR network. Moreover, there is generally less power at high frequencies in the equatorial components of the KA_fix series. The Z geocentre coordinate appears more prone to

draconitic errors when fixing station coordinates since the amplitudes of the 0.65 and 3.27 cpy sinusoidal components are larger in the KA_fix series.

For both the KA_fix and KA_est geocentre motion estimates, quadratic functional models are invariably favoured over linear models based on the AIC and BIC model-selection statistics. In the KA_est solution all three geocentre vector components prefer the AR(1) plus WN stochastic model, which is unsurprising given the high coherence between the NS and KA_est series. Conversely, in the KA_fix solution AR(1) plus WN is only preferred by the Y component, whereas the optimal noise models for the X and Z components are PL and AR(4), respectively. The estimated amplitudes of the annual signals along the X, Y and Z axis are 3.4 ± 0.3, 2.5 ± 0.3 and 7.9 ± 0.7 mm, respectively, compared to 4.3 ± 0.3, 3.3 ± 0.4 and 5.2 ± 0.5 mm in the KA_est solution. The latter set of values are similar to those obtained for the network shift estimates without adjusting the scale (see solution A1, Table 5.5).

6.3.2 Seasonally adjusted series

The bulk of power in geocentre motion time series is concentrated around the annual frequency, whereas white noise dominates at high frequencies. Removing annual and semi-annual sinusoidal components and smoothing spectral estimates should enable the identification of finer spectral features such as draconitic harmonics and aliased tidal signatures widely acknowledged to corrupt GNSS geodetic products (e.g. *Penna and Stewart*, 2003; *Griffiths and Ray*, 2013; *Ray et al.*, 2013). In broad geodetic terms, aliasing refers to the contamination of parameter estimates by unmodelled or residual effects of various physical processes. Following *Jacobs et al.* (1992), for a given sampling period Δt, the aliased frequency f_a is related to the sampling frequency f of a real geophysical signal by

$$f_a = \texttt{abs}\left[f - \frac{1}{\Delta t}\,\texttt{int}(f\Delta t + 0.5)\right], \tag{6.2}$$

where the `abs` function returns the absolute value of its argument and the integer function `int` returns the integer part of its argument.

Tidal errors can alias into geodetic parameter estimates at periods that depend on the length of the processing session or on the ground track recurrence of satellite orbits. LAGEOS-1 has a ground repeat period of 7 days, 23 hours and 45 minutes, whereas the ground track of LAGEOS-2 recurs every 8 days, 22 hours and 58 minutes (e.g. *Sośnica*, 2014). Table 6.2 lists the expected aliased periods for the main eight diurnal (Q_1, O_1, P_1, K_1) and semi-diurnal (N_2, M_2, S_2, K_2) tidal constituents due to the adopted seven-day length of SLR solutions and the orbital geometries of LAGEOS-1 and 2. The periods of the tidal constituents were extracted from Tables 8.2a and 8.2b of the IERS Conventions (2010) (*Petit and Luzum*, 2010). The tidal constituents of largest amplitudes are K_1, O_1, M_2 and S_2, but their aliased amplitudes depend on the propagation mechanism. For the seven-day sampling interval, K_1 and P_1 are predicted to alias into the annual sinusoidal

components, whereas S_2 has an infinite aliased period due to the S_2 tidal period being a divisor of the seven-day sampling period. The theoretical aliased period of the luni-solar K_2 constituent is semi-annual.

Table 6.2 Aliased periods for the principal diurnal and semi-diurnal tidal constituents assuming sampling periods equal to 7 days, the ground repeat period of LAGEOS-1 (L1 repeat) and the ground repeat period of LAGEOS-2 (L2 repeat), respectively

Constituent	Period [hours]	Aliased period [days]		
		7 days	L1 repeat	L2 repeat
Q_1	26.8683552	27.6998705	58.4682467	12139.0948584
O_1	25.8193416	14.1915854	18.7283802	27.4921810
P_1	24.0658896	365.2456473	247.4228204	132.5410870
K_1	23.9344704	365.2467038	697.3041029	483.3086183
N_2	12.6583488	25.7472984	53.9453056	503.3234953
M_2	12.4206024	14.7652538	18.2385765	29.1504799
S_2	12	∞	383.5	104.0161290
K_2	11.9672352	182.6233519	348.6520514	241.6543092

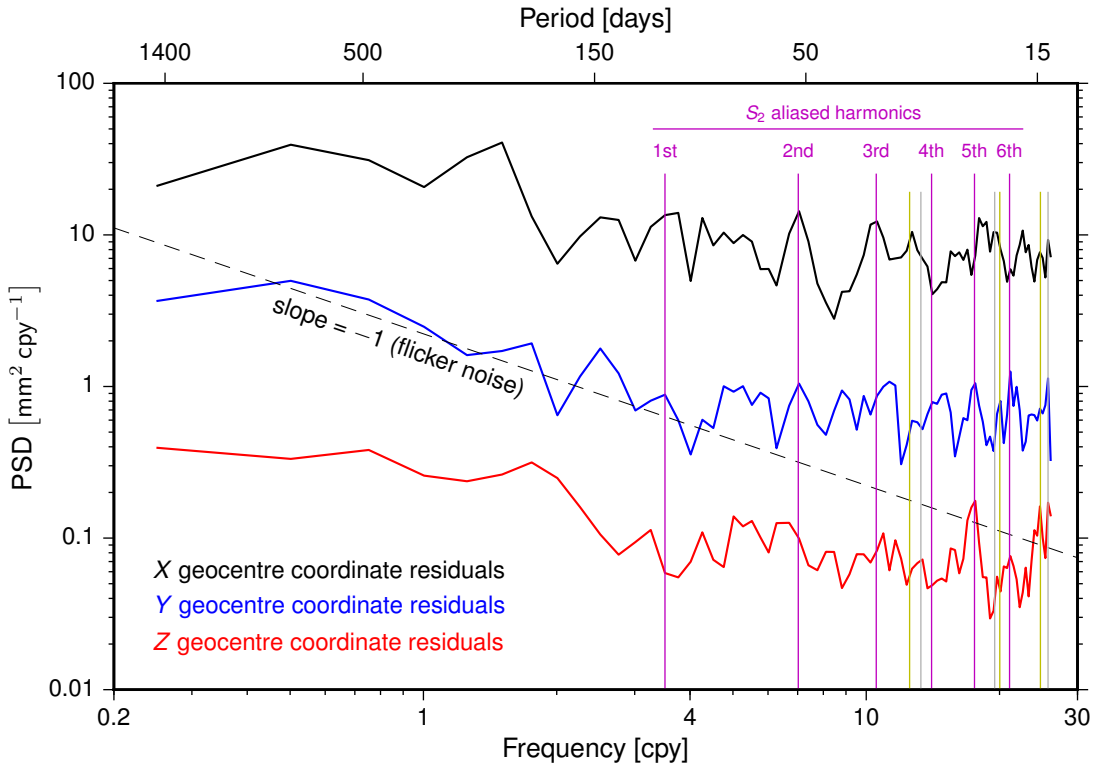

Figure 6.4 Power spectra of the geocentre coordinate residuals from the KA_est solution. For clarity, the X and Z PSDs were multiplied by factors of 10 and 20^{-1}, respectively. The *black dashed line* with a slope of -1 illustrates the spectral behaviour of flicker noise. The first six harmonics of the S_2 tidal alias due to the ground repeat period of LAGEOS-2 are indicated by *magenta vertical lines*. Also marked are aliases of the O_1 (*grey vertical lines*) and M_2 (*yellow vertical lines*) tidal constituents generated by the seven-day processing window and the ground repeat periods of LAGEOS-1 and 2

Figure 6.4 displays the PSDs of the geocentre coordinate residuals from the KA_est solution. The residuals were obtained by subtracting the best-fit quadratic model including annual and semi-annual periodic components from the estimated geocentre coordinates. An identical Welch algorithm to that described in Section 6.2 was applied for smoothing the spectral estimates to reduce their variance and better locate spectral peaks. Despite applying a seasonal filter, residual power near the semi-annual band is observed in the spectrum of the Z component, which also contains a peak of draconitic origin near 3.27 cpy, already identified in Section 5.4.1. A PL pattern is discernible at frequencies below 4 cpy, but with a less pronounced slope than the -1 slope of flicker noise. The PSDs flatten to white noise for frequencies above 4 cpy.

Each component contains O_1 and M_2 aliases predicted for the seven-day processing window at periods of 14.19 and 14.77 days, respectively. These aliased tidal signals produce the cusps distinguishable in the power spectra near the Nyquist frequency. Aliases at 18.24, 18.73, 27.49 and 29.15 days are also apparent. The prominent spectral peaks visible near 52 days in the spectra of the X and Y components and near 21 days in the spectra of the Y and Z components are remarkably well matched by harmonics with a generating frequency equal to the reciprocal of the S_2 aliased period of 104.02 days due to the LAGEOS-2 ground track recurrence. The aliasing mechanism appears most effective for the Y geocentre coordinate since four of the first six harmonics have a clear corresponding spectral peak, compared to just two in the X and Z components. Mismodelled constituents in the FES2004 ocean tide model (*Lyard et al.*, 2006) may represent the source of these tidal errors. Comparisons that fall beyond the scope of this study with results obtained using different ocean tide models may provide further clarifications.

6.3.3 Systematic and network geometry effects

The routine estimation of range biases for all SLR stations is under consideration within the ILRS AWG.[1] An alternative solution designated as KA_allrb was derived to assess the effects of this practice on the geocentre coordinates. Figure 6.5 depicts the KA_allrb solution overlaid on the KA_est solution. Also shown in Figure 6.5 is the KA_subnet solution obtained by allowing only observations acquired by the 31–station sub-network from Figure 5.22 to contribute to the determination of the geocentre coordinates. Contrary to the solution generated in Section 5.5 using the same sub-network, all available data were processed to obtain the KA_subnet time series.

As illustrated in both Figure 6.5 and Table 6.3, the estimation of range biases for all stations introduces systematic negative offsets along the Y and Z axes, apparent particularly before 2011, and increases the scatter of the geocentre coordinates by approximately 1 mm for the equatorial components and 3 mm for the Z component. These results

[1] http://ilrs.gsfc.nasa.gov/docs/2015/AWG_Minutes_Matera_2015_FINAL.pdf

are consistent with the findings of a recent independent study conducted by the Natural Environment Research Council (NERC) Space Geodesy Facility at Herstmonceux, in preparation for a planned ILRS pilot project.[2] As already concluded in Section 4.4.1, the a priori application of time-dependent range biases to observational data is desirable and may be facilitated by the anticipated release of a tailored product by the ILRS. The aliasing of draconitic errors is also exacerbated by the estimation of all range biases.

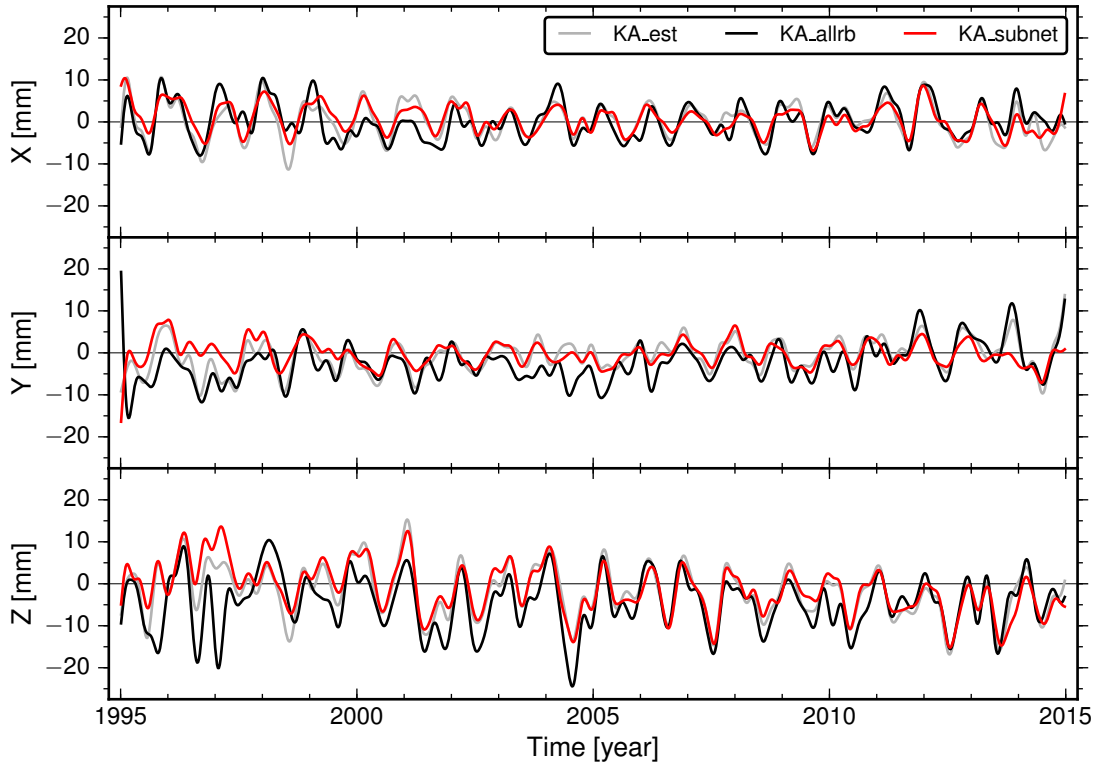

Figure 6.5 LAGEOS–only geocentre motion time series obtained using the kinematic approach by estimating station coordinates (KA_est), by additionally estimating range biases for all stations (KA_allrb) and by permitting only data from the sub-network shown in Figure 5.22 to contribute to the determination of the geocentre coordinates (KA_subnet). The time series were smoothed using a sixth-order Butterworth low-pass filter with a cut-off frequency of 3 cpy

Table 6.3 Summary statistics of the kinematic geocentre motion estimates obtained from different LAGEOS-1 and 2 solutions spanning the period 1995.0–2015.0

Solution	X [mm]			Y [mm]			Z [mm]		
	Mean	SD	RMS	Mean	SD	RMS	Mean	SD	RMS
KA_est	0.2	6.0	6.0	−0.7	5.6	5.6	−1.9	8.5	8.7
KA_allrb	0.1	7.0	7.0	−2.5	6.7	7.1	−4.5	10.8	11.7
KA_subnet	0.7	5.5	5.5	−0.2	4.8	4.8	−1.3	8.4	8.5

The KA_subnet solution shows mean values closer to zero for the Y and Z geocentre vector components and reduced variability in all three directions with respect to the

[2] http://ilrs.gsfc.nasa.gov/docs/2015/ILRS_AWG_EGU2015_VIENNA_April_16-PRESENTATIONS.pdf

KA_est solution, albeit only marginally lower in the axial direction. Similar to the KA_est solution, AR(1) plus WN is the best explanatory model of stochastic variations for all three geocentre vector components. However, the estimated amplitudes of the annual signals in the X, Y and Z Cartesian components are 0.9, 0.4 and 0.5 mm lower, respectively, in the KA_subnet solution due to the neglected contribution of unreliable data. For these reasons, KA_subnet is regarded as the optimal solution derived in this study and compared against independent results in Sections 6.3.4 and 6.4.

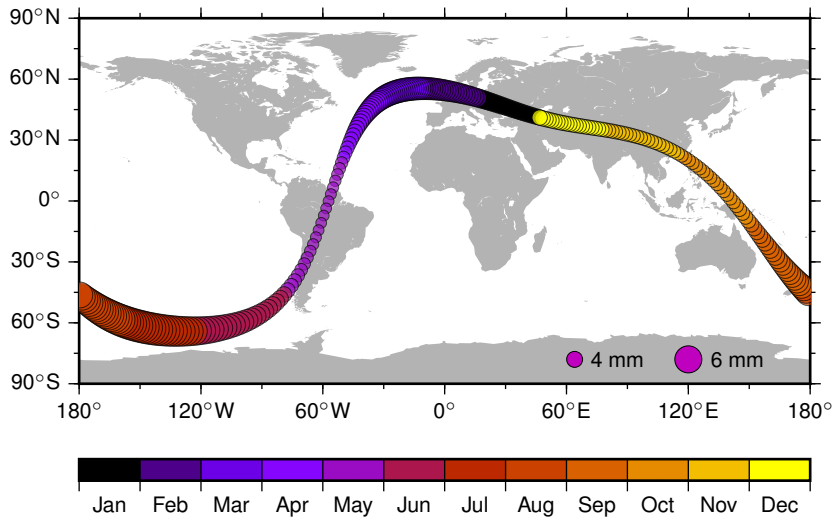

Figure 6.6 Ground track and magnitude of the geocentre vector computed using the annual and semi-annual components of the KA_subnet time series. The *colour scale* indicates the phase in months and the varying diameters of the *coloured circles* illustrate the time-dependent vector magnitude

Figure 6.6 illustrates the trajectory of the geocentre projected on the Earth's surface, as determined using the annual and semi-annual fits to the KA_subnet time series. The ground track crosses South America, Europe and Central Asia, regions with strong TWS variability (e.g. *Syed et al.*, 2008), which represents one of the major drivers of seasonal geocentre motion. The magnitude of the geocentre vector varies rapidly from approximately 3 mm in May to nearly 7 mm in July, when the direction is towards the South Pacific Ocean.

6.3.4 CSR monthly LAGEOS-1 and 2 solution

Thus far only weekly geocentre motion time series were discussed. To provide insight into the dependence of noise properties on the sampling period of geocentre motion time series, a monthly LAGEOS-1 and 2 solution generated at the University of Texas at Austin by CSR using the kinematic approach was also analysed over the time span 1995.0–2015.0 of the weekly solutions presented in this study. The data analysis procedure employed by CSR included station coordinates fixed in the SLRF2005/LPOD2005.[3] The

[3] ftp://ftp.csr.utexas.edu/pub/slr/station_coordinates/

CSR solution is shown in Figure 6.7 superimposed on the KA_subnet time series, which were downsampled by a factor of $k = 4$ using a sixth-order Butterworth filter with a cut-off frequency of $\frac{0.8}{k}\frac{1}{2\Delta t}$, where $1/2\Delta t$ is the Nyquist frequency (∼26 cpy), to suppress high-frequency noise and allow a fairer comparison. By applying this procedure, 261 estimates at 28-day intervals were obtained for each geocentre vector component. The unevenly sampled CSR time series contain 240 data points given at monthly mid-points and required resampling before being analysing using Hector. Good agreement between the decimated KA_subnet series and the CSR solution is discernible for the equatorial geocentre coordinates, whereas Z exhibits less variability in the KA_subnet solution and a marginally less prominent negative trend post-1997.

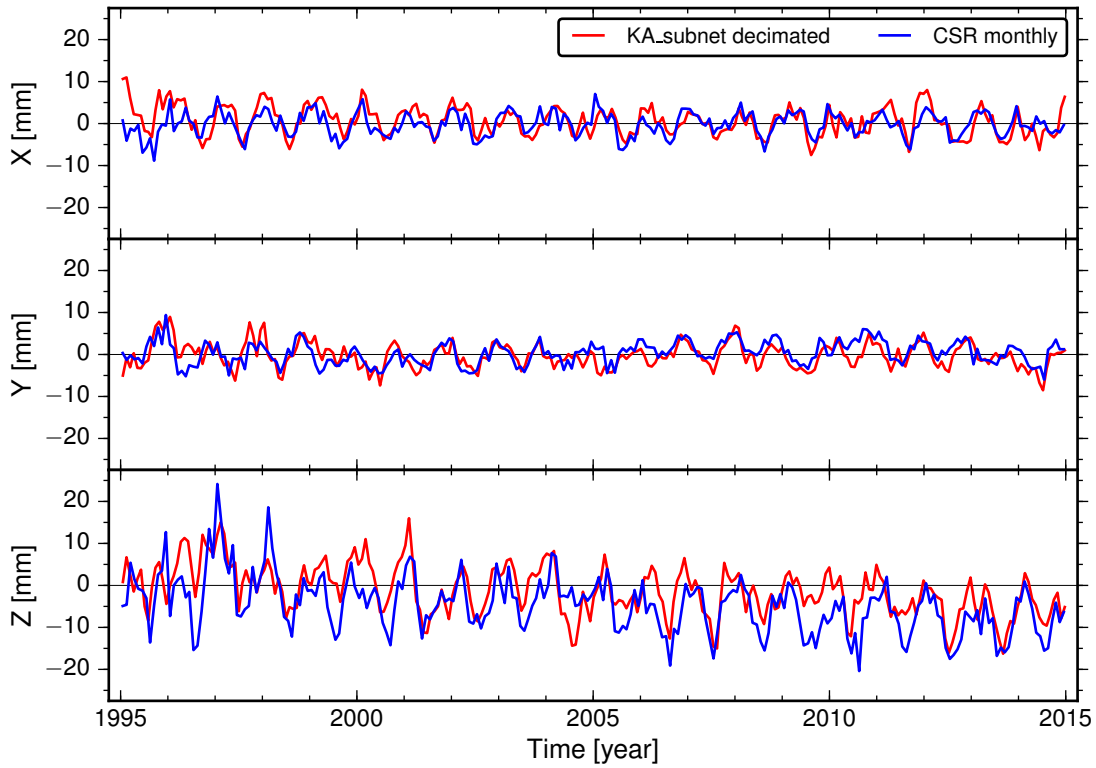

Figure 6.7 KA_subnet geocentre motion time series decimated to 28-day values and a CSR monthly LAGEOS–only solution

Increasing the sampling period has a smoothing effect similar to that obtained by decimating time series, as described above for the KA_subnet solution. The trade-off consists in a diminished frequency range, which is unproblematic for the determination of seasonal components, but likely to alter the noise characteristics by retaining long-period features with PL behaviour. It is thus unsurprising that for the resampled CSR monthly series with a Nyquist frequency of 6 cpy, the PL noise model ranks first for the Y component based on the BIC, whereas AR(1) is preferred over PL for the X and Z components. The Y component residuals have a much more pronounced slope in the spectral domain, which amplifies the velocity and acceleration uncertainties by a factor of approximately 3 compared to the case of ignored serial correlations. For X and Z, the uncertainties increase only by a factor of 1.3, but a further amplification by approximately

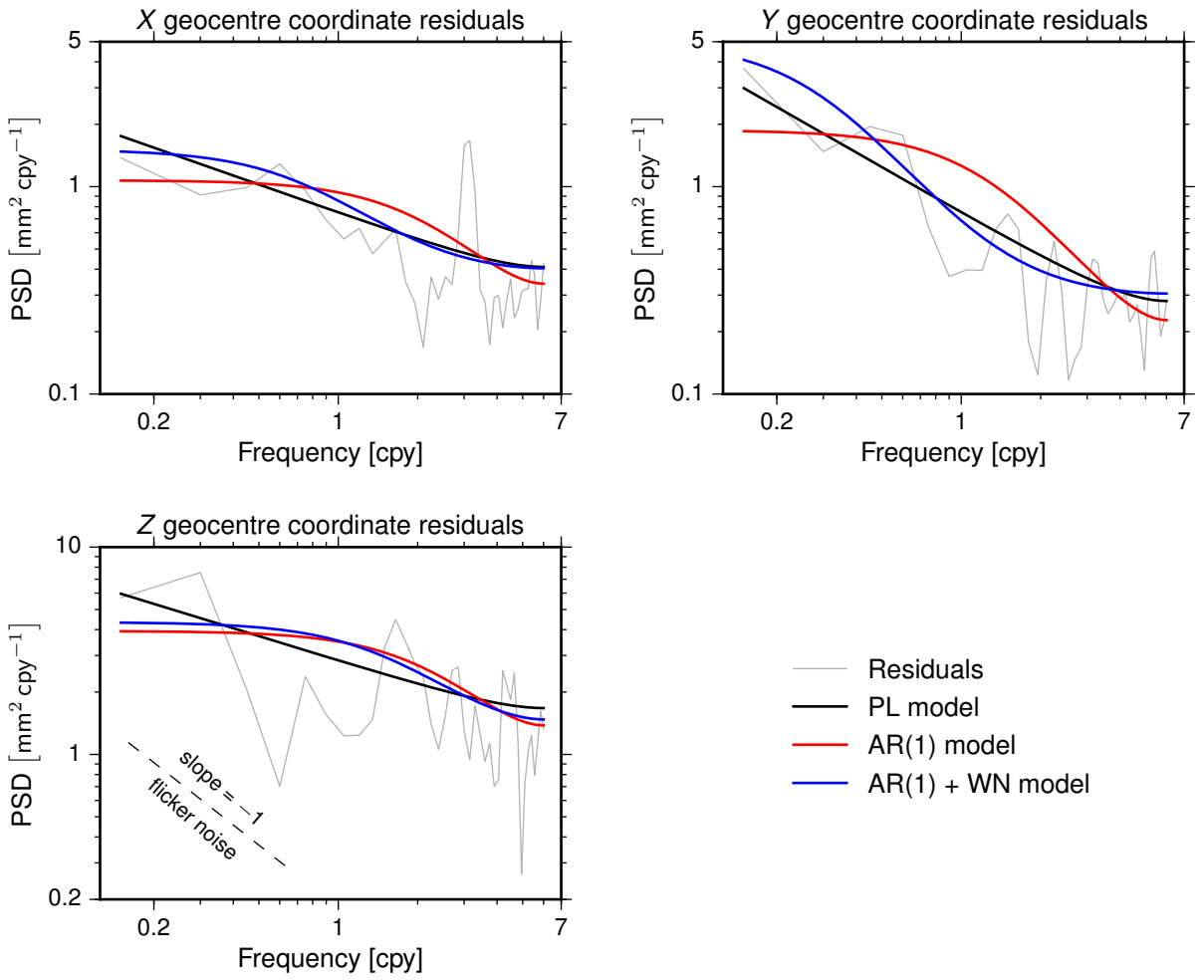

Figure 6.8 Power spectra of the geocentre coordinate residuals from the CSR monthly solution obtained by block averaging spectral estimates from five segments overlapping 50% and power spectra of three best-fit noise models. The *black dashed line* with a slope of −1 illustrates the spectral behaviour of flicker noise

1.6 is obtained when adopting the PL stochastic model. Functional models that include a quadratic term are invariably favoured.

Residual spectral power present after seasonal filtering in all three geocentre vector components near the 1.64 and 3.27 cpy frequency bands confirms the presence of draconitic errors in the CSR series (Figure 6.8). The X component also contains a prominent ter-annual signal, absent from the other two components and the weekly solutions. In analogy to weekly sampled series, white noise flattening is apparent for frequencies larger than 4 cpy.

6.4 Comparisons with independent results

As a standard validation procedure, the amplitudes and phases of the annual components from the KA_subnet series are compared in the following section with independent estimates. Differences between results produced by the various approaches described in

Chapter 3 are also discussed with reference to annual signals and geocentre velocities and accelerations along the three Cartesian axes.

6.4.1 Annual signals

Selected annual geocentre motion estimates and predictions from various studies are listed in Table 6.4 and illustrated in Figure 6.9, alongside the most robust estimate from this study. Network shift and kinematic results from SLR data dominate, as they have proven reliable for nearly two decades. In contrast, GNSS and DORIS-based translational determinations of geocentre motion are compounded by orbit modelling deficiencies and correlations between parameters (e.g. *Meindl et al.*, 2013; *Rebischung et al.*, 2014; *Gobinddass et al.*, 2009a,b) and thus unable to adequately exploit the denser and more uniformly distributed GNSS and DORIS tracking networks. The CM and rigorous parameter combination (RC) approaches yield reasonable results only when employing GNSS data due to the insufficient sampling of the Earth's surface by SLR and DORIS-derived crustal deformations. Global inversion results obtained by integrating complementary data sets to cover oceanic gaps are typically in good agreement with CM and RC estimates of annual amplitudes, as well as with predictions of geophysical fluid models. Geophysical predictions may, however, provide an incomplete account of the total annual geocentre motion due to the neglect of contributions from particular components of the Earth's fluid envelope enforced by the lack of accurate models.

Of the SLR network shift solutions in Table 6.4 only *Moore and Wang* (2003), *Collilieux et al.* (2009) and *Wu et al.* (2015) omitted the scale parameter. Excluding the estimates from the current study, the average annual amplitudes of the SLR-derived X, Y and Z geocentre coordinates from Table 6.4 are 2.7, 3.0 and 4.6 mm, respectively, whereas the average phase estimates are 43°, 318° and 25°, respectively. For Y and Z, the agreement between the results of this study and other SLR estimates is very good. Nevertheless, the X geocentre coordinate peaks approximately two weeks later than average, in better agreement with global inversion results. The X annual amplitude is also larger than the average by 0.8 mm. GNSS-based and inverse results generally show the smallest X and Z annual amplitudes, whereas loading models are unable to fully explain the annual variability observed in SLR solutions for any of the three geocentre vector components. Among the two equatorial geocentre coordinates, Y exhibits greater annual variability in most geodetic solutions, in contradiction to model predictions. As demonstrated by *Wu et al.* (2015), the reconciliation of SLR-derived annual geocentre motion estimates with global inversion results is attainable through a sequential combination of station position time series from all four space geodetic techniques contributing to the ITRF.

Table 6.4 Selected estimates of annual geocentre motion

Solution	X		Y		Z		Time span	Reference
	A [mm]	ϕ [°]	A [mm]	ϕ [°]	A [mm]	ϕ [°]		
SLR KA	3.5 ± 0.3	59 ± 5	2.9 ± 0.3	321 ± 5	4.6 ± 0.5	28 ± 6	1995.0–2015.0	This study
SLR KA	2.8 ± 0.2	45 ± 4	2.5 ± 0.2	322 ± 4	5.7 ± 0.4	32 ± 4	1995.0–2015.0	CSR monthly
SLR KA	2.7 ± 0.2	40 ± 2	2.8 ± 0.2	323 ± 2	5.2 ± 0.2	30 ± 3	1992.8–2010.9	*Cheng et al.* (2013a)
SLR NS	2.1 ± 0.5	48	2.0 ± 0.5	327	3.5 ± 1.5	43	1993.0–1996.8	*Bouillé et al.* (2000)
SLR NS	2.6 ± 0.5	32 ± 7	2.5 ± 0.1	309 ± 4	3.3 ± 1.0	36 ± 10	1993.0–2000.0	*Crétaux et al.* (2002)
SLR NS	3.5 ± 0.6	26 ± 10	4.3 ± 0.6	303 ± 8	4.6 ± 0.6	33 ± 7	1993.1–2001.7	*Moore and Wang* (2003)
SLR NS	2.7 ± 0.6	50 ± 14	3.8 ± 0.6	309 ± 10	5.4 ± 1.4	5 ± 15	1993.0–2007.6	*Angermann and Müller* (2008)
SLR NS	2.7 ± 0.3	45 ± 6	3.8 ± 0.2	327 ± 4	3.6 ± 0.4	4 ± 7	1993.0–2006.0	*Collilieux et al.* (2009)
SLR NS	2.6 ± 0.1	42 ± 3	3.1 ± 0.1	315 ± 2	5.5 ± 0.3	22 ± 10	1983.0–2009.0	*Altamimi et al.* (2011)
SLR NS	3.0 ± 0.2	55 ± 4	2.7 ± 0.2	328 ± 4	5.4 ± 0.4	22 ± 4	2002.3–2009.0	*Wu et al.* (2015)
SLR KFS	2.1 ± 0.1	45 ± 1	2.7 ± 0.1	321 ± 1	3.9 ± 0.1	21 ± 1	2002.3–2009.3	*Wu et al.* (2015)
GPS CM	2.1 ± 0.2	42 ± 4	3.2 ± 0.1	343 ± 2	3.9 ± 0.2	77 ± 2	1997.2–2004.2	*Lavallée et al.* (2006)
GPS RC	0.1 ± 0.2	39 ± 93	1.8 ± 0.2	342 ± 11	4.0 ± 0.2	22 ± 6	1994.0–2008.0	*Fritsche et al.* (2010)
GNSS RC	1.7 ± 0.3	73 ± 20	2.6 ± 0.4	295 ± 22	6.6 ± 0.6	59 ± 35	1994.0–2011.0	*Glaser et al.* (2015)
IM	1.1 ± 0.1	52 ± 4	2.7 ± 0.1	325 ± 2	1.2 ± 0.1	55 ± 5	2003.0–2007.0	*Swenson et al.* (2008)
IM	2.1	56	3.4	327	3.0	18	2003.0–2009.0	*Rietbroek et al.* (2012a)
IM	1.8 ± 0.1	49 ± 4	2.7 ± 0.1	329 ± 2	4.2 ± 0.2	31 ± 3	2002.3–2009.3	*Wu et al.* (2012)
FM	4.2	46	3.2	291	3.5	35	Variable	*Dong et al.* (1997)
FM	2.4	26	2.0	360	4.1	42	Variable	*Chen et al.* (1999)
FM	1.6	34	1.8	326	3.1	16	Variable	*Bouillé et al.* (2000)
FM	2.3	16	2.0	352	3.4	30	Variable	*Moore and Wang* (2003)
FM	2.0 ± 0.1	27 ± 2	2.0 ± 0.1	338 ± 1	2.8 ± 0.1	51 ± 2	1993.0–2006.0	*Collilieux et al.* (2009)

KA – Kinematic approach; NS – Network shift approach; KFS - Kalman filter and Rauch–Tung–Striebel smoother;
CM – CM approach; RC – Rigorous parameter combination; IM – Inverse model; FM – Forward model

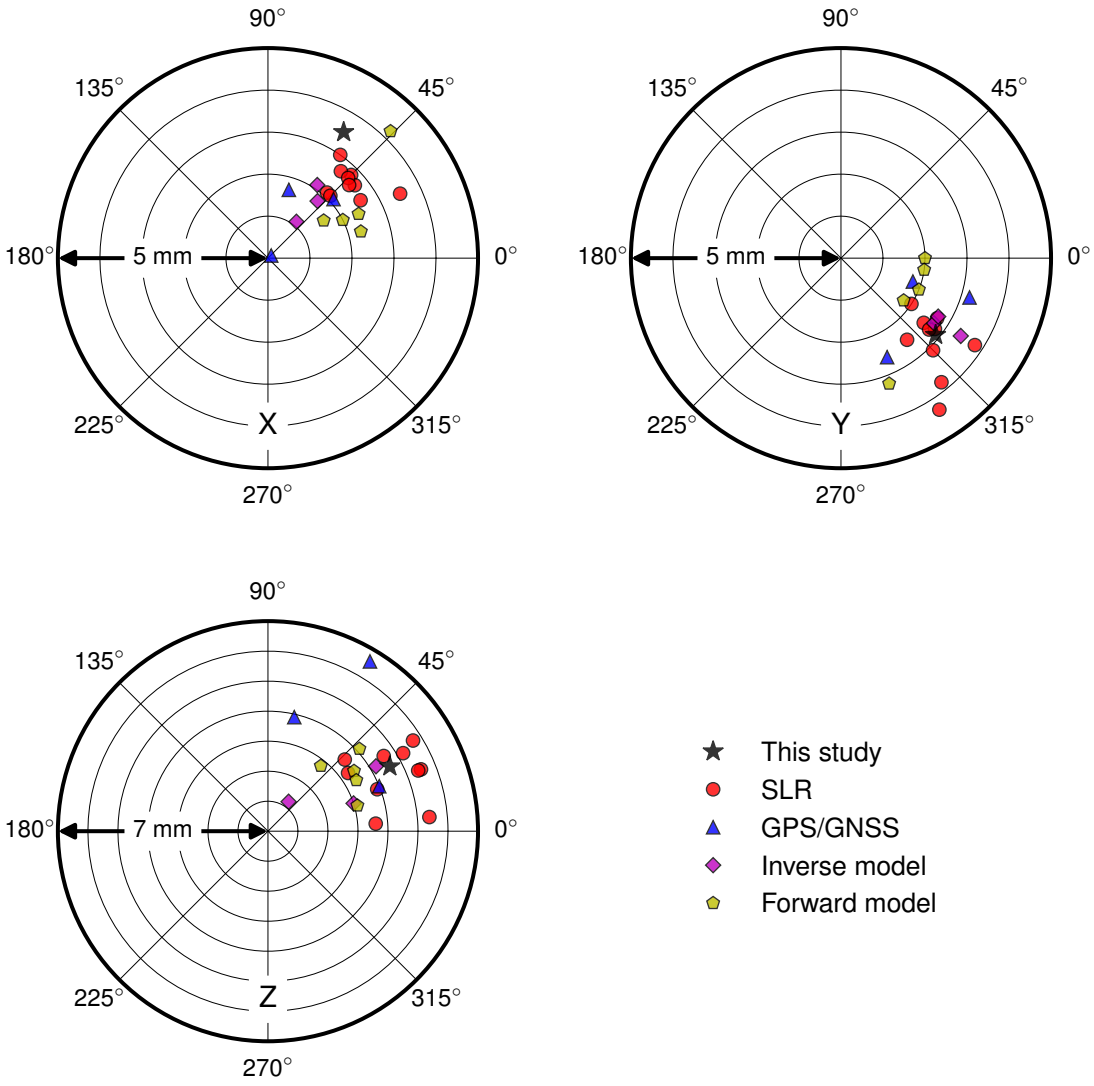

Figure 6.9 Phasor diagrams of the annual geocentre motion estimates listed in Table 6.4

6.4.2 Velocities and accelerations

Geocentre velocity estimates from satellite tracking data are unreliable for reasons already discussed in Sections 3.6 and 5.6.2. The SLR results from this study and that of *Argus* (2012) are only included in Table 6.5 for illustrative purposes as quantifications of the PDMT-induced geocentre velocity, since the net effect of GIA on the SLR network is expected to be much smaller. Unless a priori removed, the GIA signature can be recovered simultaneously with the PDMT contribution through inverse approaches that supplement GRACE gravimetry with other data sets (*Wu et al.*, 2010; *Rietbroek et al.*, 2012b). Given that the geodetic determination of the geocentre velocity is still in its infancy, the agreement between estimates of the GIA contribution and model predictions for the X and Z components is promising. The estimates of the PDMT contribution are more scattered and highly dependent on the modelling of the oceanic domain, as already noted by *Wu et al.* (2012).

Quadratic trends in the geocentre coordinates can be detected in both translational and global inversion results, but have only been recently investigated by *Wu et al.* (2015)

Table 6.5 Selected estimates of GIA and PDMT-induced geocentre velocities along the three Cartesian axes in mm yr^{-1}

Data	PDMT			GIA			Reference
	X	Y	Z	X	Y	Z	
SLR LAGEOS-1/2	-0.16 ± 0.05	-0.09 ± 0.06	-0.49 ± 0.09				This study
SLR LAGEOS-1/2	-0.22 ± 0.20	0.00 ± 0.16	0.02 ± 0.37				*Argus* (2012)
GRACE + ECCO	-0.12 ± 0.04	0.07 ± 0.03	-0.14 ± 0.05				*Swenson et al.* (2008)
GRACE + OMCT	-0.20 ± 0.04	-0.02 ± 0.03	0.06 ± 0.05				*Swenson et al.* (2008)
GRACE + SLE	-0.06 ± 0.02	0.05 ± 0.02	-0.21 ± 0.03				*Schrama et al.* (2014)
GRACE + ECCO + SV	-0.08 ± 0.04	0.29 ± 0.05	-0.16 ± 0.07	-0.10 ± 0.01	0.11 ± 0.02	-0.72 ± 0.06	*Wu et al.* (2010)
GRACE + Jason-1	-0.14	0.12	-0.37	-0.14	0.31	-0.71	*Rietbroek et al.* (2012b)
ICE-5G/LM+				-0.13	0.33	-0.81	*Klemann and Martinec* (2011)
ICE-5G/IJ05/VM2				-0.12	0.24	-0.48	*Wu et al.* (2012)

SLE – Oceanic domain replaced by a rotationally and gravitationally consistent solution of the sea level equation
SV – Surface velocities from GNSS data
LM+ – Viscosity profile with the viscosity of the lower mantle 20 times larger than that of the upper mantle

Table 6.6 Selected estimates of geocentre accelerations along the three Cartesian axes in mm yr^{-2}

Solution	X	Y	Z	Time span	Reference
SLR KA	0.02 ± 0.02	0.00 ± 0.02	0.00 ± 0.03	1995.0–2015.0	This study
SLR KA	-0.02 ± 0.01	-0.01 ± 0.02	-0.01 ± 0.02	1995.0–2015.0	CSR monthly
SLR NS	-0.01 ± 0.01	0.05 ± 0.01	-0.10 ± 0.02	1993.0–2009.0	*Wu et al.* (2015)
SLR KFS	-0.07 ± 0.02	0.05 ± 0.02	0.13 ± 0.04	2002.3–2009.3	*Wu et al.* (2015)
IM	0.03 ± 0.02	0.00 ± 0.02	0.11 ± 0.03	2002.3–2015.0	*Wu and Heflin* (2015)

and *Wu and Heflin* (2015). In the latter study, detrended GNSS-derived surface displacements, GRACE gravity data and ECCO OBP estimates were inverted for surface mass coefficients up to degree and order 60 using the methodology described by *Wu et al.* (2006). The 95% uncertainties reported by *Wu and Heflin* (2015) were downscaled to 68% (one-sigma) uncertainties in Table 6.6, which also lists the results from the current study with associated formal errors obtained using the preferred stochastic models. All other formal errors in Table 6.6 may be underestimated due to the neglect of temporal correlations. Despite the different time spans, the estimated accelerations along the X and Y axes from the current study are in good agreement with the results of *Wu and Heflin* (2015), but neither of the two equatorial components is statistically significant. For the Z component, however, the estimates are inconsistent and vary considerably as a function of the fitted time period (*Wu et al.*, 2015).

6.5 Summary

Geocentre motion estimates obtained using the kinematic approach are strongly dependent on the choice of the geodetic datum. A fixed datum results in larger scatter along the Z axis and lower variability in the equatorial geocentre vector components compared to when the SLR network is allowed to deform. Nevertheless, if concurrently solving for loosely constrained station positions and unconstrained geocentre coordinates a near one-to-one correspondence between kinematic and network shift results is achievable, despite the correlations between station coordinates and geocentre coordinates. Compared with kinematic results, network shift estimates obtained without scale adjustments are more coherent than estimates recovered simultaneously with a scale factor. This offers further justification for the omission of the scale parameter in the network shift approach.

In addition to errors of draconitic origin, weekly geocentre motion time series are corrupted by tidal aliasing errors resulting from the undersampling of diurnal and semi-diurnal tidal constituents. Aliased tidal periods arising due to unmodelled or mismodelled tides are functions of the orbital arc length or the ground track repeat period of each satellite. The main aliases identified in LAGEOS–only geocentre motion time series correspond to the O_1, M_2 and S_2 tidal constituents. Comparing results derived using a variety of ocean tide models may partially clarify the source of these aliases, but such an analysis falls beyond the scope of this study.

The routine estimation of range biases for all SLR stations was shown to result in more scattered geocentre motion estimates with negative biases along the Y and Z axes. In contrast, allowing only data from a sub-network of high-performing stations to contribute to the determination of the geocentre coordinates while estimating range biases only for recommended stations reduces the scatter and improves the centring about zero for the Y and Z axes. This latter analysis strategy yields a geocentre vector with magnitudes varying in the range 3–7 mm, as determined from the superimposed annual and semi-

annual signals. The amplitudes and phases of the Y and Z annual components are in good agreement with results from a selection of studies employing different approaches, whereas the X annual component has a larger amplitude and a phase delay of about two weeks compared to the average of other SLR estimates. An analysis of monthly geocentre motion time series computed by CSR revealed that for longer sampling periods single and less elaborate stochastic models such as PL and AR(1) are more competitive due to the narrowing of the power spectra towards low frequencies dominated by PL noise. Draconitic errors were also identified in the CSR solution, confirming that they are not singular to this study.

Chapter 7

Conclusions and outlook

This study aimed to examine the observability of the geocentre coordinates in SLR solutions involving combinations of eight spherical geodetic satellites and establish a framework for the rigorous analysis of geocentre motion time series. To achieve this aim, the collinearity diagnosis algorithm developed by *Rebischung et al.* (2014) was first employed to evaluate the formal errors of weekly geocentre coordinates obtained using the network shift approach under various parameter setups. Detrimental parameterisations for the observability of the geocentre coordinates were identified and circumvented during the subsequent determination of geocentre motion time series from data spanning 20 years. These time series were analysed in the time domain to check for temporal dependencies among estimates and in the frequency domain to assess the contamination by modelling errors, particularly of draconitic origin. Stochastic and functional model parameters of interest were then simultaneously recovered from the time series using MLE and model-selection criteria. Finally, the relationship between kinematic estimates of geocentre motion and network shift results was investigated using coherence analysis and the most robust geocentre motion model was compared to published models.

7.1 Summary of findings

The analysis of weekly geocentre coordinate uncertainties over 2013 revealed that, regardless of the satellite combination, the Z geocentre coordinate is less observable by a factor of 2–3 than the equatorial geocentre coordinates in the absence of major collinearity problems. This is potentially due to factors such as the network effect perturbing especially the X and Z coordinates (*Collilieux et al.*, 2009) and the heterogeneous quality of SLR observations acquired by different stations located predominately at mid-latitudes with benign atmospheric conditions. In standard LAGEOS-1 and 2 solutions, the recovery of geopotential coefficients beyond degree and order 3 reduces the observability of the geocentre coordinates due to the known insensitivity of the two satellites to higher-degree

harmonics and larger correlations between geopotential coefficients and OPR acceleration parameters.

Given the small increase in data set size, the incorporation of sparse Etalon data alongside LAGEOS observations has minute benefits for the determination of geocentre motion only when omitting the estimation of geopotential coefficients. Conversely, the large LEO data yields of SLR stations coupled with the higher sensitivity of LEOs to geocentre motion contribute to a significant reduction of the geocentre coordinate uncertainties in MEO–LEO solutions obtained with certain parameterisation constraints. In particular, LARES can provide an improvement of 25–30% in observability over LAGEOS–Etalon solutions with lower bound formal error estimates of approximately 1.5 mm for the equatorial geocentre coordinates and 4 mm for the Z coordinate. LARES is currently the optimal LEO target, least perturbed by non-gravitational forces in its orbit, and can be expected to improve the origin definition of the TRF upon its incorporation alongside LAGEOS and, potentially, Etalon in ILRS products. Among the LEOs considered in this study, Stella was found to be least sensitive to geocentre motion due to its quasi-polar orbit, a results which attests the findings of the simulation study of *Kuang et al.* (2015).

Two parameterisations were identified as detrimental for the observability of the geocentre coordinates in LAGEOS–Starlette–Stella–Ajisai solutions, namely (1) the estimation of sub-weekly drag coefficients for Starlette, Stella and Ajisai and (2) the simultaneous adjustment of OPR acceleration parameters for the three LEOs and geopotential coefficients. Moreover, the correlations between along-track OPR parameters and SRP coefficients inflate the geocentre coordinate uncertainties when both types of parameters are solved for, irrespective of the satellite combination. In LAGEOS–LARES solutions, even the estimation of weekly drag coefficients for LARES drastically increases the formal errors of the geocentre coordinates. This problem can, nevertheless, be mitigated with minimal effect on the orbital fit by substituting drag coefficients for LARES with empirical along-track acceleration parameters.

The results obtained by means of collinearity diagnosis are primarily driven by statistical relationships between parameters and disregard modelling errors, which do not inherently limit the observability of geophysical parameters but can propagate into parameter estimates, particularly if major collinearity issues are present. Deficiencies in the modelling of Starlette, Stella and Ajisai orbits were exposed through the analysis of 20-year geocentre motion time series obtained with the network shift approach. Although measures were taken to bypass collinearity problems, the long-term LAGEOS–Starlette–Stella–Ajisai solution of geocentre coordinates displayed degraded repeatability compared to a LAGEOS–only solution of similar length. Therefore, a beneficial contribution of Starlette, Stella and Ajisai to the determination of geocentre motion appears unlikely with the currently attainable orbital fits limited by modelling imperfections related to gravitational perturbations and atmospheric drag. Non-gravitational orbital perturba-

tions are less problematic for LARES, but its short tracking history prevents a conclusive assessment of modelling errors affecting LAGEOS–LARES solutions.

Correlograms computed for the various geocentre motion time series from this study confirmed the presence of serial correlations among geocentre coordinate residuals, in analogy to results previously reported for other geodetic parameters. The rigorous modelling of temporal correlations involves the use of statistics to select an appropriate functional-stochastic model and the concurrent estimation of noise and functional model parameters using MLE. Functional models that include a quadratic parameter in addition to an intercept, a linear trend and annual and semi-annual periodic terms were invariably preferred for solutions of at least 12 years in length. The stochastic models preferred in most cases and thus recommended for future use are AR(1) plus WN and PL. The commonly employed stochastic assumption of uncorrelated residuals may, however, hold for short time series spanning a few years, as exemplified by the LAGEOS–LARES solution. For sampling periods longer than a week, the AR(1) and PL stochastic models are more competitive on their own as a result of the narrowing power spectra towards low frequencies exhibiting PL behaviour.

The use of preferred noise models led to an inflation of the estimated annual amplitude and phase uncertainties by an average factor of 1.6 compared to the case when a classical WN model is employed. Linear and quadratic trend errors increased by a factor of 2.2–2.3. Excluding WN, an incorrect stochastic model choice affects primarily the linear trend uncertainties and has only a small effect on the formal errors of seasonal signal estimates. The observed PL behaviour at frequencies below 4 cpy is responsible for the amplification of functional model parameter uncertainties.

Due to lack of physical justification, the inclusion of a scale parameter in the functional model of the network shift approach has been deemed redundant by several authors (*Tregoning and van Dam*, 2005; *Lavallée et al.*, 2006; *Collilieux et al.*, 2012; *Wu et al.*, 2015). In support of this argument, the current study showed that draconitic errors contaminating geocentre motion estimates can be reduced when omitting the scale parameter. Moreover, network shift estimates obtained without adjusting the scale are more coherent with kinematic estimates of geocentre coordinates obtained simultaneously with station positions. Prohibiting individual station displacements by fixing station coordinates during the estimation of geocentre motion with the kinematic approach leads to considerably worse agreement between kinematic and network shift results.

In agreement with the IERS Conventions (2010), FES2004 (*Lyard et al.*, 2006) was adopted in this study to model the effects of ocean tides on the geopotential and station positions. Tidal aliasing errors potentially related to the mismodelling of tidal constituents in FES2004 were identified in the power spectra of weekly geocentre motion time series derived from LAGEOS-1 and 2 data. The main aliases correspond to the O_1, M_2 and S_2 tidal constituents and occur at long periods that are functions of the orbital arc length of seven days or the ground track repeat period of LAGEOS-2.

The most robust geocentre motion estimates from this study were obtained using a sub-network of 31 reliable stations with marginally better global distribution compared to the entire network. The analysis of data from this sub-network yielded an annual geocentre motion model in reasonable agreement with published results, particularly for the Y and Z components. Present-day annual geocentre motion has amplitudes that vary from 2–3 mm for the equatorial coordinates to 4–6 mm in the Z component, as estimated from geodetic data and predicted by geophysical fluid models. The geocentre vector magnitude peaks in July at ~ 7 mm.

7.2 Perspectives and directions for future work

SLR currently provides invaluable information for the determination of the origin and scale of the TRF and long-period variations in the Earth's gravity field. Technological developments related to SLR systems will naturally attract improvements in the ranging accuracy, whereas the densification of the ILRS network in the southern and western Earth hemispheres will provide improved data coverage and mitigate the network effect on parameter estimates. To fully exploit future developments in ground infrastructure, the models used in data reduction also need to evolve. This will particularly benefit the reprocessing of historical data affected by large biases.

Apart from the unbalanced network geometry, system and satellite-specific systematic errors and orbit modelling deficiencies represent the main barriers for improvements in SLR-derived geocentre motion estimates. The determination of CoM corrections for spherical geodetic satellites has considerably improved in recent years (*Otsubo and Appleby*, 2003; *Otsubo et al.*, 2015), but range biases known to be correlated with station heights are still routinely adjusted for a selection of stations. As shown in this study, this practice leads to additional correlations between parameters and increases the scatter of the estimated geocentre coordinates. A focused effort to resolve range biases for all past and present SLR stations over the entire observational history is well-warranted.

Atmospheric drag is one of the largest contributors to the error budget of orbit computations for low Earth satellites. Drag coefficients empirically adjusted to compensate for poor knowledge of atmospheric density affect the determination of the geocentre coordinates and likely other parameters of geophysical interest. Enhancements in atmospheric models would allow a better exploitation of LEO data by alleviating the need to estimate frequent drag coefficients that artificially improve orbital fits. Efforts are also ongoing to further improve the atmospheric refraction correction at optical frequencies using three-dimensional atmospheric ray tracing (*Hulley and Pavlis*, 2007) and dual wavelength (or two-colour) SLR observations (*Wijaya and Brunner*, 2011).

The work presented in this thesis unveiled several research gaps and software maintenance tasks that may be addressed in subsequent projects. Potential directions for future research are discussed below.

- Faust, the POD software of Newcastle University, will regularly require modifications to keep it in line with developments in data processing and background models. With the transition to the ITRF2014 in the near term, the post-seismic deformation correction to the linear station model will need to be implemented using Fortran routines provided by the IERS.[1] Additionally, EOP series consistent with the ITRF2014 should be adopted when available.
- Another foreseen Faust update is the implementation of system-depended CoM corrections for Starlette, Stella and LARES, which are expected to be released by the ILRS in the near future. This will reduce the systematic biases affecting ranges to the three LEO satellites and ultimately lead to improved estimates of geodetic parameters.
- The modelling of non-tidal effects on the geopotential and station positions is an ongoing research topic that deserves further attention. To date, the consequences for geocentre motion estimates have only been studied for non-tidal atmospheric pressure loading (*Sośnica et al.*, 2013; *König et al.*, 2015).
- In this study, the satellite-dependent scale factors were empirically derived based on typical orbital fits and are invariant from one weekly solution to another. A robust alternative based on variance component estimation using, for example, an iterative algorithm (*Bloßfeld et al.*, 2015) may be employed. This would ensure an appropriate relative calibration of scale factors that implicitly accounts for variations in data quantity and quality.
- The collinearity diagnosis algorithm could be adapted and applied to study the effects of different parameterisations on the observability of other parameters such as the scale of the TRF and low-degree geopotential coefficients. Estimates of these parameters may also exhibit temporal correlations that can be modelled using MLE.
- The refined modelling of post-seismic deformations in the ITRF2014 should attract improvements in geocentre motion determination. An evaluation of solutions based on a priori station coordinates from the SLRF2008 and the ITRF2014 constitutes another topic for future investigation.
- Further research is required to clarify the source of the tidal aliasing errors identified in the geocentre motion time series derived from LAGEOS-1 and 2 data. Such errors may be exacerbated by the incorporation of additional satellites with different ground track repeat periods. Comparisons with results obtained using more recent ocean tide models such as FES2012 and the Goddard Ocean Tide (GOT) 4.8 may prove beneficial.
- Geocentre motion time series with a sampling period of one week were derived in this study, in agreement with the current practice of ILRS ACs. Given the prevalence

[1] http://itrf.ensg.ign.fr/ITRF_solutions/2014/ITRF2014_files.php

of WN at high frequencies that lack signals of particular interest, time series with larger sampling periods may be better suited for the determination of a reliable annual geocentre motion model to serve the scientific community.

- The performance of the most robust geocentre motion model from the current study may be appraised in relation to independent models by studying the effects on the POD of altimetry satellites and GMSL estimates or on surface mass change determinations from GRACE data.
- Finally, as the LARES observational history increases, it would be beneficial to further assess the consistency between LAGEOS–only and LAGEOS–LARES solutions with the prospect of a future LARES contribution to the ITRF origin and scale definitions in sight. In view of the larger gravitational orbital perturbations sustained by LARES compared to MEOs, an informed decision has to be taken of whether to estimate corrections to the static geopotential model or adopt a model with time-variable low-degrees coefficients.

SLR remains the state-of-the-art satellite geodetic technique for geocentre motion determination, unlikely to be surpassed in the near term by GNSS and DORIS. The current study demonstrated that improvements in LAGEOS-based geocentre motion estimates are achievable using LEO data, subject to the reduction of data and force modelling errors. It is hoped that this work will act as an incentive for the geodetic community to intensify research efforts aiming to fully exploit the current constellation of spherical geodetic satellites.

References

Agnew, D. C. (1992), The time-domain behavior of power-law noises, *Geophysical Research Letters*, *19*(4), 333–336, doi:10.1029/91GL02832.

Akaike, H. (1974), A new look at the statistical model identification, *IEEE Transactions on Automatic Control*, *19*(6), 716–723, doi:10.1109/TAC.1974.1100705.

Altamimi, Z., C. Boucher, and P. Sillard (2002), New trends for the realization of the International Terrestrial Reference System, *Advances in Space Research*, *30*(2), 175–184, doi:10.1016/S0273-1177(02)00282-X.

Altamimi, Z., X. Collilieux, J. Legrand, B. Garayt, and C. Boucher (2007), ITRF2005: a new release of the International Terrestrial Reference Frame based on time series of station positions and Earth orientation parameters, *Journal of Geophysical Research: Solid Earth*, *112*(B9), doi:10.1029/2007JB004949.

Altamimi, Z., X. Collilieux, and L. Métivier (2011), ITRF2008: an improved solution of the International Terrestrial Reference Frame, *Journal of Geodesy*, *85*(8), 457–473, doi:10.1007/s00190-011-0444-4.

Amiri-Simkooei, A. R., C. C. J. M. Tiberius, and P. J. G. Teunissen (2007), Assessment of noise in GPS coordinate time series: methodology and results, *Journal of Geophysical Research: Solid Earth*, *112*(B7), doi:10.1029/2006JB004913.

Angermann, D., and H. Müller (2008), On the strength of SLR observations to realize the scale and origin of the terrestrial reference system, in *Observing our changing Earth*, *International Association of Geodesy Symposia*, vol. 133, edited by M. G. Sideris, pp. 21–29, Springer, doi:10.1007/978-3-540-85426-5_3.

Argus, D. F. (2007), Defining the translational velocity of the reference frame of Earth, *Geophysical Journal International*, *169*(3), 830–838, doi:10.1111/j.1365-246X.2007.03344.x.

Argus, D. F. (2012), Uncertainty in the velocity between the mass center and surface of Earth, *Journal of Geophysical Research: Solid Earth*, *117*(B10), doi:10.1029/2012JB009196.

Arnell, N. W. (1999), A simple water balance model for the simulation of streamflow over a large geographic domain, *Journal of Hydrology*, *217*(3–4), 314–335, doi:10.1016/S0022-1694(99)00023-2.

Azaneu, M., R. Kerr, and M. M. Mata (2014), Assessment of the representation of Antarctic bottom water properties in the ECCO2 reanalysis, *Ocean Science*, *10*(6), 923–946, doi:10.5194/os-10-923-2014.

Barletta, V. R., L. S. Sørensen, and R. Forsberg (2013), Scatter of mass changes estimates at basin scale for Greenland and Antarctica, *The Cryosphere*, *7*(5), 1411–1432, doi:10.5194/tc-7-1411-2013.

Baur, O., M. Kuhn, and W. Featherstone (2013), Continental mass change from GRACE over 2002–2011 and its impact on sea level, *Journal of Geodesy*, *87*(2), 117–125, doi:10.1007/s00190-012-0583-2.

Beckley, B. D., F. G. Lemoine, S. B. Luthcke, R. D. Ray, and N. P. Zelensky (2007), A reassessment of global and regional mean sea level trends from TOPEX and Jason-1 altimetry based on revised reference frame and orbits, *Geophysical Research Letters*, *34*(14), doi:10.1029/2007GL030002.

Bergmann-Wolf, I., L. Zhang, and H. Dobslaw (2014), Global eustatic sea-level variations for the approximation of geocenter motion from GRACE, *Journal of Geodetic Science*, *4*(1), 37–48, doi:10.2478/jogs-2014-0006.

Beutler, G. (2005), *Methods of celestial mechanics*, vol. I: Physical, mathematical and numerical principles, 464 pp., Springer, Berlin.

Blaha, G. (1982), Free networks: minimum norm solution as obtained by the inner adjustment constraint method, *Bulletin Géodésique*, *56*(3), 209–219, doi:10.1007/BF02525582.

Blewitt, G. (2003), Self-consistency in reference frames, geocenter definition, and surface loading of the solid Earth, *Journal of Geophysical Research: Solid Earth*, *108*(B2), doi:10.1029/2002JB002082.

Blewitt, G., and P. J. Clarke (2003), Inversion of Earth's changing shape to weigh sea level in static equilibrium with surface mass redistribution, *Journal of Geophysical Research: Solid Earth*, *108*(B6), ETG 13–1–ETG 13–13, doi:10.1029/2002JB002290.

Blewitt, G., M. B. Heflin, F. H. Webb, U. J. Lindqwister, and R. P. Malla (1992), Global coordinates with centimeter accuracy in the International Terrestrial Reference Frame using GPS, *Geophysical Research Letters*, *19*(9), 853–856, doi:10.1029/92GL00775.

Blewitt, G., D. A. Lavallée, P. J. Clarke, and K. Nurutdinov (2001), A new global mode of Earth deformation: seasonal cycle detected, *Science*, *294*(5550), 2342–2345, doi:10.1126/science.1065328.

Blewitt, G., et al. (2010), Geodetic observations and global reference frame contributions to understanding sea-level rise and variability, in *Understanding sea-level rise and variability*, edited by J. A. Church, P. L. Woodworth, T. Aarup, and W. S. Wilson, pp. 256–284, Wiley-Blackwell, doi:10.1002/9781444323276.ch9.

Bloßfeld, M., M. Seitz, and D. Angermann (2014), Non-linear station motions in epoch and multi-year reference frames, *Journal of Geodesy*, *88*(1), 45–63, doi:10.1007/s00190-013-0668-6.

Bloßfeld, M., H. Müller, M. Gerstl, V. Štefka, J. Bouman, F. Göttl, and M. Horwath (2015), Second-degree Stokes coefficients from multi-satellite SLR, *Journal of Geodesy*, *89*(9), 857–871, doi:10.1007/s00190-015-0819-z.

Bogusz, J., and A. Klos (2015), On the significance of periodic signals in noise analysis of GPS station coordinates time series, *GPS Solutions*, doi:10.1007/s10291-015-0478-9.

Boomkamp, H. J. (1998), Combination of altimetry data from different satellite missions, PhD Thesis, Aston University, Birmingham, UK.

Bos, M. S., R. M. S. Fernandes, S. D. P. Williams, and L. Bastos (2008), Fast error analysis of continuous GPS observations, *Journal of Geodesy*, *82*(3), 157–166, doi:10.1007/s00190-007-0165-x.

Bos, M. S., R. M. S. Fernandes, S. D. P. Williams, and L. Bastos (2013), Fast error analysis of continuous GNSS observations with missing data, *Journal of Geodesy*, *87*(4), 351–360, doi:10.1007/s00190-012-0605-0.

Bos, M. S., S. D. P. Williams, I. B. Araújo, and L. Bastos (2014), The effect of temporal correlated noise on the sea level rate and acceleration uncertainty, *Geophysical Journal International*, *196*(3), 1423–1430, doi:10.1093/gji/ggt481.

Boucher, C., Z. Altamimi, M. Feissel, and P. Sillard (1996), Results and analysis of the ITRF94, *IERS Technical Note No. 20*, Central Bureau of IERS – Observatoire de Paris.

Bouillé, F., A. Cazenave, J. M. Lemoine, and J.-F. Crétaux (2000), Geocenter motion from the DORIS space system and laser data to the Lageos satellites: comparison with surface loading data, *Geophysical Journal International*, *143*(1), 71–82, doi:10.1046/j.1365-246x.2000.00196.x.

Brockwell, P. J., and R. A. Davis (2002), *Introduction to time series and forecasting*, 2nd ed., 434 pp., Springer, New York.

Butterworth, S. (1930), On the theory of filter amplifiers, *Experimental Wireless and the Wireless Engineer*, *7*, 536–541.

Capderou, M. (2014), *Handbook of satellite orbits: from Kepler to GPS*, 922 pp., Springer, Cham.

Cerri, L., et al. (2010), Precision orbit determination standards for the Jason series of altimeter missions, *Marine Geodesy*, *33*, 379–418, doi:10.1080/01490419.2010.488966.

Chambers, D. P. (2006), Observing seasonal steric sea level variations with GRACE and satellite altimetry, *Journal of Geophysical Research: Oceans*, *111*(C3), doi:10.1029/2005JC002914.

Chambers, D. P., J. Wahr, and R. S. Nerem (2004), Preliminary observations of global ocean mass variations with GRACE, *Geophysical Research Letters*, *31*(13), doi:10.1029/2004GL020461.

Chao, B. F. (2006), Earth's oblateness and its temporal variations, *Comptes Rendus Geoscience*, *338*(14–15), 1123–1129", doi:10.1016/j.crte.2006.09.014.

Chatfield, C. (2003), *The analysis of time series: an introduction*, 6th ed., 333 pp., Chapman & Hall/CRC, Boca Raton.

Chen, J. L., and C. R. Wilson (2008), Low degree gravity changes from GRACE, Earth rotation, geophysical models, and satellite laser ranging, *Journal of Geophysical Research: Solid Earth*, *113*(B6), doi:10.1029/2007JB005397.

Chen, J. L., C. R. Wilson, R. J. Eanes, and R. S. Nerem (1999), Geophysical interpretation of observed geocenter variations, *Journal of Geophysical Research: Solid Earth*, *104*(B2), 2683–2690, doi:10.1029/1998JB900019.

Chen, J. L., C. R. Wilson, B. D. Tapley, and J. C. Ries (2004), Low degree gravitational changes from GRACE: validation and interpretation, *Geophysical Research Letters*, *31*(22), doi:10.1029/2004GL021670.

Chen, W., J. C. Li, J. Ray, W. B. Shen, and C. L. Huang (2015), Consistent estimates of the dynamic figure parameters of the earth, *Journal of Geodesy*, *89*(2), 179–188, doi:10.1007/s00190-014-0768-y.

Cheng, M., and B. D. Tapley (1999), Seasonal variations in low degree zonal harmonics of the Earth's gravity field from satellite laser ranging observations, *Journal of Geophysical Research: Solid Earth*, *104*(B2), 2667–2681, doi:10.1029/1998JB900036.

Cheng, M., C. K. Shum, and B. D. Tapley (1997), Determination of long-term changes in the Earth's gravity field from satellite laser ranging observations, *Journal of Geophysical Research: Solid Earth*, *102*(B10), 22,377–22,390, doi:10.1029/97JB01740.

Cheng, M., J. C. Ries, and B. D. Tapley (2013a), Geocenter variations from analysis of SLR data, in *Reference Frames for Applications in Geosciences*, *International Association of Geodesy Symposia*, vol. 138, edited by Z. Altamimi and X. Collilieux, pp. 19–25, Springer, Berlin, doi:10.1007/978-3-642-32998-2_4.

Cheng, M., B. D. Tapley, and J. C. Ries (2013b), Deceleration in the Earth's oblateness, *Journal of Geophysical Research: Solid Earth*, *118*(2), 740–747, doi:10.1002/jgrb.50058.

Church, J. A., N. J. White, R. Coleman, K. Lambeck, and J. X. Mitrovica (2004), Estimates of the regional distribution of sea level rise over the 1950–2000 period, *Journal of Climate*, *17*(13), 2609–2625, doi:10.1175/1520-0442(2004)017<2609:EOTRDO>2.0.CO;2.

Ciufolini, I., A. Paolozzi, E. C. Pavlis, J. C. Ries, V. Gurzadyan, R. Koenig, R. Matzner, R. Penrose, and G. Sindoni (2012), Testing general relativity and gravitational physics using the LARES satellite, *The European Physical Journal Plus*, *127*(11), 133, doi:10.1140/epjp/i2012-12133-8.

Clarke, P. J., D. A. Lavallée, G. Blewitt, T. van Dam, and J. Wahr (2005), Effect of gravitational consistency and mass conservation on seasonal surface mass loading models, *Geophysical Research Letters*, *32*(8), doi:10.1029/2005GL022441.

Clarke, P. J., D. A. Lavallée, G. Blewitt, and T. van Dam (2007), Basis functions for the consistent and accurate representation of surface mass loading, *Geophysical Journal International*, *171*(1), 1–10, doi:10.1111/j.1365-246X.2007.03493.x.

Collilieux, X., and G. Wöppelmann (2011), Global sea-level rise and its relation to the terrestrial reference frame, *Journal of Geodesy*, *85*(1), 9–22, doi:10.1007/s00190-010-0412-4.

Collilieux, X., Z. Altamimi, J. Ray, T. van Dam, and X. Wu (2009), Effect of the satellite laser ranging network distribution on geocenter motion estimation, *Journal of Geophysical Research: Solid Earth*, *114*(B4), doi:10.1029/2008JB005727.

Collilieux, X., L. Métivier, Z. Altamimi, T. Dam, and J. Ray (2011), Quality assessment of GPS reprocessed terrestrial reference frame, *GPS Solutions*, *15*(3), 219–231, doi:10.1007/s10291-010-0184-6.

Collilieux, X., T. Dam, J. Ray, D. Coulot, L. Métivier, and Z. Altamimi (2012), Strategies to mitigate aliasing of loading signals while estimating GPS frame parameters, *Journal of Geodesy*, *86*(1), 1–14, doi:10.1007/s00190-011-0487-6.

Cook, G. E. (1965), Satellite drag coefficients, *Planetary and Space Science*, *13*(10), 929–946, doi:10.1016/0032-0633(65)90150-9.

Couhert, A., et al. (2015), Towards the 1 mm/y stability of the radial orbit error at regional scales, *Advances in Space Research*, *55*(1), 2–23, doi:10.1016/j.asr.2014.06.041.

Coulot, D., A. Pollet, X. Collilieux, and P. Berio (2010), Global optimization of core station networks for space geodesy: application to the referencing of the SLR EOP with respect to ITRF, *Journal of Geodesy*, *84*(1), 31–50, doi:10.1007/s00190-009-0342-1.

Coulot, D., P. Rebischung, A. Pollet, L. Grondin, and G. Collot (2015), Global optimization of GNSS station reference networks, *GPS Solutions*, *19*(4), 569–577, doi:10.1007/s10291-014-0416-2.

Crétaux, J.-F., L. Soudarin, F. J. M. Davidson, M.-C. Gennero, M. Bergé-Nguyen, and A. Cazenave (2002), Seasonal and interannual geocenter motion from SLR and DORIS measurements: comparison with surface loading data, *Journal of Geophysical Research: Solid Earth*, *107*(B12), ETG 16–1–ETG 16–9, doi:10.1029/2002JB001820.

Davis, J. L., P. Elósegui, J. X. Mitrovica, and M. E. Tamisiea (2004), Climate-driven deformation of the solid earth from GRACE and GPS, *Geophysical Research Letters*, *31*(24), doi:10.1029/2004GL021435.

de Viron, O., G. Schwarzbaum, F. Lott, and V. Dehant (2005), Diurnal and subdiurnal effects of the atmosphere on the Earth rotation and geocenter motion, *Journal of Geophysical Research: Solid Earth*, *110*(B11), doi:10.1029/2005JB003761.

Dee, D. P., et al. (2011), The ERA-Interim reanalysis: configuration and performance of the data assimilation system, *Quarterly Journal of the Royal Meteorological Society*, *137*(656), 553–597, doi:10.1002/qj.828.

DeMets, C., R. G. Gordon, D. F. Argus, and S. Stein (1994), Effect of recent revisions to the geomagnetic reversal time scale on estimates of current plate motions, *Geophysical Research Letters*, *21*(20), 2191–2194, doi:10.1029/94GL02118.

Desai, S. D. (2002), Observing the pole tide with satellite altimetry, *Journal of Geophysical Research: Oceans*, *107*(C11), 7–1–7–13, doi:10.1029/2001JC001224.

Desai, S. D., W. Bertiger, and B. J. Haines (2014), Self-consistent treatment of tidal variations in the geocenter for precise orbit determination, *Journal of Geodesy*, *88*(8), 735–747, doi:10.1007/s00190-014-0718-8.

Devoti, R., M. Fermi, C. Sciarretta, V. Luceri, R. Pacione, P. Rutigliano, and F. Vespe (1999), CGS geocenter time series from SLR and GPS data, in *IERS Analysis Campaign to Investigate Motions of the Geocenter*, edited by J. Ray, IERS Technical Note 25, pp. 41–46, Central Bureau of IERS – Observatoire de Paris.

Dill, R. (2008), Hydrological model LSDM for operational Earth rotation and gravity field variations, *Scientific Technical Report STR08/09*, Deutsches GeoForschungsZentrum, Potsdam, doi:10.2312/GFZ.b103-08095.

Dill, R., and H. Dobslaw (2013), Numerical simulations of global-scale high-resolution hydrological crustal deformations, *Journal of Geophysical Research: Solid Earth*, *118*(9), 5008–5017, doi:10.1002/jgrb.50353.

Döll, P., F. Kaspar, and B. Lehner (2003), A global hydrological model for deriving water availability indicators: model tuning and validation, *Journal of Hydrology*, *270*(1–2), 105–134, doi:10.1016/S0022-1694(02)00283-4.

Dong, D., J. O. Dickey, Y. Chao, and M. Cheng (1997), Geocenter variations caused by atmosphere, ocean and surface ground water, *Geophysical Research Letters*, *24*(15), 1867–1870, doi:10.1029/97GL01849.

Dong, D., T. Yunck, and M. B. Heflin (2003), Origin of the International Terrestrial Reference Frame, *Journal of Geophysical Research: Solid Earth*, *108*(B4), ETG 8–1–ETG 8–10, doi:10.1029/2002JB002035.

Dong, D., W. Qu, P. Fang, and D. Peng (2014), Non-linearity of geocentre motion and its impact on the origin of the terrestrial reference frame, *Geophysical Journal International*, *198*(2), 1071–1080, doi:10.1093/gji/ggu187.

Dow, J. M., R. E. Neilan, and C. Rizos (2009), The International GNSS Service in a changing landscape of Global Navigation Satellite Systems, *Journal of Geodesy*, *83*(3–4), 191–198, doi:10.1007/s00190-008-0300-3.

Dziewonski, A. M., and D. L. Anderson (1981), Preliminary reference Earth model, *Physics of the Earth and Planetary Interiors*, *25*(4), 297–356, doi:10.1016/0031-9201(81)90046-7.

Exertier, P., P. Bonnefond, F. Deleflie, F. Barlier, M. Kasser, R. Biancale, and Y. Ménard (2006), Contribution of laser ranging to Earth's sciences, *Comptes Rendus Geoscience*, *338*(14–15), 958–967, doi:10.1016/j.crte.2006.09.019.

Faraway, J., and C. Chatfield (1998), Time series forecasting with neural networks: a comparative study using the air line data, *Journal of the Royal Statistical Society: Series C (Applied Statistics)*, *47*(2), 231–250, doi:10.1111/1467-9876.00109.

Farrell, W. E. (1972), Deformation of the Earth by surface loads, *Reviews of Geophysics*, *10*(3), 761–797, doi:10.1029/RG010i003p00761.

Feissel-Vernier, M., K. L. Bail, P. Berio, D. Coulot, G. Ramillien, and J.-J. Valette (2006), Geocentre motion measured with DORIS and SLR, and predicted by geophysical models, *Journal of Geodesy*, *80*(8–11), 637–648, doi:10.1007/s00190-006-0079-z.

Fekete, B. M., C. J. Vörösmarty, and W. Grabs (2002), High-resolution fields of global runoff combining observed river discharge and simulated water balances, *Global Biogeochemical Cycles*, *16*(3), 15–1–15–10, doi:10.1029/1999GB001254.

Ferland, R., and M. Piraszewski (2009), The IGS-combined station coordinates, earth rotation parameters and apparent geocenter, *Journal of Geodesy*, *83*(3–4), 385–392, doi:10.1007/s00190-008-0295-9.

Fritsche, M., R. Dietrich, A. Rülke, M. Rothacher, and P. Steigenberger (2010), Low-degree earth deformation from reprocessed GPS observations, *GPS Solutions*, *14*(2), 165–175, doi:10.1007/s10291-009-0130-7.

Gazeaux, J., et al. (2013), Detecting offsets in GPS time series: first results from the detection of offsets in GPS experiment, *Journal of Geophysical Research: Solid Earth*, *118*(5), 2397–2407, doi:10.1002/jgrb.50152.

Glaser, S., M. Fritsche, K. Sośnica, C. J. Rodríguez-Solano, K. Wang, R. Dach, U. Hugentobler, M. Rothacher, and R. Dietrich (2015), A consistent combination of GNSS and SLR with minimum constraints, *Journal of Geodesy*, *89*(12), 1165–1180, doi:10.1007/s00190-015-0842-0.

Gobinddass, M. L., P. Willis, O. de Viron, A. Sibthorpe, N. P. Zelensky, J. C. Ries, R. Ferland, Y. Bar-Sever, and M. Diament (2009a), Systematic biases in DORIS-derived geocenter time series related to solar radiation pressure mis-modeling, *Journal of Geodesy*, *83*(9), 849–858, doi:10.1007/s00190-009-0303-8.

Gobinddass, M. L., et al. (2009b), Improving DORIS geocenter time series using an empirical rescaling of solar radiation pressure models, *Advances in Space Research*, *44*(11), 1279–1287, doi:10.1016/j.asr.2009.08.004.

Gosling, S. N., and N. W. Arnell (2011), Simulating current global river runoff with a global hydrological model: model revisions, validation, and sensitivity analysis, *Hydrological Processes*, *25*(7), 1129–1145, doi:10.1002/hyp.7727.

Govind, R., F. G. Lemoine, J.-J. Valette, D. Chinn, and N. P. Zelensky (2010), DORIS geodesy: a dynamic determination of geocentre location, *Advances in Space Research*, *46*(12), 1593–1605, doi:10.1016/j.asr.2010.08.025.

Grafarend, E. W., J. Engels, and P. Varga (1997), The spacetime gravitational field of a deformable body, *Journal of Geodesy*, *72*(1), 11–30, doi:10.1007/s001900050144.

Greatbatch, R. J. (1994), A note on the representation of steric sea level in models that conserve volume rather than mass, *Journal of Geophysical Research: Oceans*, *99*(C6), 12,767–12,771, doi:10.1029/94JC00847.

Greff-Lefftz, M. (2000), Secular variation of the geocenter, *Journal of Geophysical Research: Solid Earth*, *105*(B11), 25,685–25,692, doi:10.1029/2000JB900224.

Greff-Lefftz, M., and H. Legros (2007), Fluid core dynamics and degree-one deformations: slichter mode and geocenter motion, *Physics of the Earth and Planetary Interiors*, *161*(3–4), 150–160, doi:10.1016/j.pepi.2006.12.003.

Greff-Lefftz, M., L. Métivier, and J. Besse (2010), Dynamic mantle density heterogeneities and global geodetic observables, *Geophysical Journal International*, *180*(3), 1080–1094, doi:10.1111/j.1365-246X.2009.04490.x.

Griffiths, J., and J. Ray (2013), Sub-daily alias and draconitic errors in the IGS orbits, *GPS Solutions*, *17*(3), 413–422, doi:10.1007/s10291-012-0289-1.

Gross, R. S., G. Beutler, and H.-P. Plag (2009), Integrated scientific and societal user requirements and functional specifications for the GGOS, in *Global Geodetic Observing System*, edited by H.-P. Plag and M. Pearlman, pp. 209–224, Springer, doi:10.1007/978-3-642-02687-4_7.

Güntner, A. (2008), Improvement of global hydrological models using GRACE data, *Surveys in Geophysics*, *29*(4–5), 375–397, doi:10.1007/s10712-008-9038-y.

Hackl, M., R. Malservisi, U. Hugentobler, and R. Wonnacott (2011), Estimation of velocity uncertainties from GPS time series: examples from the analysis of the South African TrigNet network, *Journal of Geophysical Research: Solid Earth*, *116*(B11), doi:10.1029/2010JB008142.

Hanna, E., et al. (2013), Ice-sheet mass balance and climate change, *Nature*, *498*(7452), 51–59, doi:10.1038/nature12238.

Heflin, M. B., and M. M. Watkins (1999), Geocenter estimates from the Global Positioning System, in *IERS Analysis Campaign to Investigate Motions of the Geocenter*, edited by J. Ray, IERS Technical Note 25, pp. 55–70, Central Bureau of IERS, Paris.

Heiskanen, W. A., and H. Moritz (1967), *Physical geodesy*, 364 pp., W. H. Freeman, San Francisco.

Hofmann-Wellenhof, B., and H. Moritz (2006), *Physical geodesy*, 2nd, corr. ed., 403 pp., Springer, Wien.

Hughes, C. W., and S. D. P. Williams (2010), The color of sea level: importance of spatial variations in spectral shape for assessing the significance of trends, *Journal of Geophysical Research: Oceans*, *115*(C10), doi:10.1029/2010JC006102.

Hulley, G. C., and E. C. Pavlis (2007), A ray-tracing technique for improving satellite laser ranging atmospheric delay corrections, including the effects of horizontal refractivity gradients, *Journal of Geophysical Research: Solid Earth*, *112*(B6), doi:10.1029/2006JB004834.

Hunter, J. D. (2007), Matplotlib: a 2D graphics environment, *Computing in Science Engineering*, *9*(3), 90–95, doi:10.1109/mcse.2007.55.

Ivins, E. R., and T. S. James (2005), Antarctic glacial isostatic adjustment: a new assessment, *Antarctic Science*, *17*, 541–553, doi:10.1017/S0954102005002968.

Jacobs, G. A., G. H. Born, M. E. Parke, and P. C. Allen (1992), The global structure of the annual and semiannual sea surface height variability from Geosat altimeter data, *Journal of Geophysical Research: Oceans*, *97*(C11), 17,813–17,828, doi:10.1029/92JC01708.

Jansen, M. J. F., B. C. Gunter, and J. Kusche (2009), The impact of GRACE, GPS and OBP data on estimates of global mass redistribution, *Geophysical Journal International*, *177*(1), 1–13, doi:10.1111/j.1365-246X.2008.04031.x.

Jin, S., and G. Feng (2013), Large-scale variations of global groundwater from satellite gravimetry and hydrological models, 2002–2012, *Global and Planetary Change*, *106*, 20–30, doi:10.1016/j.gloplacha.2013.02.008.

Kalnay, E., et al. (1996), The NCEP/NCAR 40-year reanalysis project, *Bulletin of the American Meteorological Society*, *77*(3), 437–471, doi:10.1175/1520-0477(1996)077<0437:TNYRP>2.0.CO;2.

Kang, Z., B. D. Tapley, J. L. Chen, J. C. Ries, and S. Bettadpur (2009), Geocenter variations derived from GPS tracking of the GRACE satellites, *Journal of Geodesy*, *83*(10), 895–901, doi:10.1007/s00190-009-0307-4.

Kar, S. (1997), Long-period variations in the geocenter observed from laser tracking of multiple Earth satellites, PhD Thesis, The University of Texas at Austin, US.

King, M. A., M. Keshin, P. L. Whitehouse, I. D. Thomas, G. Milne, and R. E. M. Riva (2012), Regional biases in absolute sea-level estimates from tide gauge data due to residual unmodeled vertical land movement, *Geophysical Research Letters*, *39*(14), doi:10.1029/2012GL052348.

Klemann, V., and Z. Martinec (2011), Contribution of glacial-isostatic adjustment to the geocenter motion, *Tectonophysics*, *511*(3–4), 99–108, doi:10.1016/j.tecto.2009.08.031.

König, R., P. Schwintzer, A. Bode, and C. Reigber (1996), GFZ-1: a small laser satellite mission for gravity field model improvement, *Geophysical Research Letters*, *23*(22), 3143–3146, doi:10.1029/96GL02574.

König, R., Z. Chen, C. Reigber, and P. Schwintzer (1999), Improvement in global gravity field recovery using GFZ-1 satellite laser tracking data, *Journal of Geodesy*, *73*(8), 398–406, doi:10.1007/s001900050259.

König, R., F. Flechtner, J.-C. Raimondo, and M. Vei (2015), Atmospheric loading and mass variation effects on the SLR-defined geocenter, International Association of Geodesy Symposia, Springer, doi:10.1007/1345_2015_60.

Kramer, H. J. (2002), *Observation of the Earth and its environment: survey of missions and sensors*, 4th ed., 1510 pp., Springer, Berlin.

Kreemer, C., G. Blewitt, and F. Maerten (2006), Co- and postseismic deformation of the 28 March 2005 Nias M_w 8.7 earthquake from continuous GPS data, *Geophysical Research Letters*, *33*(7), doi:10.1029/2005GL025566.

Kuang, D., Y. Bar-Sever, and B. Haines (2015), Analysis of orbital configurations for geocenter determination with GPS and low-Earth orbiters, *Journal of Geodesy*, *89*(5), 471–481, doi:10.1007/s00190-015-0792-6.

Kuehne, J., and C. R. Wilson (1991), Terrestrial water storage and polar motion, *Journal of Geophysical Research: Solid Earth*, *96*(B3), 4337–4345, doi:10.1029/90JB02573.

Kusche, J., and E. J. O. Schrama (2005), Surface mass redistribution inversion from global GPS deformation and Gravity Recovery and Climate Experiment (GRACE) gravity data, *Journal of Geophysical Research: Solid Earth*, *110*(B9), doi:10.1029/2004JB003556.

Kuzin, S. P., S. K. Tatevian, S. G. Valeev, and V. A. Fashutdinova (2010), Studies of the geocenter motion using 16-years DORIS data, *Advances in Space Research*, *46*(10), 1292–1298, doi:10.1016/j.asr.2010.06.038.

Langbein, J. (2004), Noise in two-color electronic distance meter measurements revisited, *Journal of Geophysical Research: Solid Earth*, *109*(B4), doi:10.1029/2003JB002819.

Langbein, J., and H. Johnson (1997), Correlated errors in geodetic time series: implications for time-dependent deformation, *Journal of Geophysical Research: Solid Earth*, *102*(B1), 591–603, doi:10.1029/96JB02945.

Lavallée, D. A., and G. Blewitt (2002), Degree-1 Earth deformation from very long baseline interferometry measurements, *Geophysical Research Letters*, *29*(20), 28–1–28–4, doi:10.1029/2002GL015883.

Lavallée, D. A., T. van Dam, G. Blewitt, and P. J. Clarke (2006), Geocenter motions from GPS: a unified observation model, *Journal of Geophysical Research: Solid Earth*, *111*(B5), doi:10.1029/2005JB003784.

Lavallée, D. A., P. Moore, P. J. Clarke, E. J. Petrie, T. van Dam, and M. A. King (2010), J2: an evaluation of new estimates from GPS, GRACE, and load models compared to SLR, *Geophysical Research Letters*, *37*(22), doi:10.1029/2010GL045229.

Lejba, P., and S. Schillak (2011), Determination of station positions and velocities from laser ranging observations to Ajisai, Starlette and Stella satellites, *Advances in Space Research*, *47*(4), 654–662, doi:10.1016/j.asr.2010.10.013.

Liang, X., D. P. Lettenmaier, E. F. Wood, and S. J. Burges (1994), A simple hydrologically based model of land surface water and energy fluxes for general circulation models, *Journal of Geophysical Research: Atmospheres*, *99*(D7), 14,415–14,428, doi:10.1029/94JD00483.

Lomb, N. R. (1976), Least-squares frequency analysis of unequally spaced data, *Astrophysics and Space Science*, *39*(2), 447–462, doi:10.1007/BF00648343.

Lucchesi, D. M., I. Ciufolini, J. I. Andrés, E. C. Pavlis, R. Peron, R. Noomen, and D. G. Currie (2004), LAGEOS II perigee rate and eccentricity vector excitations residuals and the Yarkovsky–Schach effect, *Planetary and Space Science*, *52*(8), 699–710, doi:10.1016/j.pss.2004.01.007.

Luceri, V., E. C. Pavlis, B. Pace, D. König, M. Kuzmicz-Cieslak, and G. Bianco (2015), Overview of the ILRS contribution to the development of ITRF2013, International Association of Geodesy Symposia, Springer, doi:10.1007/1345_2015_153.

Lyard, F., F. Lefevre, T. Letellier, and O. Francis (2006), Modelling the global ocean tides: modern insights from FES2004, *Ocean Dynamics*, *56*(5–6), 394–415, doi:10.1007/s10236-006-0086-x.

Maier, A., S. Krauss, W. Hausleitner, and O. Baur (2012), Contribution of satellite laser ranging to combined gravity field models, *Advances in Space Research*, *49*(3), 556–565, doi:10.1016/j.asr.2011.10.026.

Malla, R. P., S. C. Wu, and S. M. Lichten (1993), Geocenter location and variations in earth orientation using Global Positioning System measurements, *Journal of Geophysical Research: Solid Earth*, *98*(B3), 4611–4617, doi:10.1029/92JB02588.

Mao, A., C. G. A. Harrison, and T. H. Dixon (1999), Noise in GPS coordinate time series, *Journal of Geophysical Research: Solid Earth*, *104*(B2), 2797–2816, doi:10.1029/1998JB900033.

Marini, J. W., and C. W. Murray (1973), Correction of laser range tracking data for atmospheric refraction at elevations above 10 degrees, *NASA-TM-X-70555*, Goddard Space Flight Center, Greenbelt, MD.

Meindl, M., G. Beutler, D. Thaller, R. Dach, and A. Jäggi (2013), Geocenter coordinates estimated from GNSS data as viewed by perturbation theory, *Advances in Space Research*, *51*(7), 1047–1064, doi:10.1016/j.asr.2012.10.026.

Melachroinos, S. A., F. G. Lemoine, N. P. Zelensky, D. D. Rowlands, S. B. Luthcke, and O. Bordyugov (2013), The effect of geocenter motion on Jason-2 orbits and the mean sea level, *Advances in Space Research*, *51*(8), 1323–1334, doi:10.1016/j.asr.2012.06.004.

Mendes, V. B., and E. C. Pavlis (2004), High-accuracy zenith delay prediction at optical wavelengths, *Geophysical Research Letters*, *31*(14), doi:10.1029/2004GL020308.

Mendes, V. B., G. Prates, E. C. Pavlis, D. E. Pavlis, and R. B. Langley (2002), Improved mapping functions for atmospheric refraction correction in SLR, *Geophysical Research Letters*, *29*(10), 53–1–53–4, doi:10.1029/2001GL014394.

Métivier, L., M. Greff-Lefftz, and M. Diament (2006), Mantle lateral variations and elastogravitational deformations – I. Numerical modelling, *Geophysical Journal International*, *167*(3), 1060–1076, doi:10.1111/j.1365-246X.2006.03159.x.

Métivier, L., M. Greff-Lefftz, and Z. Altamimi (2010), On secular geocenter motion: the impact of climate changes, *Earth and Planetary Science Letters*, *296*(3–4), 360–366, doi:10.1016/j.epsl.2010.05.021.

Milani, A., A. M. Nobili, and P. Farinella (1987), *Non-gravitational perturbations and satellite geodesy*, 125 pp., Adam Hilger, Bristol.

Milly, P. C. D., and A. B. Shmakin (2002), Global modeling of land water and energy balances. Part I: the Land Dynamics (LaD) model, *Journal of Hydrometeorology*, *3*, 283–299, doi:10.1175/1525-7541(2002)003<0283:GMOLWA>2.0.CO;2.

Minott, P. O., T. W. Zagwodzki, T. Varghese, and M. Seldon (1993), Prelaunch optical characterization of the Laser Geodynamic Satellite, *NASA-TP-3400*, Goddard Space Flight Center, Greenbelt, MD.

Mitrovica, J. X., and W. R. Peltier (1989), Pleistocene deglaciation and the global gravity field, *Journal of Geophysical Research: Solid Earth*, *94*(B10), 13,651–13,671, doi:10.1029/JB094iB10p13651.

Montenbruck, O., and E. Gill (2000), *Satellite orbits: models, methods and applications*, 4th, corr. ed., 369 pp., Springer, Berlin.

Montgomery, D. C., E. A. Peck, and G. G. Vining (2012), *Introduction to linear regression analysis*, 5th ed., 672 pp., Wiley, Hoboken, NJ.

Moore, P., and J. Wang (2003), Geocentre variation from laser tracking of LAGEOS1/2 and loading data, *Advances in Space Research*, *31*(8), 1927–1933, doi:10.1016/S0273-1177(03)00170-4.

Moore, P., and S. D. P. Williams (2014), Integration of altimetric lake levels and GRACE gravimetry over Africa: inferences for terrestrial water storage change 2003–2011, *Water Resources Research*, *50*(12), 9696–9720, doi:10.1002/2014WR015506.

Moore, P., H. J. Boomkamp, S. Carnochan, and R. J. Walmsley (1999), Faust: multi-satellite orbital dynamics software, *Advances in Space Research*, *23*(4), 785–795, doi:10.1016/S0273-1177(99)00144-1.

Moore, P., Q. Zhang, and A. Alothman (2005), Annual and semiannual variations of the Earth's gravitational field from satellite laser ranging and CHAMP, *Journal of Geophysical Research: Solid Earth*, *110*(B6), doi:10.1029/2004JB003448.

Morel, L., and P. Willis (2005), Terrestrial reference frame effects on global sea level rise determination from TOPEX/Poseidon altimetric data, *Advances in Space Research*, *36*(3), 358–368, doi:10.1016/j.asr.2005.05.113.

Munekane, H. (2007), Ocean mass variations from GRACE and tsunami gauges, *Journal of Geophysical Research: Solid Earth*, *112*(B7), doi:10.1029/2006JB004618.

Nijssen, B., G. M. O'Donnell, D. P. Lettenmaier, D. Lohmann, , and E. F. Wood (2001), Predicting the discharge of global rivers, *Journal of Climate*, *14*, 3307–3323, doi:10.1175/1520-0442(2001)014<3307:PTDOGR>2.0.CO;2.

Noll, C. E. (2010), The crustal dynamics data information system: a resource to support scientific analysis using space geodesy, *Advances in Space Research*, *45*(12), 1421–1440, doi:10.1016/j.asr.2010.01.018.

Ohmura, A. (2010), Completing the World Glacier Inventory, *Annals of Glaciology*, *50*(53), 144–148, doi:10.3189/172756410790595840.

Ohmura, A. (2011), Observed mass balance of mountain glaciers and Greenland ice sheet in the 20th century and the present trends, *Surveys in Geophysics*, *32*(4–5), 537–554, doi:10.1007/s10712-011-9124-4.

Otsubo, T., and G. M. Appleby (2003), System-dependent center-of-mass correction for spherical geodetic satellites, *Journal of Geophysical Research: Solid Earth*, *108*(B4), doi:10.1029/2002JB002209.

Otsubo, T., R. A. Sherwood, G. M. Appleby, and R. Neubert (2015), Center-of-mass corrections for sub-cm-precision laser-ranging targets: Starlette, Stella and LARES, *Journal of Geodesy*, *89*(4), 303–312, doi:10.1007/s00190-014-0776-y.

Paolozzi, A., and I. Ciufolini (2013), LARES successfully launched in orbit: satellite and mission description, *Acta Astronautica*, *91*, 313–321, doi:10.1016/j.actaastro.2013.05.011.

Paulson, A., S. Zhong, and J. Wahr (2007), Inference of mantle viscosity from GRACE and relative sea level data, *Geophysical Journal International*, *171*(2), 497–508, doi:10.1111/j.1365-246X.2007.03556.x.

Pavlis, D. E., J. Wilmert, and J. J. McCarthy (2013), GEODYN II system description, vol. 1–5, *Contractor Report, SGT Inc.*, Goddard Space Flight Center, Greenbelt, MD.

Pavlis, E. C. (1999), Fortnightly resolution geocenter series: a combined analysis of LAGEOS 1 and 2 SLR data (1993-1996), in *IERS Analysis Campaign to Investigate Motions of the Geocenter*, edited by J. Ray, IERS Technical Note 25, pp. 75–84, Central Bureau of IERS, Paris.

Pavlis, N. K., S. A. Holmes, S. C. Kenyon, and J. K. Factor (2012), The development and evaluation of the Earth Gravitational Model 2008 (EGM2008), *Journal of Geophysical Research: Solid Earth*, *117*(B4), doi:10.1029/2011JB008916.

Pearlman, M. R., J. J. Degnan, and J. M. Bosworth (2002), The International Laser Ranging Service, *Advances in Space Research*, *30*(2), 135–143, doi:10.1016/S0273-1177(02)00277-6.

Peltier, W. R. (2004), Global glacial isostasy and the surface of the ice-age Earth: the ICE-5G (VM2) model and GRACE, *Annual Review of Earth and Planetary Sciences*, *32*(1), 111–149, doi:10.1146/annurev.earth.32.082503.144359.

Penna, N. T., and M. P. Stewart (2003), Aliased tidal signatures in continuous GPS height time series, *Geophysical Research Letters*, *30*(23), doi:10.1029/2003GL018828.

Petit, G., and B. Luzum (2010), IERS Conventions (2010), *IERS Technical Note No. 36*, Verlag des Bundesamts für Kartographie und Geodäsie, Frankfurt am Main.

Picone, J. M., A. E. Hedin, D. P. Drob, and A. C. Aikin (2002), NRLMSISE-00 empirical model of the atmosphere: statistical comparisons and scientific issues, *Journal of Geophysical Research: Space Physics*, *107*(A12), SIA 15–1–SIA 15–16, doi:10.1029/2002JA009430.

Press, W. H., S. A. Teukolsky, W. T. Vetterling, and B. P. Flannery (1992), *Numerical recipes in FORTRAN*, 2nd ed., 963 pp., Cambridge University Press, New York.

Quinn, K. J., and R. M. Ponte (2011), Estimating high frequency ocean bottom pressure variability, *Geophysical Research Letters*, *38*(8), doi:10.1029/2010GL046537.

Raup, B., A. Racoviteanu, S. J. S. Khalsa, C. Helm, R. Armstrong, and Y. Arnaud (2007), The GLIMS geospatial glacier database: a new tool for studying glacier change, *Global and Planetary Change*, *56*(1–2), 101–110, doi:10.1016/j.gloplacha.2006.07.018.

Rawlings, J. O., S. G. Pantula, and D. A. Dickey (1998), *Applied regression analysis: a research tool*, 2nd ed., 660 pp., Springer, New York.

Ray, J. (1999), IERS campaign to investigate motions of the geocenter, *IERS Technical Note No. 25*, Central Bureau of IERS – Observatoire de Paris, Paris.

Ray, J., Z. Altamimi, X. Collilieux, and T. van Dam (2008), Anomalous harmonics in the spectra of GPS position estimates, *GPS Solutions*, *12*(1), 55–64, doi:10.1007/s10291-007-0067-7.

Ray, J., J. Griffiths, X. Collilieux, and P. Rebischung (2013), Subseasonal GNSS positioning errors, *Geophysical Research Letters*, *40*(22), 5854–5860, doi:10.1002/2013GL058160.

Ray, R. D., and R. M. Ponte (2003), Barometric tides from ECMWF operational analyses, *Annales Geophysicae*, *21*(8), 1897–1910, doi:10.5194/angeo-21-1897-2003.

Rebischung, P. (2014), Can GNSS contribute to improving the ITRF definition?, PhD Thesis, Observatoire de Paris, France.

Rebischung, P., and B. Garayt (2013), Recent results from the IGS terrestrial frame combinations, in *Reference Frames for Applications in Geosciences*, *International Association of Geodesy Symposia*, vol. 138, edited by Z. Altamimi and X. Collilieux, pp. 69–74, Springer, doi:10.1007/978-3-642-32998-2_12.

Rebischung, P., J. Griffiths, J. Ray, R. Schmid, X. Collilieux, and B. Garayt (2012), IGS08: the IGS realization of ITRF2008, *GPS Solutions*, *16*(4), 483–494, doi:10.1007/s10291-011-0248-2.

Rebischung, P., Z. Altamimi, and T. Springer (2014), A collinearity diagnosis of the GNSS geocenter determination, *Journal of Geodesy*, *88*(1), 65–85, doi:10.1007/s00190-013-0669-5.

Rebischung, P., Z. Altamimi, J. Ray, and B. Garayt (2016), The IGS contribution to ITRF2014, *Journal of Geodesy*, doi:10.1007/s00190-016-0897-6.

Reigber, C. (1981), Representation of orbital element variations and force function with respect to various reference systems, *Bulletin Géodésique*, *55*(2), 111–131, doi:10.1007/BF02530834.

Ries, J. (2008), SLR center of mass offset for Starlette and Stella, GGOS Working Group on Ground Networks Communications Meeting, 16 April 2008, Vienna.

Ries, J. C., R. J. Eanes, C. K. Shum, and M. M. Watkins (1992), Progress in the determination of the gravitational coefficient of the Earth, *Geophysical Research Letters*, *19*(6), 529–531, doi:10.1029/92GL00259.

Rietbroek, R., S.-E. Brunnabend, C. Dahle, J. Kusche, F. Flechtner, J. Schröter, and R. Timmermann (2009), Changes in total ocean mass derived from GRACE, GPS, and ocean modeling with weekly resolution, *Journal of Geophysical Research: Oceans*, *114*(C11), doi:10.1029/2009JC005449.

Rietbroek, R., M. Fritsche, S.-E. Brunnabend, I. Daras, J. Kusche, J. Schröter, F. Flechtner, and R. Dietrich (2012a), Global surface mass from a new combination of GRACE, modelled OBP and reprocessed GPS data, *Journal of Geodynamics*, *59–60*, 64–71, doi:10.1016/j.jog.2011.02.003.

Rietbroek, R., S.-E. Brunnabend, J. Kusche, and J. Schröter (2012b), Resolving sea level contributions by identifying fingerprints in time-variable gravity and altimetry, *Journal of Geodynamics*, *59–60*, 72–81, doi:10.1016/j.jog.2011.06.007.

Rietbroek, R., M. Fritsche, C. Dahle, S.-E. Brunnabend, M. Behnisch, J. Kusche, F. Flechtner, J. Schröter, and R. Dietrich (2014), Can GPS-derived surface loading bridge a GRACE mission gap?, *Surveys in Geophysics*, *35*(6), 1267–1283, doi:10.1007/s10712-013-9276-5.

Rodell, M., et al. (2004), The Global Land Data Assimilation System, *Bulletin of the American Meteorological Society*, *85*(3), 381–394, doi:10.1175/BAMS-85-3-381.

Rubincam, D. P. (1988), Yarkovsky thermal drag on LAGEOS, *Journal of Geophysical Research: Solid Earth*, *93*(B11), 13,805–13,810, doi:10.1029/JB093iB11p13805.

Rubincam, D. P. (1990), Drag on the LAGEOS satellite, *Journal of Geophysical Research: Solid Earth*, *95*(B4), 4881–4886, doi:10.1029/JB095iB04p04881.

Rülke, A., R. Dietrich, M. Fritsche, M. Rothacher, and P. Steigenberger (2008), Realization of the terrestrial reference system by a reprocessed global GPS network, *Journal of Geophysical Research: Solid Earth*, *113*(B8), doi:10.1029/2007JB005231.

Salstein, D. A., R. M. Ponte, and K. Cady-Pereira (2008), Uncertainties in atmospheric surface pressure fields from global analyses, *Journal of Geophysical Research: Atmospheres*, *113*(D14), doi:10.1029/2007JD009531.

Santamaría-Gómez, A., M.-N. Bouin, X. Collilieux, and G. Wöppelmann (2011), Correlated errors in GPS position time series: implications for velocity estimates, *Journal of Geophysical Research: Solid Earth*, *116*(B1), doi:10.1029/2010JB007701.

Santamaría-Gómez, A., M. Gravelle, X. Collilieux, M. Guichard, B. Martín-Míguez, P. Tiphaneau, and G. Wöppelmann (2012), Mitigating the effects of vertical land motion in tide gauge records using a state-of-the-art GPS velocity field, *Global and Planetary Change*, *98–99*, 6–17, doi:10.1016/j.gloplacha.2012.07.007.

Scargle, J. D. (1982), Studies in astronomical time series analysis. II. Statistical aspects of spectral analysis of unevenly spaced data, *The Astrophysical Journal*, *263*, 835–853, doi:10.1086/160554.

Schrama, E. J. O., B. Wouters, and R. Rietbroek (2014), A mascon approach to assess ice sheet and glacier mass balances and their uncertainties from GRACE data, *Journal of Geophysical*

Research: Solid Earth, *119*(7), 6048–6066, doi:10.1002/2013JB010923.

Schuh, H., and D. Behrend (2012), VLBI: a fascinating technique for geodesy and astrometry, *Journal of Geodynamics*, *61*, 68–80, doi:10.1016/j.jog.2012.07.007.

Schwarz, G. (1978), Estimating the dimension of a model, *The Annals of Statistics*, *6*(2), 461–464, doi:10.1214/aos/1176344136.

Seeber, G. (2003), *Satellite geodesy*, 2nd ed., 589 pp., De Gruyter, Berlin.

Shepherd, A., et al. (2012), A reconciled estimate of ice-sheet mass balance, *Science*, *338*(6111), 1183–1189, doi:10.1126/science.1228102.

Sillard, P., and C. Boucher (2001), A review of algebraic constraints in terrestrial reference frame datum definition, *Journal of Geodesy*, *75*(2–3), 63–73, doi:10.1007/s001900100166.

Sośnica, K. (2014), Determination of precise satellite orbits and geodetic parameters using satellite laser ranging, PhD Thesis, Astronomical Institute, Faculty of Science, University of Bern, Switzerland.

Sośnica, K., D. Thaller, R. Dach, A. Jäggi, and G. Beutler (2013), Impact of loading displacements on SLR-derived parameters and on the consistency between GNSS and SLR results, *Journal of Geodesy*, *87*(8), 751–769, doi:10.1007/s00190-013-0644-1.

Sośnica, K., A. Jäggi, D. Thaller, G. Beutler, and R. Dach (2014), Contribution of Starlette, Stella, and AJISAI to the SLR-derived global reference frame, *Journal of Geodesy*, *88*(8), 789–804, doi:10.1007/s00190-014-0722-z.

Sośnica, K., A. Jäggi, U. Meyer, D. Thaller, G. Beutler, D. Arnold, and R. Dach (2015), Time variable Earth's gravity field from SLR satellites, *Journal of Geodesy*, *89*(10), 945–960, doi:10.1007/s00190-015-0825-1.

Spatar, C. B., P. Moore, and P. J. Clarke (2015), Collinearity assessment of geocentre coordinates derived from multi-satellite SLR data, *Journal of Geodesy*, *89*(12), 1197–1216, doi:10.1007/s00190-015-0845-x.

Standish, E. M., X. X. Newhall, J. G. Williams, and W. F. Folkner (1995), JPL planetary and lunar ephemerides, DE403/LE403, *Interoffice Memorandum 314.10-127*, Jet Propulsion Laboratory, Pasadena, CA.

Štěpánek, P., C. J. Rodríguez-Solano, U. Hugentobler, and V. Filler (2014), Impact of orbit modeling on DORIS station position and Earth rotation estimates, *Advances in Space Research*, *53*(7), 1058–1070, doi:10.1016/j.asr.2014.01.007.

Stolz, A. (1976a), Changes in the position of the geocentre due to seasonal variations in air mass and ground water, *Geophysical Journal of the Royal Astronomical Society*, *44*(1), 19–26, doi:10.1111/j.1365-246X.1976.tb00272.x.

Stolz, A. (1976b), Changes in the position of the geocentre due to variations in sea-level, *Bulletin Géodésique*, *50*(2), 159–168, doi:10.1007/BF02522315.

Sun, W., and J. Dong (2014), Geo-center movement caused by huge earthquakes, *Journal of Geodynamics*, *76*, 1–7, doi:10.1016/j.jog.2014.02.008.

Sutanudjaja, E. H., L. P. H. van Beek, S. M. de Jong, F. C. van Geer, and M. F. P. Bierkens (2011), Large-scale groundwater modeling using global datasets: a test case for the Rhine-Meuse basin, *Hydrology and Earth System Sciences*, *15*(9), 2913–2935, doi:10.5194/hess-15-2913-2011.

Swenson, S., D. Chambers, and J. Wahr (2008), Estimating geocenter variations from a combination of GRACE and ocean model output, *Journal of Geophysical Research: Solid Earth*, *113*(B8), doi:10.1029/2007JB005338.

Syed, T. H., J. S. Famiglietti, M. Rodell, J. L. Chen, and C. R. Wilson (2008), Analysis of terrestrial water storage changes from GRACE and GLDAS, *Water Resources Research*, *44*(2), doi:10.1029/2006WR005779.

Tapley, B. D., S. Bettadpur, M. M. Watkins, and C. Reigber (2004a), The gravity recovery and climate experiment: mission overview and early results, *Geophysical Research Letters*, *31*(9), doi:10.1029/2004GL019920.

Tapley, B. D., B. E. Schutz, and G. H. Born (2004b), *Statistical orbit determination*, 547 pp., Elsevier, Burlington, MA.

Thaller, D., R. Dach, M. Seitz, G. Beutler, M. Mareyen, and B. Richter (2011), Combination of GNSS and SLR observations using satellite co-locations, *Journal of Geodesy*, *85*(5), 257–272, doi:10.1007/s00190-010-0433-z.

Thaller, D., K. Sośnica, R. Dach, A. Jäggi, G. Beutler, M. Mareyen, and B. Richter (2014), Geocenter coordinates from GNSS and combined GNSS-SLR solutions using satellite co-locations, in *Earth on the Edge: Science for a Sustainable Planet*, *International Association of Geodesy Symposia*, vol. 139, edited by C. Rizos and P. Willis, pp. 129–134, Springer, doi:10.1007/978-3-642-37222-3_16.

Thomas, M. (2002), Ocean induced variations of Earth's rotation - results from a simultaneous model of global circulation and tides, PhD Thesis, University of Hamburg, Germany.

Thomson, R. E., and W. J. Emery (2014), *Data analysis methods in physical oceanography*, 3rd ed., 716 pp., Elsevier, Boston, MA.

Timmermann, R., S. Danilov, J. Schröter, C. Böning, D. Sidorenko, and K. Rollenhagen (2009), Ocean circulation and sea ice distribution in a finite element global sea ice–ocean model, *Ocean Modelling*, *27*(3–4), 114–129, doi:10.1016/j.ocemod.2008.10.009.

Torge, W., and J. Müller (2012), *Geodesy*, 4th ed., 434 pp., De Gruyter, Berlin.

Tregoning, P., and T. van Dam (2005), Effects of atmospheric pressure loading and seven-parameter transformations on estimates of geocenter motion and station heights from space geodetic observations, *Journal of Geophysical Research: Solid Earth*, *110*(B3), doi:10.1029/2004JB003334.

Trupin, A. S., M. F. Meier, and J. M. Wahr (1992), Effect of melting glaciers on the Earth's rotation and gravitational field: 1965–1984, *Geophysical Journal International*, *108*(1), 1–15, doi:10.1111/j.1365-246X.1992.tb00835.x.

van Beek, L. P. H., Y. Wada, and M. F. P. Bierkens (2011), Global monthly water stress: 1. Water balance and water availability, *Water Resources Research*, *47*(7), doi:10.1029/2010WR009791.

Vigue, Y., S. M. Lichten, G. Blewitt, M. B. Heflin, and R. P. Malla (1992), Precise determination of Earth's center of mass using measurements from the Global Positioning System, *Geophysical Research Letters*, *19*(14), 1487–1490, doi:10.1029/92GL01575.

Wahr, J., H. DaZhong, and A. Trupin (1995), Predictions of vertical uplift caused by changing polar ice volumes on a viscoelastic Earth, *Geophysical Research Letters*, *22*(8), 977–980, doi:10.1029/94GL02840.

Wahr, J., M. Molenaar, and F. Bryan (1998), Time variability of the Earth's gravity field: hydrological and oceanic effects and their possible detection using GRACE, *Journal of Geophysical Research: Solid Earth*, *103*(B12), 30,205–30,229, doi:10.1029/98JB02844.

Wahr, J., D. Wingham, and C. Bentley (2000), A method of combining ICESat and GRACE satellite data to constrain antarctic mass balance, *Journal of Geophysical Research: Solid Earth*, *105*(B7), 16,279–16,294, doi:10.1029/2000JB900113.

Wallace, P. T., and N. Capitaine (2006), Precession-nutation procedures consistent with IAU 2006 resolutions, *Astronomy and Astrophysics*, *459*(3), 981–985, doi:10.1051/0004-

6361:20065897.

Wang, H., L. Xiang, L. Jia, L. Jiang, Z. Wang, B. Hu, and P. Gao (2012), Load Love numbers and Green's functions for elastic Earth models PREM, iasp91, ak135, and modified models with refined crustal structure from Crust 2.0, *Computers & Geosciences*, *49*, 190–199, doi:10.1016/j.cageo.2012.06.022.

Watkins, M. M., and R. J. Eanes (1997), Observations of tidally coherent diurnal and semidiurnal variations in the geocenter, *Geophysical Research Letters*, *24*(17), 2231–2234, doi:10.1029/97GL52059.

Welch, P. D. (1967), The use of fast Fourier transform for the estimation of power spectra: a method based on time averaging over short, modified periodograms, *IEEE Transactions on Audio and Electroacoustics*, *15*(2), 70–73, doi:10.1109/TAU.1967.1161901.

Wessel, P., W. H. F. Smith, R. Scharroo, J. Luis, and F. Wobbe (2013), Generic mapping tools: improved version released, *EOS Transactions American Geophysical Union*, *94*(45), 409–410, doi:10.1002/2013EO450001.

Widén-Nilsson, E., S. Halldin, and C. yu Xu (2007), Global water-balance modelling with WASMOD-M: parameter estimation and regionalisation, *Journal of Hydrology*, *340*(1–2), 105–118, doi:10.1016/j.jhydrol.2007.04.002.

Wijaya, D. D., and F. K. Brunner (2011), Atmospheric range correction for two-frequency SLR measurements, *Journal of Geodesy*, *85*(9), 623–635, doi:10.1007/s00190-011-0469-8.

Williams, S. D. P. (2003), The effect of coloured noise on the uncertainties of rates estimated from geodetic time series, *Journal of Geodesy*, *76*(9–10), 483–494, doi:10.1007/s00190-002-0283-4.

Williams, S. D. P. (2008), CATS: GPS coordinate time series analysis software, *GPS Solutions*, *12*(2), 147–153, doi:10.1007/s10291-007-0086-4.

Williams, S. D. P., Y. Bock, P. Fang, P. Jamason, R. M. Nikolaidis, L. Prawirodirdjo, M. Miller, and D. J. Johnson (2004), Error analysis of continuous GPS position time series, *Journal of Geophysical Research: Solid Earth*, *109*(B3), B03,412 1–19, doi:10.1029/2003JB002741.

Williams, S. D. P., P. Moore, M. A. King, and P. L. Whitehouse (2014), Revisiting GRACE Antarctic ice mass trends and accelerations considering autocorrelation, *Earth and Planetary Science Letters*, *385*, 12–21, doi:10.1016/j.epsl.2013.10.016.

Willis, P., J.-P. Berthias, and Y. E. Bar-Server (2006), Systematic errors in the Z-geocenter derived using satellite tracking data: a case study from SPOT-4 DORIS data in 1998, *Journal of Geodesy*, *79*(10–11), 567–572, doi:10.1007/s00190-005-0013-9.

Willis, P., et al. (2010), The International DORIS Service (IDS): toward maturity, *Advances in Space Research*, *45*(12), 1408–1420, doi:10.1016/j.asr.2009.11.018.

Wöppelmann, G., C. Letetrel, A. Santamaría-Gómez, M.-N. Bouin, X. Collilieux, Z. Altamimi, S. D. P. Williams, and B. Martín-Míguez (2009), Rates of sea-level change over the past century in a geocentric reference frame, *Geophysical Research Letters*, *36*(12), doi:10.1029/2009GL038720.

Wöppelmann, G., M. Marcos, A. Santamaría-Gómez, B. Martín-Míguez, M.-N. Bouin, and M. Gravelle (2014), Evidence for a differential sea level rise between hemispheres over the twentieth century, *Geophysical Research Letters*, *41*(5), 1639–1643, doi:10.1002/2013GL059039.

Wu, X., and M. B. Heflin (2015), A global assessment of accelerations in surface mass transport, *Geophysical Research Letters*, *42*(16), 6716–6723, doi:10.1002/2015GL064941.

Wu, X., D. F. Argus, M. B. Heflin, E. R. Ivins, and F. H. Webb (2002), Site distribution and aliasing effects in the inversion for load coefficients and geocenter motion from GPS data, *Geophysical Research Letters*, *29*(24), 63–1–63–4, doi:10.1029/2002GL016324.

Wu, X., M. B. Heflin, E. R. Ivins, D. F. Argus, and F. H. Webb (2003), Large-scale global surface mass variations inferred from GPS measurements of load-induced deformation, *Geophysical Research Letters*, *30*(14), SDE 5–1–SDE 5–4, doi:10.1029/2003GL017546.

Wu, X., M. B. Heflin, E. R. Ivins, and I. Fukumori (2006), Seasonal and interannual global surface mass variations from multisatellite geodetic data, *Journal of Geophysical Research: Solid Earth*, *111*(B9), doi:10.1029/2005JB004100.

Wu, X., M. B. Heflin, H. Schotman, B. L. A. Vermeersen, D. Dong, R. S. Gross, E. R. Ivins, A. W. Moore, and S. E. Owen (2010), Simultaneous estimation of global present-day water transport and glacial isostatic adjustment, *Nature Geoscience*, *3*(9), 642–646, doi:10.1038/ngeo938.

Wu, X., X. Collilieux, Z. Altamimi, B. L. A. Vermeersen, R. S. Gross, and I. Fukumori (2011), Accuracy of the International Terrestrial Reference Frame origin and Earth expansion, *Geophysical Research Letters*, *38*(13), doi:10.1029/2011GL047450.

Wu, X., J. Ray, and T. van Dam (2012), Geocenter motion and its geodetic and geophysical implications, *Journal of Geodynamics*, *58*, 44–61, doi:10.1016/j.jog.2012.01.007.

Wu, X., C. Abbondanza, Z. Altamimi, T. M. Chin, X. Collilieux, R. S. Gross, M. B. Heflin, Y. Jiang, and J. W. Parker (2015), KALREF—A Kalman filter and time series approach to the International Terrestrial Reference Frame realization, *Journal of Geophysical Research: Solid Earth*, *120*(5), 3775–3802, doi:10.1002/2014JB011622.

Wunsch, C., and D. Stammer (1997), Atmospheric loading and the oceanic "inverted barometer" effect, *Reviews of Geophysics*, *35*(1), 79–107, doi:10.1029/96RG03037.

Wunsch, C., P. Heimbach, R. M. Ponte, and I. Fukumori (2009), The global general circulation of the ocean estimated by the ECCO-consortium, *Oceanography*, *22*(2), 88–103, doi:10.5670/oceanog.2009.41.

Zelensky, N. P., F. G. Lemoine, D. S. Chinn, S. Melachroinos, B. D. Beckley, J. W. Beall, and O. Bordyugov (2014), Estimated SLR station position and network frame sensitivity to time-varying gravity, *Journal of Geodesy*, *88*(6), 517–537, doi:10.1007/s00190-014-0701-4.

Zhang, J., Y. Bock, H. Johnson, P. Fang, S. D. P. Williams, J. Genrich, S. Wdowinski, and J. Behr (1997), Southern California permanent GPS geodetic array: error analysis of daily position estimates and site velocities, *Journal of Geophysical Research: Solid Earth*, *102*(B8), 18,035–18,055, doi:10.1029/97JB01380.

Zhou, J., W. Sun, and J. Dong (2015), A correction to the article "Geo-center movement caused by huge earthquakes" by Wenke Sun and Jie Dong, *Journal of Geodynamics*, *87*, 67–73, doi:10.1016/j.jog.2015.02.003.

Zwally, H. J., and M. B. Giovinetto (2011), Overview and assessment of Antarctic ice-sheet mass balance estimates: 1992–2009, *Surveys in Geophysics*, *32*(4-5), 351–376, doi:10.1007/s10712-011-9123-5.